

STANFORD RESEARCH INSTITUTE
MENLO PARK, CALIFORNIA



November 1966

Report 5

FLUX SWITCHING IN MAGNETIC CIRCUITS

Prepared for:

JET PROPULSION LABORATORY
4800 OAK GROVE DRIVE
PASADENA, CALIFORNIA 91103

CONTRACT 951383 UNDER NAS7-100
(Extension of work under Contracts
950095 under NASw-6 and
950943 under NAS7-100)

By: D. NITZAN V. W. HESTERMAN E. K. VAN DE RIET

SRI Project 5670

Approved: D. R. BROWN, MANAGER
COMPUTER TECHNIQUES LABORATORY

J. D. NOE, EXECUTIVE DIRECTOR
ENGINEERING SCIENCES AND INDUSTRIAL DEVELOPMENT

This work was performed for the Jet Propulsion Laboratory,
California Institute of Technology, sponsored by the
National Aeronautics and Space Administration under
Contract NAS7-100.

Copy No. 33

ABSTRACT

The total $\dot{\phi}(t)$ waveform of a square-loop core switched by an MMF $F(t)$ having a short rise time T_r and amplitude F_D is composed of elastic $\dot{\phi}(t)$ and inelastic $\dot{\phi}(t)$. The elastic $\dot{\phi}(t)$, $\dot{\phi}_e(t)$, has two components: a high-amplitude spike, $\dot{\phi}_{e_r}(t)$, due to rotation of magnetization, followed by a low-amplitude tail, $\dot{\phi}_{e_w}(t)$, due to domain-wall motion. When a 1200-Oe transverse field was superimposed, $\dot{\phi}_{e_w}(t)$ disappeared. Each $\dot{\phi}_e$ component is described by a second-order differential equation of the form $\phi_e + \delta \ddot{\phi}_e + \eta \dot{\phi}_e = \epsilon F$, where δ , η , and ϵ are coefficients; the initial conditions are $\phi_e = 0$ and $\dot{\phi}_e = 0$. For $\dot{\phi}_{e_w}$, this equation results directly by considering the stiffness, the viscous damping, and the mass of an average domain wall. For $\dot{\phi}_{e_r}$, the solution of this equation for a step $F(t)$ is shown to be equivalent to the component of $\dot{\phi}$ along the applied field which is obtained by solving Landau-Lifshitz or Gilbert equation for a small angle of rotation and low viscous damping. A good fit is obtained between the computed $\dot{\phi}_{e_r}(t) + \dot{\phi}_{e_w}(t) + \dot{\phi}_{air}(t)$ and the experimental $\dot{\phi}_e(t)$ of a thin ferrite core of nominal composition $[\text{Mg}_{0.32}\text{Zn}_{0.10}\text{Mn}_{0.58}]^{++}[\text{Mn}_{0.52}\text{Fe}_{1.48}]^{+++}\text{O}_4$ in the range $F_c \leq F_D \leq 44 F_c$, where $F_c = 0.9 \text{ At}$ is the coercive MMF. The values $\delta_r = 0.28 \text{ ns}$, $\eta_r = 0.08 \text{ ns}^2$ (underdamped with 490 Mc/s oscillations), and $\epsilon_r = 0.14 \cdot (1 - 0.005 F_D) nH/t^2$ were used to compute $\dot{\phi}_{e_r}$, and the values $\delta_w = 4 \text{ ns}$, $\eta_w = 2 \text{ ns}^2$ (overdamped), and $\epsilon_w = 0.266 (1 - 0.008 F_D) nH/t^2$ were used to compute $\dot{\phi}_{e_w}$. Comparing $\dot{\phi}_{e_r}(t)$ with the solution of the Gilbert equation yields the damping constant $\alpha \approx 0.57$ and the anisotropy constant $K_1 \approx -3.6 \cdot 10^4 \text{ ergs/cm}^3$. For either component, $\phi_e + \delta \ddot{\phi}_e \approx \epsilon F$ if $T_r \gg \eta/\delta$, e.g., if $T_r \gtrsim 5 \text{ ns}$. We have found that δ_r and δ_w increase with T_r . For $T_r = 65 \text{ ns}$, $\delta_r \approx \delta_w \approx 6 \text{ ns}$; hence, $\dot{\phi}_e \approx (\epsilon_r + \epsilon_w) \dot{F} = \epsilon \dot{F}$ if $T_r \gtrsim 60 \text{ ns}$. A schematic plot of energy gradient vs. wall position is used to explain the qualitative difference between elastic and inelastic wall displacements. Two components of inelastic $\dot{\phi}(t)$ are distinguished: Decaying $\dot{\phi}(t)$, $\dot{\phi}_i(t)$, due to minor inelastic wall displacements of essentially constant wall area, and the bell-shaped main $\dot{\phi}(t)$, $\dot{\phi}_{ma}(t)$, due to major inelastic wall displacements (involving domain collisions) of varying wall areas.

Semiempirical models for $\dot{\phi}_i$ and $\dot{\phi}_{ma}$ were proposed previously:

$$\dot{\phi}_i(t) = \lambda_i (F - F_i)^{\nu_i} \exp [-(t - T_i)(F - F_i)/C_i],$$

where λ_i , F_i , ν_i , and C_i are $\dot{\phi}_i$ -switching parameters, and

$$\dot{\phi}_{ma}(t) = \dot{\phi}_p(F) \{1 - [(2\phi + \phi_r - \phi_d)/(\phi_r + \phi_d)]^2\},$$

where $\dot{\phi}_p(F)$ is the peak of $\dot{\phi}_{ma}$ and $\phi_d = \phi_d(F)$ is the ϕ value on the static $\phi(F)$ curve. A previous two-region curve fitting for $\dot{\phi}_p(F)$ is extended by adding a third region for low F between the static threshold, F_d^{\min} , and the dynamic threshold F_0'' . A good agreement is obtained between computed $\dot{\phi}_{\epsilon_r}(t) + \dot{\phi}_{\epsilon_w}(t) + \dot{\phi}_{air}(t) + \dot{\phi}_i(t) + \dot{\phi}_{ma}(t)$ and the experimental $\dot{\phi}(t)$ of the above thin ferrite core in the range $0.67 F_c \leq F_D \leq 40 F_c$. An approximation of $\dot{\phi}_i + \dot{\phi}_{ma}$ is used to compute $F(t)$ of a core driven by rectangular and sinusoidal voltage-drive pulses. The resulting $F(t)$ waveforms have not yet been verified experimentally, but they are very similar in shape to published data on measured $F(t)$ of various core materials. Experiments on switching from a partially-set state were performed for the case where the TEST pulse, used for determining the switching properties, follows immediately the rectangular PARTIAL-SET pulse. The slope and threshold of the resulting $\dot{\phi}_p(F)$ and the peaking time of $\dot{\phi}(t)$ were found to be essentially the same as those obtained previously for a large separation (50 μ s) between the two pulses. It is concluded that the relaxation of magnetization following the PARTIAL-SET pulse has a relatively small effect on the properties of switching from a partially set state.

A computer-aided analysis was developed for worst-case analysis and design verification of a core-diode-transistor binary counter. Each stage is composed of two ferrite cores, two diodes, one transistor, one inductor, and two resistors. The two cores are linked by three windings, and one core is also coupled to the cores of a second stage behind. The operation of each stage is divided into four modes, Modes I - IV; each of Modes II and IV occurs twice in a row. Operation fails if the supply voltage, V_s , is below $V_{s,\min}$ or above $V_{s,\max}$ because of spurious transistor turn-off in Mode III. Nonlinear models are used to describe each core, inductor, diode, and transistor in the circuit. The core model includes elastic and inelastic $\dot{\phi}$ components, as described above. The inductor model is

$$L = L_0 \exp (-i/I_{con}) ,$$

where L_0 and I_{con} are constants. The diode model is composed of a resistance R_d in series with the following elements in parallel: a current source $i_{fd} = I_{sd} [\exp (V_d/\theta_{md}) - 1]$, where I_{sd} is the saturation current, V_d is the voltage across the source, and θ_{md} is a constant voltage; a leakage resistance, R_{ld} ; a diffusion capacitance

$$C_{dd} = k_d (i_{fd} + I_{sd}) ,$$

where k_d is a constant; and a junction capacitance

$$C_{jd} = C_{j0d} [1 - (V_d/V_{\phi d})]^{-N_d} ,$$

where C_{j0d} , $V_{\phi d}$, and N_d are constants. The transistor model is composed of two back-to-back diodes, each represented by a model similar to the above diode model, which are shunted by forward and reverse current sources, $\alpha_n i_{fe}$ and $\alpha_i i_{fc}$, and a base resistance, R_b . Measurement techniques, measured data, and computer programs for least-mean-square curve fitting of these data are provided for determination of the parameters of these models. The resulting parameter values are used in a computer analysis of the counter. The analysis is based on general equations for all the operation modes, and uses a simple predictor-corrector numerical method for solving a set of differential equations and the Newton-Raphson method for solving a set of implicit equations. The core and circuit parameters are read in by the computer, and the time variables are computed at every time increment throughout the four modes of operation. The resulting machine-plotted waveforms agree favorably with experimental oscillograms in three cases: $T = -10^\circ\text{C}$ and $V_s = 15\text{ V}$ (extreme low), $T = 25^\circ\text{C}$ and $V_s = 28\text{ V}$ (nominal), and $T = 85^\circ\text{C}$ and $V_s = 50\text{ V}$ (extreme high). In case of an operation failure, the computation terminates for the given V_s . Computation of $V_{s,\min}$ is done by repeating the computation using increasing values of V_s until a proper four-mode operation is achieved. Computed and experimental $V_{s,\min}$ were found to be 16.1 V and 15.0 V, respectively. Worst-case $V_{s,\min}$ is computed in a similar manner by changing each parameter value by a given nonuniformity percentage in a direction to increase $V_{s,\min}$. It was thus found that $V_{s,\min} = 16.8, 18.8, 19.8, 21.3, \text{ and } 23.3\text{ V}$ for worst-case parameter variation of 5, 10, 15, 20, and 25 percent, respectively. The specified minimum supply voltage of 22.4 V requires that no parameter variation should exceed 23 percent. As a safety factor, the variation limit should be lower than 23 percent.

PRECEDING PAGE BLANK NOT FILMED.

CONTENTS

ABSTRACT	iii
LIST OF ILLUSTRATIONS	ix
LIST OF TABLES	xiii
LIST OF SYMBOLS	xv
ACKNOWLEDGMENTS	xxvii
PREFACE	xxix
I INVESTIGATION OF FLUX SWITCHING	1
A. Elastic and Inelastic Flux Switching	1
1. Introduction	1
2. Domain-Wall Displacements	2
3. Rotation of Magnetization	8
4. Flux-Switching Models	15
5. Experimental Verification	26
6. Discussion	37
B. Voltage Drive	45
1. Introduction	45
2. Computation of $F(\dot{\phi}, \phi)$	45
3. Examples of $\dot{\phi}(t)$ Drives	46
4. Computation of $F(t)$ for Given $\dot{\phi}(t)$	48
C. Flux Switching from a Partially Set State	51
1. Introduction	51
2. Experiment	52
3. Results and Discussion	54
4. Conclusions	65
II COMPUTER-AIDED ANALYSIS OF A CORE-DIODE-TRANSISTOR BINARY COUNTER	67
A. Introduction	67
B. Binary-Counter Operation	68
1. Circuit	68
2. Modes of Operation	68
3. COUNT-State Propagation	71
4. Range of Supply Voltage	74
C. Device Models	81
1. Core Model	81
2. Inductor Model	83
3. Diode Model	85
4. Transistor Model	87

CONTENTS

D. Determination of Parameters	90
1. Core Parameters	91
2. Inductor Parameters	108
3. Diode Parameters	109
4. Transistor Parameters	120
5. Summary	140
E. Computer Analysis	140
1. Circuit Equations	144
2. Computation Methods	150
3. Computer Program	161
4. Experimental and Computed Time-Variable Waveforms	175
5. Computed $V_{s,min}$ for Various Worst-Case Conditions	182
6. Conclusions	
APPENDIX A	183
APPENDIX B	187
APPENDIX C	191
APPENDIX D	195
APPENDIX E	197
APPENDIX F	199
APPENDIX G	201
REFERENCES	213
INDEX	215

ILLUSTRATIONS

Fig. 1	Schematic Plot of Energy <i>vs.</i> Domain-Wall Position	2
Fig. 2	Schematic Plots of Energy Gradient <i>vs.</i> Wall Position and Elastic (Dotted Line) and Inelastic (Dashed Line) Displacements of Two Domain Walls	3
Fig. 3	Schematic Construction of Static $M(H)$ Major Curve and Minor Loop Due to Reversible and Irreversible Displacements of a Single Domain Wall	6
Fig. 4	Relation Between a Static $M(H)$ Curve for Positive H and a Probability-Density Function of H_{th}	7
Fig. 5	Damped Precession of a Magnetization Vector Toward Alignment with the Total Field H_t	10
Fig. 6	Flux-Switching Experiment	16
Fig. 7	Postulated Waveforms of $\dot{\phi}_\epsilon(t)$ and its Components $\dot{\phi}_{\epsilon r}(t)$ and $\dot{\phi}_{\epsilon w}(t)$, in Response to Applied $F(t)$ of Amplitude F_D and Short Rise Time T_r	17
Fig. 8	Superposition of Experimental Waveforms of $\dot{\phi}_\epsilon(t)$ Without a Magnet, $\dot{\phi}_\epsilon(t)$ with a Magnet, and $\dot{\phi}_{air}(t)$, in Response to a Step $F(t)$ of $T_r = 0.4$ ns and Amplitude $F_D = 4.0$ At	18
Fig. 9	Experimental (Solid Line) and Computed (Dashed Line) $\dot{\phi}(t)$ Waveforms of Unloaded Core E-6 During the Beginning of Switching, Using $F(t)$ with $T_r \approx 65$ ns and Various Values of Amplitude F_D	27
Fig. 10	Experimental (Solid Line) and Computed (Dashed Line) $\dot{\phi}(t)$ Waveforms of Unloaded Core E-6 During the Beginning of Switching, Using $F(t)$ with $T_r \approx 13$ ns and Various Values of Amplitude F_D	28
Fig. 11	Cutaway View of a Coaxial Core Holder	30
Fig. 12	A Circuit for Core Switching by Bipolar Current Pulses of 0.4 ns Rise Times	31
Fig. 13	Experimental (Dotted and Solid Line) and Computed (Dashed Line) $F(t)$ and $\dot{\phi}_\epsilon(t)$ Waveforms of Unloaded Core E-6, Using $F(t)$ with $T_r = 0.4$ ns and Various Values of Amplitude F_D	35
Fig. 14	Experimental (Dotted and Solid Line) and Computed (Dashed Line) $\dot{\phi}(t)$ Waveforms of Unloaded Core E-6, Using $F(t)$ with $T_r = 0.4$ ns and Various Values of Amplitude F_D	38
Fig. 15	Computed $F(t)$ Waveforms of Core E-6 for Two Given $\dot{\phi}(t)$ Drives	50
Fig. 16	Pulse Sequence for Partial-Setting Experiment	53
Fig. 17	$\dot{\phi}_p(F)$ with T_{ps} as a Parameter	55
Fig. 18	Plots of F_0'' , λ , and ν <i>vs.</i> Log T_{ps} for $T_b = 0$ and for $T_b \approx 50$ μs	56
Fig. 19	Plot of $t_p^{-1}(F)$ with T_{ps} as a Parameter	59
Fig. 20	Comparison of $\dot{\phi}(t)$ with a sech^2 Function of Time	61
Fig. 21	Family of $\dot{\phi}(t)$ Waveforms with F as a Parameter	62
Fig. 22	Comparison of $\dot{\phi}(t)$ Waveforms for Two T_{ps} Values	62
Fig. 23	Waveforms of $\dot{\phi}(t)$ for Two F Values and Two T_{ps} Values	64

ILLUSTRATIONS

Fig. 24	Waveform of $\dot{\phi}(t)$ for $\phi_{ps} \approx +\phi_r$	65
Fig. 25	First Three Stages of a Core-Diode-Transistor Binary Counter	69
Fig. 26	Drive Currents and Flux Changes in Cores 1 and 2 During Four Modes of Normal Operation	70
Fig. 27	Variation of $\phi_1(F_1)$ and $\phi_2(F_2)$ for V_s Slightly Above $V_{s,min}$ (Proper Operation) and for V_s Slightly Below $V_{s,min}$ (Operation Failure)	75
Fig. 28	Flow Chart Explaining The Causes of Spurious Transistor Turn-Off in Mode III-C as V_s is lowered Below $V_{s,min}$	76
Fig. 29	Variations of $\phi_1(F_1)$ and $\phi_2(F_2)$ for V_s Slightly Below $V_{s,max}$ (Proper Operation) and for V_s Slightly Above $V_{s,max}$ (Operation Failure)	79
Fig. 30	Flow Chart Explaining the Causes of Spurious Transistor Turn-Off in Mode III-C as V_s is Raised Above $V_{s,max}$	80
Fig. 31	Exponential Model for $\psi(i)$ and Incremental $L(i)$ of a Ferrimagnetic Inductor	84
Fig. 32	An Equivalent Circuit for a pn Junction Diode	85
Fig. 33	An Equivalent Circuit for an nnp Transistor	88
Fig. 34	Flux-Switching and Drive-Current Program for Measurement of a Static $\phi(F)$ Curve	92
Fig. 35	Semiautomatic Static- $\phi(F)$ Plotter	94
Fig. 36	Measured and Computed Static $\phi(F)$ Curves at Different Temperature Values	98
Fig. 37	Static $\phi(F)$ Parameters $vs.$ Temperature	101
Fig. 38	Measured and Computed $\dot{\phi}_p(F)$ Curves $vs.$ Temperature	103
Fig. 39	$\dot{\phi}_p(F)$ Parameters $vs.$ Temperature	106
Fig. 40	A Circuit for Measurement of the Parameters of a Nonlinear Inductor	108
Fig. 41	Experimental $i(t)$ and $\psi(t)$ Oscillograms of a Nonlinear Inductor	109
Fig. 42	Experimental and Computed Incremental Inductance $vs.$ Current of Nonlinear Inductors	110
Fig. 43	Nonlinear-Inductor Parameters $vs.$ Temperature	114
Fig. 44	Measured (Data Points) and Computed (Solid Curve) Forward V-I Characteristics $vs.$ Temperature of an FD643 Diode	115
Fig. 45	Static Forward V-I Parameters $vs.$ Temperature of an FD643 Diode	117
Fig. 46	Reverse Characteristic of an FD643 Diode	118
Fig. 47	Leakage Resistances $R\ell_d$ of an FD643 Diode and $R\ell_e$ and $R\ell_c$ of a 2N956 Transistor $vs.$ Temperature	119
Fig. 48	Determination of Base-Emitter Forward Static Characteristics	122
Fig. 49	Measured and Computed Base Current $vs.$ Base-Emitter and Base-Collector Voltages of a 2N956 Transistor.	124
Fig. 50	Static Forward Parameters $vs.$ Temperature of a 2N956 Transistor	128
Fig. 51	Measured β_n $vs.$ I_c of a 2N956 Transistor	129
Fig. 52	Measured β_i $vs.$ I_e of a 2N956 Transistor	130
Fig. 53	A Circuit for Measuring C_{je} $vs.$ V_e	131
Fig. 54	Measured Junction Capacitances $vs.$ Voltage and Temperature of a 2N956 Transistor	132

ILLUSTRATIONS

Fig. 55	Parameters of Emitter and Collector Junction Capacitances vs. Temperature of a 2N956 Transistor	134
Fig. 56	A Measurement Circuit for Determination of Emitter Diffusion Capacitance . . .	135
Fig. 57	Transient Waveforms of Collector Current in Response to a Small Step Change in Base Current of a 2N956 Transistor in the active region	138
Fig. 58	Diffusion-Capacitance Parameters k_e and k_c vs. Temperature of a 2N956 Transistor	139
Fig. 59	Experimental (Heavy Line) and Computed (Light Line) Current and Voltage Waveforms in Four Modes of Operation of a Core-Diode-Transistor Binary Counter at $T = -10^\circ\text{C}$ and $V_s = 15\text{V}$	162
Fig. 60	Experimental (Heavy Line) and Computed (Light Line) Current and Voltage Waveforms in Four Modes of Operation of a Core-Diode-Transistor Binary Counter at $T = 25^\circ\text{C}$ and $V_s = 28\text{V}$	166
Fig. 61	Experimental (Heavy Line) and Computed (Light Line) Current and Voltage Waveforms in Four Modes of Operation of a Core-Diode-Transistor Binary Counter at $T = 85^\circ\text{C}$ and $V_s = 50\text{V}$	170
Fig. 62	Variations of $\phi_1(F_1)$ and $\phi_2(F_2)$ During Four Modes of Operation of a Core-Diode-Transistor Binary Counter at $T = -10^\circ\text{C}$ and $V_s = 15\text{V}$	176
Fig. 63	Variations of $\phi_1(F_1)$ and $\phi_2(F_2)$ During Four Modes of Operation of a Core-Diode-Transistor Binary Counter at $T = 25^\circ\text{C}$ and $V_s = 28\text{V}$	177
Fig. 64	Variations of $\phi_1(F_1)$ and $\phi_2(F_2)$ During Four Modes of Operation of a Core-Diode-Transistor Binary Counter at $T = 85^\circ\text{C}$ and $V_s = 50\text{V}$	178
Fig. 65	The Effect of Worst-Case Parameter Variation on Computed $V_{s,\min}$	181

PRECEDING PAGE BLANK NOT FILMED.

TABLES

Table I	Propagation of States in a Core-Diode-Transistor Binary Counter	72
Table II(a)	Specifications of the Current Driver in the Static $\phi(F)$ Plotter	96
Table II(b)	Specifications of the Flux Reference in the Static $\phi(F)$ Plotter	97
Table III	Device Parameter Values (in MKS Units) vs. Temperature and the Sign S of a Change in the Parameter Value Which Increases $V_{s,min}$ of a Core-Diode-Transistor Binary Counter	141
Table IV	Values or Expressions for the Terms in the General Loop Equation Corresponding to Each Drive Current	143

PRECEDING PAGE BLANK NOT FILMED.

LIST OF SYMBOLS

<u>Symbol</u>	<u>Definition</u>	<u>Reference</u>
A	Cross-sectional area of a core	
A_w	Area of a domain wall	p. 3
B	Flux density	
B_e	Elastic change in B	p. 41
C_{dc}	Collector-base diffusion capacitance	Eq. (100), p. 89
C_{dd}	Diode diffusion capacitance	Eq. (87), p. 86
C_{de}	Emitter-base diffusion capacitance	Eq. (93), p. 88
C_i	Parameter in model for $\dot{\phi}_i(t)$	Eq. (44), p. 22
C_{jc}	Collector-junction capacitance	Eq. (101), p. 89
C_{jd}	Diode-junction capacitance	Eq. (88), p. 86
C_{je}	Emitter-junction capacitance	Eq. (94), p. 88
C_{j0c}	C_{jc} for $V_c = 0$	Eq. (101), p. 89
C_{j0d}	C_j for $V_d = 0$	Eq. (88), p. 86
C_{j0e}	C_j for $V_e = 0$	Eq. (94), p. 88
c	Abbreviation for $(2\mu_0 M_s A_w)^{-1}$	Fig. 2, p. 3
d_{max}	Maximum percentage deviation from a nominal value of a core or circuit parameter	Eq. (163), p. 150
E	Energy	
F	MMF	
F_B	MMF at boundary between nonlinear and linear regions of $\dot{\phi}_p(F)$	Eq. (48), p. 25
F_c	Coercive F	Fig. 6(a), p. 16

SYMBOLS

<u>Symbol</u>	<u>Definition</u>	<u>Reference</u>
F_D	Amplitude of drive MMF	Fig. 7, p. 17
F_d	F value on static $\phi(F)$ curve	Fig. 6(a), p. 16
F_{dB}	MMF boundary between the two nonlinear regions of $\dot{\phi}_p(F)$	Eq. (48), p. 25
F_d^{\min}	Static- F threshold	Fig. 4, p. 7, and p. 25
F_i	MMF threshold for decaying inelastic $\dot{\phi}_i$	Eq. (44), p. 22
F_z	Initial F value under voltage drive	p. 46
F_0	MMF threshold obtained by extrapolating linear $\dot{\phi}_p(F)$ to F axis	Eq. (48), p. 25
F_0''	Dynamic- F threshold	Eq. (48), p. 25
F_{0i}	Asymptotic value for F_i	Eq. (45), p. 23
f	Frequency	
f_r	Resonance frequency	footnote, p. 42
f_r'	f_r for μ'	footnote, p. 42
f_r''	f_r for μ''	footnote, p. 42
f_{rr}	f_r due to rotation of magnetization	footnote, p. 42
f_{rr}'	f_{rr} for μ_r'	footnote, p. 42
f_{rr}''	f_{rr} for μ_r''	footnote, p. 42
f_{rw}	f_r due to wall motion	footnote, p. 42
f_{rw}'	f_{rw} for μ_{rw}'	footnote, p. 42
f_{rw}''	f_{rw} for μ_{rw}''	footnote, p. 42
H	Applied magnetic field	Fig. 5, p. 10
H_a	Parameter in the hyperbolic model for static $B(H)$	Eq. (82), p. 82
H_d	Demagnetizing H	p. 9

SYMBOLS

<u>Symbol</u>	<u>Definition</u>	<u>Reference</u>
H_d^{min}	Static H threshold	Fig. 4, p. 7
H_i	H threshold for decaying inelastic \dot{B}	p. 21
H_i	Internal field due to anisotropy and demagnetizing fields	p. 9
H_k	Anisotropy H	p. 9
H_n, H_q	Parameters in the hyperbolic model for static $B(H)$	Eq. (82), p. 82
H_t	Total H	p. 8
H_{th}	Threshold H	Fig. 2, p. 3
H_{0i}	Asymptotic value of H_i	p. 23
h	Height of a core	
I	Current amplitude	
I_b	Base-current amplitude	Fig. 33, p. 88
I_c	Collector-current amplitude	Fig. 33, p. 88
I_{CL}	CLEAR-current amplitude	p. 74
I_{con}	Current constant (parameter in nonlinear L model)	Eq. (84), p. 83
ID	Inside diameter	
I_e	Emitter-current amplitude	Fig. 33, p. 88
I_L	Amplitude of i_L	Fig. 26, p. 70
I_s	Average value of i_s	Eq. (164), p. 155
I_{sc}	Collector-junction saturation current	Eq. (98), p. 89
I_{sd}	Diode saturation current	Eq. (85), p. 85
I_{se}	Emitter-junction saturation current	Eq. (91), p. 87
i_b	Base current	Fig. 33, p. 88

SYMBOLS

<u>Symbol</u>	<u>Definition</u>	<u>Reference</u>
i_c	Collector current	Fig. 33, p. 88
i_{CL}	CLEAR current	Fig. 25, p. 69
i_d	Current linking Cores 1 and 2 in series with a diode or transistor in a binary counter	Fig. 25, p. 69
i_e	Emitter current	Fig. 33, p. 88
i_f	Semiconductor-junction current	<i>e.g.</i> , i_{fd} , p. 85
i_{fc}	Collector-junction i_f	Fig. 33, p. 88
i_{fd}	Diode i_f	p. 85
i_{fe}	Emitter-junction i_f	Fig. 33, p. 88
i_L	Current source in a binary counter	Fig. 25, p. 69
i_s	Drive current in a binary counter	Fig. 25, p. 69
k	A constant proportional to diffusion capacitance	<i>e.g.</i> , k_d , Eq. (87), p. 86
k_c	Collector k	Eq. (100), p. 89
k_d	Diode k	Eq. (87), p. 86
k_e	Emitter k	Eq. (93), p. 88
K_1	First-order anisotropy constant	p. 40
L	Incremental inductance	pp. 83-84
L_0	L at $i = 0$	pp. 83-84
l	Average core length	
l_i	Inside l	p. 91
l_o	Outside l	p. 91
M	Magnetization	Fig. 5, p. 10
\dot{M}	dM/dt	

SYMBOLS

<u>Symbol</u>	<u>Definition</u>	<u>Reference</u>
M_a	Component of M along the applied field	p. 10
M_{a0}	Initial M_a	Fig. 5, p. 10
M_r	Remanent M	Fig. 4, p. 7
M_s	Saturation M	p. 10
M_0	Initial M	Fig. 5, p. 10
$M_{\epsilon w}$	Elastic ΔM due to wall motion	p. 7
m	m factor varying between 1 and ≈ 2	p. 86
m_c	Collector-junction m	Eq. (99), p. 89
m_d	Diode m	Eq. (85a), p. 86
m_e	Emitter-junction m	Eq. (92), p. 88
m_w	Domain-wall mass	Eq. (4), p. 7
N_{CL}	Number of turns of CLEAR winding	Fig. 5, p. 69
N_c	Power coefficient of C_{jc} model	Eq. (101), p. 89
N_d	Power coefficient of C_{jd} model	Eq. (88), p. 86
N_e	Power coefficient of C_{je} model	Eq. (94), p. 88
NV	Negligible value of $\dot{\phi}$ in computer program	Eq. (166), p. 155
n	Number of inelastic wall displacements	p. 21
OD	Outside diameter	
P	Parameter value	Eq. (163), p. 150
P_n	Nominal parameter value	Eq. (163), p. 150
p	Portion of inelastic domain displacements that are minor	p. 21
R_b	Base resistance	Fig. 33, p. 88

SYMBOLS

<u>Symbol</u>	<u>Definition</u>	<u>Reference</u>
R_{bc}	$R_b + R_c$	Eq. (119), p. 126
R_c	Collector resistance	Fig. 33, p. 88
R_d	Diode resistance	Fig. 32, p. 85
R_e	Emitter resistance	Fig. 33, p. 88
$R_{\ell c}$	Collector-junction leakage resistance	Fig. 33, p. 88
$R_{\ell d}$	Diode leakage resistance	Fig. 32, p. 85
$R_{\ell e}$	Emitter-junction leakage resistance	Fig. 33, p. 88
r_i	Inside radius	p. 91
r_o	Outside radius	p. 91
S	Sign of worst-case parameter change	Eq. (163), p. 150
S_i	$\dot{\phi}_i$ - switching coefficient	p. 22
s	Laplace's complex frequency	
T	Temperature	
T	Duration of pulse	Fig. 6(a), p. 16
T_i	Time when $\dot{\phi}_i$ begins to rise	Eq. (44), p. 22
T_r	10% - 90% rise time	Fig. 7, p. 17
t	Time	
V_{BC}	Base-collector terminal voltage	Fig. 33, p. 88
V_{BE}	Base-emitter terminal voltage	Fig. 33, p. 88
V'_{BE}	dV_{BE}/di_b	Eq. (158), p. 149
V_{bc}	Base-collector junction voltage	Fig. 33, p. 88
V_{be}	Base-emitter junction voltage	Fig. 33, p. 88
V_{CE}	Collector-emitter terminal voltage	Fig. 33, p. 88
V_c	Collector-junction voltage	Fig. 33, p. 88

SYMBOLS

<u>Symbol</u>	<u>Definition</u>	<u>Reference</u>
V_d	Diode-junction voltage	Fig. 32, p. 85
V_e	Emitter-junction voltage	Fig. 33, p. 88
V_{pn}	Voltage across a diode	Fig. 32, p. 85
V'_{pn}	dV_{pn}/di_d	Eq. (157), p. 148
V_s	Supply voltage of a binary counter	Fig. 25, p. 69
$V_{s, \max}$	Maximum V_s above which operation fails	p. 78
$V_{s, \min}$	Minimum V_s below which operation fails	p. 74
V_1	Abbreviation for $(\phi_s - \phi_r)/[(l_o - l_i)H_a]$	Eq. (82), pp. 82-83
V_2	Abbreviation for $[(\phi_s + \phi_r)H_q]/[(l_o - l_i)H_n]$	Eq. (82), pp. 82-83
V_{ϕ_c}	Collector-junction contact potential	Eq. (101), p. 89
V_{ϕ_d}	Diode-junction contact potential	Eq. (88), p. 86
V_{ϕ_e}	Emitter-junction contact potential	Eq. (94), p. 88
z	Domain-wall position	Fig. 2, p. 3
α	Damping constant	Eq. (7), p. 8
α_i	Reverse-injection common-base current gain of a transistor	Eq. (108), p. 89
α_n	Forward-injection common-base current gain of a transistor	Eq. (107), p. 89
β	Domain-wall viscous damping	Eq. (4), p. 7
β_i	Inverse current gain of a transistor	Eq. (108), p. 89
β_n	Forward current gain of a transistor	Eq. (107), p. 89
$\beta_{n, \max}$	Maximum β_n	Eq. (133), p. 137

SYMBOLS

<u>Symbol</u>	<u>Definition</u>	<u>Reference</u>
γ	Gyromagnetic ratio	Eqs. (6) and (7), p. 8
Δt	Small time increment used in computation of time variables	p. 145
$\Delta\phi$	Flux change	
$\Delta\phi_i$	Inelastic $\Delta\phi$ due to $\dot{\phi}_i$	p. 23
$\Delta\phi_{i\infty}$	Maximum $\Delta\phi_i$	Eq. (46), p. 23
$\Delta\phi_e$	Elastic $\Delta\phi$	p. 44; Eq. (167), p. 155
$\Delta\phi_{e_r}$	$\Delta\phi_e$ due to rotation of magnetization	p. 44
$\Delta\phi_{e_w}$	$\Delta\phi_e$ due to domain-wall motion	p. 44
δ	First-derivative coefficient in elastic-switching differential equation	
δ_r	δ for rotation of magnetization	Eq. (19), p. 11
δ_w	δ for domain-wall motion	Eq. (5), p. 8
ϵ	Coefficient of elastic-switching drive	Eq. (42), p. 20
ϵ_r	ϵ for rotation of magnetization	Eq. (39), p. 20
ϵ_w	ϵ for domain-wall motion	Eq. (36), p. 19
ζ_r	Damping coefficient for $\dot{\phi}_{e_r}$ ($\zeta_r < 1$, $\zeta_r = 1$, and $\zeta_r > 1$ correspond to underdamped, critically damped, and overdamped cases, respectively)	Eq. (21a), p. 12
η	Second-derivative coefficient in elastic-switching differential equation	
η_r	η for rotation of magnetization	Eq. (19), p. 11
η_w	η for domain-wall motion	Eq. (5), p. 8
θ	Angle of magnetization switching	Fig. 5, p. 10

SYMBOLS

<u>Symbol</u>	<u>Definition</u>	<u>Reference</u>
θ_m	Parameter in p - n junction model ($\theta_m = kTm/q$)	p. 86
θ_{mc}	Collector-junction θ_m	Eq. (99), p. 89
θ_{md}	Diode θ_m	Eq. (85a), p. 86
θ_{me}	Emitter-junction θ_m	Eq. (92), p. 88
θ_0	Initial θ	Fig. 5, p. 10
λ	Constant proportional to viscous damping	Eq. (6), p. 8
λ	Coefficient proportional to $\dot{\phi}_p(F)$ for $F_{dB} \leq F \leq F_B$	Eq. (48), p. 25
λ_d	Coefficient proportional to $\dot{\phi}_p(F)$ for $F_d^{\min} \leq F \leq F_{dB}$	Eq. (48), p. 25
λ_i	Coefficient proportional to $\dot{\phi}_i$	Eq. (44), p. 22
μ	Complex initial permeability	Eq. (57), p. 41
μ'	Real Component of μ	Eq. (58), p. 41
μ''	Imaginary component of μ	Eq. (59), p. 42
$\mu_{r(0)}$	$\mu_{(0)}$ due to rotation of magnetization	p. 43
μ_0	Vacuum permeability ($\mu_0 = 4\pi \cdot 10^{-7} Hm^{-1} t^{-2}$)	p. 7
$\mu_{(0)}$	Value of $ \mu $ or μ' at zero frequency	Eq. (56a), p. 41
ν	Power coefficient of $\dot{\phi}_p(F)$ for $F_{dB} \leq F \leq F_B$	Eq. (48), p. 25
ν_d	Power coefficient of $\dot{\phi}_p(F)$ for $F_d^{\min} \leq F \leq F_{dB}$	Eq. (48), p. 25
ν_i	Power coefficient of $\dot{\phi}_i$ model	Eq. (44), p. 22
ρ_p	Coefficient proportional to $\dot{\phi}_p(F)$ for $F_B \leq F$	Eq. (48), p. 25

<u>Symbol</u>	<u>Definition</u>	<u>Reference</u>
τ	Relaxation time constant	
τ_s	Flux-switching time	<i>e.g.</i> , Eq. (73a), p. 47
φ	Angle of magnetization precession	Fig. 5, p. 10
ϕ	Magnetic flux	
ϕ_{air}	Air (vacuum) flux	p. 33
ϕ_c	Parameter in parabolic $\dot{\phi}(\phi)$ model for inelastic switching from a partially set state	Eq. (77), p. 58
ϕ_d	ϕ value on static $\phi(F)$ curve	Fig. 6(a), p. 16
ϕ'_d	$d\phi_d/dF$	Eq. (156), p. 148
ϕ_r	Maximum residual ϕ	Fig. 6(a), p. 16
ϕ_s	Saturation ϕ	p. 44
ϕ_{ϵ_r}	Elastic change in ϕ due to rotation of magnetization	Eq. (39), p. 20
ϕ_{ϵ_w}	Elastic change in ϕ due to domain-wall motion	Eq. (36), p. 19
$\dot{\phi}$	$d\phi/dt$	Eq. (33), p. 15
$\dot{\phi}_{air}$	$d\phi_{air}/dt$	Eq. (49), p. 33
$\dot{\phi}_i$	Decaying $\dot{\phi}$ due to inelastic minor wall displacements	Eq. (44), p. 22
$\dot{\phi}_{inel}$	Inelastic $\dot{\phi}$	Eq. (34), p. 15
$\dot{\phi}_{ip}$	Peak $\dot{\phi}_i$	Eq. (46), p. 23
$\dot{\phi}_m$	Amplitude of $\dot{\phi}$ drive	<i>e.g.</i> , p. 47
$\dot{\phi}_{ma}$	Main inelastic $\dot{\phi}$	Eq. (47), p. 25
$\dot{\phi}_p$	Peak $\dot{\phi}_{ma}$	Eq. (48), p. 25
$\dot{\phi}_\epsilon$	Elastic $\dot{\phi}$	Eq. (35), p. 18

SYMBOLS

<u>Symbol</u>	<u>Definition</u>	<u>Reference</u>
$\dot{\phi}_{\epsilon r}$	$\dot{\phi}_{\epsilon}$ due to rotation of magnetization	Eq. (39), p. 20
$\dot{\phi}_{\epsilon w}$	$\dot{\phi}_{\epsilon}$ due to domain-wall motion	Eq. (36), p. 19
$\dot{\phi}'_p$	$d\dot{\phi}_p/dF$	Eq. (155), p. 148
χ_w	Domain-wall susceptibility	Eq. (5), p. 8
χ_r	Rotational susceptibility	Eq. (19), p. 11
ω	Angular velocity	
ω_r	ω at $ \mu $ resonance	Eq. (63), p. 42
ω'_r	ω at μ' resonance	Eq. (61), p. 42
ω''_r	ω at μ'' resonance	Eq. (62), p. 42
ψ	Angle between net field and applied field	Fig. 5, p. 10
ψ	Flux linkage	pp. 83-84
ψ_{sat}	Saturation flux linkage of a nonlinear inductor	pp. 83-84
Ω	Angular velocity of oscillation of M_a	Eq. (17), p. 11

ACKNOWLEDGMENTS

Barbara B. Wheeler wrote the computer programs in Appendices B - F and assisted in writing the programs in Appendices A and G.

We thank C. T. Kleiner of Autonetics, a division of North American Aviation, Inc., for his valuable remarks relative to the model and parameter measurement of a transistor.

PRECEDING PAGE BLANK NOT FILMED.

PREFACE

This report is a continuation of a series of four reports entitled "Flux Switching in Multipath Cores." The first report deals primarily with flux switching in multipath cores. In subsequent reports, however, the emphasis is shifted gradually toward understanding and modeling of flux switching in toroidal cores and the application of the resulting models to computer analyses of circuits including square-loop magnetic cores. Consequently, we have finally decided to change the report title to "Flux Switching in Magnetic Circuits."

The report is divided into two sections. The first section deals with the physics of flux switching and updates the resulting semiempirical flux-switching models. These models are verified experimentally by switching a thin ferrite core with step-MMF drives of very short rise time (less than 0.4 ns) and different amplitudes (0.6 At to 40 At). The second section employs a simplified version of these models in a computer analysis of a core-diode-transistor binary counter. Here, the emphasis is on the models of semiconductor elements as well as the ferrimagnetic elements, the measurement techniques and data processing for evaluating the parameters of these models, and the application of these models in computing the circuit behavior under nominal, extreme, and worst-case conditions.

I INVESTIGATION OF FLUX SWITCHING

A. Elastic and Inelastic Flux Switching

1. Introduction

Elastic and inelastic flux-switching models have been developed in the previous four reports^{1,2,3,4*} of this project. A further investigation in this area has resulted in a better physical understanding of these models, improvement in the models themselves, and an experimental verification for the models using $F(t)$ pulses with very short rise time (0.4 ns).

The objectives of this section are as follows:

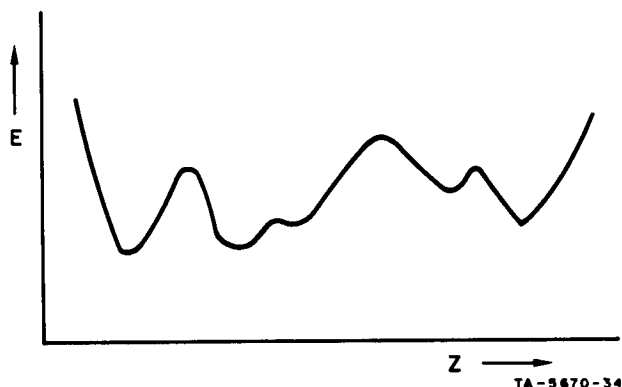
- (1) To explain the different types of domain-wall displacement in terms of the variations of energy gradient *vs.* wall position, from which an elastic wall motion was shown to be described by a second-order differential equation
- (2) To show that on the basis of the Landau-Lifshitz equation or the Gilbert equation, the component of \vec{M} along the applied magnetic field, which is induced by small-angle rotation of magnetization in a medium of low viscous damping, is described by a second-order differential equation
- (3) On the basis of experimental observation and the physical mechanism of wall motion and rotation of magnetization, to present our latest semiempirical flux-switching models for the elastic and inelastic components of $\dot{\phi}(t)$
- (4) To compare oscillograms of experimental $\dot{\phi}(t)$, induced by rectangular $F(t)$ pulses of 0.4-nanosecond rise time and variable amplitude, with computed $\dot{\phi}(t)$ waveforms.

* References are listed at the end of this report.

2. Domain-Wall Displacements

a. Energy vs. Domain-Wall Position

Consider a 180° Bloch wall of area A_w in a ferromagnetic or ferrimagnetic crystallite. The wall lies in the x - y plane and separates two domains whose saturation magnetization vectors are along the $+x$ and $-x$ directions. The total energy E of the specimen varies with the wall position z because of inhomogeneities (impurities, strains, voids, lattice imperfections, etc.) in the material.⁵ Since these inhomogeneities vary randomly, we can only plot E vs. z schematically (see Fig. 1).



We shall use the schematic plot of E vs. z to explain qualitatively the mechanism of flux switching by domain-wall motion. However, let us first examine the thermodynamic considerations associated with this plot.

Following the first law of thermodynamics,

$$dE = dQ + \mu_0 H dM, \quad (1)$$

FIG. 1 SCHEMATIC PLOT OF ENERGY
vs. DOMAIN-WALL POSITION

where Q is heat ($dQ > 0$ if heat is transferred into the system).

In general, E is a function of M , H , and the temperature T . However, since M , H , and T are related to each other by the equation of state of equilibrium, it is sufficient to express the change in E as

$$dE = \left(\frac{\partial E}{\partial T} \right)_M dT + \left(\frac{\partial E}{\partial M} \right)_T dM. \quad (2)$$

In an isothermal magnetic process, $dT = 0$, and hence,

$$\Delta E = \int_{M_0}^{M_f} \left(\frac{\partial E}{\partial M} \right)_T dM, \quad (3)$$

where M_0 and M_f are the initial and final values of M . Hence, the change in E in an isothermal condition can be expressed by the change in M only.

Recall, however, that M is proportional to the wall position, z . Thus, in examining the mechanism of flux switching in terms of E vs. z , we shall assume a constant temperature. This assumption is justified by the fact that the small amount of dissipated energy during the switching time causes a negligible change in temperature. (However, the change in temperature is not negligible for an alternate flux switching during many cycles.)

b. Elastic and Inelastic Wall Displacements

In the absence of an applied magnetic field H , the wall settles where E is minimum, i.e., where $dE/dz = 0$ and $d^2E/dz^2 > 0$. If H is now applied along the \mp direction, a force $2\mu_0 M_s H A_w$ moves the wall along the $\pm z$ direction, where M_s is the saturation magnetization. Assuming an *isothermal* condition, this motion is opposed by a restoring (or stiffness) force dE/dz . It is convenient to examine the net effect on the wall motion by comparing the applied H with $c(dE/dz)$, where $c = 1/(2\mu_0 M_s A_w)$, as functions of z . Schematic plots of $c(dE/dz)$ vs. z are shown in Fig. 2 for two typical walls (in the same crystallite) whose positions at

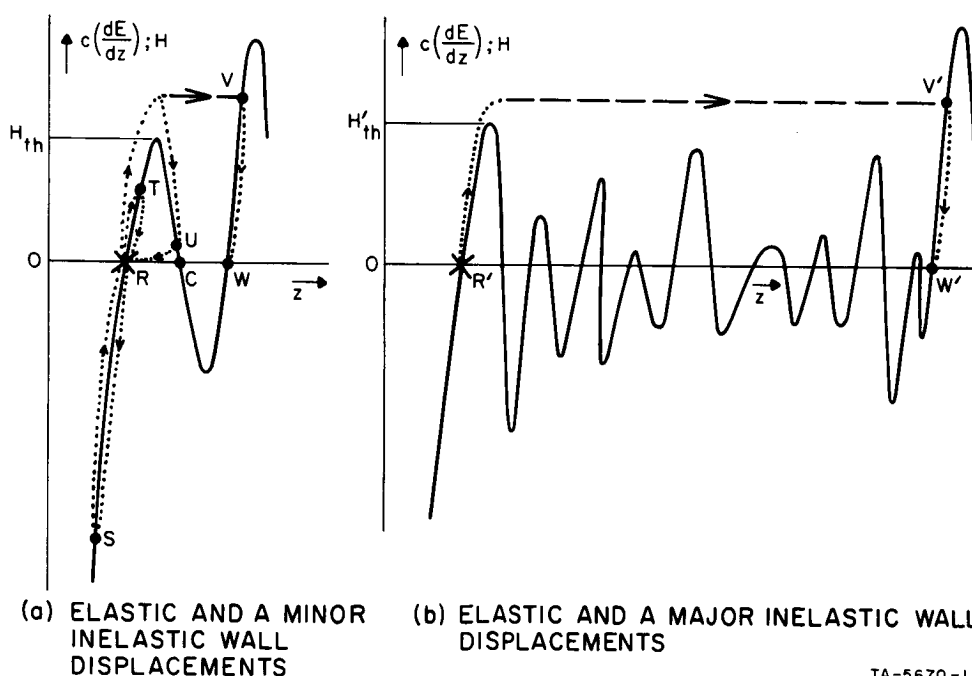


FIG. 2 SCHEMATIC PLOTS OF ENERGY GRADIENT vs. WALL POSITION AND ELASTIC (Dotted Line) AND INELASTIC (Dashed Line) DISPLACEMENTS OF TWO DOMAIN WALLS

Points R and R' , respectively, correspond to the remanent state $M = -M_r$ of the crystallite. By definition, as H is applied, a wall is displaced elastically if, upon removal of H , the restoring field $c(dE/dz)$ returns the wall to its original position; but if a new position is reached, the wall displacement is inelastic.

Suppose that the wall of Fig. 2(a) is situated at Point R . The threshold field imposed by the first energy hill is marked by H_{th} . Three types of *elastic* wall displacement are distinguished:

- (1) Due to a negative H pulse, *e.g.*, Displacement $R-S$
- (2) Due to a positive H pulse, provided that $H < H_{th}$, *e.g.*, Displacement $R-T$
- (3) Due to a positive H pulse whose amplitude exceeds H_{th} , provided that the pulse duration is short enough to prevent z from exceeding the position of maximum energy, z_C , at Point C , *e.g.*, Displacement $R-U$.

If $H > H_{th}$ and the pulse duration is not as short as in Case (3) above, the wall overcomes its energy barrier, and its displacement is *inelastic*. Here, we distinguish between minor and major wall displacements. A *minor* inelastic wall displacement is short or local; hence, the wall area is *essentially constant* during the switching time. On the other hand, a wall experiencing a *major* inelastic displacement travels a relatively long distance and thus may collide with other walls; its area will *vary* during the switching time (increasing in the beginning and decreasing in the end). A minor inelastic wall displacement results from the obstruction of the wall motion by an energy hill whose $c(dE/dz)_{max} > H$ in the *vicinity* of the initial wall position. For example, Displacement $R-V$ in Fig. 2(a) is composed of an elastic displacement followed by a minor inelastic displacement. (In order to avoid ambiguity, we might assume that the displacement is elastic if $z < z_C$ and inelastic if $z > z_C$. However, because of the effect of the wall mass, the boundary value of z is smaller than z_C .) Upon termination of the H pulse, the wall is pulled back (elastically) to Point W , and the net Δz is the difference between the z values at Points W and R . In contrast, a major inelastic wall displacement is long because no obstructing energy hill is encountered by the wall in the vicinity of its original position. For example, the larger of the positive H pulses of

Fig. 2(a) can force another wall in the same specimen to experience a major inelastic displacement, such as Displacement $R'-V'$ in Fig. 2(b).

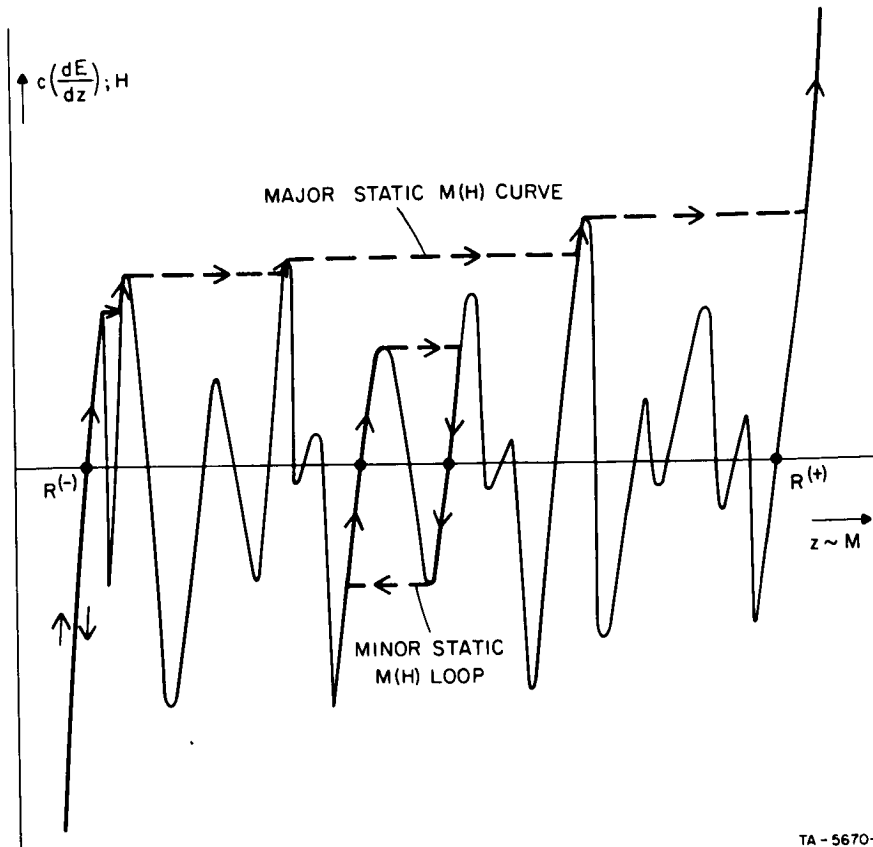
c. Reversible and Irreversible Wall Displacements

To be exact, a distinction should be made between elasticity and reversibility of a magnetic process (wall motion or rotation of magnetization). Reversibility is a thermodynamic property: a magnetic process is reversible if it is performed *quasistatically* (infinitely slowly) with *no energy dissipation*; otherwise, it is irreversible. The area enclosed between the transition path and the plot of $c(dE/dz)$ is proportional to the dissipated energy. Thus, all the elastic and inelastic wall displacements shown in Fig. 2 are irreversible. Only if H were changed quasistatically would Displacements $R-S$ and $R-T$ be reversible, because they would follow the plot $c(dE/dz)$ (which thermodynamically represents the equation of states of equilibrium at a constant temperature), and would thus involve no energy dissipation. However, if H reaches H_{th} , the wall will break free and move irreversibly to a position between Points V and W , where $c(dE/dz) = H_{th}$. Note that reversible tracking of H along $c(dE/dz)$ in the region where $dE/dz < 0$ is unrealizable, because wall positioning in this region is unstable.

d. Static $M(H)$ Curves

Suppose that the magnetization M of a crystallite changes by the motion of a single wall and, hence, ΔM is proportional to Δz . In Fig. 3, the *major static $M(H)$ curve* of this crystallite is obtained by essentially reversible and irreversible wall displacements as H is changed by small increments in the negative and the positive directions. The two extreme stable positions of the wall, designated by $R^{(-)}$ and $R^{(+)}$, correspond to the remanent values of magnetization, $-M_r$ and $+M_r$, respectively. For M between $-M_r$ and M_r , H_{th} may be smaller than H_{th} near $M = -M_r$. An example is shown in Fig. 3, where a *minor static $M(H)$ loop* is traversed. Furthermore, if the peaks of $c(dE/dz)$ near $R^{(-)}$ are higher than the following ones, the major $M(H)$ curve is *re-entrant*.

So far we have examined the displacements of a single 180° domain wall. Usually, however, a square-loop specimen contains many walls having different $c(dE/dz)$ vs. z plots. The features of these plots vary randomly. For example, the distribution of H_{th} may be



TA-5670-2

FIG. 3 SCHEMATIC CONSTRUCTION OF STATIC $M(H)$ MAJOR CURVE AND MINOR LOOP DUE TO REVERSIBLE AND IRREVERSIBLE DISPLACEMENTS OF A SINGLE DOMAIN WALL

described by a probability-density function $f(H_{th})$ with a mean value in the neighborhood of the threshold H_d^{min} of the major static $M(H)$ curve,⁶ as shown in Fig. 4. The length of an irreversible wall displacement is also a random variable with a similar probability-density function. Due to these random distribution functions, the static $M(H)$ curve of the specimen is *smooth*, as shown in Fig. 4. In addition to elastic wall displacements and elastic rotation of magnetization, this curve results from minor inelastic wall displacements in the region $0 < H \lesssim H_d^{min}$ and from major and minor inelastic wall displacements in the region $H_d^{min} \lesssim H$.

We shall next examine the equation of motion for elastic wall displacements. The equations of motion for inelastic wall motion are more complicated, and are beyond the scope of this work.

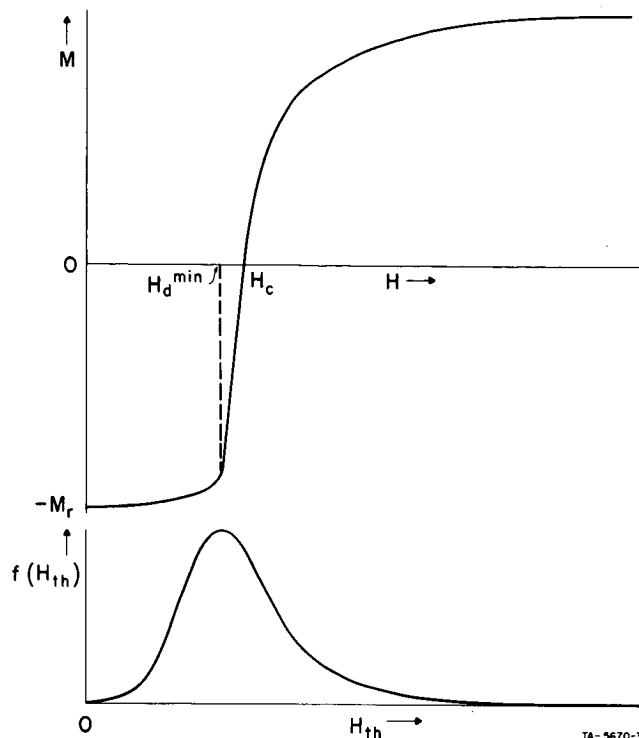


FIG. 4 RELATION BETWEEN A STATIC $M(H)$ CURVE FOR POSITIVE H AND A PROBABILITY-DENSITY FUNCTION OF H_{th} . Major inelastic wall displacement occurs only if $H \gtrsim H_d^{\min}$

e. Equation of Elastic Wall Motion

Consider a small elastic wall displacement in the z direction as a result of an applied H field. Per unit wall area, the applied force $2\mu_0 M_s H$ is opposed by three forces: by $dE/dz \approx kz$, where $k = d^2E/dz^2$ is the stiffness coefficient of a restoring force; by $\beta \dot{z}$, where β is the viscous-damping coefficient; and by $m_w \ddot{z}$, where m_w is the effective mass of the wall. The equation of motion of such a small wall displacement from equilibrium is⁷

$$kz + \beta \dot{z} + m_w \ddot{z} = 2\mu_0 M_s H \quad . \quad (4)$$

Assuming that Eq. (4) describes the motion of a typical wall whose properties are the average properties of all the walls moving elastically, we may replace z by bM_{ϵ_w} , where b is a proportionality constant and M_{ϵ_w} is the change in M due to the elastic wall motion. Thus,

$$M_{\epsilon w} + \delta_w \dot{M}_{\epsilon w} + \eta_w \ddot{M}_{\epsilon w} = \chi_w H \quad , \quad (5)$$

where

$$\delta_w = \beta/k \quad , \quad (5a)$$

$$\eta_w = m_w/k \quad , \quad (5b)$$

and

$$\chi_w = \frac{2\mu_0 M_s}{kb} \quad . \quad (5c)$$

3. Rotation of Magnetization⁸

a. Derivation of $M(t)$ Along an Applied Field from Landau-Lifshitz and Gilbert Equations

The spiral rotation of magnetization \mathbf{M} of a crystallite (or a domain) in a total magnetic field \mathbf{H}_t is described by the Landau-Lifshitz equation

$$\dot{\mathbf{M}} = -\gamma \mathbf{M} \times \mathbf{H}_t - \frac{\lambda}{M_s^2} (\mathbf{M} \times \mathbf{M} \times \mathbf{H}_t) \quad (6)$$

or by the Gilbert equation

$$\dot{\mathbf{M}} = -\gamma \mathbf{M} \times \mathbf{H}_t + \frac{\alpha}{M_s} (\mathbf{M} \times \dot{\mathbf{M}}) \quad , \quad (7)$$

where $M_s = \mathbf{M} \cdot \mathbf{M}$ is the saturation magnetization, γ is the gyromagnetic ratio, α is a unitless viscous damping, and $\lambda = \alpha\gamma M_s$ [assuming that the dissipative terms in Eqs. (6) and (7) are the same]. It can be shown by using spherical coordinates M , θ , and φ that either equation becomes a set of two differential equations,

$$\dot{\theta} = -\frac{1}{\tau} \sin \theta \quad (8)$$

and

$$\dot{\varphi} = \Omega \quad , \quad (9)$$

where

$$\tau = \begin{cases} M_s/(\lambda H_t) & \text{(Landau-Lifshitz)} \\ (1 + \alpha^2)/(\alpha \gamma H_t) & \text{(Gilbert)} \end{cases} \quad (10)$$

and

$$\Omega = \begin{cases} \gamma H_t & \text{(Landau-Lifshitz)} \\ \gamma H_t/(1 + \alpha^2) & \text{(Gilbert)} \end{cases} \quad (11)$$

Here, H_t designates the magnitude of the total field \mathbf{H}_t due to the internal field, \mathbf{H}_i , and the applied field \mathbf{H} .

The solutions of Eqs. (8) and (9) are

$$\tan \left(\frac{\theta}{2} \right) = \tan \left(\frac{\theta_0}{2} \right) e^{-t/\tau} \quad (12)$$

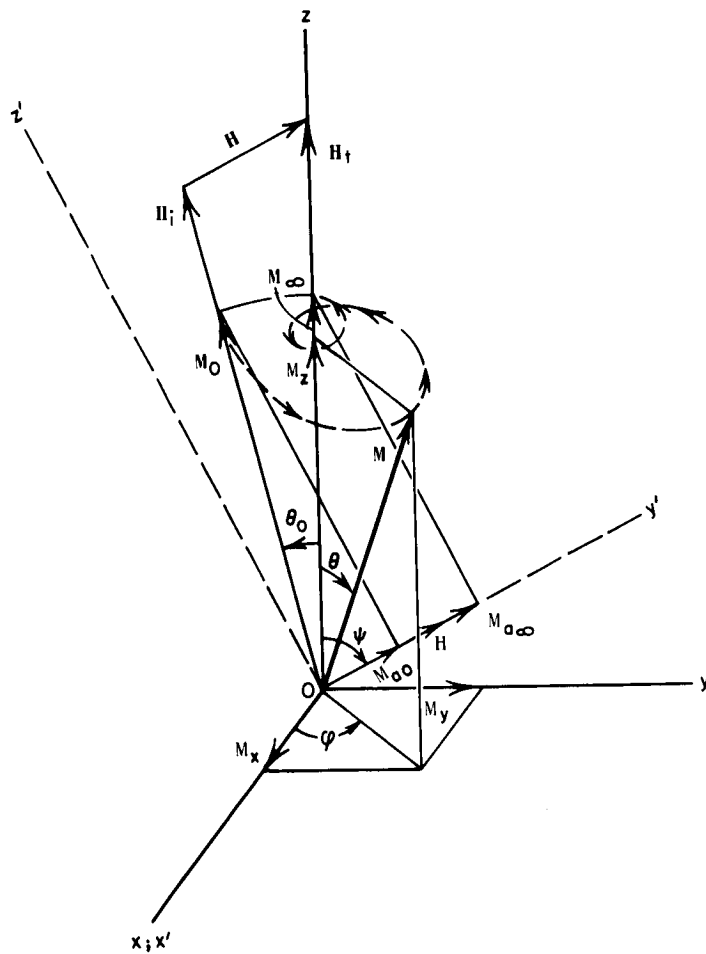
and

$$\varphi = \varphi_0 + \Omega t, \quad (13)$$

where θ_0 and φ_0 are initial values. Equations (12) and (13) define a *damped precession* of \mathbf{M} around \mathbf{H}_t , as it spirals from its initial orientation toward its final orientation.

Initially, \mathbf{M} is along the internal field, $\mathbf{H}_i = \mathbf{H}_k + \mathbf{H}_d$, where \mathbf{H}_k is the anisotropy field due to crystalline anisotropy and strain anisotropy, and \mathbf{H}_d is the demagnetizing field. An external field \mathbf{H} is now applied. Let the plane formed by \mathbf{H}_i and \mathbf{H} define the $y-z$ plane, and let the resultant total field $\mathbf{H}_t = \mathbf{H}_i + \mathbf{H}$ be along the z axis, as shown in Fig. 5. The angle between \mathbf{H}_t and \mathbf{M}_0 (the initial \mathbf{M}) is θ_0 , and the angle between \mathbf{H}_t and \mathbf{H} is ψ .

Following the application of \mathbf{H} , \mathbf{M} spirals from its initial orientation along \mathbf{H}_i into alignment with \mathbf{H}_t . During the transient time, the component of $\dot{\mathbf{M}}(t)$ along \mathbf{H} is sensed. Defining the direction of \mathbf{H} as the y' axis (see Fig. 5) we wish to calculate $M_a(t)$, the component of $\mathbf{M}(t)$ along the y' axis.



TA-5670-68

FIG. 5 DAMPED PRECESSION OF A MAGNETIZATION VECTOR TOWARD ALIGNMENT WITH THE TOTAL FIELD H_t

The components of \mathbf{M} in the (x, y, z) coordinate system are

$$\left. \begin{aligned} M_x &= M_s \sin \theta \cos \varphi \\ M_y &= M_s \sin \theta \sin \varphi \\ M_z &= M_s \cos \theta \end{aligned} \right\} \quad (14)$$

Since the (x', y', z') coordinate system is obtained by rotating the (x, y, z) coordinate system around the x axis by the angle $\pi/2 - \psi$, we obtain

$$M_a = M_s (\sin \theta \sin \varphi \sin \psi + \cos \theta \cos \psi). \quad (15)$$

Substitution of Eqs. (12) and (13) into Eq. (15) yields the following expression:

$$M_a(t) = M_s \frac{\left[1 - e^{-2(t/\tau)} \tan^2 \left(\frac{\theta_0}{2} \right) \right] \cos \psi - 2e^{-(t/\tau)} \tan \left(\frac{\theta_0}{2} \right) \cos(\Omega t) \sin \psi}{1 + e^{-2(t/\tau)} \tan^2 \left(\frac{\theta_0}{2} \right)} \quad (16)$$

b. Equations of Motion of Elastic Rotation of Magnetization

If θ_0 is smaller than the angle between \mathbf{M}_0 and the nearest hard axis, then the change in \mathbf{M} is elastic. In ferrites, whose easy axes are along the $[111]$ body diagonals, the *maximum* value the latter may have is 54.73° . Thus, for elastic switching of a polycrystalline ferrite, the average value of θ_0 under elastic-switching conditions is small enough to justify the assumption that $\tan^2(\theta_0/2) \ll 1$. Hence, Eq. (16) is reduced to the following:

$$M_a(t) = M_s \cos \psi - 2M_s \sin \psi \tan \left(\frac{\theta_0}{2} \right) e^{-(t/\tau)} \cos(\Omega t) \quad (17)$$

Differentiating Eq. (17) with respect to time, we have

$$\dot{M}_a(t) = 2M_s \sin \psi \tan \left(\frac{\theta_0}{2} \right) \sqrt{\frac{1}{\tau^2} + \Omega^2} e^{-(t/\tau)} \sin \left[\Omega t + \tan^{-1} \left(\frac{1}{\Omega \tau} \right) \right] \quad (18)$$

Consider now the second-order differential equation

$$M_a + \delta_r \dot{M}_a + \gamma_r \ddot{M}_a = \chi_r H + M_{a0} \quad (19)$$

where H is the magnitude of the applied field and M_{a0} is the initial value of M_a . If $H(t)$ is a step function, then the Laplace transform of Eq. (19) is

$$M_a(s) = M_{a0} \frac{s^2 + s \frac{\delta_r}{\eta_r} + \frac{\chi_r H + M_{a0}}{M_{a0} \eta_r}}{s \left[\left(s + \frac{\delta_r}{2\eta_r} \right)^2 + \frac{1}{\eta_r} - \left(\frac{\delta_r}{2\eta_r} \right)^2 \right]} \quad (20)$$

The inverse function of Eq. (20) yields

$$M_a(t) = M_{a0} + \chi_r H - \frac{\chi_r H}{\sqrt{1 - \frac{\delta_r^2}{4\eta_r}}} e^{-(\delta_r/2\eta_r)t} \cos \left[\sqrt{\frac{1}{\eta_r} - \left(\frac{\delta_r}{2\eta_r} \right)^2} t - \sin^{-1} \zeta_r \right] \quad (21)$$

where

$$\zeta_r = \frac{\delta_r}{2\sqrt{\eta_r}} \quad (21a)$$

Differentiating Eq. (21) with respect to time,

$$\dot{M}_a(t) = \frac{\chi_r H}{\eta_r \sqrt{\frac{1}{\eta_r} - \left(\frac{\delta_r}{2\eta_r} \right)^2}} e^{-(\delta_r/2\eta_r)t} \sin \left[\sqrt{\frac{1}{\eta_r} - \left(\frac{\delta_r}{2\eta_r} \right)^2} t \right] \quad (22)$$

Equations (17) and (21) are of the same form, except for the phase angle $\sin^{-1}\zeta_r$ in the latter. The presence of $\sin^{-1}\zeta_r$ in Eq. (21) results from assuming the initial condition $\dot{M}_{a0} = 0$ in deriving Eq. (20), which agrees with Eq. (22). In contrast, according to Eq. (18), $\dot{M}_{a0} = 2M_s \sin \psi \tan(\theta_0/2)/\tau$. However, if $\delta_r \ll 2\sqrt{\eta_r}$ (low damping), then $\zeta_r \ll 1$, and $\sin^{-1}\zeta_r \approx 0$. Under this condition, the expressions for $M_a(t)$ in Eqs. (17) and (21) are equivalent, and by equating the terms representing the decay time constant and the frequency of oscillation, we obtain the relations

$$\tau = \frac{2\eta_r}{\delta_r} \quad (23)$$

and

$$\Omega = \sqrt{\frac{1}{\eta_r} - \left(\frac{\delta_r}{2\eta_r}\right)^2} \quad (24)$$

Hence,

$$\eta_r = \frac{1}{\frac{1}{\tau^2} + \Omega^2} \quad (25)$$

and

$$\delta_r = \frac{2/\tau}{\frac{1}{\tau^2} + \Omega^2} \quad (26)$$

Using Eqs. (23) and (24), the condition $\delta_r \ll 2\sqrt{\eta_r}$ is equivalent to the condition $\Omega\tau \gg 1$. This is in agreement with the condition required for the expressions for $\dot{M}_a(t)$ in Eqs. (18) and (22) to be equivalent. Referring to Eqs. (10) and (11), the low-damping condition of $\Omega\tau \gg 1$ amounts to $\lambda \ll \gamma M_s$ according to the Landau-Lifshitz equation, and $\alpha \ll 1$ according to the Gilbert equation. Note that in Eqs. (10) and (11), since $\lambda = \alpha\gamma M_s$, $\Omega\tau \gg 1$ is also the condition under which the Landau-Lifshitz and Gilbert equations become equivalent.

Substituting Eqs. (10) and (11) into Eqs. (25) and (26), we obtain the following relations:

$$\eta_r = \begin{cases} \frac{1}{H_t^2 \left[\gamma^2 + \left(\frac{\lambda}{M_s} \right)^2 \right]} & \text{(Landau-Lifshitz)} \\ \frac{1 + \alpha^2}{H_t^2 \gamma^2} & \text{(Gilbert)} \end{cases} \quad (27)$$

and

$$\delta_r = \begin{cases} \frac{2(\lambda/M_s)}{H_t \left[\gamma^2 + \left(\frac{\lambda}{M_s} \right)^2 \right]} & \text{(Landau-Lifshitz)} \\ \frac{2\alpha}{H_t \gamma} & \text{(Gilbert)} \end{cases} \quad (28)$$

Usually, $H \ll H_i$, and so $H_t \approx H_i$.

Equating the initial and final values of M_a in Eqs. (16) and (21), we obtain the relations

$$M_{a0} = M_s \cos (\theta_0 + \psi) \quad (29)$$

and

$$M_s \cos \psi = M_{a0} + \chi_r H \quad (30)$$

Substituting Eq. (29) and the trigonometric relation $H = H_i \sin \theta_0 / \sin \psi$ into Eq. (30), we get

$$\chi_r = \frac{M_s}{2H_i} \left[\tan \psi + \tan \left(\frac{\theta_0}{2} \right) \right] \sin 2\psi \quad (31)$$

Since $\psi \gg \theta_0/2$, Eq. (31) is reduced to

$$\chi_r \approx \frac{M_s}{H_i} \sin^2 \psi \quad (32)$$

We have seen that the second-order differential equation, Eq. (19), may be used to describe the component of elastic rotation of magnetization of a single crystallite (or a domain) along the applied magnetic field that causes this rotation. If we now apply Eq. (19) to every j th crystallite of volume v_j in a polycrystalline ferrite, the overall M_a is still described by Eq. (19), except that χ_r represents an average value:

$$X_r = \frac{1}{\sum_j v_j} \sum_j X_j v_j = \frac{1}{\sum_j v_j} \sum_j \frac{M_s v_j \sin^2 \psi_j}{H_{ij}} \quad (32a)$$

4. Flux-Switching Models

a. Experiments

Consider the flux-switching experiment shown in Fig. 6(a). A thin toroidal ferrite core is switched in the negative direction (clockwise) by a CLEAR current pulse I_c in N_c turns to negative remanence $\phi = -\phi_r$, and then switched by a TEST current pulse I having a rise time T_r in a concentric, single-turn winding.* An induced voltage $N_v \dot{\phi}(t)$ is sensed and integrated during the switching time. Typical waveforms of $F(t)$ and $\dot{\phi}(t)$ as well as the variations of ϕ vs. F and $\dot{\phi}$ vs. ϕ during a full switching cycle are shown in Fig. 6(b). In order to assure a reproducible remanent state of $\phi = -\phi_r$, the CLEAR MMF $F_c = -N_c I_c$ and its duration T_c must be large enough to switch ϕ far into negative saturation. In some cases, it is also necessary to switch ϕ into positive saturation, before switching it into negative saturation, in order to wipe out possible 360° domain walls.⁹

The models proposed here describe the properties of switching from $\phi = -\phi_r$ by means of positive or negative TEST current I . The same properties, except for a change in sign, are characteristic of switching from $+\phi_r$. The total $\dot{\phi}(t)$ is

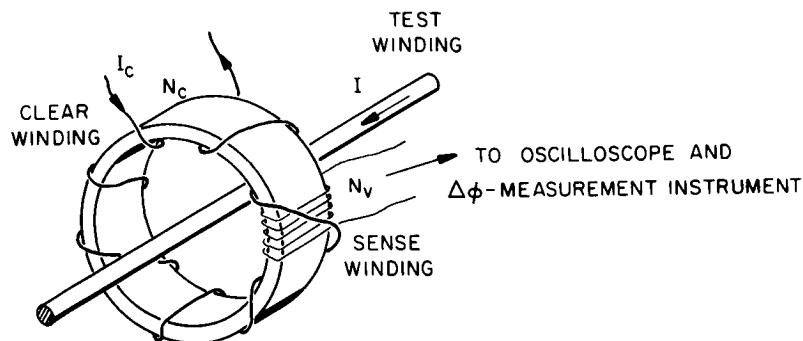
$$\dot{\phi}(t) = \dot{\phi}_e(t) + \dot{\phi}_{inel}(t) \quad (33)$$

where $\dot{\phi}_e(t)$ is the elastic $\dot{\phi}(t)$, and $\dot{\phi}_{inel}(t)$ is the inelastic $\dot{\phi}(t)$. As discussed in Reports 3 and 4, and as shown in Fig. 6(b),

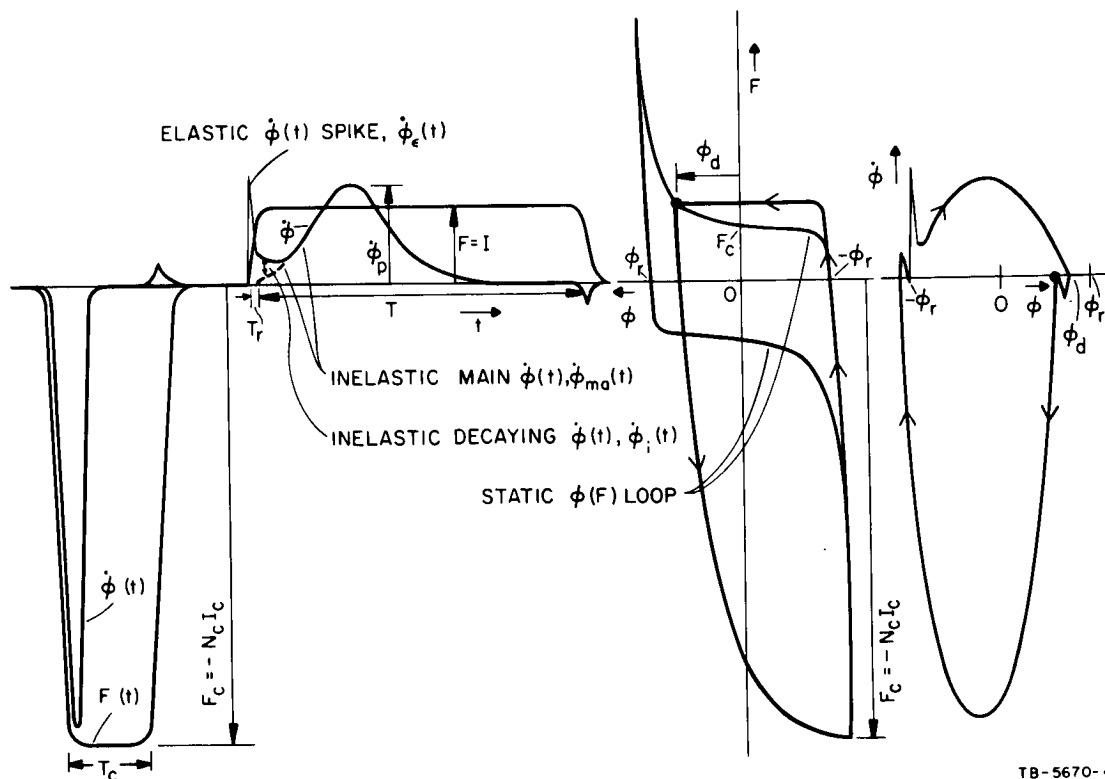
$$\dot{\phi}_{inel}(t) = \dot{\phi}_i(t) + \dot{\phi}_{ma}(t) \quad (34)$$

where $\dot{\phi}_i(t)$ is the decaying inelastic $\dot{\phi}(t)$ component and $\dot{\phi}_{ma}(t)$ is the bell-shaped, main inelastic $\dot{\phi}(t)$ component.¹⁰⁻¹³ The smaller the values

* Unlike T_r in Report 4 (defined as twice the time it takes a current pulse to reach half of its amplitude), T_r in this report designates the time for a current to rise from 10 percent to 90 percent of its amplitude.



(a) CORE AND WINDINGS

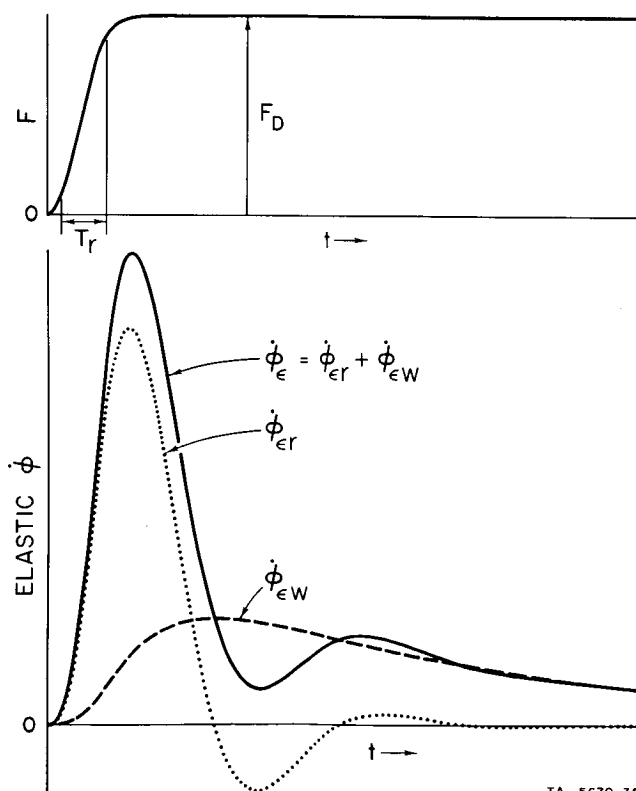


(b) WAVEFORMS OF $F(t)$ AND $\dot{\phi}(t)$ AND VARIATIONS OF $\phi(F)$ AND $\dot{\phi}(\phi)$ DURING A FULL CYCLE

FIG. 6 FLUX-SWITCHING EXPERIMENT

of T_r and F are, the more distinguishable are the initial $\dot{\phi}(t)$ components $\dot{\phi}_\epsilon(t)$ and $\dot{\phi}_i(t)$. Masking of these components by the main $\dot{\phi}(t)$ component during the CLEAR time is due to the relatively long rise time and high amplitude of the CLEAR MMF pulse.

If the flux-switching experiment in Fig. 6 is performed without the CLEAR winding, application of repetitive $F(t)$ pulses of sufficient magnitude results in purely elastic flux switching from remanence ($\phi = \phi_r$) further into saturation and back ("shuttle" switching). Such an experiment was performed on a thin ferrite core using $F(t)$ pulses with very short T_r (0.4 ns). The resulting elastic $\dot{\phi}(t)$ was found⁸ to be composed of two components, as shown in Fig. 7: an initial $\dot{\phi}_\epsilon(t)$ spike, $\dot{\phi}_{\epsilon r}(t)$, of high amplitude and short duration, followed by a decaying $\dot{\phi}_\epsilon(t)$, $\dot{\phi}_{\epsilon w}(t)$, of relatively low peak value and long duration.



TA-5670-35

FIG. 7 POSTULATED WAVEFORMS OF $\dot{\phi}_\epsilon(t)$ AND ITS COMPONENTS $\dot{\phi}_{\epsilon r}(t)$ AND $\dot{\phi}_{\epsilon w}(t)$, IN RESPONSE TO APPLIED $F(t)$ OF AMPLITUDE F_D AND SHORT RISE TIME T_r

Thus,

$$\dot{\phi}_{\epsilon}(t) = \dot{\phi}_{\epsilon r}(t) + \dot{\phi}_{\epsilon w}(t) \quad (35)$$

We shall next examine qualitatively the physical sources of the various $\dot{\phi}$ components and present a semiempirical model for each component.

b. Models for the Two Elastic $\dot{\phi}(t)$ Components

As shown in Fig. 7, an experimental elastic $\dot{\phi}(t)$ waveform induced by what is essentially a step $F(t)$ appears to be composed of two components, $\dot{\phi}_{\epsilon r}(t)$ and $\dot{\phi}_{\epsilon w}(t)$. The $\dot{\phi}_{\epsilon r}(t)$ component is generated by elastic rotation of magnetization and the $\dot{\phi}_{\epsilon w}(t)$ component is likely to be generated by elastic domain-wall motion. These conclusions are based on the following arguments.

First, the $\dot{\phi}_{\epsilon r}(t)$ waveform has a high peak and short duration, whereas the $\dot{\phi}_{\epsilon w}(t)$ waveform has a low peak and relatively long duration. This is typical for fast switching by rotation of magnetization and relatively slow switching by domain-wall motion.

Second, when a field of 1200 Oe, produced by a permanent magnet, was superimposed transversely to the circumferentially applied field, the $\dot{\phi}_{\epsilon w}(t)$ component disappeared, as shown in Fig. 8. The demagnetizing field was roughly 700 Oe, and so the net transverse field of about 500 Oe was high enough to

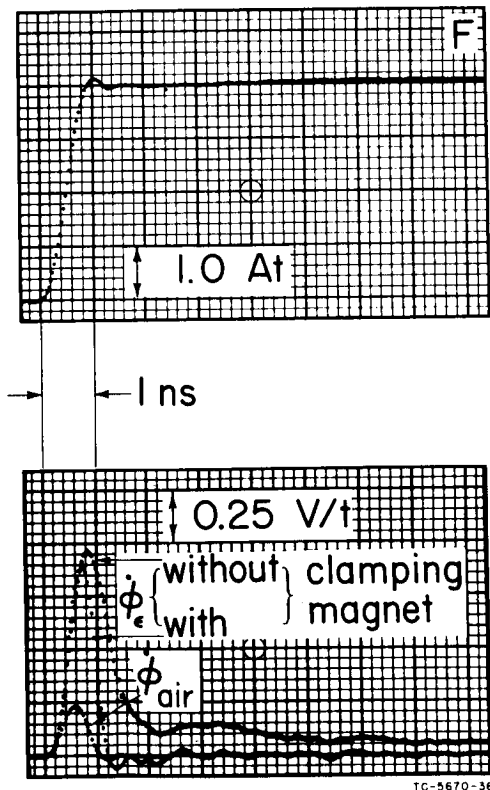


FIG. 8 SUPERPOSITION OF EXPERIMENTAL WAVEFORMS OF $\dot{\phi}_{\epsilon}(t)$ WITHOUT A MAGNET, $\dot{\phi}_{\epsilon}(t)$ WITH A MAGNET, AND $\dot{\phi}_{air}(t)$, IN RESPONSE TO A STEP $F(t)$ OF $T_r = 0.4$ ns AND AMPLITUDE $F_D = 4.0$ At

annihilate the domain walls, which explains why $\dot{\phi}_{\epsilon_w}(t)$ disappeared. For higher transverse fields, $\dot{\phi}_{\epsilon_r}(t)$ became narrower and lower in amplitude because of a higher Ω [see Eq. (11)] and a smaller θ_0 . See Eq. (18).

Third, as will be shown later, it was found that the $\dot{\phi}_{\epsilon_r}$ component is underdamped with 490 Mc/s frequency of oscillation (which is in the microwave region) and that the $\dot{\phi}_{\epsilon_w}$ component is overdamped for positive switching from $\phi = \phi_r$, but slightly underdamped with 82 Mc/s oscillation (which is in the radio-frequency region) for positive switching from $\phi = -\phi_r$. It is well known¹⁴⁻¹⁷ from the frequency dependence of the complex initial permeability, $\mu = \mu' - j\mu''$, that a resonance occurring in the microwave region is due to rotation of magnetization. In the radio-frequency region, on the other hand, the plot of $(\mu' - 1)$ vs. frequency (called "dispersion") may or may not have a peak¹⁴⁻¹⁷ (resonance). Rado^{14,16} showed that the radio-frequency dispersion and the static initial permeability are due to domain-wall displacements. Although his conclusions are controversial, no convincing arguments that contradict his statements have yet been presented.

For simplicity, suppose that the core is thin enough to assume uniform circumferential M and applied H across it, so that $H = F/l$, where F is the applied MMF, and $M = \phi/(\mu_0 A)$.

i. Wall-Motion $\dot{\phi}_{\epsilon}(t)$, $\dot{\phi}_{\epsilon_w}(t)$

Multiplying Eq. (5) by $\mu_0 A$ and replacing H by F/l , we obtain

$$\phi_{\epsilon_w} + \delta_w \dot{\phi}_{\epsilon_w} + \eta_w \ddot{\phi}_{\epsilon_w} = \epsilon_w F, \quad (36)$$

where

$$\epsilon_w = \chi_w \mu_0 A / l. \quad (36a)$$

The term $\eta_w \ddot{\phi}_{\epsilon_w}$ in Eq. (36) may be neglected if T_r is much larger than η_w / δ_w (more precisely, $2\eta_w / \delta_w$), e.g., if $T_r \gtrsim 10 \eta_w / \delta_w$. Under this condition, Eq. (36) may be simplified to

$$\phi_{\epsilon_w} + \delta_w \dot{\phi}_{\epsilon_w} \approx \epsilon_w F. \quad (37)$$

Furthermore, if $T_r \gg \delta_w$, then Eq. (37) may be simplified to

$$\phi_{\epsilon_w} \approx \epsilon_w F \quad . \quad (38)$$

ii. Rotational $\dot{\phi}_\epsilon(t)$, $\dot{\phi}_{\epsilon_r}(t)$

Multiplying Eq. (19) by $\mu_0 A$ and replacing H by F/l , we obtain

$$\phi_{\epsilon_r} + \delta_r \dot{\phi}_{\epsilon_r} + \eta_r \ddot{\phi}_{\epsilon_r} = \epsilon_r F \quad , \quad (39)$$

where

$$\phi_{\epsilon_r} = \mu_0 A (M_a - M_{a0}) \quad (39a)$$

is the elastic *change* in the component of flux along the applied field, and

$$\epsilon_r = \chi_r \mu_0 A / l \quad . \quad (39b)$$

If $T_r \gg \eta_r / \delta_r$, then

$$\phi_{\epsilon_r} + \delta_r \dot{\phi}_{\epsilon_r} \approx \epsilon_r F \quad (40)$$

and if, in addition, $T_r \gg \delta_r$, then

$$\phi_{\epsilon_r} \approx \epsilon_r F \quad . \quad (41)$$

iii. Total $\dot{\phi}_\epsilon(t)$

The overall elastic $\dot{\phi}$ is $\dot{\phi}_\epsilon(t) = \dot{\phi}_{\epsilon_w}(t) + \dot{\phi}_{\epsilon_r}(t)$ [See Eq. (35)]. The parameters δ , η , and ϵ corresponding to either $\dot{\phi}_{\epsilon_w}$ or $\dot{\phi}_{\epsilon_r}$ may depend on T_r , the rise time of $F(t)$.

If $T_r \gg \max(\eta_w / \delta_w; \eta_r / \delta_r)$ and $\delta_w \approx \delta_r \equiv \delta$, then Eqs. (37) and (40) may be combined to describe the overall $\dot{\phi}_\epsilon$:

$$\phi_\epsilon + \delta \dot{\phi}_\epsilon \approx \epsilon F \quad , \quad (42)$$

where $\epsilon = \epsilon_w + \epsilon_r$. Furthermore, if $T_r \gg \max(\delta_w; \delta_r)$, then Eqs. (38) and (41) may be combined to

$$\phi_\epsilon \approx \epsilon F \quad . \quad (43)$$

c. Models for the Two Inelastic $\dot{\phi}(t)$ Components

It was shown in Report 4, pp. 1-3, by means of an interrupted step- F switching experiment that $\dot{\phi}_i(t)$ is induced by inelastic domain-wall motions. It was further suggested (Report 3, pp. 11-12; Report 4, p. 6) that unlike the domain-wall motions generating $\dot{\phi}_{ma}(t)$, such motions involve no domain-wall collision. Although this distinction is valid, it appears that a more direct distinction between the sources of the two inelastic $\dot{\phi}$ components should be related to the length of the wall displacement because the variations of wall areas depend on this length.

As before, suppose that the core is thin enough to assume uniform M and H across it; hence, $F = lH$ and $\dot{\phi} = \mu_0 A \dot{M}$. Upon application of a step- H drive, a finite number n of domain walls will move inelastically. A fraction p of these n walls will move locally, as in Fig. 2(a), and generate the $\dot{\phi}_i(t)$ component, while the remaining $n(1-p)$ walls will experience major displacements, as in Fig. 2(b), and generate the $\dot{\phi}_{ma}(t)$ component. The waveform of each of these inelastic $\dot{\phi}(t)$ components depends on the average velocity, the expected number, the average area, and the motion time of the corresponding walls. The first two features affect $\dot{\phi}_i(t)$ and $\dot{\phi}_{ma}(t)$ in a similar fashion, whereas the third and fourth features affect each $\dot{\phi}$ component differently.

i. Decaying Inelastic $\dot{\phi}(t)$, $\dot{\phi}_i(t)$

The average velocity of walls moving inelastically is proportional to the excess of the applied H over an average threshold, \bar{H}_{th} .^{7,10} Denoting \bar{H}_{th} corresponding to minor wall displacements by H_i , $\dot{\phi}_i$ is thus proportional to $(H - H_i)$. The magnitude of $\dot{\phi}_i$ also increases with the number np of the walls experiencing minor displacements. Referring to Fig. 4, n increases with H because n is proportional to $\int_0^H f(H_{th}) dH_{th}$. Assuming that major inelastic wall displacements can occur only if $H \gtrsim H_d^{min}$, p is essentially unity in the region $0 < H \lesssim H_d^{min}$.

As H increases beyond H_d^{\min} , p decreases gradually; but since n increases with H , the product np continues to increase, reaches a peak, and then decreases. For the $\dot{\phi}_i(t)$ model proposed here, we shall assume that H is below the value at which np reaches peak, i.e., that np increases with H . It has been found experimentally that to a good approximation $\dot{\phi}_i$ is proportional to $(H - H_i)^{\nu_i}$, where $\nu_i > 1$ (e.g., $\nu_i \approx 1.5$). Since $\dot{\phi}_i$ is proportional to $(H - H_i)$ due to the effect of wall velocity, the increase of np with H is proportional to $(H - H_i)^{\nu_i - 1}$.

Since $\dot{\phi}_i(t)$ is generated by minor wall displacements, the corresponding average wall area is likely to change by a negligible amount, and so $\dot{\phi}_i(t)$ for a single wall displacement should be essentially rectangular. However, since the length of the minor wall displacement is a random variable and since the wall velocities are not necessarily the same, the *termination times* of these displacements will vary randomly among the walls. When a step H is applied, *all* np walls begin moving and generate $\dot{\phi}_i$; as one wall after another terminates its motion, $\dot{\phi}_i(t)$ decays in an exponential-like manner. The time constant τ_i associated with the $\dot{\phi}_i(t)$ decay is assumed to be inversely proportional to the average wall velocity; hence $\tau_i = S_i/(H - H_i)$, where S_i is a constant. Thus, $\dot{\phi}_i(t)$ generated by a step H is proportional to $(H - H_i)^{\nu_i} \exp[-t(H - H_i)/S_i]$.

Suppose now that $H(t)$ increases from zero to above H_i . Letting T_i be the time when H reaches H_i and replacing H by F/l , then during $t \geq T_i$,

$$\dot{\phi}_i(t) = \lambda_i (F - F_i)^{\nu_i} \exp[-(t - T_i)(F - F_i)/C_i] \quad , \quad (44)$$

where λ_i is a constant of proportionality, $F_i = H_i l$, and $C_i = S_i l$. Equation (44) holds for an arbitrary waveform of $F(t)$, provided that $F \geq F_i$. (During $0 \leq t \leq T_i$, $\dot{\phi}_i = 0$.)

It can be shown from the probability-density function $f(H_{th})$ in Fig. 4 that as the magnitude H of a step $H(t)$ increases from zero, H_i increases from zero to an asymptotic value, which is denoted by H_{0i} . Since $1 \gtrsim p \geq 0$ if $H \gtrsim H_d^{\min}$, the averaging process of H_{th} results in $H_{0i} < \bar{H}_{th} \approx H_d^{\min}$. Furthermore, since $H_i \leq H$ (the equality sign corresponds to $H = 0$, i.e., $T_i = 0$), H_i vs. H should start at the

origin with a unity slope, and gradually approach H_{0i} . Letting $F_{0i} = H_{0i} l$, one function that satisfies this condition⁴ is

$$F_i = F_{0i} \tanh (F/F_{0i}) \quad . \quad (45)$$

In order to obtain a satisfactory agreement between the observed $\dot{\phi}_i(t)$ and the model proposed in Eq. (44), it was necessary in Report 4 (pp. 25 and 35) to use a smaller value of C_i for a shorter rise time T_r of $F(t)$, whose amplitude is F_D . This dependence may be partially explained by the following argument: Assuming that minor and major inelastic wall displacements are independent, the maximum flux change due to $\dot{\phi}_i(t)$, $\Delta\phi_{i(\infty)} = \int_0^\infty \dot{\phi}_i dt$, of a given core is fixed for a given value of F_D (but increases asymptotically with F_D). If T_r is considerably smaller than the decay time constant τ_i , then $\Delta\phi_{i(\infty)} \approx \dot{\phi}_{ip}(0.5 T_r + \tau_i) \approx \dot{\phi}_{ip}\tau_i$, and since $\tau_i = C_i/(F_D - F_i)$,

$$C_i \approx \Delta\phi_{i(\infty)}(F_D - F_i)/\dot{\phi}_{ip} \quad . \quad (46)$$

For a given value of F_D , $\dot{\phi}_{ip}C_i \approx \text{constant}$, and since $\dot{\phi}_{ip}$ increases as T_r decreases, C_i must decrease as T_r decreases. Although C_i depends also on F_D [see Eq. (46)], the increase of $\dot{\phi}_{ip}$ with F_D is such that $\dot{\phi}_{ip}/(F_D - F_i)$ may be approximated by a constant in a wide range of F_D . This is evident from the plots of computed $\dot{\phi}_{ip}$ vs. F_D for different values of T_r in Fig. 14 of Report 4 (p. 40). As F_D or T_r or both decrease, $\dot{\phi}_{ip}$ vs. F_D becomes less linear, and hence the dependence of C_i on F_D increases.

It is proper at this point to show the significance of the $\dot{\phi}_i(t)$ component in connection with the signal-to-noise ratio of a coincident-current memory. Consider two essentially identical cores, one in an undisturbed ONE state ($\phi \approx \phi_r$) and the other in an undisturbed ZERO state ($\phi \approx -\phi_r$). The difference between the $\dot{\phi}$ outputs of the two undisturbed cores, generated by a PARTIAL-READ pulse of amplitude around F_d^{\min} , is the maximum *delta noise*. Since the difference in $\dot{\phi}_e(t)$ between the two cores is considerably smaller than $\dot{\phi}_i(t)$ of the core driven away from saturation, this delta noise is essentially $\dot{\phi}_i(t)$. Application of a POST-WRITE DISTURB pulse decreases the delta noise appreciably by causing minor inelastic wall displacements to new stable positions

[e.g., from Point R to Point W in Fig. 2(a)]. The longer the duration of this pulse is, the larger is the number of completed minor inelastic wall displacements, and so the smaller is the following delta noise. Furthermore, previous PARTIAL-READ and PARTIAL-WRITE pulses also affect the delta noise by causing minor inelastic wall displacements in opposite directions. Since $\dot{\phi}_i(t)$ is due to domain-wall motion only, one could possibly describe any delta noise by incorporating the switching history into Eq. (44).

ii. Main Inelastic $\dot{\phi}(t)$, $\dot{\phi}_{ma}(t)$

Referring to Fig. 4, the average threshold \bar{H}_{th} corresponding to major inelastic wall displacements increases from a value of H_d^{min} to a finite value as H increases above H_d^{min} . The corresponding number of walls, $n(1-p)$, increases with H from zero to a finite number because n increases and p decreases as H increases. Thus, as in the case of $\dot{\phi}_i(t)$, $\dot{\phi}_{ma}(t)$ is proportional to $(H - \bar{H}_{th})^\nu$, where $\nu > 1$. However, unlike $\dot{\phi}_i(t)$, $\dot{\phi}_{ma}(t)$ is affected appreciably by a change in the average domain-wall area *vs.* time. According to Menyuk and Goodenough,¹⁰ this area increases in the early portion of switching, reaches a peak in the middle of switching (while domains collide with each other), and decreases with time toward the end of switching. The distribution function of the switching time is more complex than in the case of $\dot{\phi}_i(t)$ because it depends on domain collisions. Haynes¹¹ extended Goodenough's work by calculating a model for $\dot{\phi}_{ma}(t)$ based on the assumption that the nucleation centers (where major wall displacements begin) are distributed randomly according to Poisson's distribution function. Independently, Lindsey¹² calculated a model similar to Haynes', except that he assumed the domains to be cylindrical. These types of models were treated in a general way by Hilberg.¹³ Each of these models for $\dot{\phi}_{ma}(t)$ yields a satisfactory agreement with experimental data. However, we prefer to use the parabolic $\dot{\phi}_{ma}(\phi)$ model (see Report 4, pp. 11-15) simply because its agreement with experimental data of many square-loop materials is the best (but not by far). According to this model, $\dot{\phi}_{ma}$ is proportional to a parabolic function of ϕ which reaches a peak in the middle of switching. Thus, *qualitatively*, the parabolic model has the physical features hypothesized by Menyuk and Goodenough.¹⁰

Following Eqs. (18) and (21) in Report 4,

$$\dot{\phi}_{ma} = \dot{\phi}_p(F) \left\{ 1 - \left[\frac{2\phi + \phi_r - \phi_d(F)}{\phi_r + \phi_d(F)} \right]^2 \right\}, \quad (47)$$

where $\dot{\phi}_p(F)$ is the peak $\dot{\phi}_{ma}$ vs. F . The experimental $\dot{\phi}_p(F)$ curve may be fitted by the following functions:

$$\dot{\phi}_p(F) = \begin{cases} 0 & \text{if } 0 \leq F \leq F_d^{\min} \\ \lambda_d (F - F_d^{\min})^{\nu_d} & \text{if } F_d^{\min} \leq F \leq F_{dB} \\ \lambda (F - F_0'')^{\nu} & \text{if } F_{dB} \leq F \leq F_B \\ \rho_p (F - F_0) & \text{if } F_B \leq F \end{cases}, \quad (48)$$

where λ_d , λ , and ρ_p are proportionality constants, $F_d^{\min} = H_d^{\min} l$, F_0'' , and F_0 are threshold constants, and F_{dB} and F_B are F -boundary constants. A model for $\phi_d(F)$, based on the one in Report 2, is given on pp. 82-83.

The expressions for $\dot{\phi}_p$ vs. F in Eq. (48) are identical with the ones given in Eq. (19) of Report 4 (p. 11), except that Eq. (48) includes an additional expression for the very low- F region, $F_d^{\min} \leq F \leq F_{dB}$ (e.g., $F_{dB} \approx 1.1 F_0'' \approx 1.15 F_c$). The excess MMF in this region is so low that the variations in threshold during the switching time become significant. The assumption in Eq. (48) that the MMF threshold for $F_d^{\min} \leq F \leq F_{dB}$ is constant may result in an appreciable error. It is more exact to replace F_d^{\min} by $F_d(\phi)$, where $F_d(\phi)$ is the F value on the static $\phi(F)$ curve for a given ϕ . As a result, for a step $F(t)$ of amplitude F_D between F_d^{\min} and F_{dB} , $\dot{\phi}_{ma}(t)$ peaks earlier than predicted by Eq. (47) and $\dot{\phi}_{ma}(\phi)$ is not parabolic. Further work needs to be done in using $F_d(\phi)$ as a general threshold function instead of the threshold values given in Eq. (48).

It turns out that Eqs. (47) and (48) are also applicable for $F(t)$ other than a step function. For example, a good agreement with experimental data was obtained in Report 4 (pp. 91-106) for $F(t) = kt$ using the same switching parameters in a wide range of k , e.g., 100:1

[λ , F_0'' and other parameters of the same nature in Eq. (48) are smaller for ramp $F(t)$ than for step $F(t)$ by about 30 percent].

5. Experimental Verification

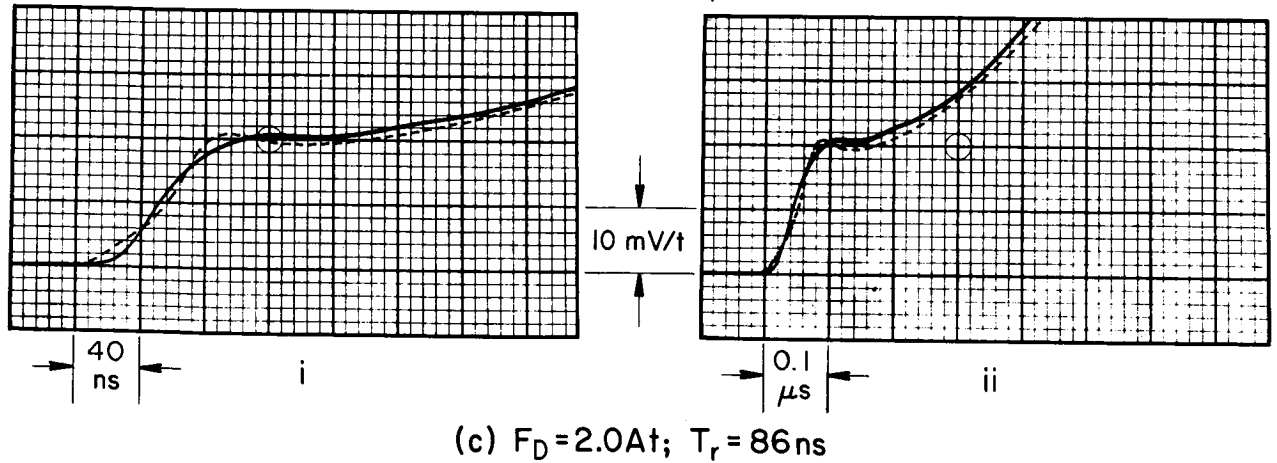
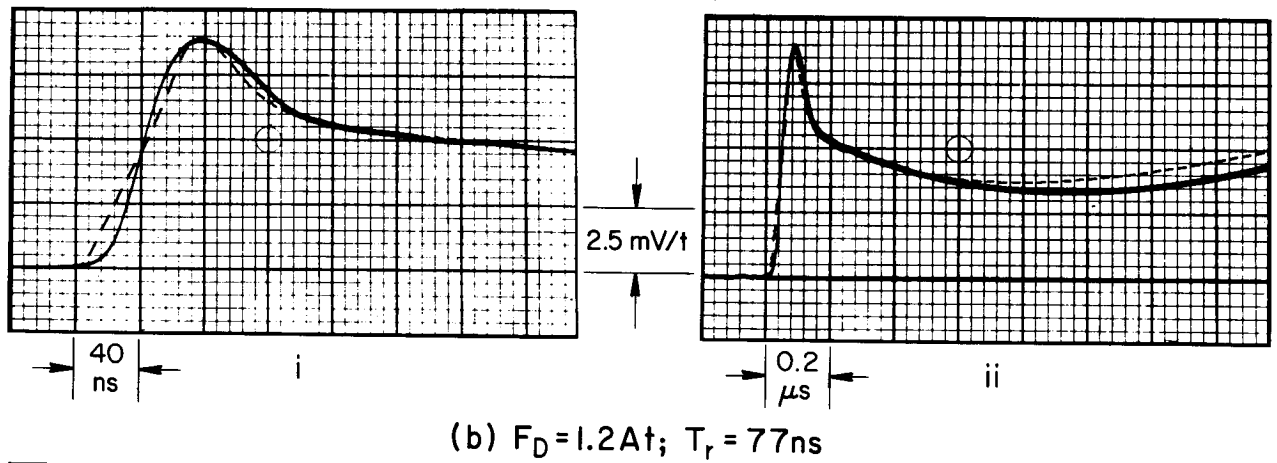
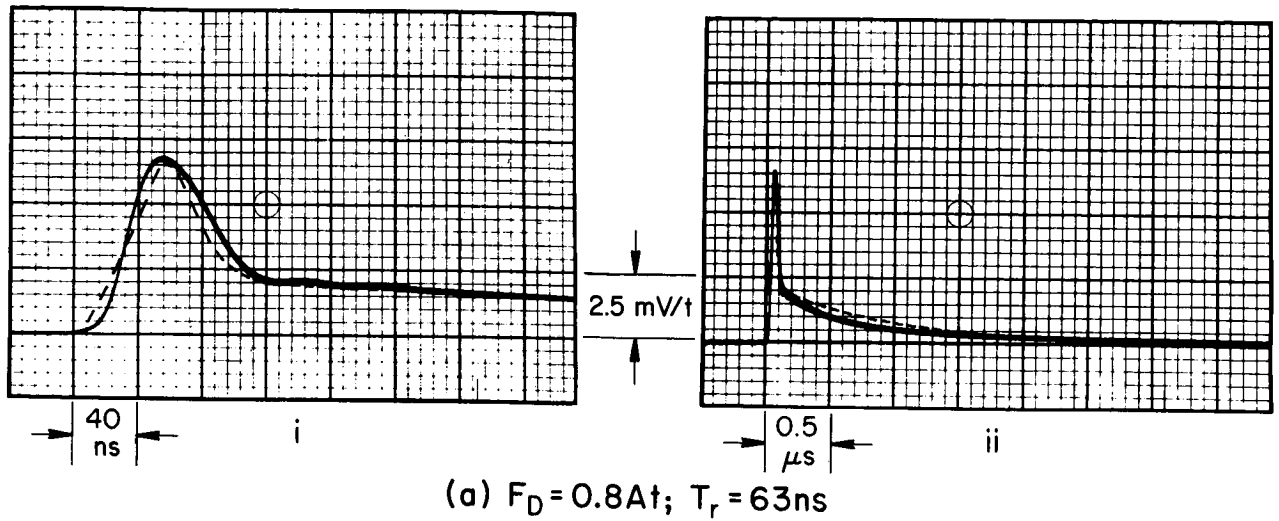
a. Applied $F(t)$ Pulses with $T_r \approx 65$ ns and $T_r \approx 13$ ns

The experimental data in Report 4 (pp. 18-42) were obtained by driving Core E-6 (see Report 3, p. 23 or Report 4, p. 25), as shown in Fig. 6, with constant-amplitude $F(t)$ pulses of several values of amplitude F_D and two values of rise time, $T_r \approx 65$ ns and $T_r \approx 13$ ns. (Recall that, unlike T_r in Report 4, T_r in this report designates the rise time of $F(t)$ from $0.1 F_D$ to $0.9 F_D$. See the footnote on p. 15.) The computation of the $\dot{\phi}_\epsilon(t)$ component was based on Eq. (43), but it was concluded (Report 4, p. 35) that the short delay between the computed and the observed $\dot{\phi}_\epsilon(t)$ waveforms could be reduced by adding a viscous-damping term into the model, i.e., by using Eq. (42). This was subsequently done, and it was found that for $T_r \approx 65$ ns, $\delta_w \approx \delta_r \approx 6$ ns, and for $T_r \approx 13$ ns, $\delta_w \approx \delta_r \approx 3$ ns. Thus, the use of Eq. (43) instead of Eq. (42) is justified if $T_r \gtrsim 60$ ns.

Using Eq. (42) for the $\dot{\phi}_\epsilon(t)$ component, computed initial $\dot{\phi}(t)$ waveforms for $F_D = 0.8$, $F_D \approx 1.2$, and $F_D = 2.0$ At are compared in Fig. 9 ($T_r \approx 65$ ns) and in Fig. 10 ($T_r \approx 13$ ns) with the corresponding experimental $\dot{\phi}(t)$ waveforms [see Figs. 10(b), (e), and (g) and 11(b), (e), and (g) of Report 4, pp. 27-34]. The agreements between experimental and computed $\dot{\phi}(t)$ waveforms in Fig. 9 and especially in Fig. 10 are better than the agreements in Report 4.

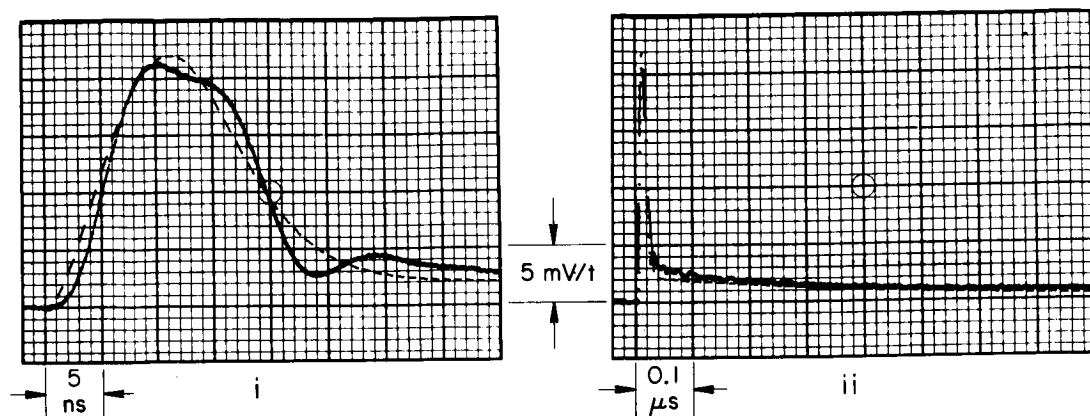
b. Applied $F(t)$ Pulses with $T_r = 0.4$ ns

The use of Eq. (42) is not justified if T_r is not much larger than $\max(\eta_w/\delta_w; \eta_r/\delta_r)$. Thus, in order to observe the effects of the inertial terms $\eta_w \ddot{\phi}_{\epsilon_w}$ and $\eta_r \ddot{\phi}_{\epsilon_r}$ on the $\dot{\phi}(t)$ waveforms [Eqs. (36) and (39)], $F(t)$ drives with very short rise time ($T_r \lesssim 1$ ns) should be applied. In addition, the sensed $\dot{\phi}(t)$ must be free of ringing and distortion pickup. These conditions were achieved in the experimental setup discussed next.

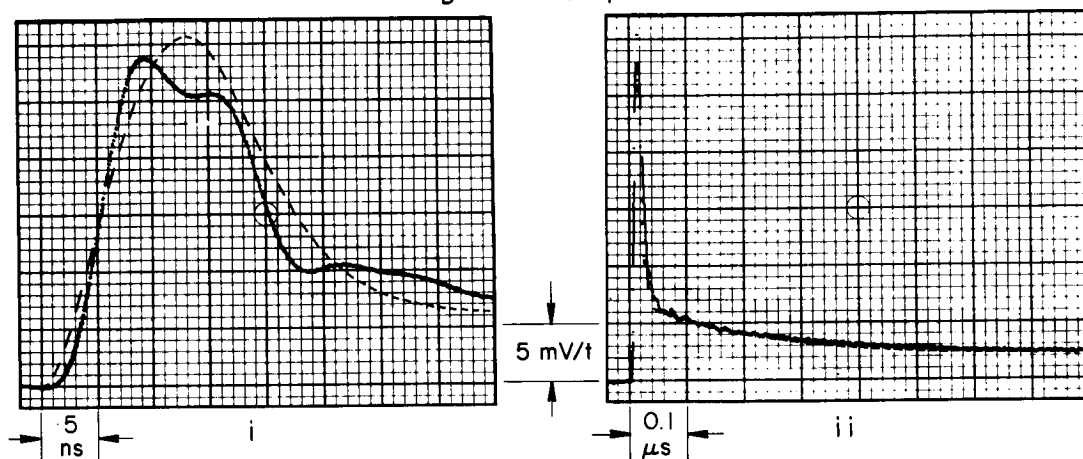


TD-5670-37

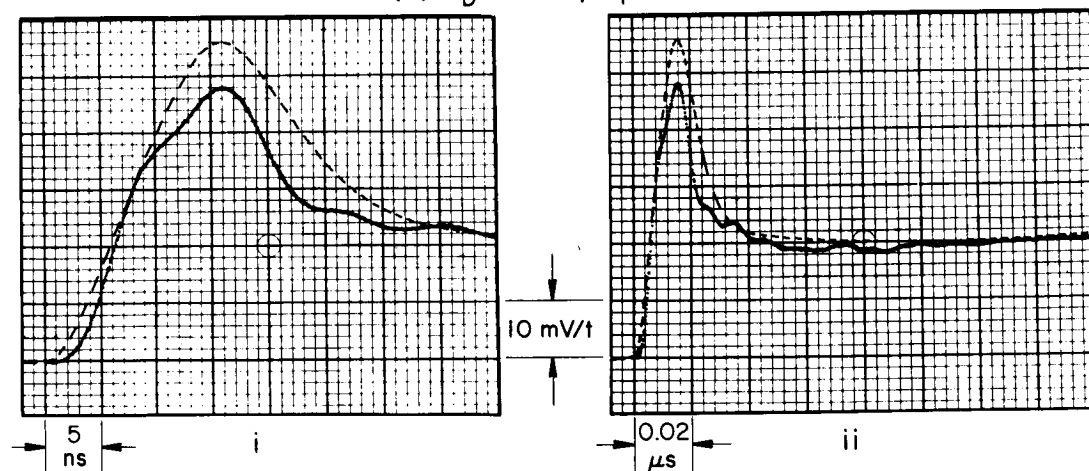
FIG. 9 EXPERIMENTAL (Solid Line) AND COMPUTED (Dashed Line) $\dot{\phi}(t)$ WAVEFORMS OF UNLOADED CORE E-6 DURING THE BEGINNING OF SWITCHING, USING $F(t)$ WITH $T_r \approx 65\text{ ns}$ AND VARIOUS VALUES OF AMPLITUDE F_D



(a) $F_D = 0.8At$; $T_r = 11.7ns$



(b) $F_D = 1.18At$; $T_r = 13ns$



(c) $F_D = 2.0At$; $T_r = 15.6ns$

TD-5670-38

FIG. 10 EXPERIMENTAL (Solid Line) AND COMPUTED (Dashed Line) $\dot{\phi}(t)$ WAVEFORMS OF UNLOADED CORE E-6 DURING THE BEGINNING OF SWITCHING, USING $F(t)$ WITH $T_r \approx 13 ns$ AND VARIOUS VALUES OF AMPLITUDE F_D

i. Experiment

The experimental measurements consisted basically of setting the core with a TEST $F(t)$ pulse having a short rise time and a variable amplitude, clearing the core with a high-amplitude pulse, and photographing the resulting $\dot{\phi}(t)$ during the setting time. The TEST pulse had a rise time T_r of slightly less than 0.4 ns, a fall time less than 1 ns, and a maximum amplitude of 40A; its duration was adjusted from less than 1 ns to almost 1 μ s at the lower amplitudes by changing the length of a 50 Ω transmission-line cable. The CLEAR pulse used for these experiments had an amplitude of 20A, a duration of 0.5 μ s, and rise and fall times of less than 1 ns.

The major difficulty in the experiment was the attainment of a fast-rise TEST pulse free of reflections or other irregularities, and the sensing of the true $\dot{\phi}(t)$, free of ringing and distortion. It was desirable that the rise time and rise shape of the TEST pulse be relatively independent of the amplitude of the TEST pulse in the entire range of amplitude (zero to 40A). The noise problem increased because the observations were made during and immediately following the rise, and because the decaying tail of the initial spike is small compared to the main $\dot{\phi}(t)$ component.

The short-rise-time TEST pulse was generated by discharging a coaxial 50 Ω transmission line into a 50 Ω termination via a mercury-relay switch. The core was mounted coaxially in a section of the 50 Ω transmission line, as shown in Fig. 11. The core was cleared by sending a CLEAR pulse through the same transmission line. This technique, which is described below, obviates the need for a separate CLEAR winding which would be very troublesome with regard to reflections and ringing. The $\dot{\phi}$ was sensed by a one-turn winding made of a short (1.1 cm) fine (Awg. No. 48) wire. A wire of such a small diameter (about 1.2 mil) has a very small capacitance by itself and with the central conductor of the core holder. The central conductor carried a voltage pulse of $50 \cdot F_D$ volts.

The circuit is shown in Fig. 12. The 20 dB high-power attenuator absorbs most of the short-duration power to protect the signal sampler, attenuates the signal for observation (at maximum output of 40A, the voltage pulse before attenuation is 2000V), and attenuates reflections from the signal sampler before they reach the core. The

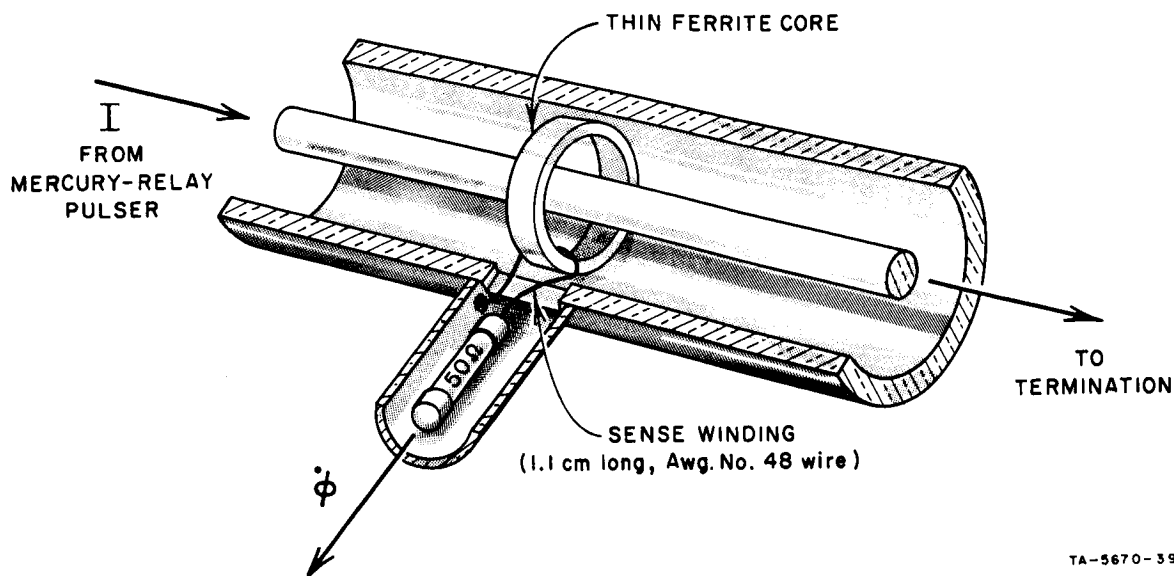


FIG. 11 CUTAWY VIEW OF A COAXIAL CORE HOLDER

circuit produces a positive TEST pulse and a negative CLEAR pulse in the following way: Delay-line 1 is charged to $+V_1$ through the $2\text{ M}\Omega$ charging resistor, R_1 . At the same time, Delay-line 2 is charged to $-V_2$. Mercury-relay 1 is then closed by means of a solenoid exterior to the outer conductor. This initiates the TEST pulse by discharging Delay-line 1, and triggers the sampling oscilloscope. The duration of the TEST pulse is determined by the length of Delay-line 1. After the TEST pulse is completed, but while Mercury-relay 1 is still closed, Mercury-relay 2 is closed. This discharges Delay-line 2, thereby generating a negative CLEAR pulse which passes through Mercury-relay 1, through the core (thus clearing the core) and then to the attenuators and termination. The duration of this pulse is determined by the length of Delay-line 2. Following the CLEAR pulse, both relays open and the two delay lines recharge for the next cycle.

The primary advantage of this technique for generating bipolar pulses is that the $50\ \Omega$ system need not be disturbed with extra switches in the system or an extra core winding that can cause troublesome reflections. In this way a smooth and clean rise can be achieved. The primary disadvantage of this method is that the fall of the TEST pulse is not smooth; however, by careful construction of Mercury-relay 2,

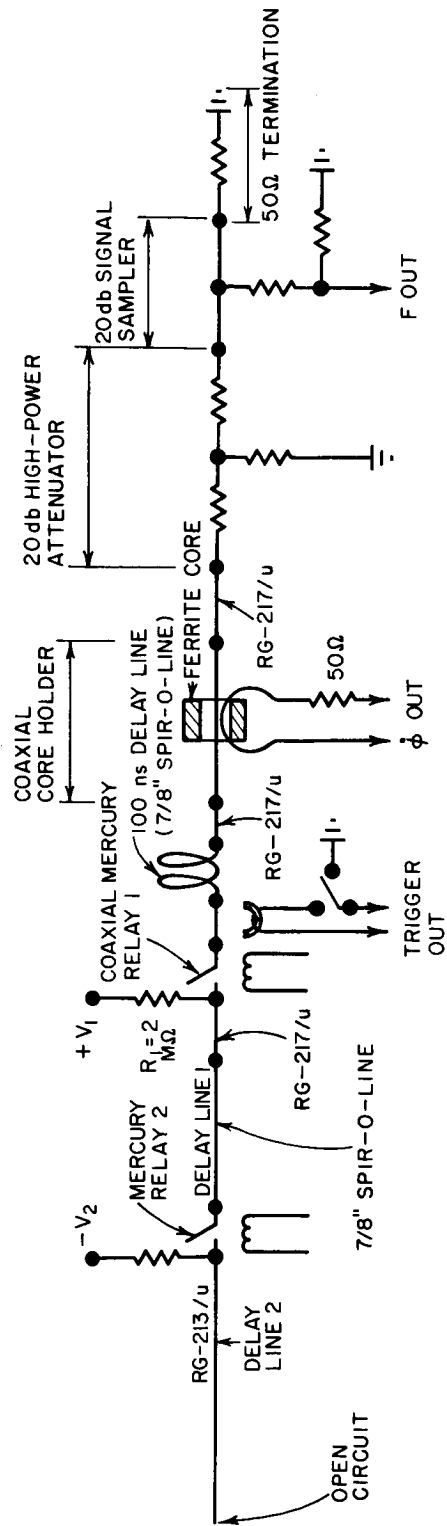


FIG. 12 A CIRCUIT FOR CORE SWITCHING BY BIPOLAR CURRENT PULSES OF 0.4 ns RISE TIMES

TB-5670-40

this drawback can be minimized. Furthermore, for the measurements described in this report, the fall time was of little concern.

The F and $\dot{\phi}$ signals were observed on a Hewlett-Packard Model 185A sampling oscilloscope with a Model 187B vertical amplifier. The oscilloscope response time was 0.4 ns. The actual 10 to 90 percent rise time, T_r , of the TEST pulse was calculated to be slightly less than 0.4 ns by using a Hewlett-Packard 188A vertical amplifier with 90 ps response time. There is about a 3 ns delay between the points at which $\dot{\phi}$ and F are monitored. This delay was eliminated by shifting the horizontal position on the sampling oscilloscope. The trigger signal was obtained across a 5-turn winding of half a ferrite core located near the center conductor at the output of Mercury-relay 1 (see Fig. 12). This trigger output was switched off during the CLEAR pulse to avoid undesired triggering of the sampling oscilloscope. The 100 ns delay line was required in order to trigger the oscilloscope *before* the $\dot{\phi}$ and F signals arrived. The mercury-relay pulser (comprising the $+V_1$ supply, R_1 , Relay 1 contacts, Relay 1 solenoid, and the trigger core) was a modified version of the Model-961 Nanosecond Pulser, made by a Menlo Park Engineering company (now made by Huggins Laboratory, Sunnyvale, California).

The output current pulse from the mercury-relay pulsers contains a small step-up on top of the pulse (about 4 percent of the pulse amplitude) for part of the range. This is presumably due to the mechanical closure of the relay, because the initiation of the pulse is started by an arc discharge in the mercury relay capsule, prior to the mechanical closure. (The Model-961 pulser used here has a small window on the side for obtaining nanosecond light pulses from the arc discharge.) At low current amplitudes, the arc discharge never occurs. At high current amplitudes, the mechanical closure occurs after the pulse is completed. The current step-up occurs in the middle range. For the Model-961 pulser used here, with a 630 ns pulse width, this middle current-amplitude range was from 1.5A to 3.6A (this corresponds to the voltage range of 75V to 180V in the 50Ω system). This range can easily be avoided by using a 10 dB microwave attenuator ahead of the core holder. It has been noted that the time jitter in the output pulse and the exact voltage for which the step-up occurs (also the time of the step-up in the middle range) are influenced by the angle of the

mercury-relay from the vertical. A 30° angle was optimum for minimizing the middle range given above.

The high-power attenuator was a Weinschel Model 693, rated at 10 kW peak power (for microwaves). The peak pulse power used here is 80 kW; therefore, it was necessary to limit the duration of the pulse at the maximum amplitudes. (An exact specification cannot be given, but 10 ns at 40A was not too long.) The signal sampler used was a Microlab AB-20N. The temperature of the coaxial core holder was regulated at 30°C .

ii. Elastic Flux Switching

The elastic flux-switching parameters were determined by fitting the sum $[\dot{\phi}_{\epsilon_r}(t) + \dot{\phi}_{\epsilon_w}(t) + \dot{\phi}_{\text{air}}(t)]$ to the observed $\dot{\phi}_e(t)$ in response to $F(t)$ drives of different values of amplitude F_D . The values of $\dot{\phi}_{\epsilon_r}(t)$ and $\dot{\phi}_{\epsilon_w}(t)$ were computed by numerical integration of the second-order differential equations, Eqs. (36) and (39), respectively. The $\dot{\phi}$ due to air flux was computed using the simple relation

$$\dot{\phi}_{\text{air}}(t) = \frac{\mu_0 A_{sw}}{l} \dot{F} \quad , \quad (49)$$

where A_{sw} is the projection of the sense-winding area normal to the applied field $H = F/l$. The value of $\mu_0 A_{sw}/l$ was determined by dividing the peak values of the observed $\dot{F}(t)$ and $\dot{\phi}_{\text{air}}(t)$ waveforms in Fig. 8. All the computations were performed on a Burroughs B-5500 digital computer. The computer program, written in the Burroughs extended version of ALGOL-60, was similar to the one given in Appendix E of Report 4 (pp. 141-145) in which $\dot{\phi}_i$ and $\dot{\phi}_{ma}$ were set to zero, except for the addition of a PROCEDURE for solving second-order differential equations using the Kutta-Merson method.

We found that the same values of δ_r , η_r , δ_w , and η_w can be used for all F_D values but that the ϵ_r and ϵ_w values decrease with F_D . These values are given as follows:

$$\delta_r = 0.28 \text{ ns}, \quad \eta_r = 0.08 \text{ ns}^2, \quad \epsilon_r = 0.14 (1 - 0.005 F_D) \cdot 10^{-9} H/t^2 ;$$

and

$$\delta_w = 4.0 \text{ ns}, \quad \eta_w = 2.0 \text{ ns}^2, \quad \epsilon_w \approx 0.266 (1 - 0.008 F_D) \cdot 10^{-9} H/t^2.$$

Additional parameters of Core E-6 are $\phi_r = 3.45 \text{ Mx}$ and $\phi_s = 3.726 \text{ Mx}$.

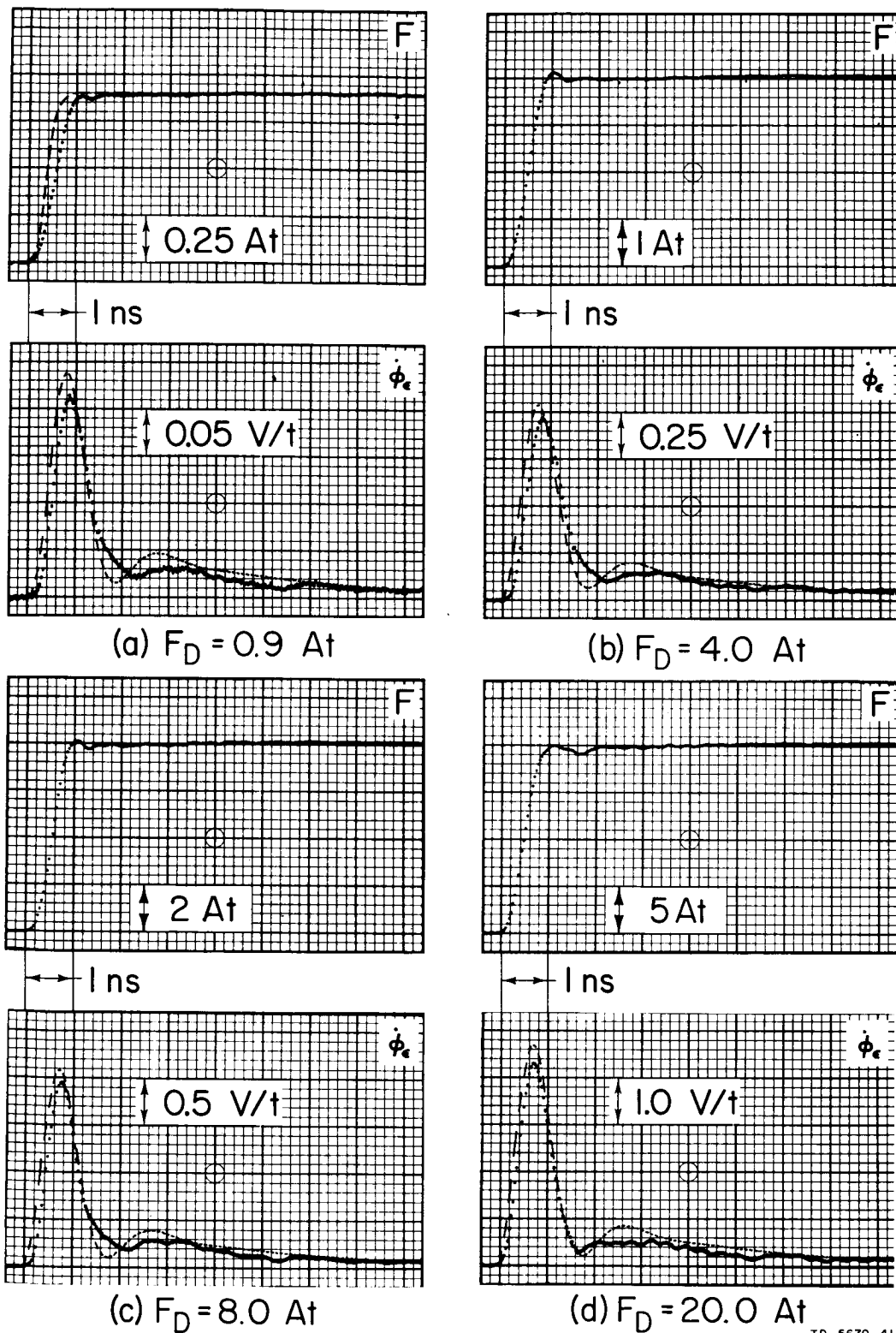
Experimental and computed $F(t)$ and $\dot{\phi}_\epsilon(t)$ waveforms are compared in Fig. 13 for $F_D = 0.9, 4.0, 8.0, 20.0, \text{ and } 40.0 \text{ At}$. The oscilloscope response time was accounted for by assuming the computed $F(t)$ to rise earlier than the experimental $F(t)$ according to the relation

$$T_{r,obs} = \sqrt{T_r^2 + T_{r,osc}^2}, \quad (50)$$

where $T_{r,obs}$ is the observed T_r and $T_{r,osc}$ is the response time of the oscilloscope. It can be seen in Fig. 13 that $T_{r,obs} \approx 0.56 \text{ ns}$ for all values of F_D , and since $T_{r,osc} = 0.4 \text{ ns}$, $T_r \approx 0.4 \text{ ns}$ for all values of F_D . As expected, the experimental $\dot{\phi}_\epsilon(t)$ waveforms lag behind the computed waveforms due to the oscilloscope response time. For the same reason, the peaks of the computed $\dot{\phi}_\epsilon(t)$ waveforms are intentionally higher than the observed $\dot{\phi}_\epsilon$ peaks. These peaks were obtained by adjusting the value of ϵ_r so that the ratio of the computed and the experimental $\dot{\phi}_\epsilon$ peaks was equal to the ratio of experimental peaks of the same $\dot{\phi}_\epsilon(t)$ pulse obtained by using vertical amplifiers with response times of 0.09 ns and 0.4 ns , respectively.

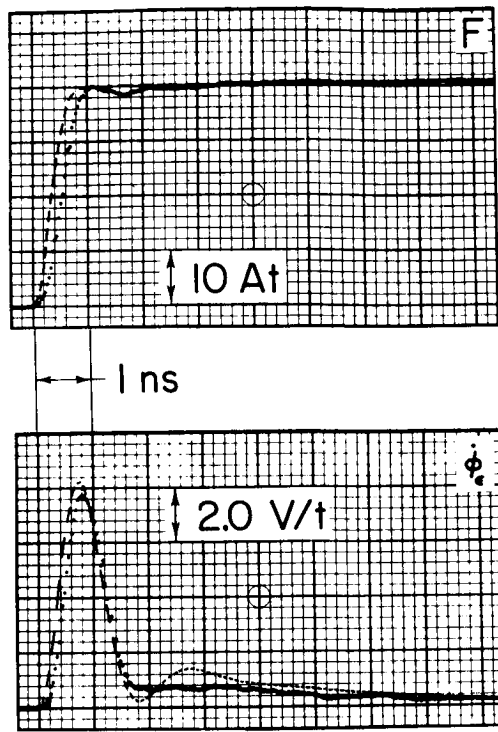
iii. Elastic and Inelastic Flux Switching

The elastic and inelastic flux-switching parameters were determined by fitting the sum $[\dot{\phi}_{\epsilon_r}(t) + \dot{\phi}_{\epsilon_w}(t) + \dot{\phi}_{air}(t) + \dot{\phi}_i(t) + \dot{\phi}_{ma}(t)]$ to the observed $\dot{\phi}(t)$ waveforms in response to $F(t)$ drives of different F_D values. It may seem that the fitting job is very difficult because the number of the parameters involved is large. However, most of these parameter values were known *a priori* from the simpler cases of waveform fitting described earlier. The rotational parameters δ_r and η_r were found to have the same values as for elastic switching only, but δ_w and η_w were found to have somewhat different values. The values of the inelastic switching parameters were close to the ones used in Report 4 and in Figs. 9 and 10. The values of all the parameters of Core E-6 at 30°C for switching under step $F(t)$ with $T_r = 0.4 \text{ ns}$ are listed on page 36.



TD-5670-41

FIG. 13 EXPERIMENTAL (Dotted and Solid Line) AND COMPUTED (Dashed Line) $F(t)$ AND $\dot{\phi}_e(t)$ WAVEFORMS OF UNLOADED CORE E-6, USING $F(t)$ WITH $T_r = 0.4 \text{ ns}$ AND VARIOUS VALUES OF AMPLITUDE F_D



(e) $F_D = 40.0 \text{ At}$

TC-5670-42

FIG. 13 Concluded

Parameters of Core E-6 at $T = 30^\circ\text{C}$

Dimensions: $l_i = 22.19 \text{ mm}$; $l_o = 23.54 \text{ mm}$; $A = 0.1486 \text{ mm}^2$.

Static $\phi(F)$ parameters: $\phi_r = 3.45 \text{ Mx}$; $\phi_s = 3.726 \text{ Mx}$; $H_a = 950 \text{ Atm}^{-1}$;
 $H_q = 35.0 \text{ Atm}^{-1}$; $H_n = 30.0 \text{ Atm}^{-1}$.

$\dot{\phi}_e$ parameters: $\delta_r = 0.28 \text{ ns}$; $\eta_r = 0.08 \text{ ns}^2$; $\epsilon_r = 0.127 \cdot 10^{-9} \text{ Ht}^{-2}$;
 $\delta_w = 1.8 \text{ ns}$; $\eta_w = 1.2 \text{ ns}^2$; $\epsilon_w = 0.127 \cdot 10^{-9} \text{ Ht}^{-2}$.

$\dot{\phi}_i$ parameters: $F_{0i} = 0.55 \text{ At}$; $\nu_i = 1.33$; $\lambda_i = 0.013 \Omega \text{t}^{-2.33} \text{A}^{-0.33}$;
 $C_i = 0.1 \text{ At } \mu\text{s}$.

$\dot{\phi}_{ma}$ parameters: $F_d^{\text{min}} = 0.781 \text{ At}$; $\nu_d = 2.5$; $\lambda_d = 0.124 \Omega \text{t}^{-3.5} \text{A}^{-1.5}$;
 $F_0'' = 0.92 \text{ At}$; $\nu = 1.33$; $\lambda = 0.069 \Omega \text{t}^{-2.33} \text{A}^{-0.33}$;
 $F_0 = 1.45 \text{ At}$; $\rho_p = 0.1132 \Omega \text{t}^{-2}$;
 $F_{dB} = 1.078 \text{ At}$; $F_B = 3.12 \text{ At}$.

The parameters above were used to compute the total $\dot{\phi}(t)$ on a Burroughs B-5500 digital computer, where

$$\dot{\phi}(t) = \dot{\phi}_{\epsilon_r}(t) + \dot{\phi}_{\epsilon_w}(t) + \dot{\phi}_{\text{air}}(t) + \dot{\phi}_i(t) + \dot{\phi}_{ma}(t) .$$

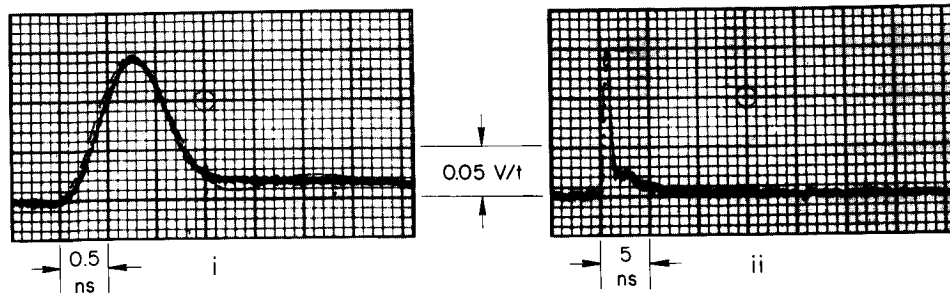
The computer program was the same as given in Appendix E of Report 4 (pp. 141-145), except for the addition of the Kutta-Merson PROCEDURE for numerical solution of second-order differential equations. The computed and the experimental $\dot{\phi}(t)$ waveforms are compared in Fig. 14 for $F_D = 0.6, 0.9, 1.5, 4.0, 8.0, 20.0$, and 36.0 At. The waveforms of $F(t)$ are not shown because they are very similar to the ones shown in Fig. 13. In the cases of $F_D = 20.0$ At and $F_D = 40$ At it was found necessary to equate $\dot{\phi}_i(t)$ to zero in order to obtain a satisfactory fit between the computed $\dot{\phi}(t)$ and the experimental $\dot{\phi}(t)$.

6. Discussion

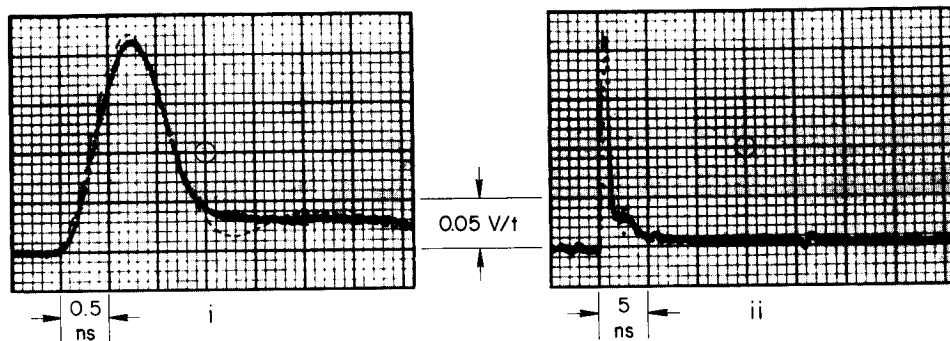
a. Elastic Switching Coefficients

We found that the values of δ_r and η_r are the same regardless of whether inelastic switching takes place. This is possible because the anisotropy field that opposes the rotation of magnetization is essentially independent of the inelastic switching. In contrast, the values of δ_w and η_w for (elastic) switching *toward* saturation were found to be different than for (elastic and inelastic) switching *away* from saturation. This is possible because the restoring forces in the two cases may be different (see Fig. 2). For the same reason, δ_w and η_w for switching from a demagnetized state ($\phi = 0$) should be the same for positive and negative switching.

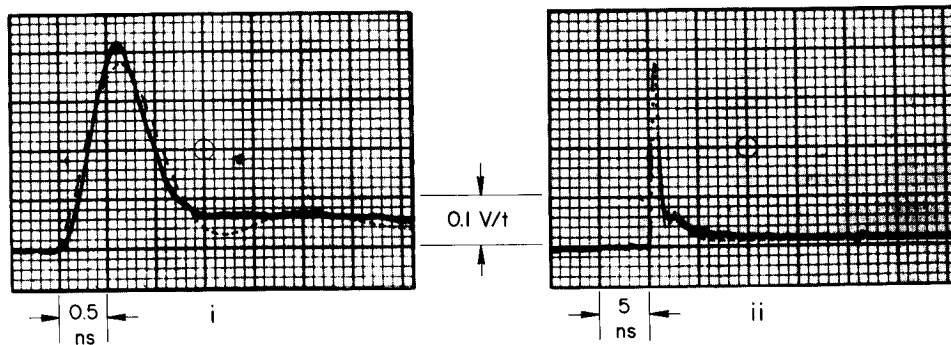
The $\dot{\phi}_{\epsilon_r}$ component is underdamped with $\zeta_r = \frac{1}{2} \delta_r \eta_r^{1/2} = 0.495 \approx 0.5$, and its frequency of oscillation is $(\eta_r^{-1} - \frac{1}{4} \delta_r^2 \eta_r^{-2})^{1/2} / (2\pi) = 487$ Mc/s. For switching toward saturation, the $\dot{\phi}_{\epsilon_w}$ component is overdamped with $\zeta_w = \frac{1}{2} \delta_w \eta_w^{1/2} = 1.414$; however, for switching away from saturation, $\dot{\phi}_{\epsilon_w}$ is slightly underdamped with $\zeta_w = 0.822$, and its frequency of oscillation is $(\eta_w^{-1} - \frac{1}{4} \delta_w^2 \eta_w^{-2})^{1/2} / (2\pi) = 82.5$ Mc/s. These results are consistent with magnetic spectra (plots of the real and the imaginary components of the complex permeability vs. frequency) of polycrystalline ferrites, which exhibit resonance in the microwave region but may or may not exhibit resonance in the radio-frequency region.¹⁴⁻¹⁷



(a) $F_D = 0.6 At$



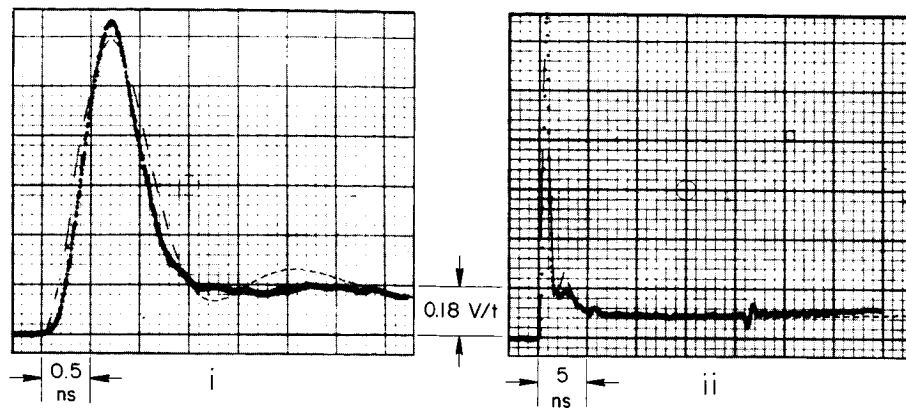
(b) $F_D = 0.9 At$



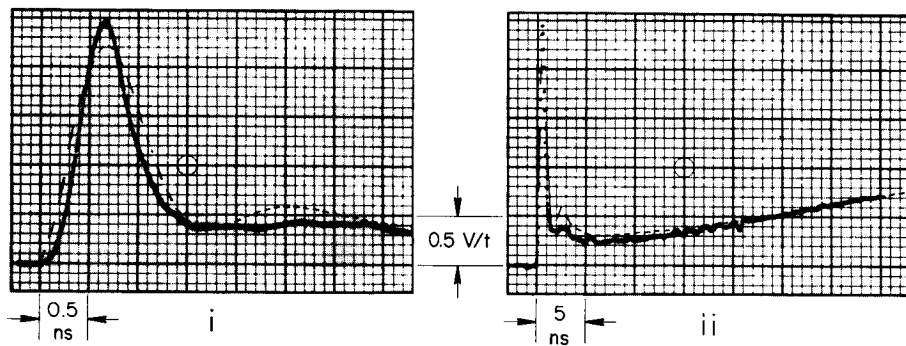
(c) $F_D = 1.5 At$

TD-5670-43

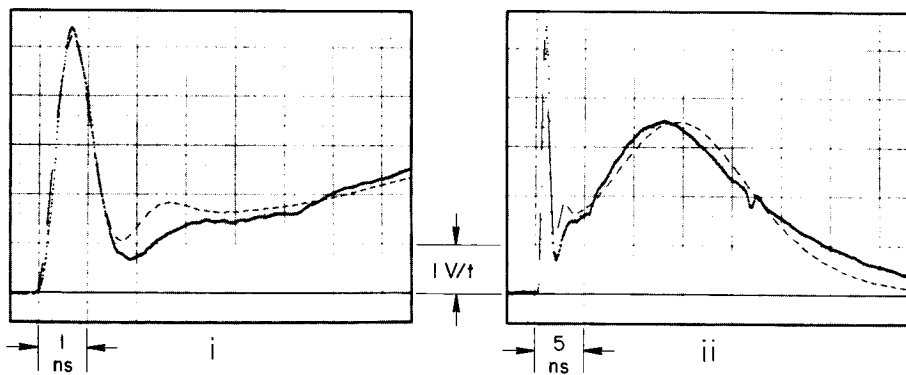
FIG. 14 EXPERIMENTAL (Dotted and Solid Line) AND COMPUTED (Dashed Line) $\phi(t)$ WAVEFORMS OF UNLOADED CORE E-6, USING $F(t)$ WITH $T_r = 0.4$ ns AND VARIOUS VALUES OF AMPLITUDE F_D



(d) $F_D = 4.0 \text{ At}$



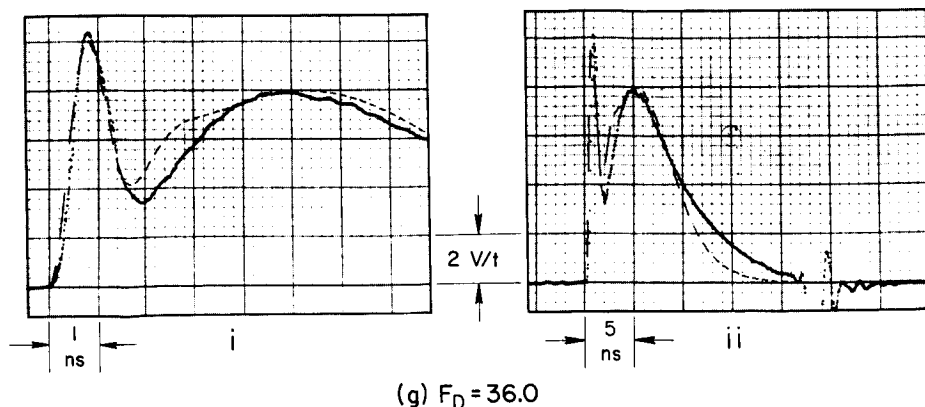
(e) $F_D = 8.0 \text{ At}$



(f) $F_D = 20.0 \text{ At}$

TD-5670-44

FIG. 14 Continued



TC-5670-45

FIG. 14 Concluded

b. Determination of Viscous Damping and Anisotropy Constant

Following Eqs. (27) and (28),

$$\alpha = \frac{\delta_r}{\sqrt{4\eta_r - \delta_r^2}} \quad (51)$$

and

$$H_t \approx H_i = \frac{2}{\gamma \sqrt{4\eta_r - \delta_r^2}} \quad (52)$$

Substituting $\delta_r = 0.28$ ns and $\eta_r = 0.08$ ns² into Eqs. (51) and (52), we find that $\alpha = 0.57$ and, since $H_i \gg H$ and $\gamma = 1.76 \cdot 10^7$ (Oe-s)⁻¹, that $H_i \approx 232$ Oe. The anisotropy constant K_1 of materials whose easy axes are body diagonals, such as ferrites, is given by

$$K_1 = -\frac{3}{4} H_k M_s \quad (53)$$

For Core E-6, whose nominal composition is

$[Mg_{0.32}Zn_{0.10}Mn_{0.58}]^{++}[Mn_{0.52}Fe_{1.48}]^{+++}O_4$, $M_s = 208$ G, and if $H_d \ll H_k$, then $H_i \approx H_k \approx 232$ Oe, and $K_1 \approx -3.6 \cdot 10^4$ ergs/cm³. This value lies

between values of K_1 for magnesium and manganese polycrystalline ferrites measured by other methods.^{16,17} Using the technique presented in this report, magnetic coefficients may thus be measured in the time domain, in addition to the frequency domain.^{16,17}

c. Magnetic Spectrum

Equations (36) and (39) may be used to calculate the magnetic spectrum (the complex permeability $\mu = \mu' - j\mu''$ vs. the frequency f) due to elastic rotation of magnetization and elastic wall motion. Let us drop the corresponding subscripts r and w in the following derivation because the resulting expressions are valid for either rotation of magnetization or domain-wall motion. Dividing Eq. (36) or Eq. (39) by A and replacing F by Hl , we obtain

$$B_\epsilon + \delta \dot{B}_\epsilon + \eta \ddot{B}_\epsilon = (\epsilon l/A) H, \quad (54)$$

where both B_ϵ and H designate changes from zero values. The Laplace transform of Eq. (54) gives

$$\mu(s) = \frac{B_\epsilon(s)}{H(s)} = \frac{\epsilon l}{A} \frac{1}{1 + s\delta + s^2\eta}. \quad (55)$$

Letting $s \rightarrow j\omega$, where $\omega = 2\pi f$, Eq. (55) becomes

$$\mu(j\omega) = \mu_{(0)} \frac{1 - \omega^2\eta - j\omega\delta}{(1 - \omega^2\eta)^2 + \omega^2\delta^2}, \quad (56)$$

where

$$\mu_{(0)} = \epsilon l/A. \quad (56a)$$

Following the definition

$$\mu = \mu' - j\mu'' \quad (57)$$

equating Eqs. (56) and (57) gives

$$\mu' = \mu_{(0)} \frac{1 - \omega^2\eta}{(1 - \omega^2\eta)^2 + \omega^2\delta^2}, \quad (58)$$

$$\mu'' = \mu_{(0)} \frac{\omega\delta}{(1 - \omega^2\eta)^2 + \omega^2\delta^2} \quad (59)$$

and

$$|\mu| = \mu_{(0)} \frac{1}{\sqrt{(1 - \omega^2\eta)^2 + \omega^2\delta^2}} \quad (60)$$

Note that as $\omega \rightarrow 0$, $\mu' \rightarrow \mu \rightarrow \mu_{(0)}$ and $\mu'' \rightarrow 0$, and that as $\omega \rightarrow \infty$, $\mu' \rightarrow \mu'' \rightarrow \mu \rightarrow 0$.

Equating $d\mu'/d\omega$, $d\mu''/d\omega$, and $d|\mu|/d\omega$ to zero, we find that μ' , μ'' , and $|\mu|$ peak at the following resonance ω values, respectively:*

$$\omega'_r = \sqrt{\frac{1}{\eta} (1 - \delta\eta^{-1/2})} \quad (61)$$

$$\omega''_r = \sqrt{2\eta - \delta^2 + \sqrt{(2\eta - \delta^2)^2 + 12\eta^2}} / (\eta\sqrt{6}), \quad (62)$$

and

$$\omega_r = \sqrt{\frac{1}{\eta} \left(1 - \frac{1}{2} \delta^2 \eta^{-1}\right)} \quad (63)$$

Examining Eqs. (61), (62), and (63), we find the following:

- (1) If $\delta = 0$, then $\omega'_r = \omega''_r = \omega_r = \eta^{-1/2}$.
- (2) If $\zeta < 1$, where $\zeta = \frac{1}{2} \delta\eta^{-1/2}$, then $\omega'_r < \omega_r < \omega''_r$.
- (3) By equating ω'_r , ω_r , and ω''_r to zero, we find that if $\zeta > 0.5$, then $\mu'(\omega)$ has no resonance peak, that if $\zeta > 0.707$, then $|\mu(\omega)|$ has no resonance peak, and that ω''_r always has a resonance peak, unless $\eta = 0$.

* The subscript r in ω'_r , ω''_r , and ω_r denotes resonance, not rotation. Thus, ω'_{rr} , ω''_{rr} , and ω_{rr} are resonance ω 's due to rotation of magnetization, whereas ω'_{rw} , ω''_{rw} , and ω_{rw} are resonance ω 's due to wall motion. Similar subscripts will be used to denote the frequency $f = \omega/(2\pi)$ at resonance.

Substitutions of Eq. (61) into Eq. (58), Eq. (62) into Eq. (59), and Eq. (63) into Eq. (60) give the peak values of μ' , μ'' , and $|\mu|$, respectively, at resonance. Thus

$$\mu'_r = \frac{\mu_{(0)}}{\frac{\delta}{\sqrt{\eta}} \left(2 - \frac{\delta}{\sqrt{\eta}} \right)} \quad (64)$$

and

$$|\mu_r| = \frac{\mu_{(0)}}{\frac{\delta}{\sqrt{\eta}} \sqrt{1 - \left(\frac{\delta}{2\sqrt{\eta}} \right)^2}} \quad (65)$$

The rotational coefficients of Core E-6 were found to be $\delta_r = 0.28$ ns, $\eta_r = 0.08$ ns², and $\epsilon_r = 0.14$ nH/t². The magnetic spectrum due to rotation of magnetization only may thus be computed by substituting these values into Eqs. (58) through (65). In so doing we find that $f'_{rr} = 56.3$ Mc/s, $f_{rr} = 402$ Mc/s, and $f''_{rr} = 495$ Mc/s. We also find that μ'_{rr} is very slightly above $\mu_{r(0)}$ (because $\zeta_r = 0.495$ is very close to 0.5), $\mu''_{rr} = 1.07 \mu_{r(0)}$, and $|\mu_{rr}| = 1.162 \mu_{r(0)}$, where $\mu_{r(0)} = \epsilon_r l/A = 17.17 \mu_0 = 21.55 \mu\text{H}/(\text{m-t}^2)$. The value of f'_{rr} relative to f_{rr} is small compared with measured magnetic spectra.¹⁴⁻¹⁷ Referring to Eq. (61), $\delta_r \eta_r^{-1/2} = 0.28/\sqrt{0.08} \approx 0.99$, which is close to unity; hence, ω'_{rr} is very sensitive to any errors in δ_r and η_r . In contrast, ω''_{rr} , Eq. (62), is not so sensitive to these errors. For example, a decrease in δ_r by 5 percent and an increase in η_r by 5 percent will result in the values $f'_{rr} = 157$ Mc/s and $f''_{rr} = 492$ Mc/s, which are quite reasonable.¹⁴⁻¹⁷

Using Eqs. (61) and (62), one may compute δ_r and η_r from the values of f'_{rr} and f''_{rr} in the microwave region of measured magnetic spectrum. If there is also a resonance in the radio-frequency region, then Eqs. (61) and (62) may also be used to compute δ_w and η_w from the values of f'_{rw} and f''_{rw} .

d. ϕ_r/ϕ_s Ratio .

Referring to Eqs. (36) and (39), as $t \rightarrow \infty$, the total elastic flux change in response to a step $F(t)$ of amplitude F_D is $(\epsilon_r + \epsilon_w)F_D$, where $\epsilon_r F_D$ and $\epsilon_w F_D$ are the contributions due to rotation of magnetization and domain-wall motion, respectively. A drive of $F_D = 40.0$ At, which is 44.5 times larger than the coercive MMF F_c , is high enough to saturate the core material. By fitting the computed $\dot{\phi}_e(t)$ to the experimental $\dot{\phi}_e(t)$, we have found empirically that $\epsilon_r \approx 0.14(1 - 0.005 F_D) \cdot 10^{-9} \text{H/t}^2$ and $\epsilon_w \approx 0.266(1 - 0.008 F_D) \cdot 10^{-9} \text{H/t}^2$. Thus, for $F_D = 40$ At, $\epsilon_r \approx 0.1123 \cdot 10^{-9} \text{H/t}^2$ and $\epsilon_w \approx 0.1814 \cdot 10^{-9} \text{H/t}^2$. The corresponding elastic flux changes are $\Delta\phi_{\epsilon_r} = 0.45$ Mx, $\Delta\phi_{\epsilon_w} = 0.725$ Mx, and $\Delta\phi_e = 1.175$ Mx. Since $\phi_r = 3.45$ Mx, we find that the true saturation flux is $\phi_s = \phi_r + \Delta\phi_e = 4.625$ Mx, and hence $\phi_r/\phi_s = 0.746$. Theoretically, in polycrystalline ferrites with no domains of reverse magnetization, $\phi_r/\phi_s = 0.87$. This value is close to the value of $(\phi_r + \Delta\phi_{\epsilon_w})/\phi_s = 0.90$ that results from the empirical approximations for ϵ_r and ϵ_w at $F = 40$ At.

In the calculation of inelastic flux switching we have assumed that $\phi_r/\phi_s \approx 0.9$ in order to obtain a good agreement between the computed and the measured static $\phi(F)$ curve for practical F values, e.g., $F \lesssim 10 F_c$. This approximation is invalid if F is considerably larger than $10 F_c$ because ϕ_r/ϕ_s may be appreciably smaller than 0.9. For example, as was shown above, $\phi_r/\phi_s = 0.746$ for $F_D = 40$ At $\approx 44 F_c$. It was similarly found that $\phi_r/\phi_s \approx 0.83$ for $F_D = 20$ At $\approx 22 F_c$. Since the main inelastic flux switching [see Eq. (47)] terminates when ϕ reaches ϕ_d , and since $\phi_d \rightarrow \phi_s$ as $F \rightarrow \infty$ (see Report 2, pp. 3-6), the flux change $\Delta\phi_{ma} = \int_0^\infty \dot{\phi}_{ma} dt$ computed from Eq. (47) will be too low if ϕ_s is lower than the actual value. This explains why the computed $\Delta\phi$ and the computed $\dot{\phi}(t)$ waveforms toward the end of switching for $F_D = 20.0$ At and $F_D = 40.0$ At in Figs. 14(f) and (g) are lower than the experimental ones.

e. Disappearance of $\dot{\phi}_i(t)$ at High F

The fact that $\dot{\phi}_i(t)$ had to be equated to zero in order to obtain a reasonable agreement between the computed and the experimental $\dot{\phi}(t)$ waveforms in the cases of $F_D = 20$ At and $F_D = 40$ At is not surprising. This behavior was predicted in the past (Report 3, p. 12 and Ref. 18, p. 224) on the basis of the interpretation of the physical mechanism of the $\dot{\phi}_i$ component. As F exceeds a certain value, the

contribution of $\dot{\phi}_i(t)$ to the total $\dot{\phi}(t)$ starts to diminish because the decrease in the portion p of the minor wall displacements outweighs the increase in the total number n of inelastic wall displacements. If F is high enough, the contribution of $\dot{\phi}_i(t)$ becomes negligible compared with $\dot{\phi}_{na}(t)$. It appears from the results of Fig. 14 that $\dot{\phi}_i(t)$ of Core E-6 becomes negligible if $F > 20 F_c$.

B. Voltage Drive

1. Introduction

Computation of flux switching has so far been based on evaluation of $\dot{\phi}$ for given values of F and ϕ . In this way, the voltage induced across a core winding is computed as a function of the driving current(s). However, in many applications, a core is driven by a voltage source rather than a current source, and there is a need to compute the corresponding net magnetizing current. The same switching models used so far are applicable in this case of voltage drive. In other words, the models used for computation of $\dot{\phi}(F, \phi)$ are also applicable for computation of $F(\dot{\phi}, \phi)$ [or $\phi(F, \dot{\phi})$ for that matter]. This is so because the functional relationship among the three variables F , $\dot{\phi}$, and ϕ is the same regardless of which variable is solved for. Thus, if two of these variables are given, we can solve for the third one.

2. Computation of $F(\dot{\phi}, \phi)$

As an illustration, let us consider the approximation for the total inelastic $\dot{\phi}$ given in Eq. (22) of Report 4, p. 14:

$$\dot{\phi} = \dot{\phi}_p(F) \left\{ 1 - \left[\frac{2\phi + \phi_s - \phi_d(F)}{\phi_s + \phi_d(F)} \right]^2 \right\}, \quad (66)$$

where

$$\dot{\phi}_p(F) = \begin{cases} 0 & \text{if } 0 \leq F \leq F_0'' \\ \lambda(F - F_0'')^\nu & \text{if } F_0'' \leq F \leq F_B \\ \rho_p(F - F_0) & \text{if } F_B \leq F \end{cases}. \quad (67)$$

For given $\dot{\phi}$ and ϕ , Eq. (66) is an *implicit* equation in F . We shall use the Newton-Raphson iterative method to solve for F transcendently. At each j th iteration, F will be corrected according to

$$F_j = F_{j-1} - \frac{g(F_j)}{g'(F_j)} \quad (68)$$

where, following Eq. (66),

$$g(F) = \dot{\phi}_p(F) \left\{ 1 - \left[\frac{2\phi + \phi_s - \phi_d(F)}{\phi_s + \phi_d(F)} \right]^2 \right\} - \dot{\phi} \quad (69)$$

and $g'(F) = dg(F)/dF$. Differentiation of Eq. (69) with respect to F gives

$$g'(F) = \dot{\phi}'_p(F) \left\{ 1 - \left[\frac{2\phi + \phi_s - \phi_d(F)}{\phi_s + \phi_d(F)} \right]^2 \right\} + \frac{4\dot{\phi}_p(F)\phi'_d(F)}{[\phi_s + \phi_d(F)]^3} (\phi + \phi_s) [2\phi + \phi_s - \phi_d(F)] \quad (70)$$

where $\dot{\phi}'_p(F) = d\dot{\phi}_p(F)/dF$ and $\phi'_d(F) = d\phi_d(F)/dF$. The expressions for $\dot{\phi}'_p(F)$ and $\phi'_d(F)$ are given in Report 3, pp. 19-20. See also p. 148.

The time increment, Δt , is chosen to be a small fraction of the switching time, τ_s ; e.g., $\Delta t = 0.002 \tau_s$. Thus, for a given waveform of the $\dot{\phi}(t)$ drive, we need to estimate τ_s .

For given initial values of $\dot{\phi}$ and ϕ , the initial value of F , F_z , may be solved for explicitly using Eq. (66). This solution will depend on the waveform of $\dot{\phi}(t)$.

3. Examples of $\dot{\phi}(t)$ Drives

Rectangular and sinusoidal $\dot{\phi}(t)$ drive pulses of width T and amplitude $\dot{\phi}_m$ are considered as examples. Assuming that initially $\phi = -\phi_r$ and finally $\phi = \phi_r$, $\phi(t)$, τ_s , and the initial F are calculated for each case as follows.

a. Rectangular $\dot{\phi}(t)$

A rectangular $\dot{\phi}(t)$ pulse is defined as

$$\dot{\phi}(t) = \begin{cases} \dot{\phi}_m & \text{if } 0 < t < T \\ 0 & \text{otherwise} \end{cases} \quad (71a)$$

Hence,

$$\phi(t) = -\phi_r + \dot{\phi}_m t \quad (72a)$$

Since the core may reach saturation at $t < T$,

$$\tau_s = \begin{cases} 2\phi_r/\dot{\phi}_m & \text{if } \dot{\phi}_m \geq 2\phi_r/T \\ T & \text{otherwise} \end{cases} \quad (73a)$$

Initially $\phi = -\phi_r$, and as $\dot{\phi}$ jumps from zero to $\dot{\phi}_m$, F jumps from zero to a value high enough to assume that $\phi_d(F) \approx \phi_s$. The initial value of $\dot{\phi}_p(F)$ in Eq. (66) is, therefore, $\dot{\phi}_p = \dot{\phi}_m/[1 - (\phi_r/\phi_s)^2]$. Equating this value to each of the expressions for $\dot{\phi}_p(F)$ in Eq. (67), the initial value of F is found to be

$$F_z = \begin{cases} F_0'' + \left\{ \frac{\dot{\phi}_m}{\lambda[1 - (\phi_r/\phi_s)^2]} \right\}^{\frac{1}{\nu}} & \text{if } 0 < \dot{\phi}_m \leq \rho_p(F_B - F_0)[1 - (\phi_r/\phi_s)^2] \\ F_0 + \frac{\dot{\phi}_m}{\rho_p[1 - (\phi_r/\phi_s)^2]} & \text{otherwise} \end{cases} \quad (74a)$$

b. Sinusoidal $\dot{\phi}(t)$

A sinusoidal $\dot{\phi}(t)$ pulse is defined as

$$\dot{\phi}(t) = \begin{cases} \dot{\phi}_m \sin(\omega t) & \text{if } 0 \leq t \leq T \\ 0 & \text{otherwise} \end{cases} \quad (71b)$$

where $\omega = \pi/T$. Time integration of Eq. (71b) gives

$$\varphi(t) = -\phi_r + \frac{\dot{\phi}_m}{\omega} (1 - \cos \omega t) \quad . \quad (72b)$$

Since the core may saturate at $t < T$,

$$\tau_s = \begin{cases} \frac{1}{\omega} \cos^{-1} [1 - (2\phi_r \omega / \dot{\phi}_m)] & \text{if } \dot{\phi}_m > \phi_r \omega \\ T & \text{otherwise} \end{cases} \quad . \quad (73b)$$

Initially, $\phi = -\phi_r$ and $\dot{\phi} = 0$. Following Eqs. (66) and (67), the initial value of F is simply

$$F_z = F_0'' \quad . \quad (74b)$$

4. Computation of $F(t)$ for Given $\dot{\phi}(t)$

a. Computer Program

A computer program for computation of $F(t)$ for a given $\dot{\phi}(t)$ waveform was written on the basis of Eqs. (66) through (74). The program was written in the Burroughs extended version of ALGOL-60, and is given in Appendix A for the case of sinusoidal $\dot{\phi}(t)$. The outline of this program is given as follows:

- (1) Declare global identifiers of core parameters, circuit parameters, time variables, miscellaneous, input-output lists and formats, and PROCEDURES.
- (2) Read in the core parameters.
- (3) For a given $\dot{\phi}(t)$ drive:
 - (a) Declare $\dot{\phi}(t)$ and $\phi(t)$ PROCEDURES, Eqs. (71) and (72).
 - (b) Set $\dot{\phi}_m$ and T values; compute $\omega = \pi/T$ if $\dot{\phi}(t) = \dot{\phi}_m \sin(\omega t)$.
 - (c) Compute τ_s and F_z , Eqs. (73) and (74).
- (4) Set $\Delta t = 0.002 \tau_s$.
- (5) Print the core parameters, the $\dot{\phi}(t)$ parameters, and output heading.
- (6) Set and print the initial conditions of the time variables.

- (7) For every Δt during flux-switching time, compute the following:
 $t = t_{-1} + \Delta t$; $\dot{\phi}$ [call $\dot{\phi}(t)$ PROCEDURE];
 ϕ [call $\phi(t)$ PROCEDURE]; Approximate F ,
 $AF = 2F_{-1} + F_{-2}$; F [call MMF ($\dot{\phi}, \phi, AF, \phi_d$) PROCEDURE];
reset F_{-2} to F_{-1} and F_{-1} to F .
Flux switching terminates ($\dot{\phi} = 0$) if $\phi > \phi_d$ or
 $F > 5 F_0''$.
- (8) Print output ($t, \dot{\phi}, \phi, F, \phi_d$, and the number of iterations) every, say, 10th Δt .

The outline of the PROCEDURE MMF ($\dot{\phi}, \phi, AF, \phi_d$) which is called in Step (7), is as follows:

- (a) Set F to Approximate F , AF .
(b) Compute the following in a loop until convergence is achieved: ϕ_d and ϕ_d' [Report 3, Eqs. (30) through (35)]; ϕ_p and ϕ_p' [Report 3, Eqs. (36) through (39)]; $g(F)$ [Eq. (69)]; $g'(F)$ [Eq. (70)]; F [Eq. (68)]. Repeat the loop if $|g(F)/g'(F)| > |0.0001F|$.

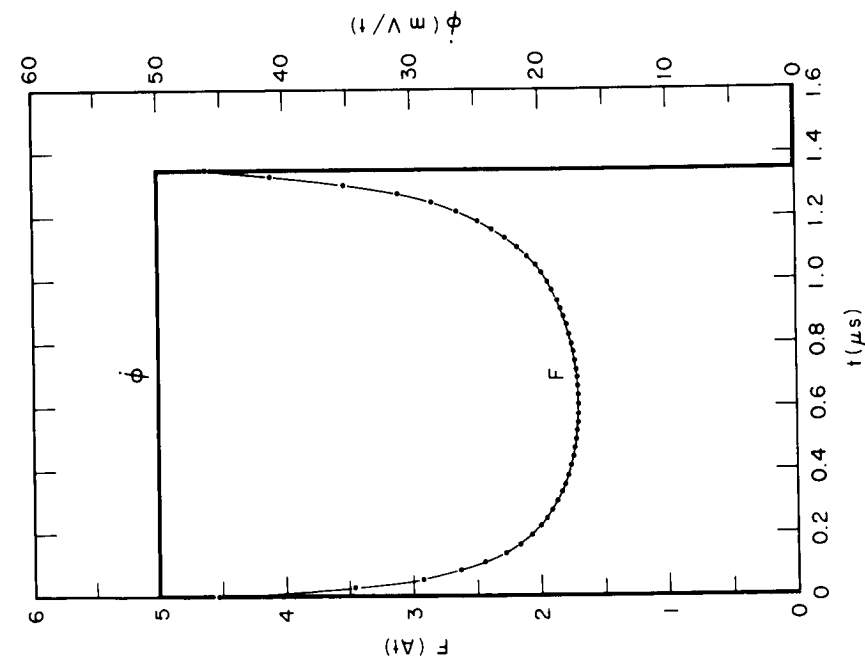
b. Results

Computed $F(t)$ waveforms for rectangular and sinusoidal $\dot{\phi}(t)$ drive pulses, both of amplitude $\dot{\phi}_m = 0.05$ V/t and of maximum duration $T = 3.0 \mu s$, are shown in Fig. 15. The assumed core was Core E-6, and the core parameters for inelastic switching used in the computation included ϕ_r , ϕ_s , H_a , H_q , H_n , λ , F_0'' , ν , ρ_p , F_0 , and F_B . The values of these parameters are given on p. 36.

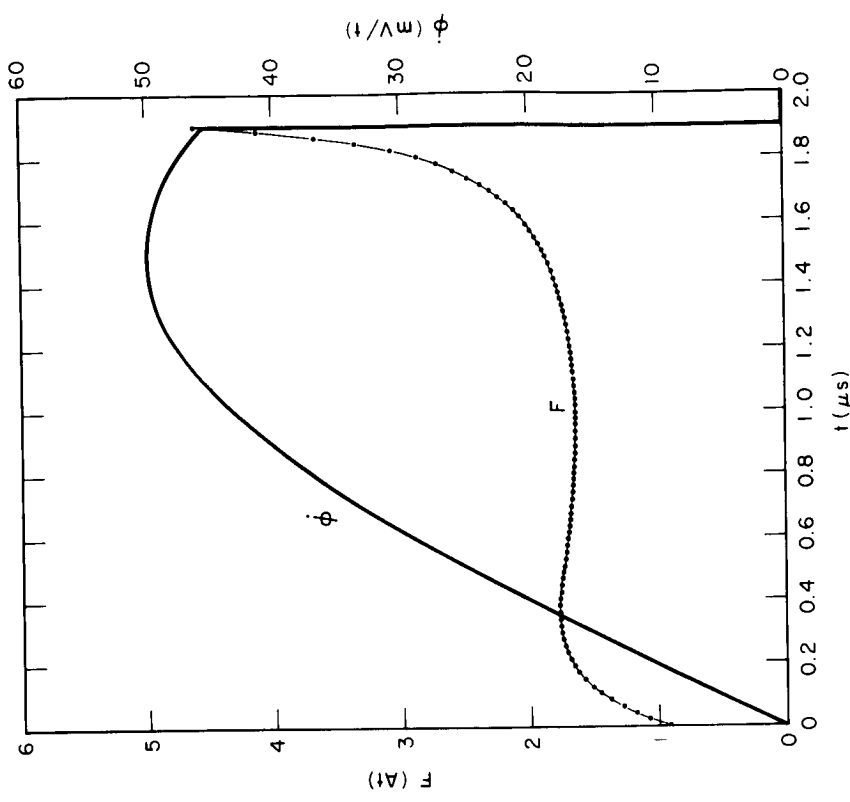
c. Discussion

The computed $F(t)$ waveforms in Fig. 15 are very similar in shape to typical experimental $F(t)$ corresponding to rectangular and sinusoidal $\dot{\phi}(t)$ drives. However, it would be more convincing to compare these computed results with $F(t)$ waveforms observed on Core E-6 itself. Because of other commitments, such an experimental verification was deferred to the future.

An additional computer program was written for computation of flux switching in a core driven by a voltage source in series with a



(a) RECTANGULAR $\dot{\phi}(t)$ DRIVE



(b) SINUSOIDAL $\dot{\phi}(t)$ DRIVE

TC-5670-47

FIG. 15 COMPUTED $F(t)$ WAVEFORMS OF CORE E-6 FOR TWO GIVEN $\dot{\phi}(t)$ DRIVES

variable internal resistance, R_i . This drive is an intermediate case between voltage and current sources. Here, again, the switching models were found to be valid.

C. Flux Switching From a Partially Set State

1. Introduction

The properties of flux switching from a partially demagnetized state (*i.e.*, one where the initial flux level is not $\pm\phi_r$) are history-dependent: they depend not only upon the initial flux level, but also upon how that flux level was attained. Considerable data have been obtained^{3,19,20} for the special case in which the core is partially demagnetized by a rectangular PARTIAL-SET current pulse of amplitude F_{ps} and duration T_{ps} . These data clearly demonstrate that there are several very significant effects [*e.g.*, reduction of the threshold and slope of the $\dot{\phi}_p(F)$ curves, and anomalous variation of the peaking time, t_p] that have not yet been satisfactorily explained on the basis of the physics of magnetization reversal. Most of these data were taken with a large time duration, T_b (relative to the relaxation of the magnetization, *e.g.*, $\gg 1 \mu s$), between the PARTIAL-SET pulse and the subsequent TEST pulse used to determine the resulting switching properties.

The limited data for $T_b \ll 1 \mu s$ indicated, but did not conclusively prove, that the anomalous partial-setting effects result from the partial setting itself and not from the cessation of switching (*e.g.*, relaxation effects) during the T_b period. It is the primary purpose of this section to demonstrate that, indeed, the anomalous effects of partial setting exist also for $T_b = 0$. In the previous experiments a small T_b was achieved by bringing the two pulses together. This required that the rise of the TEST pulse be adjusted to match the fall of the PARTIAL-SET pulse, which is a troublesome task. Another difficulty was the measurement of the partially set flux level, ϕ_{ps} . The value of ϕ_{ps} was measured for large T_b , after which T_b was reduced to zero without adjusting the PARTIAL-SET pulse to keep ϕ_{ps} precisely constant. Thus it could not be determined how much of the effect of reducing T_b to zero was due to the small increase in ϕ_{ps} , and how much was due to the elimination of the T_b period. The experiments to be described here achieved a $T_b = 0$ condition by superimposing a shorter positive or negative pulse on top of the latter part of a longer pulse. The value

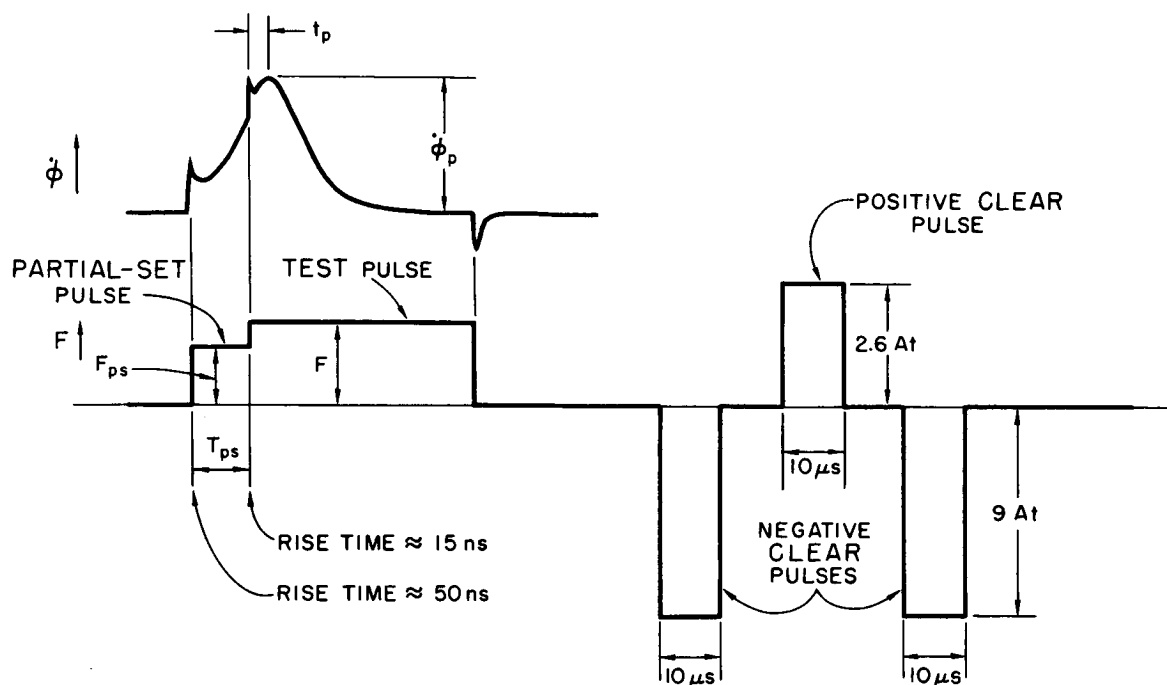
of F of the TEST pulse is thus the algebraic sum of these two pulse amplitudes, and T_{ps} is the time duration between the beginnings of these two pulses. In addition, the value of ϕ_{ps} was measured at the beginning of the TEST pulse to eliminate the ambiguity in ϕ_{ps} . A secondary purpose of these experiments was to include measurements of peaking time, t_p . It was noted in Refs. 3, 19, and 20 that t_p was affected in an anomalous manner by partial setting. However, only very limited information was obtained on how t_p varied with F and T_{ps} ; furthermore, this information was limited to $T_b \gg 1 \mu s$ only.

No attempt will be made here to develop switching models to describe these experimental results because there are still too many unresolved problems. Instead, the experimental data will be given in a form which can be readily used for any future attempts at modeling.

2. Experiment

The experiments were performed on the same polycrystalline ferrite core that had been studied for $T_b \gg 1 \mu s$ so that direct comparisons could be made. It was desirable to use a thin-ring core ($OD/ID \approx 1$) so that complicating geometric effects would not be introduced. Core E-6 (see p.36) was thus chosen. Since only one core was tested, the results cannot be considered to be general, but only a measure of one possible set of partial-setting effects.

The experiments consisted of clearing the core to a reproducible reference state, $-\phi_r$, and then applying the two superimposed pulses which make up the PARTIAL-SET pulse and the TEST pulse. See Fig. 16. A particular partially set flux level ϕ_{ps} was established by adjusting F_{ps} for the desired T_{ps} value. Then, with ϕ_{ps} , F_{ps} , and T_{ps} held fixed, F was varied and $\dot{\phi}_p$ and t_p were measured for each F value. Oscillograms of $\dot{\phi}(t)$ were taken for several F values. These measurements were then repeated for different T_{ps} and F_{ps} values. Only one ϕ_{ps} value was studied, $\phi_{ps} = -0.46 \phi_r$. This corresponds to the value used for much of the data of Ref. 19 ($T_b \gg 1 \mu s$) to be used for comparison. Three T_{ps} values were studied, $0.5 \mu s$, $1.0 \mu s$, and $10 \mu s$. For much smaller T_{ps} values, $\dot{\phi}_p$ and t_p could not be determined because t_p became very small or nonexistent and the tail of the initial spike increased somewhat (see Fig. 6, p. 16, Ref. 19), thus obscuring the peak in $\dot{\phi}(t)$.



TA-5670-46

FIG. 16 PULSE SEQUENCE FOR PARTIAL-SETTING EXPERIMENT

The core was mounted coaxially in a section of 50Ω transmission line so that pulses with short rise times could be applied. The core holder used was the same as that described on p. 85 of Report 3 except that the four-conductor one-turn winding was changed to a ten-conductor one-turn winding, and the number of turns of the sense winding was increased from five to ten. The integrator used for flux measurement was that described on pp. 86 and 87 of Report 3. The integrated $\dot{\phi}(t)$ waveform was observed on the oscilloscope and the flux change produced by the PARTIAL-SET pulse was measured using a voltage reference and a chopper.

The oscilloscope had a response time of 15 ns. The response of the oscilloscope was checked for overshoot and rise time by using a mercury relay pulser with a rise time less than 1 ns. The horizontal calibration factors for each horizontal scale of the oscilloscope were determined with a time-mark generator. The negative CLEAR pulses were supplied from a vacuum-tube pulser having a $0.1 \mu s$ rise time. The positive CLEAR pulse and the PARTIAL-SET pulse were supplied from transistor pulsers

having 50 ns rise times. The TEST pulse was made up by adding or subtracting a pulse with a 15 ns rise time to the latter part of the PARTIAL-SET pulse (see Fig. 16).

3. Results and Discussion

a. $\dot{\phi}_p(F)$

The $\dot{\phi}_p(F)$ curves with T_{ps} as a parameter are given in Fig. 17. The curve for no partial setting is included for reference. These $\dot{\phi}_p(F)$ curves are very similar to the ones previously obtained for $T_b \gg 1 \mu s$.¹⁹ The two major effects of partial setting seen in Fig. 17 are the reduction in both λ and F_0'' , i.e., the reduction in the slopes and thresholds of the $\dot{\phi}_p(F)$ curves. The reduction in λ tends to decrease the switching speed, and therefore to decrease $\dot{\phi}_p$, whereas the reduction in F_0'' tends to increase $\dot{\phi}_p$. Since $T_b = 0$ for these curves, $\dot{\phi}_p$ is unchanged for $F = F_{ps}$ because this corresponds to the no-partial-setting case. Therefore, each $\dot{\phi}_p(F)$ curve must cross the no-partial-setting curve at $F = F_{ps}$. This is not the case for $T_b > 0$.

It can be seen in Fig. 17 that λ and ν are not much affected by changes in T_{ps} , whereas F_0'' is significantly reduced as T_{ps} is decreased. This was also the case for $T_b \gg 1 \mu s$, as shown in Ref. 19. One curve ($T_{ps} = 1.0 \mu s$) for $T_b = 50 \mu s$ is included in Fig. 17 to clearly illustrate the effect of reducing T_b to zero. (The general effect is nearly the same for $T_{ps} = 0.5 \mu s$ and $10 \mu s$.) In every region of F where data points were taken, $\dot{\phi}_p$ was increased by reducing T_b to zero. This means that the major effect of reducing T_b to zero (with ϕ_{ps} held constant) is to increase λ and not to decrease F_0'' . This clarifies the uncertainty expressed on p. 124 of Report 3 where it was stated that reducing T_b , with ϕ_{ps} actually maintained constant, must result in either a reduction of F_0'' , or an increase in λ , or both. Apparently, the reduction in F_0'' when T_b is reduced (see p. 122 of Report 3) is due to the small decrease in ϕ_{ps} . The values of F_0'' , λ , and ν are plotted vs. T_{ps} in Fig. 18. Corresponding values from Ref. 19 for $T_b = 50 \mu s$ are also included for comparison. Note that λ and ν are more nearly constant for $T_b = 0$ than for $T_b = 50 \mu s$. Thus, the curvature in λ and ν vs. T_{ps} for $T_b = 50 \mu s$ must be due mostly to relaxation effects following the PARTIAL-SET pulse. Figure 18 shows that λ for $T_b = 0$ is consistently above the values for $T_b = 50 \mu s$, whereas F_0'' is

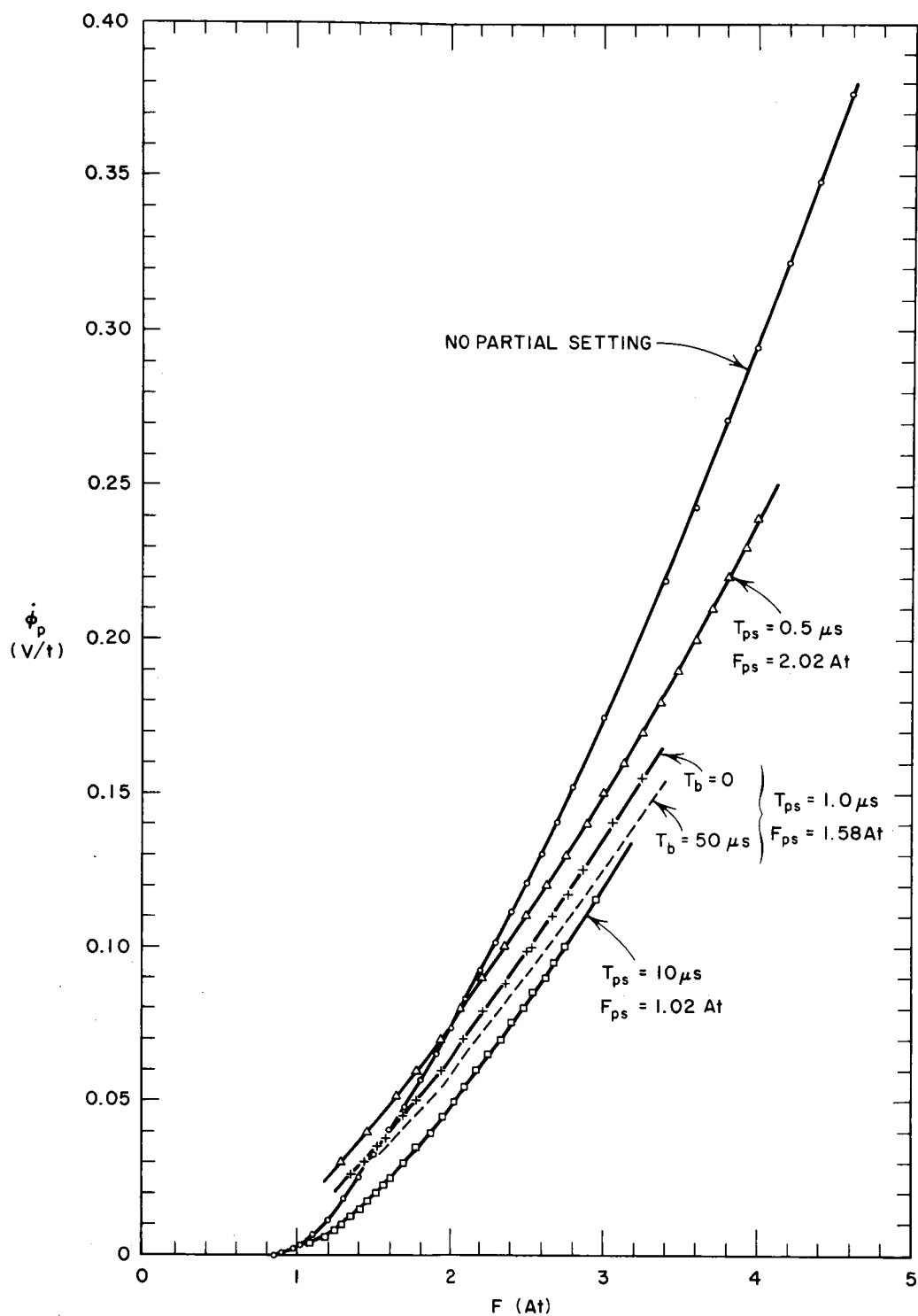


FIG. 17 $\dot{\phi}_p (F)$ WITH T_{ps} AS A PARAMETER
 $(\phi_{ps} = -0.46 \phi_r; T_b = 0; \text{Core E-6})$

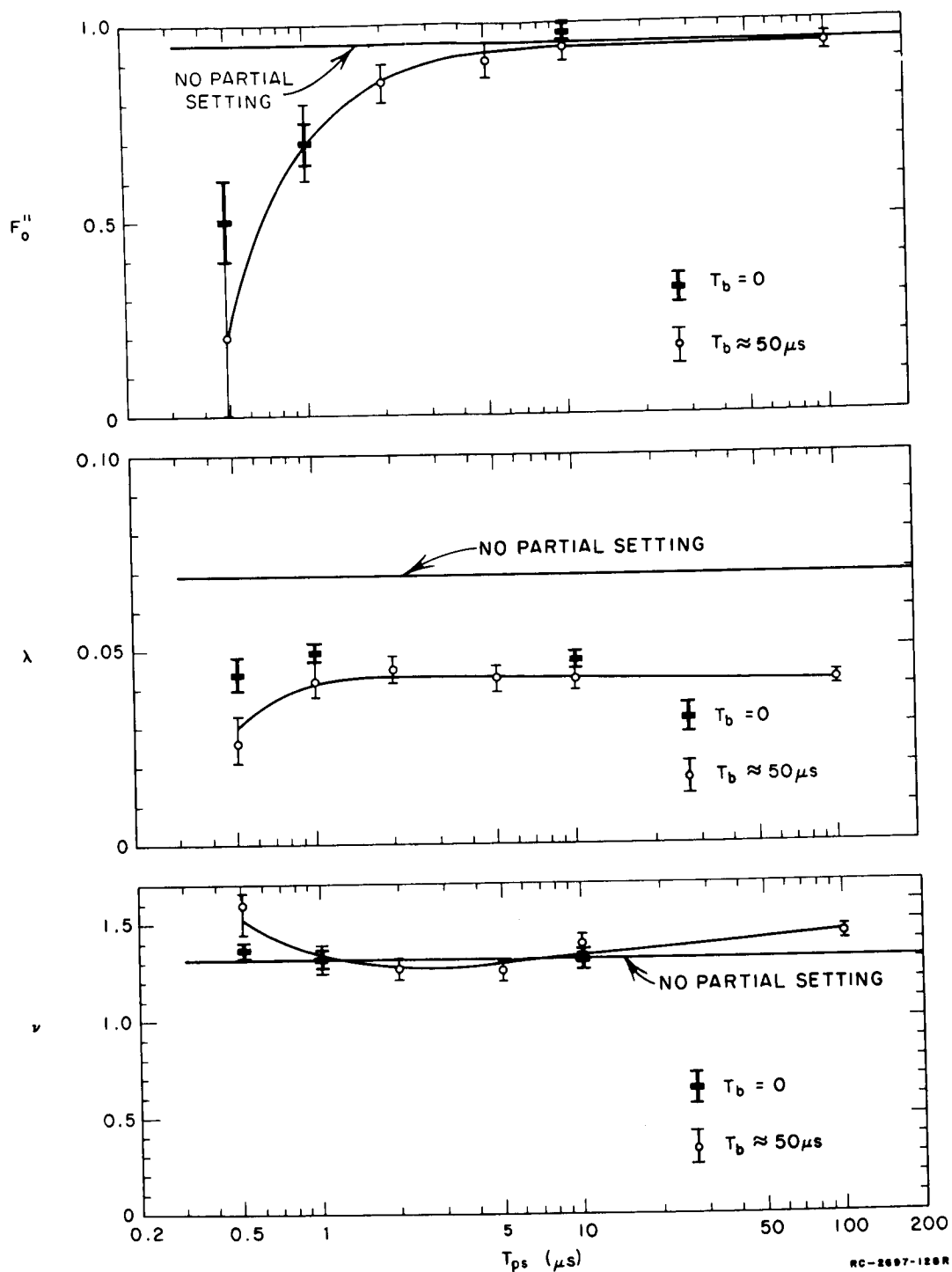


FIG. 18 PLOTS OF F_0'' , λ , AND ν vs. $\log T_{ps}$ FOR $T_b = 0$ AND FOR $T_b \approx 50 \mu s$
 $(\phi_{ps} = -0.46\phi_r; \text{Core E-6})$

not much different for the two extreme values of T_b . The value of F''_0 at $T_{ps} = 0.5 \mu s$ has large error bars because the $\dot{\phi}_p(F)$ data points could not be taken to very low F values. The difference indicated in F''_0 at $T_{ps} = 0.5 \mu s$, which is comparable to the error bars, results in the two $\dot{\phi}_p(F)$ curves for $T_{ps} = 0.5 \mu s$ crossing below any data points, *e.g.*, at about $F \approx 0.9 \text{ At}$.

Shahan and Gutwin²¹ studied the effects of T_b on the threshold of the $\phi(F)$ curve of a copper-manganese ferrite. Their results showed a large asymptotic decrease in threshold as T_b was reduced to 10 ns . This apparent disagreement in the effect of T_b may be due to the difference between the types of measured threshold [the threshold of the static $\phi(F)$ curves *vs.* the threshold of the $\dot{\phi}_p(F)$ curves]. The fact that different ferrite materials were used may also have contributed to this apparent disagreement. Further investigation is needed on this point. It is not surprising that the large differences in F''_0 , λ , and ν occur for small values of T_{ps} because these values correspond to large F_{ps} values which are generally associated with the generation of many domain walls. The large number of domain walls will probably have a large relaxation effect following the PARTIAL-SET pulse. If $T_b = 0$, then these relaxation effects cannot occur.

The major conclusion to be drawn from these results is that for $T_b = 0$, just as for $T_b \gg 1 \mu s$, large effects are produced by partial setting. Thus, the source of these effects cannot be explained by any kind of relaxation occurring after the PARTIAL-SET pulse. One might have attributed these partial-setting effects to the relaxation of noncoherent switching to a different configuration at the termination of the PARTIAL-SET pulse. The above results rule out this explanation. The explanation for these partial setting effects is not likely to be associated with rotational switching anyway, since these effects occur at very low H values for which switching is generally assumed to be by domain-wall motion.

b. $\underline{t_p^{-1}(F)}$

The measurement of t_p has been included because the data of Refs. 3, 19, and 20 shows that t_p varied drastically with T_{ps} , even though F and ϕ_{ps} were kept constant. However, these references included only limited data on the variations of t_p , and for $T_b \gg 1 \mu s$ only.

Curves of $t_p^{-1}(F)$ with T_{ps} as a parameter and $T_b = 0$ are shown in Fig. 19. The no-partial-setting curve is included for comparison. In order to interpret these curves with reference to the parabolic model, consider Eqs. (66) and (67). If these equations are solved for a step $F(t)$, one obtains for $F_0'' \leq F \leq F_B$

$$\dot{\phi}(t) = \lambda(F - F_0'')^\nu \operatorname{sech}^2 \left\{ \frac{2\lambda(F - F_0'')^\nu t}{(\phi_s + \phi_d)} - \tanh^{-1} \left[\frac{-2\phi_{ps} - \phi_s + \phi_d}{\phi_s + \phi_d} \right] \right\}. \quad (75)$$

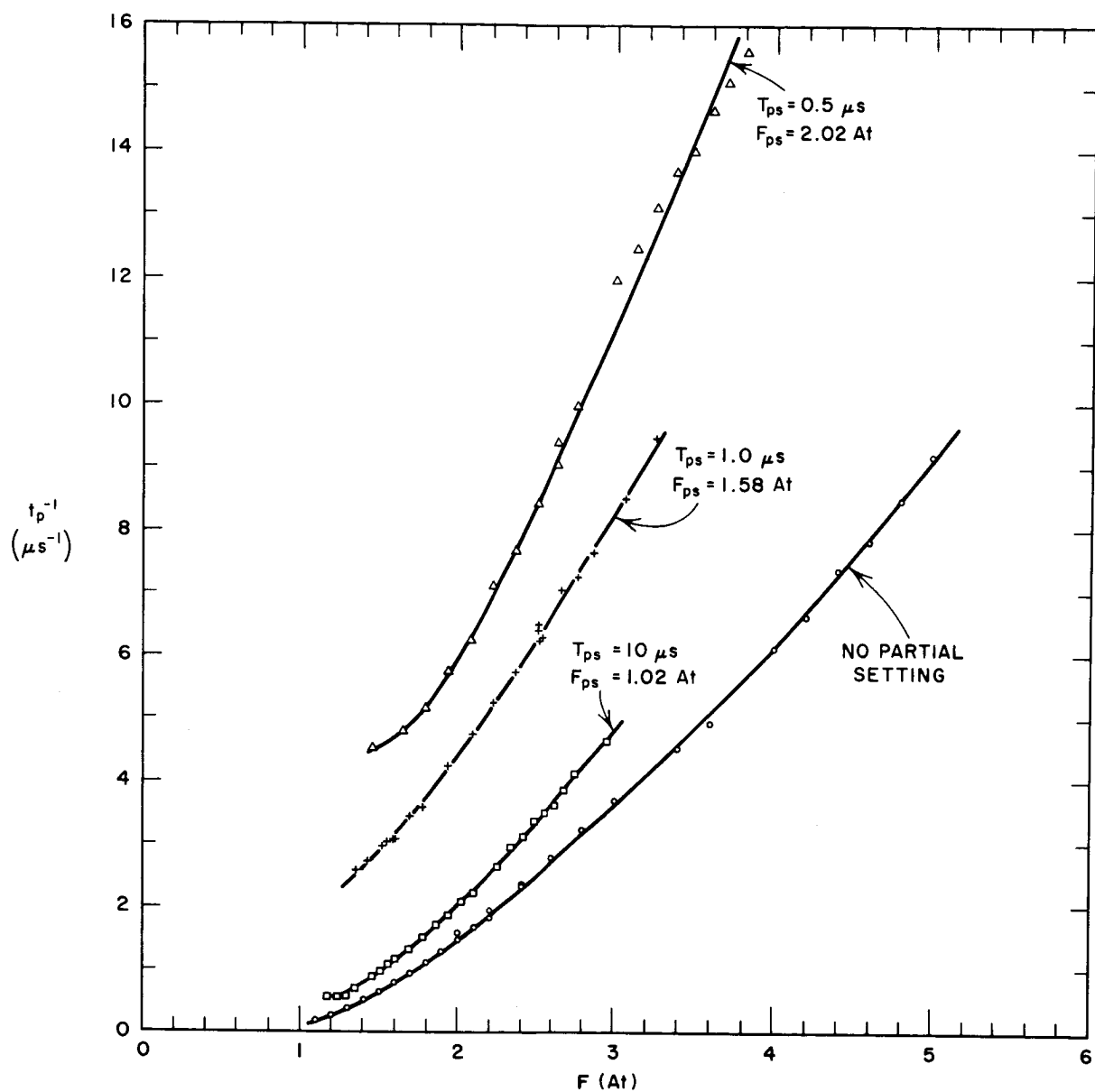
From this equation we can obtain $t_p^{-1}(F)$ by equating the argument of the sech to zero:

$$t_p^{-1} = \frac{\lambda(F - F_0'')^\nu}{\frac{1}{2}(\phi_s + \phi_d) \tanh^{-1} \left[\frac{-2\phi_{ps} - \phi_s + \phi_d}{\phi_s + \phi_d} \right]}. \quad (76)$$

We see from Eq. (76) that $t_p^{-1}(F)$ is proportional to $\dot{\phi}_p(F)$ by a factor equal to the reciprocal of the denominator. For $F \gtrsim 1.5 F_0''$, ϕ_d is roughly constant (i.e., independent of F). Thus, for $F \gtrsim 1.5 F_0''$ and a constant ϕ_{ps} , the denominator of Eq. (76) is roughly constant. As T_{ps} is decreased, the numerator of Eq. (76) varies in the same way as $\dot{\phi}_p(F)$, i.e., the slope is nearly constant and the threshold decreases.

Roughly, these are the effects observed in Fig. 19; however, the slope is not as constant as for the $\dot{\phi}_p(F)$ curves (see Fig. 17), and the threshold decreases as T_{ps} increases far more for $t_p^{-1}(F)$ than for $\dot{\phi}_p(F)$. This demonstrates that this switching model is no longer valid for switching from a partially set state. One possible solution to consider is the introduction of a new parameter, ϕ_c , into the model, as was done in Refs. 19 and 20. Equation (93) on p. 95 of Report 3 gives $\dot{\phi}(t)$ for this modified parabolic model. Solution of this equation for $t_p^{-1}(F)$ gives

$$t_p^{-1} = \frac{\lambda(F - F_0'')^\nu}{\left[\phi_c + \frac{1}{2}(\phi_s + \phi_d) \right] \tanh^{-1} \left[\frac{-2\phi_{ps} - 2\phi_c - \phi_s + \phi_d}{2\phi_c + \phi_s + \phi_d} \right]}. \quad (77)$$



TC-5670-74

FIG. 19 PLOT OF $t_p^{-1}(F)$ WITH T_{ps} AS A PARAMETER
 $(\phi_{ps} = -0.46 \phi_r; T_b = 0; \text{Core E-6})$

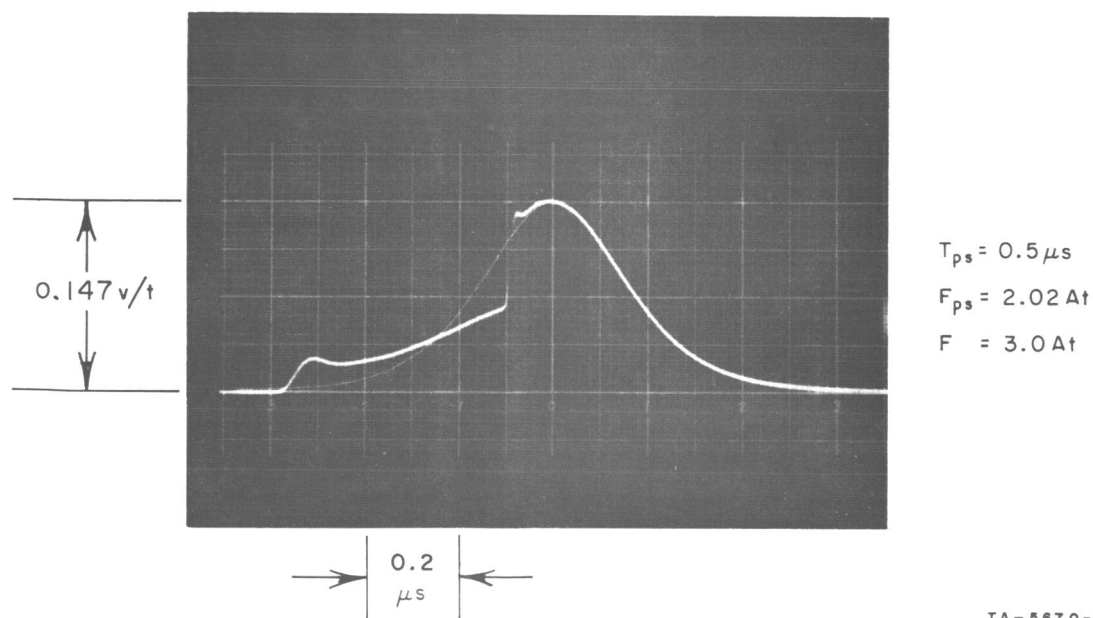
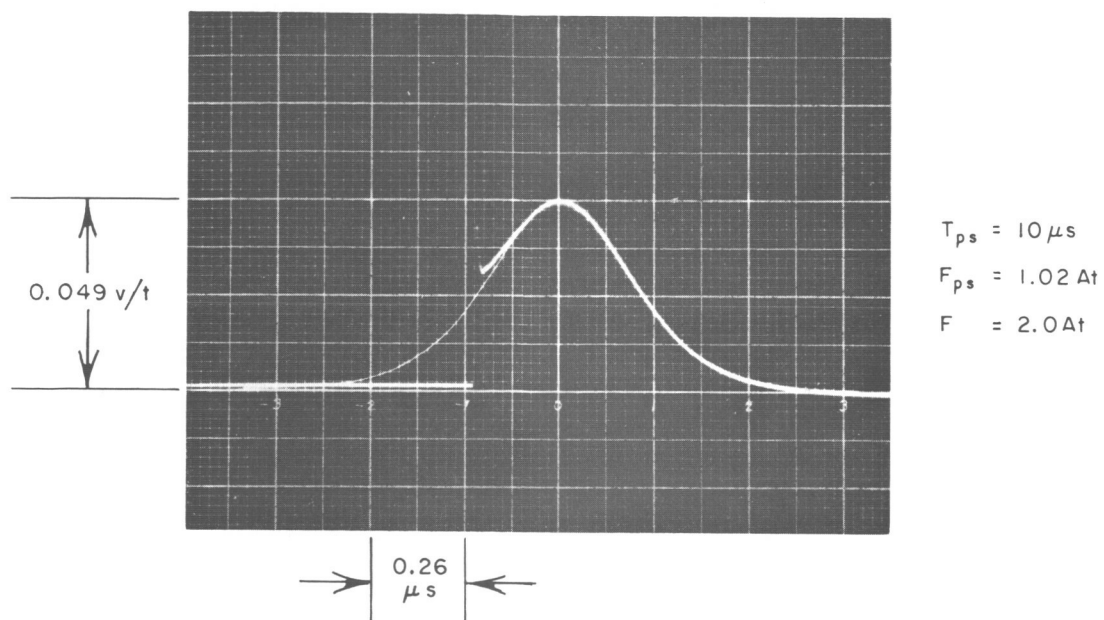
If this modified model describes $t_p^{-1}(F)$ of Fig. 19 properly, then ϕ_c should be a function of T_{ps} , because T_{ps} does not appear in Eq. (77). More investigation needs to be done before it can be determined whether the ϕ_c modification is valid for the modeling of switching from a partially set state, or whether some other modification will be necessary.

c. Waveforms of $\dot{\phi}(t)$

The shape of the $\dot{\phi}(t)$ waveform has been compared to a sech^2 function of time in order to determine whether the basic part of the parabolic model, the parabolic function $\eta(\phi)$, is valid for positive switching from a partially set state. Comparisons made in Report 3 (p. 96) and in Ref. 19 (p. 17) for $T_b \gg 1 \mu s$ indicated that the parabolic $\eta(\phi)$ was still valid for positive F [i.e., $\dot{\phi}(t)$ has the shape of a sech^2 function of time for a step- F drive]. This was now repeated for $T_b = 0$. It was found that the $\dot{\phi}(t)$ is still sech^2 in shape. Two comparisons are shown in Fig. 20, one for $F = 2 \text{ At}$ and $T_{ps} = 10 \mu s$ and the other for $F = 3 \text{ At}$ and $T_{ps} = 0.5 \mu s$. Since the shapes of the $\dot{\phi}(t)$ waveforms are in good agreement with a sech^2 function of time, it might be possible to modify the parabolic model so that it can describe switching from a partially set state.

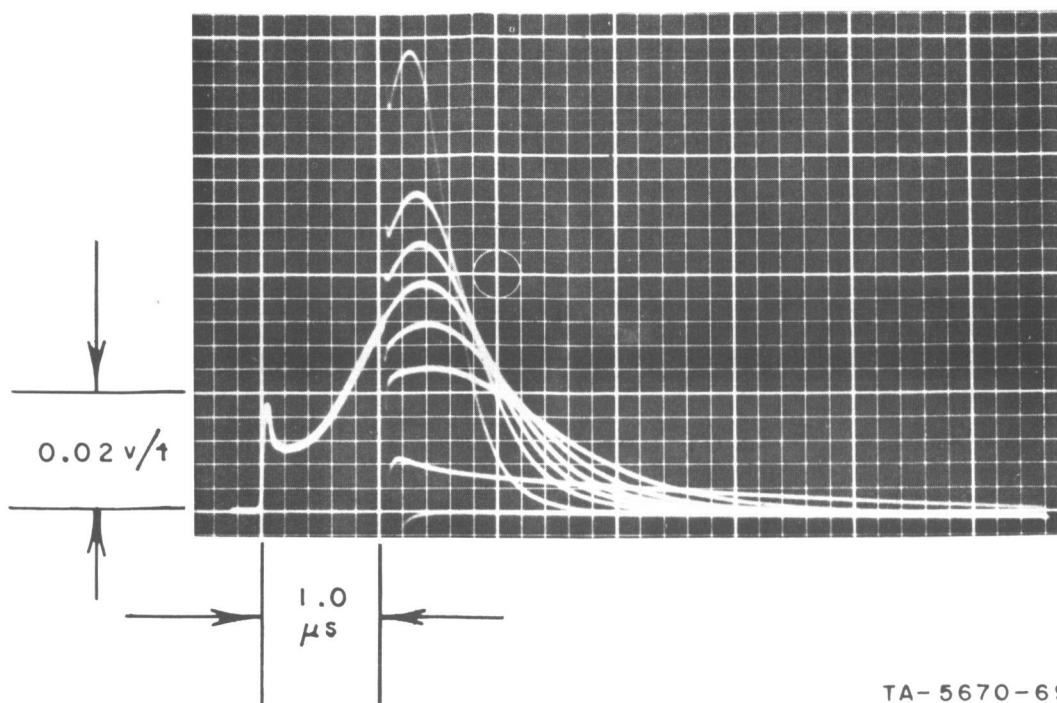
A general idea of the kind of waveforms obtained for switching from a partially set state can be obtained from the family of curves in Fig. 21. The left part of this oscillogram shows $\dot{\phi}(t)$ during the PARTIAL-SET pulse. The remaining curves show $\dot{\phi}(t)$ during the TEST pulse for various F values of the TEST pulse. The area of the left part of $\dot{\phi}(t)$ corresponds to $\Delta\phi_{ps}$ which is constant ($\Delta\phi_{ps} = 0.54 \phi_r$) for this oscillogram. Note that for low F values the peak becomes obscured. It is for this reason that the curves in Figs. 17 and 19 are truncated at the low- F end.

A comparison of two $\dot{\phi}(t)$ curves for different T_{ps} values is shown in Fig. 22 for fixed values of F and ϕ_{ps} . The results are very similar to Fig. 34(a), p. 100 in Report 3 and Fig. 6, p. 16, in Ref. 19, both taken with $T_b \gg 1 \mu s$. The switching for $T_{ps} = 0.5 \mu s$ is nearly undisturbed by the TEST pulse because F is nearly equal to F_{ps} . Note that $\dot{\phi}(t)$ for $T_{ps} = 10 \mu s$ is very low during the PARTIAL-SET pulse because F_{ps} is so low (only the last part of this switching is included



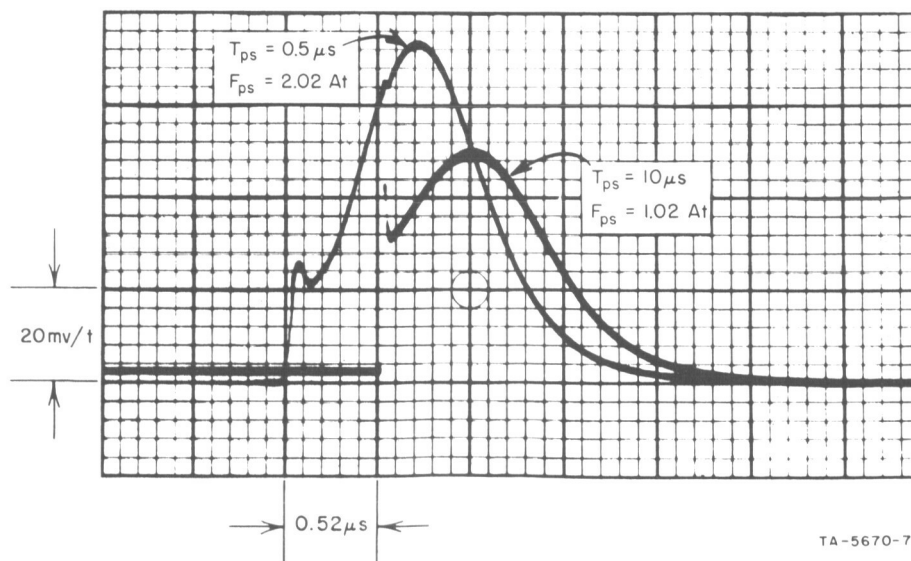
TA-5670-70

FIG. 20 COMPARISON OF $\dot{\phi}(t)$ WITH A sech^2 FUNCTION OF TIME
 ($\phi_{ps} = -0.46 \phi_r$; Core E-6)



TA-5670-69

FIG. 21 FAMILY OF $\dot{\phi}(t)$ WAVEFORMS WITH F AS A PARAMETER
 $(\phi_{ps} = -0.46 \phi_r; T_{ps} = 1.0 \mu\text{s}; F_{ps} = 2.02 \text{ At}; \text{Core E-6}; \text{in order of decreasing } \phi_p, F = 2.22, 1.84, 1.70, 1.59, 1.47, 1.33, 0.95, \text{ and } 0.35 \text{ At})$

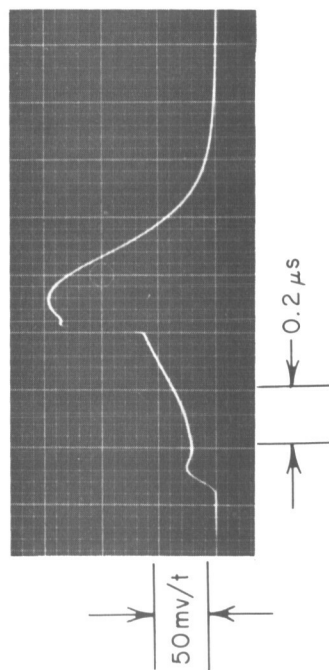
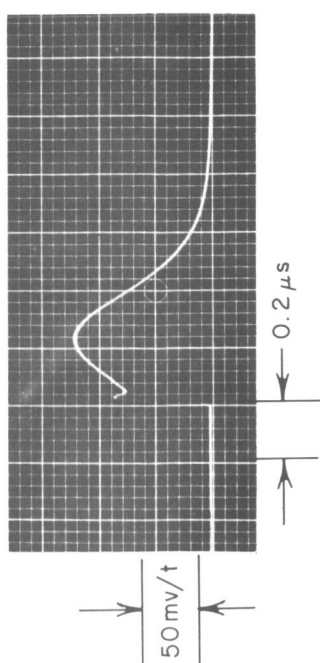


TA-5670-79

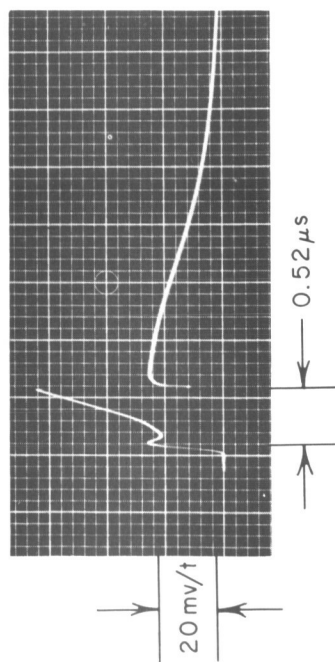
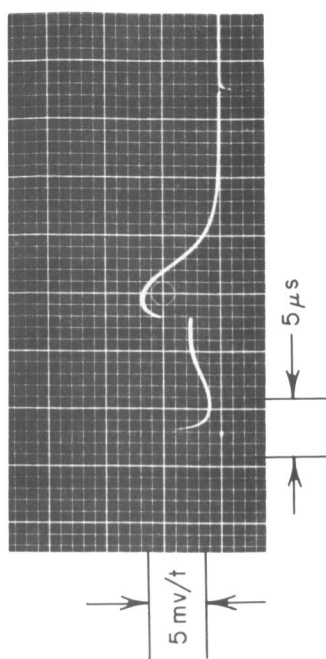
FIG. 22 COMPARISON OF $\dot{\phi}(t)$ WAVEFORMS FOR TWO T_{ps} VALUES
 $(F = 2.00 \text{ At}; \phi_{ps} = -0.46 \phi_r; \text{Core E-6})$

in the figure). The important result of this figure is that even though F and ϕ_{ps} are constant, $\dot{\phi}_p$ and t_p change significantly as T_{ps} varies. Similar comparisons for higher and lower F values are given in Fig. 23. The curves are not superimposed in this figure but are shown side-by-side for easy comparison. Note that for $F = 1.2$ At and $T_{ps} = 0.5 \mu s$ no $\dot{\phi}_p$ is obtained during either the PARTIAL-SET or the TEST pulses, whereas for $F = 1.2$ At and $T_{ps} = 10 \mu s$ a peak in $\dot{\phi}$ is obtained during both pulses. A peak is obtained during the PARTIAL-SET pulse for $T_{ps} = 10 \mu s$ even though $\phi_{ps} < 0$ because F_{ps} is low enough to result in a ϕ_d considerably less than ϕ_s . This corresponds to a parabolic $\dot{\phi}(\phi)$ with a peak at $\phi < 0$. Notice that t_p is much smaller for $T_{ps} = 0.5 \mu s$ than for $10 \mu s$ for both $F = 3.0$ At and $F = 1.2$ At [For $F = 1.2$ At and $T_{ps} = 0.5 \mu s$, $\dot{\phi}_p$ does not appear to exist; however, t_p must certainly be less than the $1.8 \mu s$ value observed at $T_{ps} = 10 \mu s$.] This is consistent with the curves of Fig. 19, where the $T_{ps} = 0.5 \mu s$ curve is well above the $10 \mu s$ curve.

All of the data discussed so far have been for $\phi_{ps} = -0.46 \phi_r$. One exception to this will now be given. It was observed during the course of the experiments that if T_{ps} is increased to allow complete switching to occur during the PARTIAL-SET pulse, additional switching can still be obtained during the TEST pulse if $F > F_{ps}$. This is shown in Fig. 24, where $F_{ps} = 2.0$ At and $F = 3.9$ At. This additional switching during the TEST pulse is not surprising if it is recalled that ϕ_d is an increasing function of F even if F is well above the F threshold (see Fig. 12, p. 37 of Report 3). The interesting factor in this oscillogram is the shape of the $\dot{\phi}(t)$ during the TEST pulse. It is very similar to the initial spike and decaying tail obtained for switching from $\phi = -\phi_r$ for F below the threshold [see Fig. 10(b), p. 27, Report 4]. In the situation of Fig. 24 no domain-wall collisions are likely to occur during the TEST pulse because most of the ferrite grains are already switched. Thus we can expect to have a certain number of domain walls moving at first, and then, as some of these terminate because of energy hills with steep slopes or because of completion of local switching, the number of moving walls gradually decreases. This accounts for the decreasing $\dot{\phi}$ in a manner very similar to the explanation given on pp. 11 and 12 of Report 3 for switching from $-\phi_r$. Thus, that physical explanation is substantiated.



$F = 3.0 \text{ At}$



$F = 1.2 \text{ At}$

$T_{ps} = 10 \mu\text{s}$
 $F_{ps} = 1.02 \text{ At}$

$T_{ps} = 0.5 \mu\text{s}$
 $F_{ps} = 2.02 \text{ At}$

TA-5670-71

FIG. 23 WAVEFORMS OF $\dot{\phi}(t)$ FOR TWO F VALUES AND TWO T_{ps} VALUES
 $(\dot{\phi}_{ps} = -0.46 \phi_r; \text{Core E-6})$

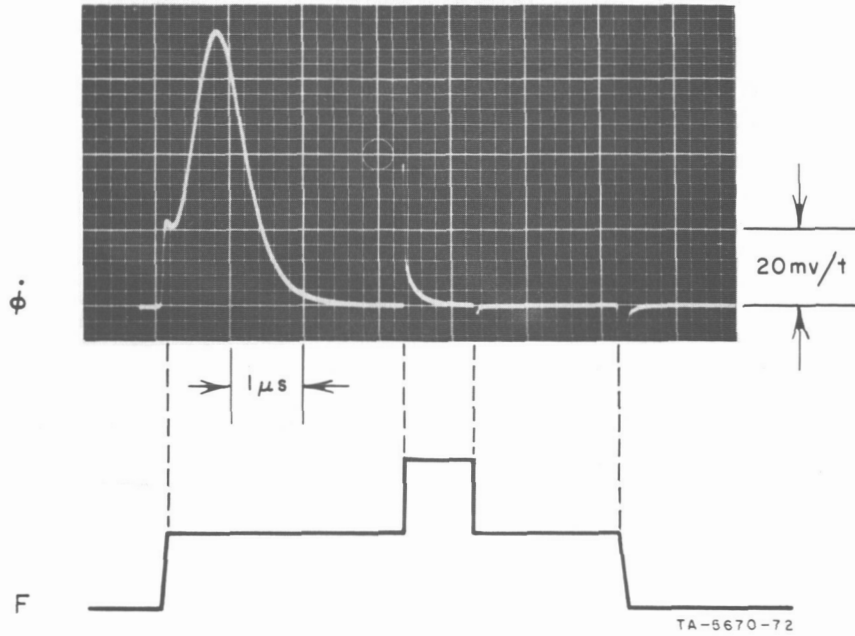


FIG. 24 WAVEFORM OF $\dot{\phi}(t)$ FOR $\phi_{ps} \approx + \phi_r$
 $(F_{ps} = 2.0 \text{ At}; F = 3.9 \text{ At}; \text{Core E-6})$

4. Conclusions

The major conclusion to be drawn from these partial-setting experiments is that the physical mechanisms which are responsible for the observed effects of partial setting do not originate from any relaxation effects following the PARTIAL-SET pulse. The values of F_0'' , λ , and ν for $T_b = 0$ are nearly the same as for $T_b \gg 1 \mu s$, if $T_{ps} \gtrsim 1 \mu s$. Below $T_{ps} = 1 \mu s$, the effect of varying T_b becomes significant. The peaking time t_p is very sensitive to the changes in T_{ps} . This variation in t_p cannot be accounted for in the present form of the parabolic model. More investigation needs to be done before the switching from partially set states can be described by switching models. However, considerable data are given which should be useful for future work in developing appropriate models for switching from partially set states and for explaining the physical mechanisms that are responsible for the effects of partial setting.

II COMPUTER-AIDED ANALYSIS OF A CORE-DIODE-TRANSISTOR BINARY COUNTER

A. Introduction

The operation of a core-diode-transistor binary counter, to be employed in a future Jet Propulsion Laboratory spacecraft, was described in Report 4 (pp. 49-56). The first of four modes of operation was analyzed numerically (Report 4, pp. 56-61), and the computation was performed on a digital computer (Report 4, pp. 61-68; 153-166). The results were then compared with experimental waveforms of the currents and voltages involved in the circuit (Report 4, pp. 65-66).

As pointed out in Report 4, the flux switching in Modes II, III, and IV is slower than the flux switching in Mode I by about a factor of four. To a very rough approximation, Modes II-IV may then be analyzed manually by assuming that the net MMF of each core follows its static $\phi(F)$ curve (see Report 4, p. 56). However, the error involved in such an approximation is considerably larger than the error involved in a computer analysis that takes into account the nonlinearities of the circuit elements. The success or failure of the binary counter's performance is determined by its transient behavior, *i.e.*, by the waveforms of the time variable. Determination of such waveforms requires the accuracy of a computer analysis.

In order to ensure that there will be no circuit failure within the specified temperature range (-10°C to $+85^{\circ}\text{C}$) and supply-voltage range ($28 \pm 5.6\text{V}$), worst-case analysis of the circuit is required. This requirement stems from the fact that although it is impractical to intentionally build a circuit using components with worst parameter values, the probability that this will actually happen is nonzero. Thus, the objectives in this section are twofold:

- (1) To extend the computer analysis of Mode I to all four modes of operation
- (2) To perform a worst-case analysis of the binary counter for design verification.

The circuit operation was described in Report 4. However, for the convenience of the reader and since the description in Report 4 is incomplete, we shall describe this operation by referring to the first three stages of the binary counter, before extending the computer analysis to all the modes of operation.

B. Binary-Counter Operation

1. Circuit

The circuit diagram of the first three stages of a core-diode-transistor binary counter is shown in Fig. 25. (This circuit diagram and the boundaries between adjacent stages are slightly different from the ones given in Report 4, Fig. 17.) Each stage is composed of Resistances R_1 and R_2 (R_3 and R_4 are inherent winding resistances), Inductor L , Diodes d_1 and d_2 , an *npn* Transistor T , and Cores 1 and 2. A subscript in parentheses attached to each component designates the corresponding stage number. The unpaired Core D , Diode $d_{1(0)}$, Transistor $T_{(0)}$, Resistance $R_{1(0)}$, and Inductor $L_{(0)}$ are part of a monostable COUNT-input driver (most of which is not shown in Fig. 25), which feeds the input signal to the first stage of the binary counter.

The supply voltage, V_s , is applied in parallel to all stages and to the monostable input circuit. Referring to Stage (2) as a typical stage, the MMF drives applied to Core 1 are $N_{s1}i_s$, $N_{B1}i_d$, $N_{c1}i_c$, and $-N_{CL}i_{CL}$, and the MMF drives applied to Core 2 are $N_{s2}i_s$, $-N_{B2}i_d$, and $-N_{c2}i_c$. Currents i_L and i_s rise rapidly to peak values and then decay nearly exponentially; Currents i_c and i_{CL} rise nearly exponentially from zero.

2. Modes of Operation

The circuit behavior may be examined by dividing the operation of each counter stage during a complete cycle into four modes, Modes I-IV. In every stage, except Stage (1), Modes II and IV occur twice in a row. The drive currents and the inelastic flux changes during the four modes of normal operation of each stage are shown in Fig. 26, and are summarized briefly as follows by referring to Stage (2). (A more detailed description is given in Sec. II-B-3, pp. 71-73.)

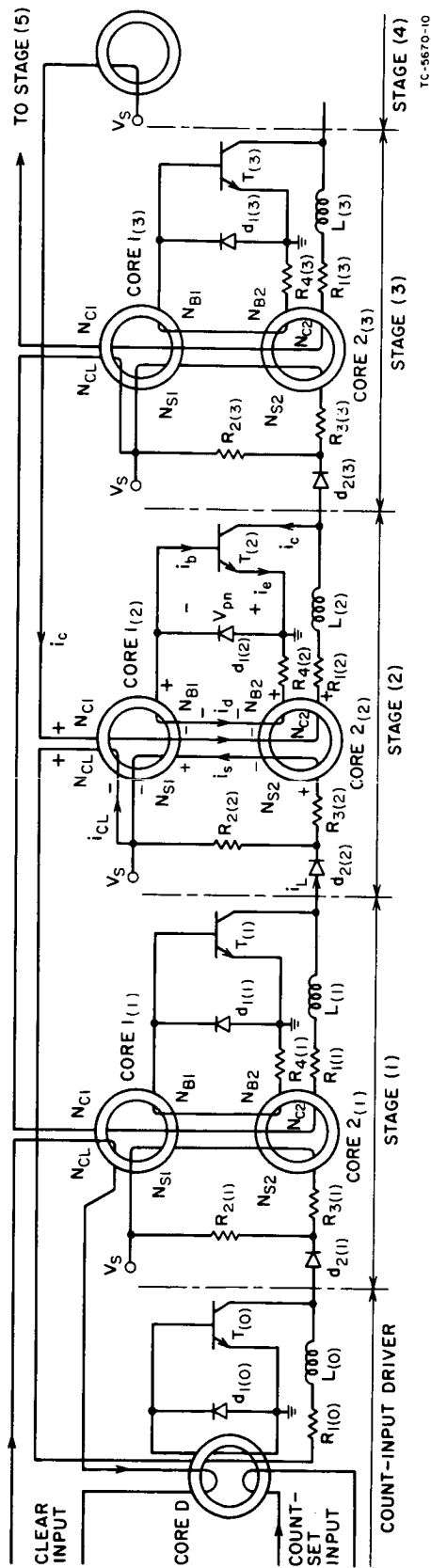


FIG. 25 FIRST THREE STAGES OF A CORE-DIODE-TRANSISTOR BINARY COUNTER

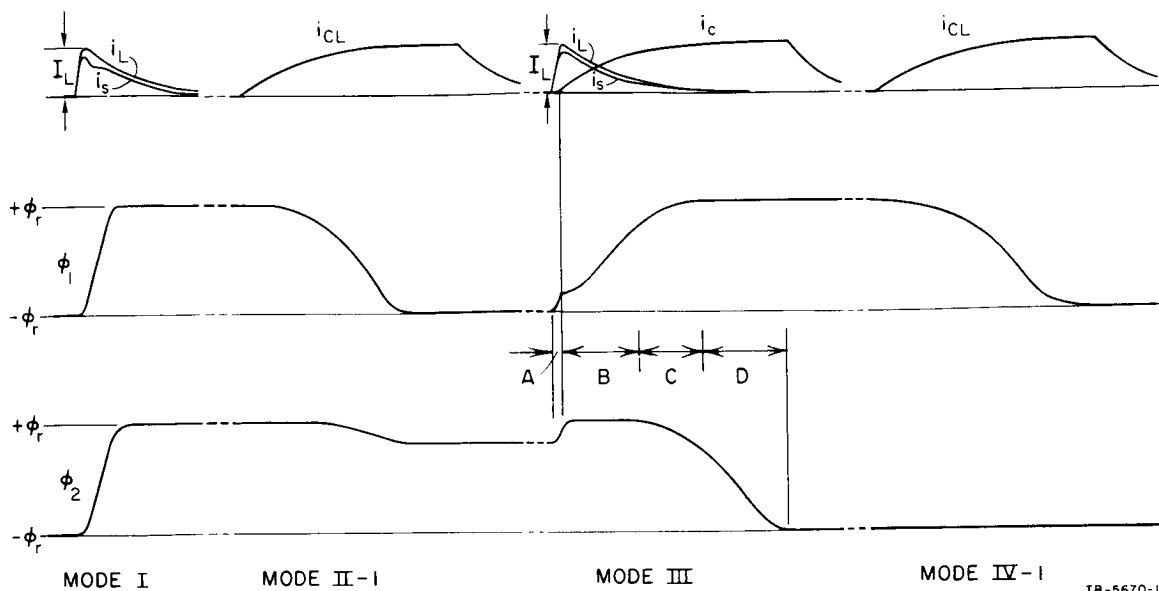


FIG. 26 DRIVE CURRENTS AND FLUX CHANGES IN CORES 1 AND 2 DURING FOUR MODES OF NORMAL OPERATION

Mode I—As Transistor $T_{(1)}$ turns off, Current i_L builds up to a peak value I_L , from which it decays essentially exponentially. The portion i_s of i_L sets Cores 1 and 2 simultaneously.

Mode II-1—The exponentially rising and falling current i_{CL} clears Core 1. The induced current i_d may unset Core 2 by a small amount of $\Delta\phi$.

Mode II-2 (not shown in Fig. 26)—Same as Mode II-1. If clearing of Core 1 during Mode II-1 is complete, Mode II-2 has no effect.

Mode III—Four submodes are distinguished:

A—Cores 1 and 2 are both switched positively by i_s (as in Mode I), while Transistor $T_{(2)}$ is cut off, until ϕ_2 approaches saturation, and the base current, induced by $N_{B1}\dot{\phi}_1 - N_{B2}\dot{\phi}_2$, switches the transistor via the active region into saturation.

B—The base current due to $N_{B1}\dot{\phi}_1 - N_{B2}\dot{\phi}_2$ maintains Transistor $T_{(2)}$ in saturation, and Core 1 is set by the drives due to both i_s and i_c while Core 2 remains in saturation.

C—As ϕ_1 approaches positive saturation, ϕ_2 departs from positive saturation and there is a drop in $N_{B1}\dot{\phi}_1 - N_{B2}\dot{\phi}_2$. For low V_s within the range of operation, the base current may become negative ($i_d > 0$); as a result, Transistor $T_{(2)}$ may

shift from the saturation region (emitter and collector forward-biased) to the active region (emitter forward-biased; collector reverse-biased).

D—The excess of $N_{c2}i_c$ over $N_{s2}i_s$ is large enough to clear Core 2. The induced positive base current keeps Transistor $T_{(2)}$ in the saturation region. As ϕ_2 approaches negative saturation, Transistor $T_{(2)}$ switches from saturation to the active region and from there to the cutoff region. [While Transistor $T_{(2)}$ is being cut off, i_L corresponding to the following stage rises to its peak value and begins to set Cores $1_{(3)}$ and $2_{(3)}$.]

Mode IV-1—The exponentially rising and falling i_{CL} clears Core 1. Core 2 remains in negative saturation.

Mode IV-2 (Not shown in Fig. 26)—Same as Mode IV-1. If clearing of Core 1 during Mode IV-1 is complete, Mode IV-2 has no effect.

3. COUNT-State Propagation

The propagation of the counter states as COUNT inputs are fed in is described next by referring to Fig. 25 and to Table I and disregarding Submodes III-A and III-C. Initially, all cores are in a CLEAR state ($\phi = -\phi_r$).

The first COUNT input sets Core D, and Transistor $T_{(0)}$ is turned on; Current i_{CL} builds up and helps the input current to set Core D (blocking-oscillator action). Upon termination of Core-D switching, Transistor $T_{(0)}$ turns off, Diode $d_{2(1)}$ becomes unblocked, and the energy stored in Inductor $L_{(0)}$ is dissipated in switching Cores $1_{(1)}$ and $2_{(1)}$ to the SET states [Mode I₍₁₎], and in Resistances $R_{1(0)}$ and $R_{2(1)}$. A CLEAR pulse from the driver circuit clears Core D and Core $1_{(1)}$ [Mode II₍₁₎].

A second COUNT results in Mode III₍₁₎ switching. Since Core $2_{(1)}$ is already in a SET state, following the turning off of Transistor $T_{(0)}$, only Core $1_{(1)}$ is set. As a result, Transistor $T_{(1)}$ is turned on and is held on by the induced voltage $N_{B1}\dot{\phi}_{1(1)}$, while the collector current builds up exponentially. Upon termination of Core $1_{(1)}$ switching, the net MMF of Core $2_{(1)}$ is of sufficient magnitude to clear Core $2_{(1)}$, and Transistor $T_{(1)}$ is further kept on by $N_{B2}\dot{\phi}_{2(1)}$. Upon termination of Core $2_{(1)}$ switching, Transistor $T_{(1)}$ turns off, Diode $d_{2(2)}$ becomes unblocked, and Cores $1_{(2)}$ and $2_{(2)}$ are set [Mode I₍₂₎]. Cores D and $1_{(1)}$ are then cleared by the driver [Mode IV₍₁₎].

Table I

PROPAGATION OF STATES IN A CORE-DIODE-TRANSISTOR BINARY COUNTER.

[A change in flux state of a core is designated by S (for SET) or C (for CLEAR)]

COUNT	CORE D	TRANSISTOR $T_{(0)}$	STAGE (1)				STAGE (2)				STAGE (3)			
			MODE	CORE 1 ₍₁₎	CORE 2 ₍₁₎	TRANSISTOR $T_{(1)}$	MODE	CORE 1 ₍₂₎	CORE 2 ₍₂₎	TRANSISTOR $T_{(2)}$	MODE	CORE 1 ₍₃₎	CORE 2 ₍₃₎	TRANSISTOR $T_{(3)}$
Initial	C			C	C			C	C			C	C	
1	S	on	I	S	S									
	C		II	C										
2	S	on	III {	S	C	on	I	S	S					
	C		IV	C			II-1	C						
3	S	on	I	S	S									
	C		II	C										
4	S	on	III {	S	C	on	II-2	C						
	C		IV	C			III {	S	C	on	I	S	S	
5	S	on	I	S	S		IV-1	C						
	C		II	C										
6	S	on	III {	S	C	on	IV-2	C			II-1	C		
	C		IV	C			I	S	S					
7	S	on	I	S	S		II-1	C						
	C		II	C										
8	S	on	III {	S	C	on	II-2	C			II-2	C		
	C		IV	C			III {	S	C	on	III {	S	C	on

A *third* COUNT input results in the same switching as the first COUNT, except that in addition, while Core D is being set, Core $1_{(2)}$ is being cleared by the exponentially rising current i_{CL} [Mode II-1 $_{(2)}$].

A *fourth* COUNT results in a similar switching following the second COUNT. The exponentially rising Current i_{CL} constitutes a CLEAR MMF on Core $1_{(2)}$. Hence, in addition to Mode II following the third COUNT, Stage (2) experiences a second Mode II following the fourth COUNT. These modes are designated by II-1 and II-2, respectively (see Sec. I-B-2, p. 70). If the flux switching is completed during Mode II-1, then Mode II-2 has no effect. However, if $\Delta\phi_1$ during Mode II-1 is time-limited (i_{CL} does not last long enough to complete the flux switching), then Core 1 is cleared further during Mode II-2. When Transistor $T_{(0)}$ is cut off, Transistor $T_{(1)}$ is turned on, and Stage (1) experiences Mode III of operation. Then, when Transistor $T_{(1)}$ is cut off, Transistor $T_{(2)}$ is turned on, and Stage (2) experiences Mode III of operation. Finally, when Transistor $T_{(2)}$ is cut off, Diode $d_{2(3)}$ becomes unblocked, and Stage (3) experiences Mode I of operation [Cores $1_{(3)}$ and $2_{(3)}$ are set].

A *fifth* COUNT causes a flux switching similar to that caused by the third COUNT, except that Stage (2) experiences Mode IV-1 instead of Mode II-1 of operation.

The flux switching following the *sixth* COUNT is similar to the one following the fourth COUNT, except that Stage (2) experiences Modes IV-2 and I instead of Modes II-2 and III, and Stage (3) experiences Mode II-1 while Transistor $T_{(1)}$ is on instead of Mode I after Transistor $T_{(1)}$ turns off.

The changes in the flux states following the *seventh* and *eighth* COUNTs are similar in nature to the ones described above, and are shown in Table I.

Note in Table I that every COUNT is represented by the final flux states of Cores 2.

It can be seen from Fig. 25 and Table I that every stage except Stage (1) experiences two Modes II and two Modes IV of operation. The duration of each of these modes is determined by the on-time of the transistor of the stage before the previous one. It is desired to have the same on-time for all stages.

4. Range of Supply Voltage

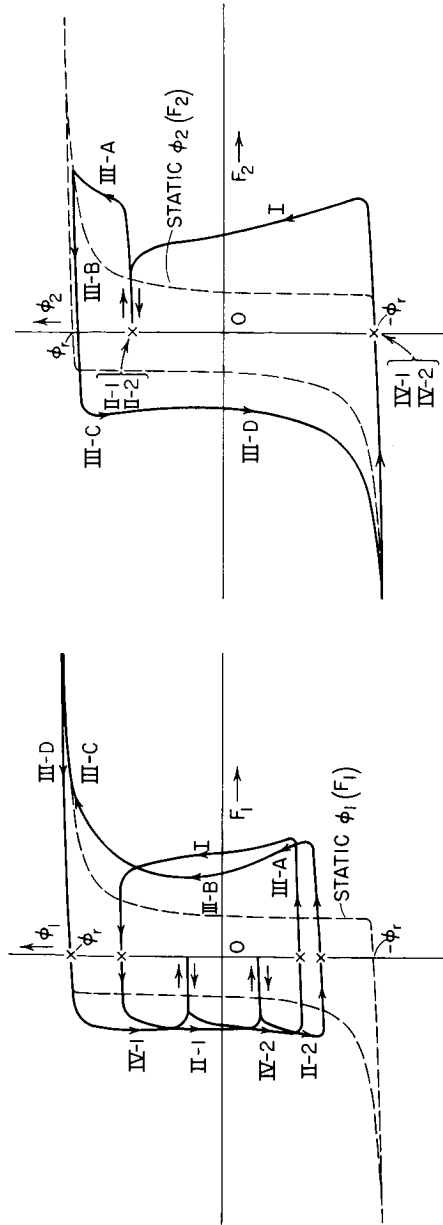
a. Minimum V_s

Operation fails when the supply voltage drops below a certain minimum value, $V_{s, \min}$. Such a failure occurs when the transistor turns off during Submode III-C, as a result of which Core 2 cannot be cleared. The net effect is that the normal cyclic operation (which is composed of Modes I-IV) collapses into a spurious cyclic operation (which is composed of Mode II and Submode III-B) in which only Core 1 is switched while Core 2 remains in positive saturation. This effect is shown in Fig. 27 by sketching the variations of $\phi_1(F_1)$ and $\phi_2(F_2)$ superimposed on the static $\phi(F)$ loops for V_s slightly above $V_{s, \min}$ and for V_s slightly below $V_{s, \min}$. Note that, since V_s is low, the clearing of Core 1 in Fig. 27(a) during Modes II-1 and IV-1 is incomplete and consequently a substantial clearing is continued during Modes II-2 and IV-2.

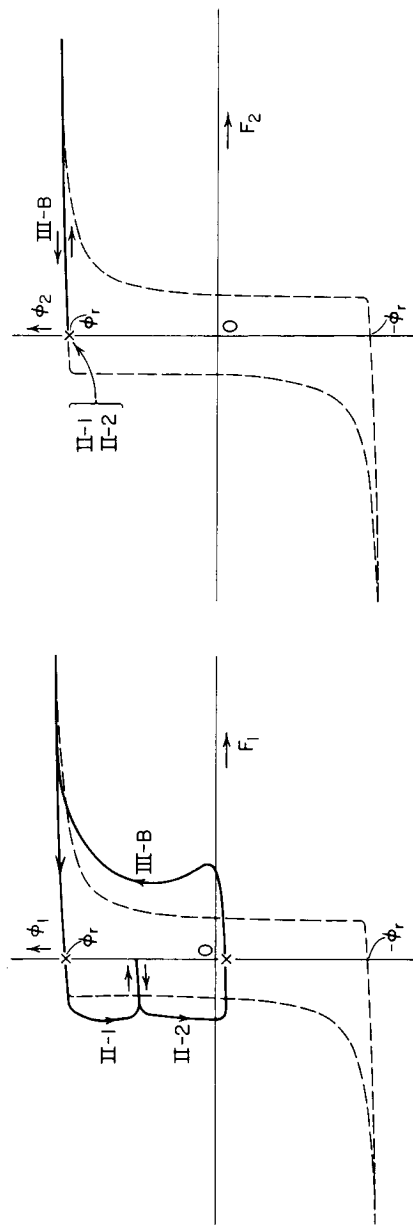
The causes of the spurious transistor turn-off in Mode III-C are summarized in a flow chart in Fig. 28, using the terms "low" and "high" relative to the values of the corresponding quantities before V_s is lowered. A low V_s results in a low V_s/R_1 , which is approximately equal to I_L , I_{CL} , and I_c , the peak values of i_L , i_{CL} , and i_c , respectively. The effects of low I_L , I_{CL} , and I_c are explained as follows.

A low I_L results in a low i_L , which in turn results in a low i_s , and hence in a low F_2 during Mode I. The excess charge-turns $\int_0^{T_I} (F_{2I} - F_0) dt$ is thus small, and hence $\Delta\phi_{2I}$ (the flux change of Core 2 during Mode I) is small (see Report 2, p. 18). Consequently, the initial ϕ_2 in Mode III is low, and $\Delta\phi_2$ during Submode III-A (while both Core 1 and Core 2 are switching simultaneously, as in Mode I, keeping the transistor off) is large.

A low I_{CL} results in a low i_{CL} and, hence, in a low $|F_1|$ during the composite Mode II (Modes II-1 and II-2). Consequently, the excess of charge-turns $\int_0^{T_{II}} (|F_{1II}| - F_0) dt$ is small and the total $\Delta\phi_1$ clearing during the composite Mode II is small. As a result, the initial ϕ_1 in Mode III is high. This factor together with a larger $\Delta\phi_{2III-A}$ yield a small $\Delta\phi_1$ during Submode III-B. Since ϕ_{1III-B} is essentially fixed by Diode d_1 , a small $\Delta\phi_{1III-B}$ results in a short duration of Submode III-B, and i_c is not given enough time to build up. This factor, together with a low I_c , yields a low i_c during Submode III-C. Furthermore, a short T_{III-B} does not give i_s a



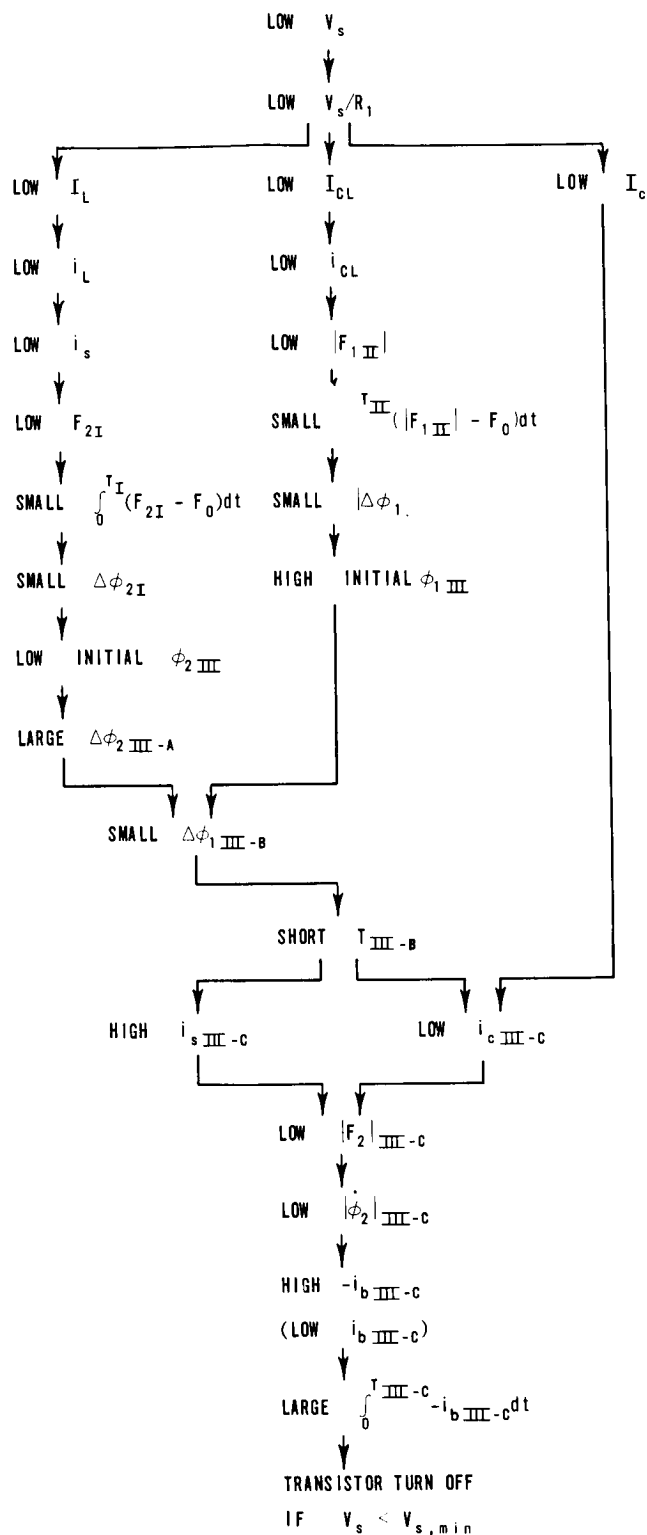
(a) PROPER FOUR-MODE CYCLIC OPERATION ($V_s > V_{s,min}$)



(b) SPURIOUS TWO-MODE CYCLIC OPERATION ($V_s < V_{s,min}$)

FIG. 27 VARIATION OF $\phi_1(F_1)$ AND $\phi_2(F_2)$ FOR V_s SLIGHTLY ABOVE $V_{s,min}$ (Proper Operation) AND FOR V_s SLIGHTLY BELOW $V_{s,min}$ (Operation Failure). Dashed lines are static $\phi(F)$ curves.

TD-5670-48



TB-5670-12

FIG. 28 FLOW CHART EXPLAINING THE CAUSES OF SPURIOUS TRANSISTOR TURN-OFF IN MODE III-C AS V_s IS LOWERED BELOW $V_{s,min}$

chance to decay to a low value. Both a low $i_{c\text{III-C}}$ and a high $i_{s\text{III-C}}$ yield a low $|F_2|_{\text{III-C}}$, and consequently $|\dot{\phi}_2|$ during Submode III-C is low. With low $\dot{\phi}_1$ and low $|\dot{\phi}_2|$ ($\dot{\phi}_1 > 0$ and $\dot{\phi}_2 < 0$), the positive $N_{B1}\dot{\phi}_1 - N_{B2}\dot{\phi}_2$ becomes smaller than the voltage across the base-emitter storage charge, and the base current becomes negative. Consequently, the base-collector storage charge is decreased: While this charge is positive, the transistor stays saturated, but when the charge becomes negative, the transistor enters the active region. For V_s slightly above $V_{s,\min}$, the transistor remains in the active region for only a short time before $|\dot{\phi}_2|$ increases and i_b becomes positive again and resaturates the transistor. However, if $V_s < V_{s,\min}$, the collector-base voltage continues to grow, and $|\dot{\phi}_2|$ drops as i_c drops to zero, and the transistor turns off.

It is evident from the discussion above that as V_s is lowered below $V_{s,\min}$, several factors may cause an operation failure in a rather intricate way. Referring to Fig. 28, the failure may result primarily because $N_{CL}I_{CL}$ is too low to clear Core 1 by a sufficient amount during the composite Mode II. In this case, the sum

$$|\Delta\phi_{1\text{II}}| = |\Delta\phi_{1\text{II-1}}| + |\Delta\phi_{1\text{II-2}}|$$

could be considerably smaller than shown in Fig. 27(b); in the extreme case, as $|\Delta\phi_{1\text{II}}| \rightarrow 0$, $T_{\text{III-B}} \rightarrow 0$, the transistor never turns on, and no flux switching takes place.

A contribution to a failure may also stem from using a fast-switching transistor whose diffusion and junction capacitances are too small. In this case, $|\Delta\phi_{1\text{II}}|$ may be essentially complete, but the base charge during Submode III-C is too small to prevent the transistor turning off as the base current becomes negative (for a limited time). It appears from this argument that a slow-switching transistor (which costs less than a fast-switching transistor) is preferred. On the other hand, if the transistor switches too slowly, the long turn-off time at the end of Submode III-D causes I_L to be low, and following the explanation for operation failure given previously (see Fig. 28), $V_{s,\min}$ increases. We conclude, therefore, that for a given circuit there is an optimum transistor switching speed.

b. Maximum V_s

As shown in Fig. 26, under normal operation conditions, Core 2 is unset slightly during Mode II-1, while Core 1 is switched by the CLEAR drive $N_{CL}i_{CL}$ (see Fig. 25). Such flux unsetting occurs while $N_{B2}i_d$ exceeds the threshold of Core 2. The higher V_s is, the higher are i_{CL} and i_d , and hence the larger is the $|\Delta\phi_{2II-1}|$ unsetting. Since clearing of Core 1 during Mode II-1 is complete, $\Delta\phi_1 = 0$ during Mode II-2 and there is no $\Delta\phi_2$ unsetting during Mode II-2.

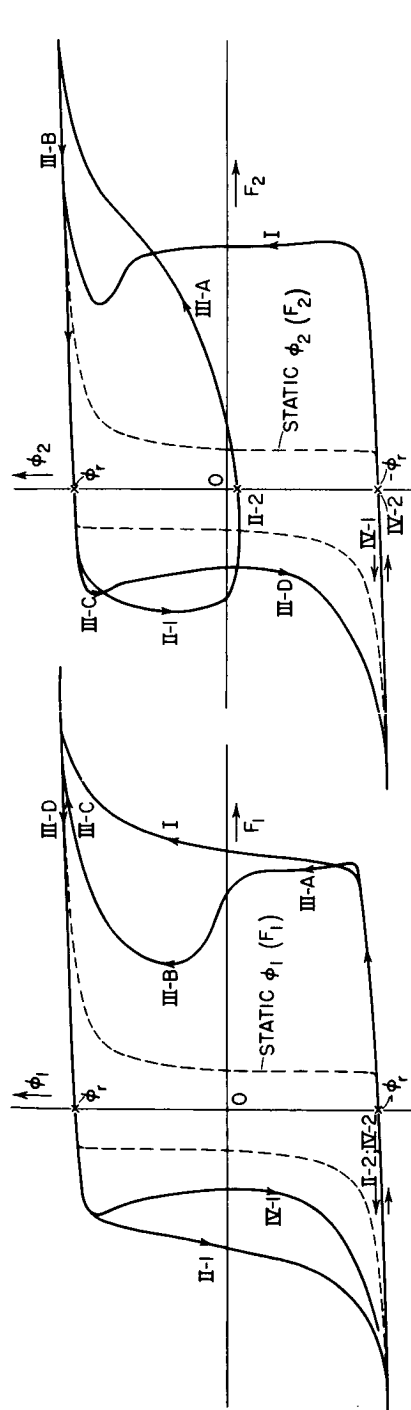
If V_s is raised above a critical value $V_{s,max}$, operation failure will occur due to excessive $|\Delta\phi_{2II-1}|$ unsetting. In Fig. 29(a), the $|\Delta\phi_{2II-1}|$ unsetting is appreciable, but a proper four-mode cyclic operation is still maintained. However, a slight increase in V_s to above $V_{s,max}$ causes the transistor to turn off during Submode III-C. As a result, the four-mode operation collapses into a two-mode operation: Mode II followed by Submodes III-A and III-B.

The causes of the operation failure as V_s is raised above $V_{s,max}$ are shown in a flow chart in Fig. 30. As with the case of $V_s < V_{s,min}$ (Fig. 28), a low initial ϕ_{2III} is a factor in turning the transistor off spuriously. However, the initial ϕ_{2III} is too low for $V_s > V_{s,max}$ because of an excessive $\Delta\phi_2$ unsetting in Mode II, whereas for $V_s < V_{s,min}$ the initial ϕ_{2III} is too low because of insufficient $\Delta\phi_2$ setting in Mode I.

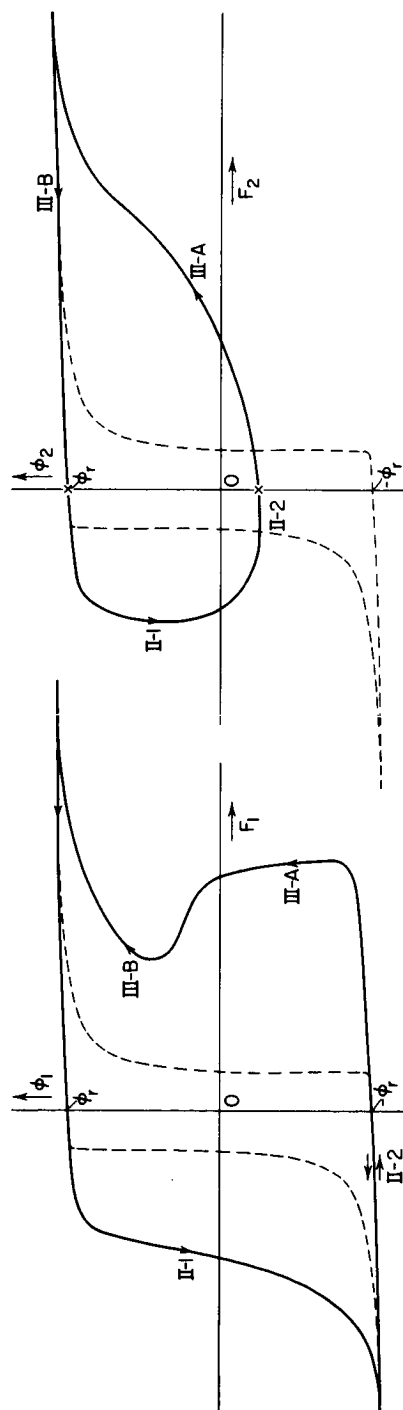
The effect of the magnitude of i_s on the transistor turn-off is also different in the two extreme values for V_s : If $V_s < V_{s,min}$, i_s is low and consequently $\Delta\phi_2$ -setting in Mode I is too low. On the other hand, if $V_s > V_{s,max}$, i_s is high and the resulting $|F_2|$ in Submode III-C is too low.

c. Conclusions

During Submode III-C of a proper four-mode operation, the function of keeping the transistor in the saturation region or the active region is transferred from Core 1 to Core 2, while both cores are near positive saturation. If $|\dot{\phi}_2|$ during Submode III-C is too small, Core 2 fails to prevent the transistor from turning off. As a result, Core 2 is not cleared during Mode III (Submode III-D does not exist), and the four-mode operation collapses into a spurious two-mode operation. Such a failure occurs because the setting current i_s and clearing current i_{CL} are either too small ($V_s < V_{s,min}$) or too large ($V_s > V_{s,max}$). The causes



(a) PROPER FOUR-MODE CYCLIC OPERATION ($V_s < V_{s,max}$)



(b) SPURIOUS TWO-MODE CYCLIC OPERATION ($V_s > V_{s,max}$)

FIG. 29 VARIATIONS OF $\phi_1(F_1)$ AND $\phi_2(F_2)$ FOR V_s SLIGHTLY BELOW $V_{s,max}$ (Proper Operation) AND FOR V_s SLIGHTLY ABOVE $V_{s,max}$ (Operation Failure). Dashed lines are static $\phi(F)$ curves.

10-5670-49

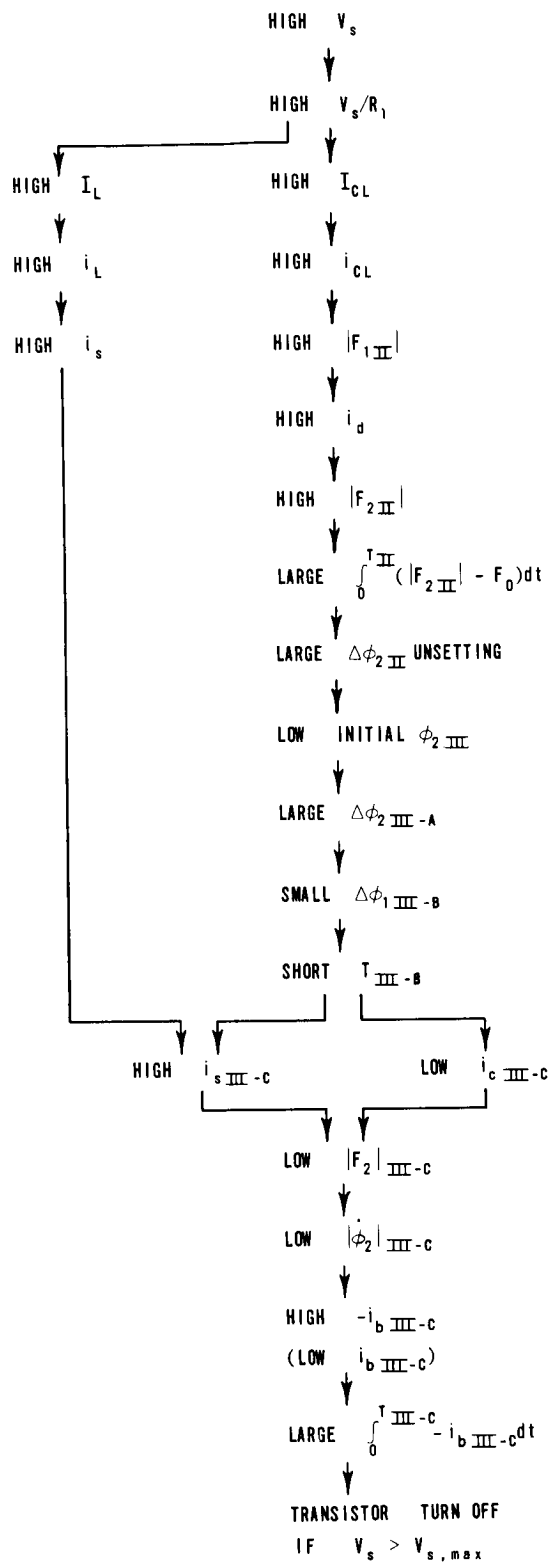


FIG. 30 FLOW CHART EXPLAINING THE CAUSES OF SPURIOUS TRANSISTOR TURN-OFF IN MODE III-C AS V_s IS RAISED ABOVE $V_{s,max}$

and effects of spurious transistor turn-off are shown in Figs. 28 and 27(b) for $V_s < V_{s, \min}$, and in Figs. 30 and 29(b) for $V_s > V_{s, \max}$.

In order to assure a proper binary-counter operation throughout the specified ranges of temperature and supply voltage, it is necessary to analyze this circuit under worst-case conditions of parameter values because of component nonuniformity. Such an analysis must be quantitative; i.e., the analysis should be able to compute $V_{s, \min}$ and $V_{s, \max}$ for given worst-case parameter values. It is evident from the above given qualitative explanations for the transistor turn-off that several factors affect this failure in a complex way. These factors can be accounted for quantitatively in computation of $V_{s, \min}$ and $V_{s, \max}$ by developing a computer-aided transient analysis. Such an analysis must be based on mathematical models for both the static and dynamic properties of every circuit component throughout the specified temperature range. Our next topics are these component models, the techniques of measuring their parameters, and the resulting parameter values *vs.* temperature.

C. Device Models

In Fig. 25, the cores, the inductors, the diodes, and the transistors are nonlinear devices. Mathematical models that describe the static and dynamic behavior of these devices are needed for the computer analysis of the binary counter. These models are described next.

1. Core Model

The total $\dot{\phi}$ of a core is

$$\dot{\phi} = \dot{\phi}_e + \dot{\phi}_{inel} \quad , \quad (78)$$

where $\dot{\phi}_e$ and $\dot{\phi}_{inel}$ are the elastic and inelastic components of $\dot{\phi}$, respectively. Since the rise of $F(t)$ is slow enough to neglect the viscous damping, following Eq. (43),

$$\dot{\phi}_e = \epsilon \dot{F} \quad , \quad (79)$$

where $\epsilon = d\phi_d/dF$. Extending Eq. (34) of Report 1 (p. 23) to positive as well as negative F , and ignoring the term due to air flux, we get

$$\tau = \frac{\phi_s - \phi_r}{(l_o - l_i)H_a} \left[|F| \left(\frac{1}{|F| + H_a l_o} - \frac{1}{|F| + H_a l_i} \right) + \ln \left(\frac{|F| + H_a l_o}{|F| + H_a l_i} \right) \right] \quad (79a)$$

Although $\dot{\phi}_{inel} = \dot{\phi}_i + \dot{\phi}_{ma}$, it was shown in Report 4 (p. 14) that to a good approximation,

$$\dot{\phi}_{inel} = \dot{\phi}_p(F) \left\{ 1 - \left[\frac{2\phi + \phi_s - \phi_d(F)}{\phi_s + \phi_d(F)} \right]^2 \right\} \quad (80)$$

Following Eq. (48), four-region analytical expressions for $\dot{\phi}_p(F)$ are based on the curve fitting of experimental $\dot{\phi}_p$ vs. step- F amplitude:

$$\dot{\phi}_p(F) = \begin{cases} 0 & \text{if } 0 \leq F \leq F_d^{\min} \\ \lambda_d (F - F_d^{\min})^{\nu_d} & \text{if } F_d^{\min} \leq F \leq F_{dB} \\ \lambda (F - F_0)^{\nu} & \text{if } F_{dB} \leq F \leq F_B \\ \rho_p (F - F_0) & \text{if } F_B \leq F \end{cases} \quad (81)$$

The three-region analytical expressions for $\phi_d(F)$ are based on Eqs. (12) - (18) in Report 2:

$$\phi_d(F) = \begin{cases} V_1 F \ln \left(\frac{F - H_a l_o}{F - H_a l_i} \right) - \phi_r & \text{if } F \leq F_d^{\min} \\ V_2 \left[\frac{F}{H_d^{\min}} - l_i + F \left(\frac{1}{H_n} - \frac{1}{H_q} \right) \ln \left(\frac{1 - \frac{H_n}{H_d^{\min}}}{1 - \frac{H_n l_i}{F}} \right) \right] - \phi_r & \text{if } F_d^{\min} \leq F \leq H_d^{\min} l_o \\ V_2 \left[l_o - l_i + F \left(\frac{1}{H_n} - \frac{1}{H_q} \right) \ln \left(\frac{F - H_n l_o}{F - H_n l_i} \right) \right] - \phi_r & \text{if } H_d^{\min} l_o \leq F \end{cases} \quad (82)$$

where

$$V_1 = \frac{\phi_s - \phi_r}{(l_o - l_i)H_a} \quad , \quad (82a)$$

$$V_2 = \frac{(\phi_s + \phi_r)H_q}{(l_o - l_i)H_n} \quad , \quad (82b)$$

$$F_d^{\min} = H_d^{\min} l_i \quad , \quad (82c)$$

$$H_d^{\min} = \frac{1}{4} \left[H_s - \sqrt{H_s^2 - 8 \left(1 + \frac{\phi_r}{\phi_s} \right) H_a H_q} \right] \quad , \quad (82d)$$

and

$$H_s = H_a + H_q + H_n + \frac{\phi_r}{\phi_s} (H_a + H_q - H_n) \quad . \quad (82e)$$

Thus, sixteen parameters are needed for this core model: l_i , l_o , ϕ_r , ϕ_s , H_a , H_q , H_n , λ_d , ν_d , F_{dB} , F_0'' , λ , ν , F_B , F_0 , and ρ_p .

2. Inductor Model

The inductor used in this circuit includes a ferrimagnetic material; thus, the inductance decreases nonlinearly with the current. The experimental flux linkage ψ vs. i may be fit by the exponential function

$$\psi = \psi_{sat} \left(1 - e^{-i/I_{con}} \right) \quad , \quad (83)$$

where ψ_{sat} and I_{con} are two parameters, one describing the saturation flux linkage and the other the rate of rise of ψ with i , as shown in Fig. 31.

Differentiation of Eq. (83) with respect to i gives

$$L = L_0 e^{-i/I_{con}} \quad (84)$$

where

$$L_0 = \frac{\psi_{sat}}{I_{con}} \quad . \quad (84a)$$

Thus, L is described by two parameters, L_0 (initial inductance) and I_{con} .

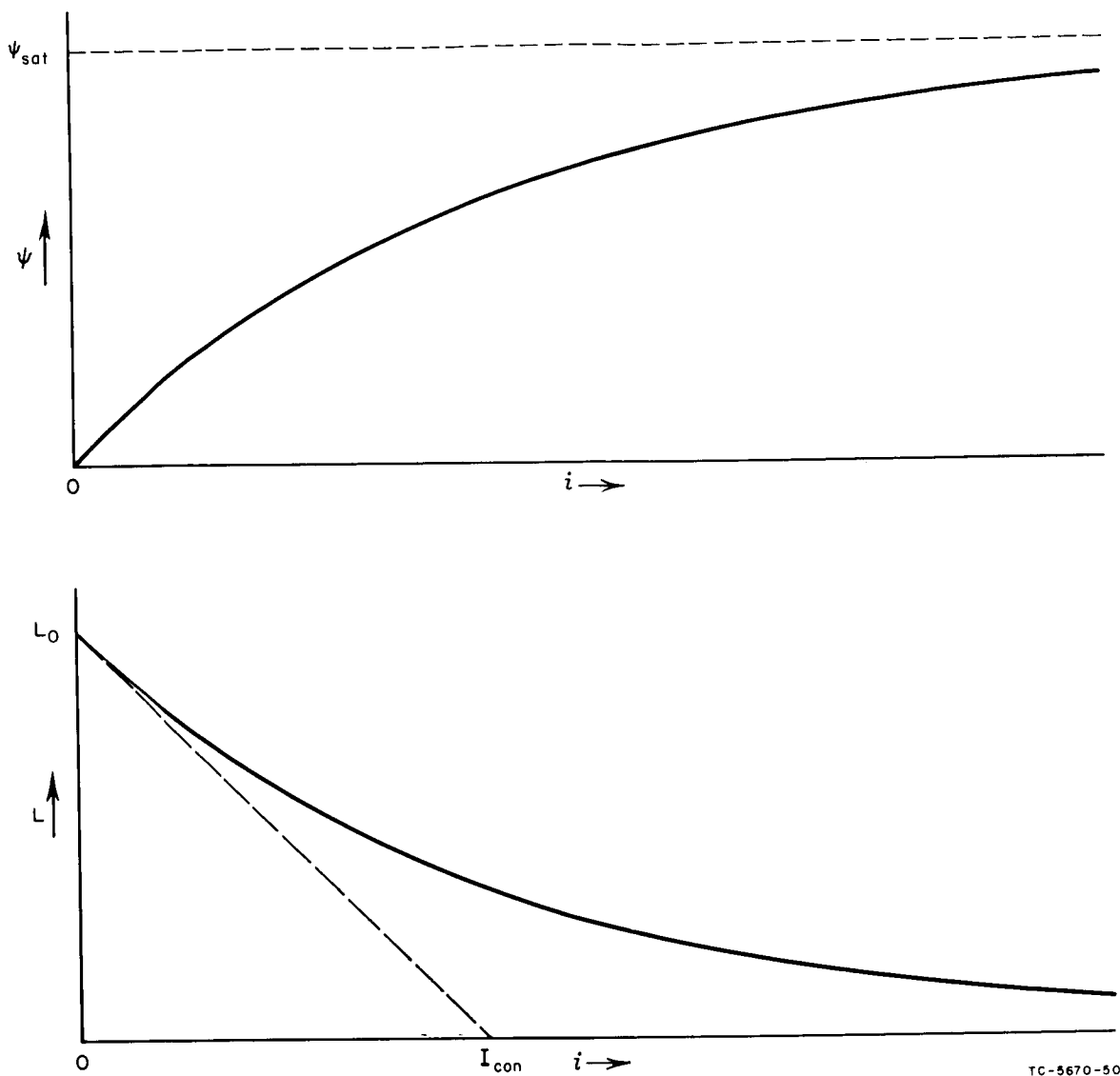


FIG. 31 EXPONENTIAL MODEL FOR $\psi(i)$ AND INCREMENTAL $L(i)$ OF A FERRIMAGNETIC INDUCTOR

Alternatively, the nonlinear $\psi(i)$ curve might be described by a polynomial of a suitable degree. However, unlike the exponential function of Eq. (83), its application beyond the region of the experimental data may be erroneous, e.g., it may yield a negative inductance. For this reason, we have chosen not to use a polynomial fit.

The winding capacitance of the inductor is not included in our model because the high-frequency components of the voltage across the inductor in this application are negligible.

3. Diode Model

An equivalent circuit for a p - n junction diode^{22,23} is shown in Fig. 32. It is composed of static and dynamic components.

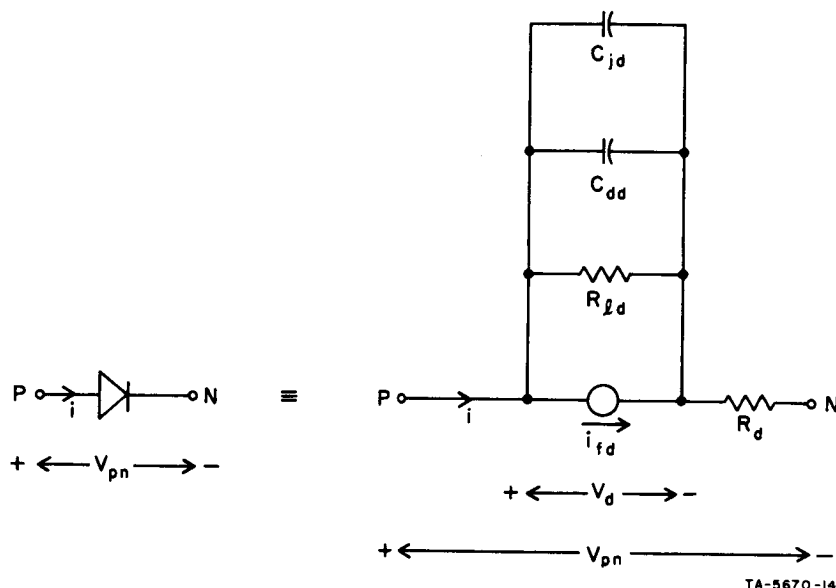


FIG. 32 AN EQUIVALENT CIRCUIT FOR A pn JUNCTION DIODE

a. Static Properties

The current generator i_{fd} represents the static currents due to minority-carrier diffusion and minority-carrier recombination in the junction. On the basis of the relationship between the junction voltage V_d of an ideal diode and the excess concentration of the minority carriers, it can be shown²³ that

$$i_{fd} = I_{sd}(e^{V_d/\theta_{md}} - 1) \quad , \quad (85)$$

where I_{sd} is the saturation current of the diode, and

$$\theta_{md} = \frac{kT}{q} m_d = 0.86 \cdot 10^{-4} T m_d \quad . \quad (85a)$$

In Eq. (85a), k is Boltzman's constant ($k = 1.381 \cdot 10^{-23}$ J/°K), q is the charge of an electron ($q = 1.602 \cdot 10^{-19}$ C), T is the absolute temperature, and m_d is the diode m factor, which varies between 1 and 2. (The diffusion-current component is governed by $m_d = 1$; the current component due to recombination in the junction space-charge layer is governed by $m_d \approx 2$. The overall m_d is thus between 1 and approximately 2.)

The shunt resistance $R_{\mathcal{L}d}$ represents the surface leakage resistance. Its magnitude is several megohms, and may be neglected when the diode is forward biased. The converse is true for the series resistance R_d : Its magnitude is of the order of one ohm and it should not be neglected when the diode is forward-biased. Using Eq. (85), the forward static V - I characteristic of a diode is thus described by the equation

$$V_{pn} = IR_d + \theta_{md} \ln \left(1 + \frac{I}{I_{sd}} \right) \quad . \quad (86)$$

b. Dynamic Properties

In a transient condition, capacitive components are added to the equivalent circuit representing the static properties of the diode. The total capacitance is the sum of a diffusion capacitance, C_{dd} , and a junction capacitance, C_{jd} .²³ The diffusion capacitance is associated with the minority-carrier currents, which are injected into the neutral regions that sandwich the space-charge layer;²² it is approximately proportional to the steady-state current of an ideal diode:

$$C_{dd} = k_d (i_{fd} + I_{sd}) = k_d I_{sd} e^{V_d / \theta_{md}} \quad . \quad (87)$$

The junction capacitance is associated with the majority-carrier displacement currents due to the changes in the dipole layer of the space charge that straddles the metallurgical junction;²² it is a function of the junction voltage V_d :

$$C_{jd} = C_{j0d} [1 - (V_d / V_{\phi d})]^{-N_d} \quad , \quad (88)$$

where C_{j0d} is the junction capacitance for $V_d = 0$, $V_{\phi d}$ is the contact potential (typically, less than 1 volt), and N_d is a power coefficient lying between 1/3 (graded junction) and 1/2 (abrupt junction).²²

Referring to Fig. 32, the relations between the voltage across a diode and the current through it are

$$V_{pn} = iR_d + V_d \quad (89)$$

and

$$i = i_{fd} + \frac{V_d}{R_{\ell d}} + (C_{dd} + C_{jd})\dot{V}_d \quad (90)$$

Thus, the diode model in Fig. 32 is described by eight parameters: I_{sd} , θ_{md} (or m_d), R_d , $R_{\ell d}$, k_d , C_{j0d} , $V_{\phi d}$, and N_d .

4. Transistor Model

An equivalent circuit for an npn transistor²²⁻²⁴ is shown in Fig. 33. It may be regarded as the equivalent circuits of two back-to-back diodes plus forward-injected and reverse-injected current sources, $\alpha_n i_{fe}$ and $\alpha_i i_{fc}$. The parameters α_n and α_i (sometimes denoted by α_F and α_R) are the forward-injection and reverse-injection common-base short-circuit current gains, respectively. In addition, there is a base resistance, R_b , between the junction of the diodes and the base terminal.

The relations between the emitter voltage and emitter current are similar to those of a diode, Eqs. (85) through (90), except for the addition of the reverse-injection current $\alpha_i i_{fc}$. The collector voltage and collector current are also related in a similar way to those of a diode. For future reference, these relations are given as follows: voltages, currents, resistances, and capacitances are defined in Fig. 33; the base-emitter and base-collector parameters corresponding to those of a diode are designated by the subscripts e and c , respectively, instead of the subscript d .

Base-Emitter Equations:

$$i_{fe} = I_{se} \left(e^{V_e / \theta_{me}} - 1 \right) \quad (91)$$

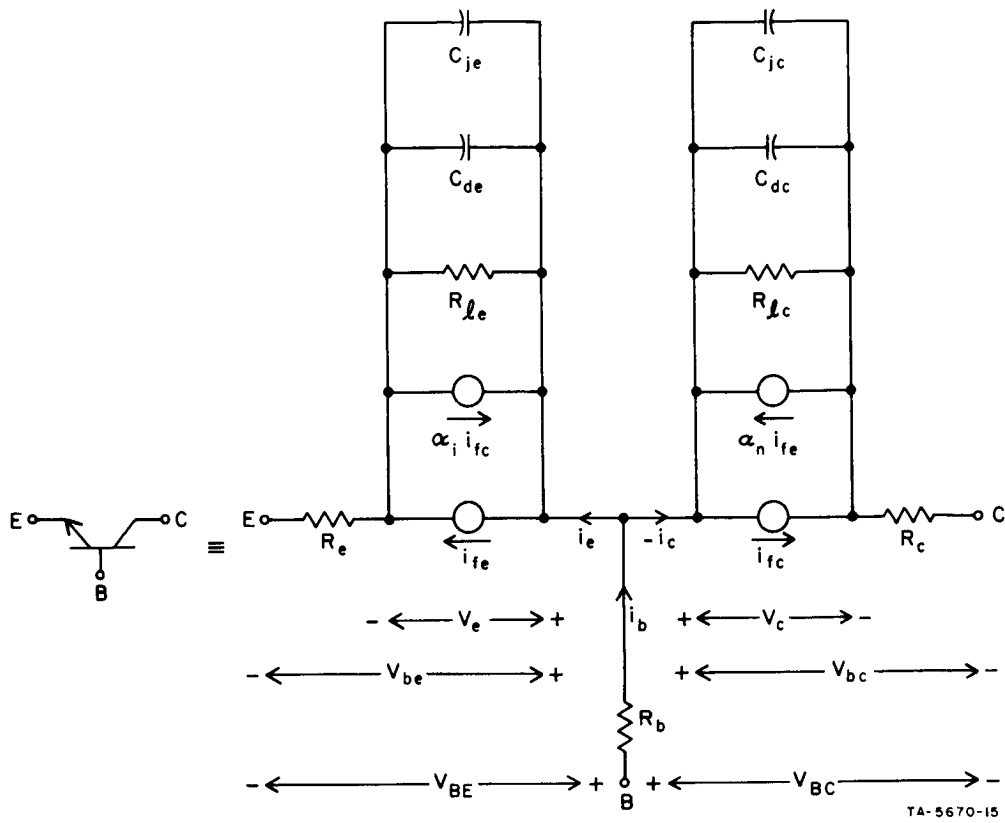


FIG. 33 AN EQUIVALENT CIRCUIT FOR AN npn TRANSISTOR

where

$$\theta_{me} = 0.86 \cdot 10^{-4} T_{me} \quad , \quad (92)$$

$$C_{de} = k_e (i_{fe} + I_{se}) = k_e I_{se} e^{V_e / \theta_{me}} \quad , \quad (93)$$

$$C_{je} = \frac{C_{j0e}}{\left(1 - \frac{V_e}{V_{\phi e}}\right)^{N_e}} \quad , \quad (94)$$

$$V_{be} = i_e R_e + V_e \quad , \quad (95)$$

$$i_e = i_{fe} - \alpha_i i_{fc} + \frac{V_e}{R_{le}} + (C_{de} + C_{je}) \dot{V}_e \quad , \quad (96)$$

and

$$V_{BE} = V_{be} + i_b R_b \quad . \quad (97)$$

Base-Collector Equations:

$$i_{fc} = I_{sc} \left(e^{V_c / \theta_{mc}} - 1 \right) , \quad (98)$$

where

$$\theta_{mc} = 0.86 \cdot 10^{-4} T_{mc} , \quad (99)$$

$$C_{dc} = k_c (i_{fc} + I_{sc}) = k_c I_{sc} e^{V_c / \theta_{mc}} , \quad (100)$$

$$C_{jc} = \frac{C_{j0c}}{\left(1 - \frac{V_c}{V_{\phi c}} \right)^{N_c}} , \quad (101)$$

$$V_{bc} = -i_c R_c + V_c , \quad (102)$$

$$-i_c = i_{fc} - \alpha_n i_{fe} + \frac{V_c}{R_{\ell c}} + (C_{dc} + C_{jc}) \dot{V}_c , \quad (103)$$

and

$$V_{BC} = V_{bc} + i_b R_b . \quad (104)$$

By inspection of Fig. 33,

$$i_b = i_e - i_c \quad (105)$$

and

$$V_{CE} = V_{be} - V_{bc} = i_e R_e + V_e + i_c R_c - V_c . \quad (106)$$

The common-base parameters α_n and α_i are related to the corresponding common-emitter parameters by

$$\alpha_n = \frac{\beta_n}{1 + \beta_n} \quad (107)$$

and

$$\alpha_i = \frac{\beta_i}{1 + \beta_i} , \quad (108)$$

where β_n and β_i (also known as h_{fe_n} and h_{fe_i}) are the common-emitter short-circuit current gains due to forward and reverse injections, respectively. Both β_n and β_i vary with the collector or emitter current. Since no models for calculation of β_n and β_i are available at the present time, these will be computed by interpolation of measured data.

Under a static condition, $\dot{V}_e = \dot{V}_c = 0$, and so Eqs. (91), (96), (98), and (103) can be simplified. Ignoring the negligible leakage currents V_e/R_{ℓ_e} and V_c/R_{ℓ_c} , and using capital letters to designate a static state, the simplified equations are known as the Ebers-Moll model:^{2,23}

$$I_e = I_{se} \left(e^{V_e / \theta_{me}} - 1 \right) - \alpha_i I_{sc} \left(e^{V_c / \theta_{mc}} - 1 \right) \quad (109)$$

$$I_c = \alpha_n I_{se} \left(e^{V_e / \theta_{me}} - 1 \right) - I_{sc} \left(e^{V_c / \theta_{mc}} - 1 \right) \quad (110)$$

The transistor model of Fig. 33 is described by nineteen parameters: I_{se} , θ_{me} (or m_e), R_e , R_{ℓ_e} , k_e , C_{j0e} , $V_{\phi e}$, N_e , I_{sc} , θ_{mc} (or m_c), R_c , R_{ℓ_c} , k_c , C_{j0c} , $V_{\phi c}$, N_c , R_b , α_n , and α_i . As we shall see, α_n and α_i are computed from experimental data of β_n vs. I_c and β_i vs. I_e , respectively, using Eqs. (107) and (108).

D. Determination of Parameters

Each of the device models described previously includes a number of parameters. There are sixteen parameters in the core model, two parameters in the inductor model, eight parameters in the diode model, and nineteen parameters in the transistor model. Except for the static parameters of a diode and a transistor, these parameters cannot be measured at the present time by standard, commercially available equipment to the necessary accuracy and over the range required.

In this part of the report we wish to describe the procedure for determining the parameters of each model. Such a procedure involves the following steps: setting up the measurement equipment and housing the tested device in an insulated enclosure whose temperature is regulated automatically at $T \pm 0.5^\circ\text{C}$; obtaining the experimental data and transferring these data to punched cards; and computing the parameters on a digital computer by curve fitting based on least-mean-square error. Repeating this procedure at various temperatures results in the plots of these parameters vs. temperature.

1. Core Parameters

Determination of the core parameters is based on measurements of the dimensions, the static $\phi(F)$ curve, and the $\dot{\phi}_p(F)$ curve. The measurements were performed on three Lockheed 100SC1 ferrite cores ($OD = 100$ mils; $ID = 70$ mils; $h = 30$ mils), referred to as Cores A, B, and C. Cores A and B were used as Cores 1 and 2 of the second stage of the binary counter, Fig. 25.

a. Dimension Parameters

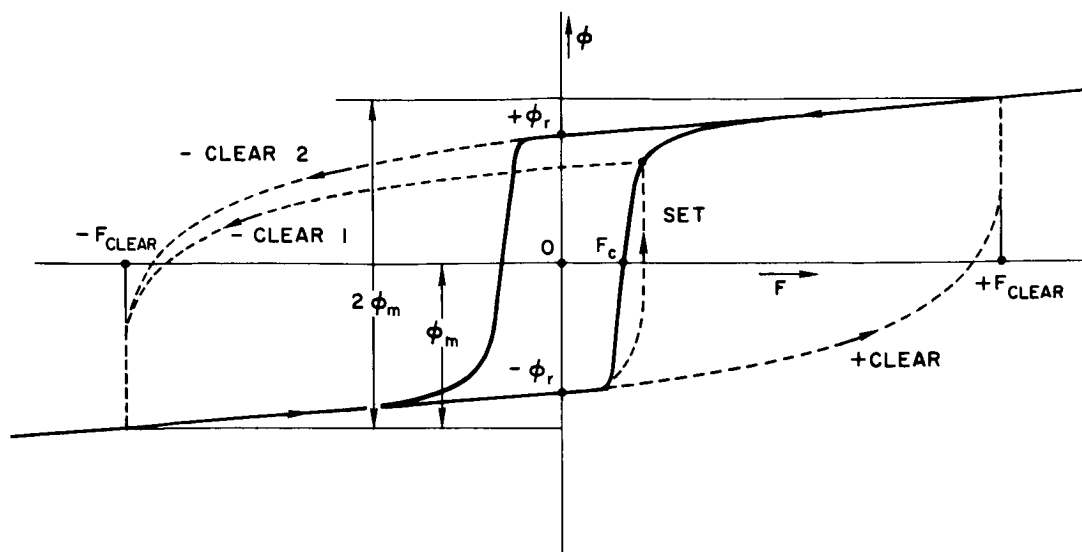
The parameters l_i and l_o are in general the short and long lengths of a leg in a multipath core. In the case of a toroidal core, $l_i = 2\pi r_i$ and $l_o = 2\pi r_o$, where r_i and r_o are the inside and outside radii of the toroid, respectively. Due to the possible tapering of a core, r_i and r_o were measured on both sides and averaged. There is no need to measure the core thickness for the core model because it is accounted for in measuring the flux capacity of the core.

b. Static Core Parameters

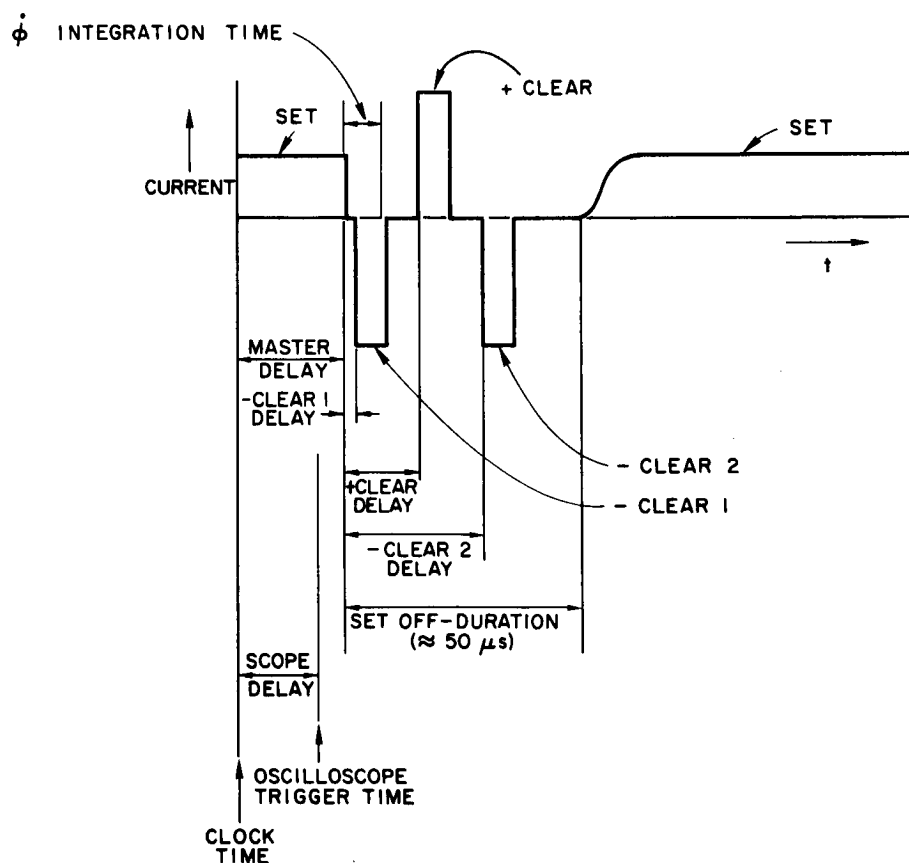
i. Experiment

The main problem in the measurement of the static $\phi(F)$ curve is the integrator decay. In addition, it is economically desirable to have an automatic or semiautomatic means for such a measurement. An equipment that essentially overcomes these problems was built by personnel of the Magnetics Group of Stanford Research Institute, and is presented briefly as follows.

The principle of operation is that of setting the core with a very long SET pulse and clearing the core with a large-amplitude, short-duration CLEAR pulse. The long SET pulse allows the core to switch very slowly for the low F values so that essentially static properties are obtained. The flux change is measured at the time of clearing, which is relatively fast, because this permits easy integration of $\dot{\phi}$. A positive CLEAR pulse and another negative CLEAR pulse are also included to assure adequate clearing (see pp. 83 and 84 of Report 3). Figure 34(a) shows the paths of operation in the $\phi(F)$ plane. The pulse sequence is shown in Fig. 34(b).



(a) $\phi(F)$ PATHS



(b) CURRENT-DRIVER OUTPUT

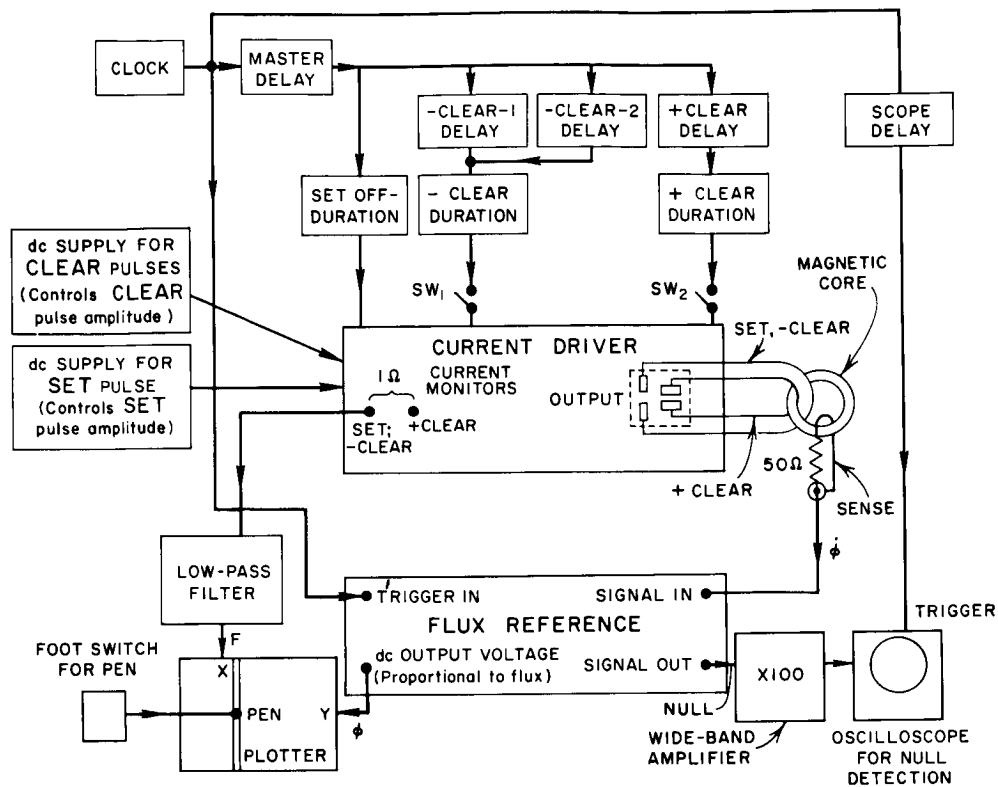
TB-5670-51

FIG. 34 FLUX-SWITCHING AND DRIVE-CURRENT PROGRAM FOR MEASUREMENT OF A STATIC $\phi(F)$ CURVE

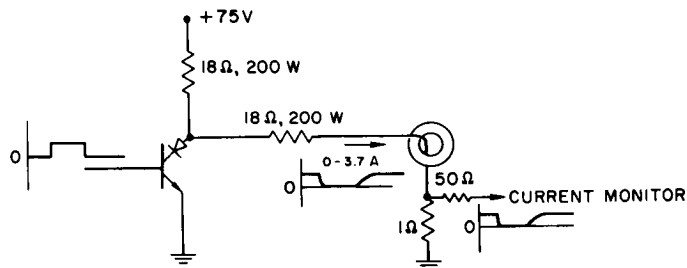
A block diagram for the static $\phi(F)$ plotter is shown in Fig. 35(a). The pulse sequence is generated in the logic blocks at the top of the figure. The current driver converts these pulses into the current-pulse program shown in Fig. 34(b). The amplitudes of the SET and CLEAR pulses are controlled by the output voltages of the power supplies at the left of Fig. 35(a). The $N\dot{\phi}$ output of the core being tested is integrated and then nulled in the flux reference. The oscilloscope with an external amplifier is used for null detection. The dc output voltage of the flux reference, which is proportional to the time integral of $N\dot{\phi}$ for a null condition, drives the Y-axis of the plotter. The X-axis of the plotter is driven by the voltage across a $1\ \Omega$ current-monitor resistance in the current driver. This voltage is the same as the waveform shown in Fig. 34(b), except that the positive CLEAR pulse is absent. The repetition rate is very low, e.g., about 60 pps, so that the duty factor of the SET pulse is nearly unity (≈ 0.997). Therefore, by low-pass filtering, a dc voltage is obtained which is very nearly equal to the amplitude of the SET pulse (the minus CLEAR pulses are also removed by the filtering).

The flux reference was described on pp. 137-141 of Report 2, except for the dc output-voltage circuit. The source of this dc voltage is a mercury-battery voltage reference which is ganged to the null controls of the flux reference (by two ten-position switches and one one-turn potentiometer). This voltage reference is calibrated to give a choice of either 10 mV/Mx or 5 mV/Mx, so that the ϕ -axis scale of the $\phi(F)$ plot can be labeled directly in maxwells with a convenient scale factor (e.g., 1, 2, or 5 maxwells/division).

The output stage of the current driver is shown in Fig. 35(b); it is unconventional for two reasons: (1) the average dc output current of the SET pulse is large (up to 3.4A), and (2) reverse current spikes and spikes in excess of the SET pulse amplitude had to be avoided. The problem of the high magnitude of the current was solved by having the current turned off by turning the transistor on. Since the off time of the current was small, the problem of dissipation in the collector was negligible. This technique also solved the problem of reverse current spikes on the output-current waveforms. In the case of turning on the SET current (turning off the transistor), a small spike in the CLEAR direction is obtained because of the input pulse feeding through the collector capacitance to the output, but this is in the CLEAR



(a) BLOCK DIAGRAM



(b) SET OUTPUT CIRCUIT OF CURRENT DRIVER

TC-5670-52

FIG. 35 SEMIAUTOMATIC STATIC- $\phi(F)$ PLOTTER

direction and the core has just been cleared anyway, so the spike does no harm. In turning off the SET current (turning on the transistor), two effects prevent any significant spike from appearing on the SET current before it turns off: (1) the transistor has a lower collector capacitance because the voltage on it is high, and (2) the diode in the collector circuit blocks the signal which comes through the collector capacitance.

The step-by-step instructions to the operator of the static $\phi(F)$ plotter are as follows:

- (1) Wire and mount the core in the temperature-controlled oven.
- (2) Determine the plotter ϕ and F scale factors by traversing through the $\phi(F)$ curve.
- (3) Adjust I_{SET} equal to I_{CLEAR} .
- (4) Null the flux reference and divide the readings on the dials (arbitrary units) by two.
- (5) Set the flux reference dials to these new values. This setting corresponds to $\phi = 0$ and is used to locate the origin on the graph paper.
- (6) Set I_{SET} to zero and adjust the zero- X and zero- Y positions ($I_{\text{SET}} = 0$; $\phi = 0$) of the plotter at the desired point (e.g., intersection of left edge of graph paper and a grid line half way between top and bottom of sheet).
- (7) Set $I_{\text{SET}} = 0$ and null the flux reference. Plot this point by depressing a foot pedal. This point corresponds to $-\phi_r$.
- (8) Increase I_{SET} to the next desired value and null the flux reference. Plot this point. The value of the MMF, F , applied to the core is I_{SET} times the number of turns of the SET winding (typically two).
- (9) Repeat Step (8) for as many points as desired between $I_{\text{SET}} = 0$ and the maximum I_{SET} available (3.4A for the equipment being described).

- (10) Label the ϕ axis in maxwells, using the mV/Mx calibration factor of the flux reference, the Y-axis gain of the plotter, and the number of sense turns. Also label the F axis using the X-axis gain of the plotter, the number of turns in the SET winding, and the 1.00Ω value of the monitor resistance.
- (11) From the resulting $\phi(F)$ plot determine the absolute value of ϕ_r as read at the $-\phi_r$ point. Using this value, mark the $+\phi_r$ point on the graph sheet.
- (12) Set the flux reference dials on zero, and adjust the Y-axis zero position control to position the plotter pen at the $+\phi_r$ point. This prepares the plotter for plotting the elastic $\phi(F)$ curve in positive saturation [the top of the $\phi(F)$ curve].
- (13) Remove all the CLEAR pulses from the pulse program. This can be accomplished by opening Switches Sw_1 and Sw_2 in Fig. 35(a).
- (14) Set $I = 0$, null the flux reference, and mark the point. This puts a data point at $+\phi_r$.
- (15) Increase I to the next desired value, null the flux reference and mark the point.
- (16) Repeat Step (15) for as many values of I as desired.

The specifications of the static $\phi(F)$ plotter are given in Table II.

Table II(a)

SPECIFICATIONS OF THE CURRENT DRIVER IN THE STATIC $\phi(F)$ PLOTTER

CURRENT DRIVER				
	Maximum Pulse Amplitude (amperes)	Pulse Duration	Rise Time	Fall Time
SET	3.4	16.7 ms (@ 60 pps)	5 μ s	0.5 μ s
SET OFF-DURATION	--	50 μ s		
-CLEAR(1)	3.4	10 μ s		
-CLEAR(2)	3.4	10 μ s		
+CLEAR	3.4	10 μ s		

Table II(b)
SPECIFICATIONS OF THE FLUX REFERENCE IN THE STATIC $\phi(F)$ PLOTTER

FLUX REFERENCE	
Maximum Flux Capacity:	40 units = 120 maxwell-turns
Resolution:	0.03 units = 0.1 maxwell-turns
Calibration Factor:	3.60 maxwells/unit
Integration Time Constant:	50 μ s
dc Output Calibration Factor:	10 mV/maxwell or 5 mV/maxwell
Reference Core Oven Temperature:	55°C

ii. Measured Data

Measured data of the static $\phi(F)$ curves of Cores A, B, and C at $T = -10^\circ\text{C}$, 25°C , 55°C , and 85°C are shown in Fig. 36. The cores appear to be quite uniform. As F reaches the threshold value F_d^{min} , ϕ is unstable and jumps to around $-\phi_r/3$.

The computed static $\phi(F)$ curves of Core A are drawn as solid lines, and will be discussed later.

The experimental data of the static $\phi(F)$ curve of each core at each temperature were read on an OSCAR Model N-2 machine. The output of this machine was a deck of punched cards for each core at a given temperature. Each card contained the ϕ and F coordinates of one point on the static $\phi(F)$ curve. The cards in each deck were divided into two groups: the first group included the data in the positive-saturation region (for computation of H_a), and the second group included the data in the nonsaturation region (for computation of H_q and H_n). The data at negative saturation for $0 < F < F_d^{\text{min}}$ were ignored because they included the inelastic $\Delta\phi_i$ (see Sec. I-A-4-c-i, p. 21).

iii. Computation

The value of ϕ_r is readily available from the experimental static $\phi(F)$ curve, $\phi_d(F)$. We assume that $\phi_s/\phi_r = 1.1$ because such a ratio has been found to yield a good agreement between computed and measured static $\phi(F)$ curves for $F \lesssim 10F_c$. Thus, the only static $\phi(F)$ parameters that need to be computed are H_a , H_q , and H_n .

A computer program for computation of H_a , H_q , and H_n from measured static $\phi(F)$ data is given in Appendix B. The program is based

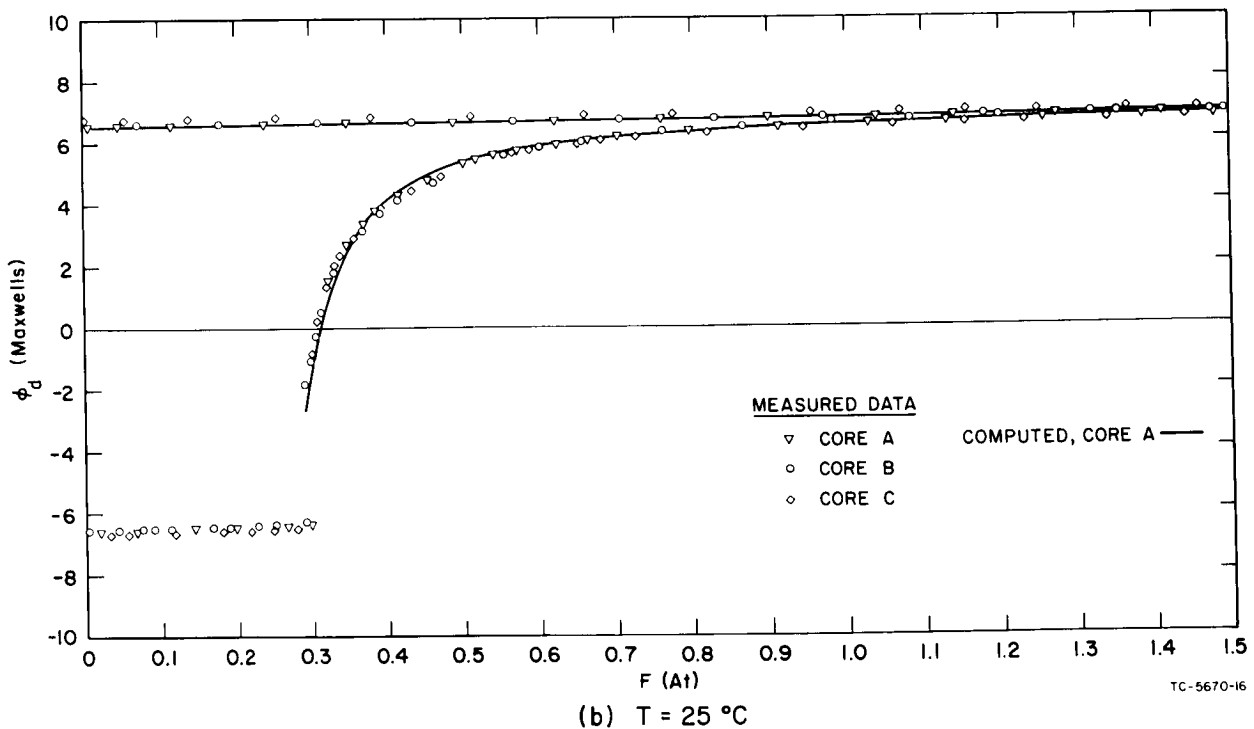
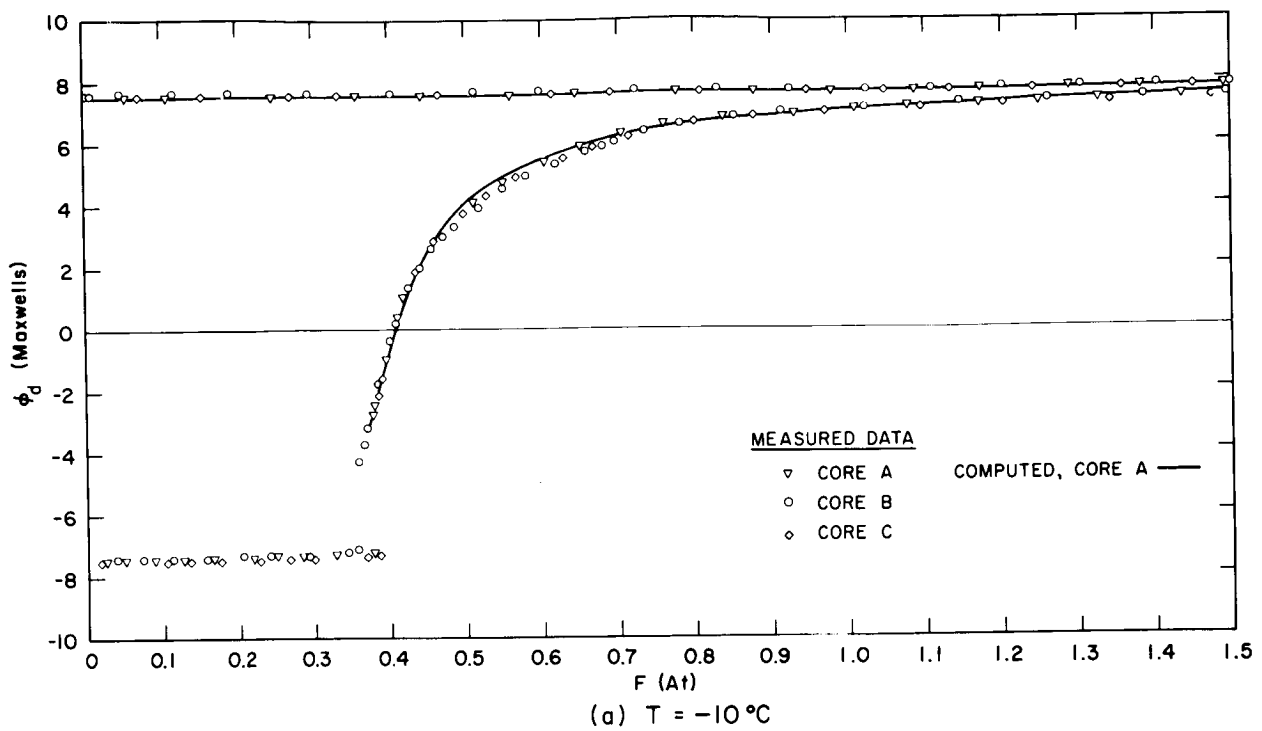


FIG. 36 MEASURED AND COMPUTED STATIC $\phi(F)$ CURVES AT DIFFERENT TEMPERATURE VALUES. Core Type - Lockheed 100SC1.

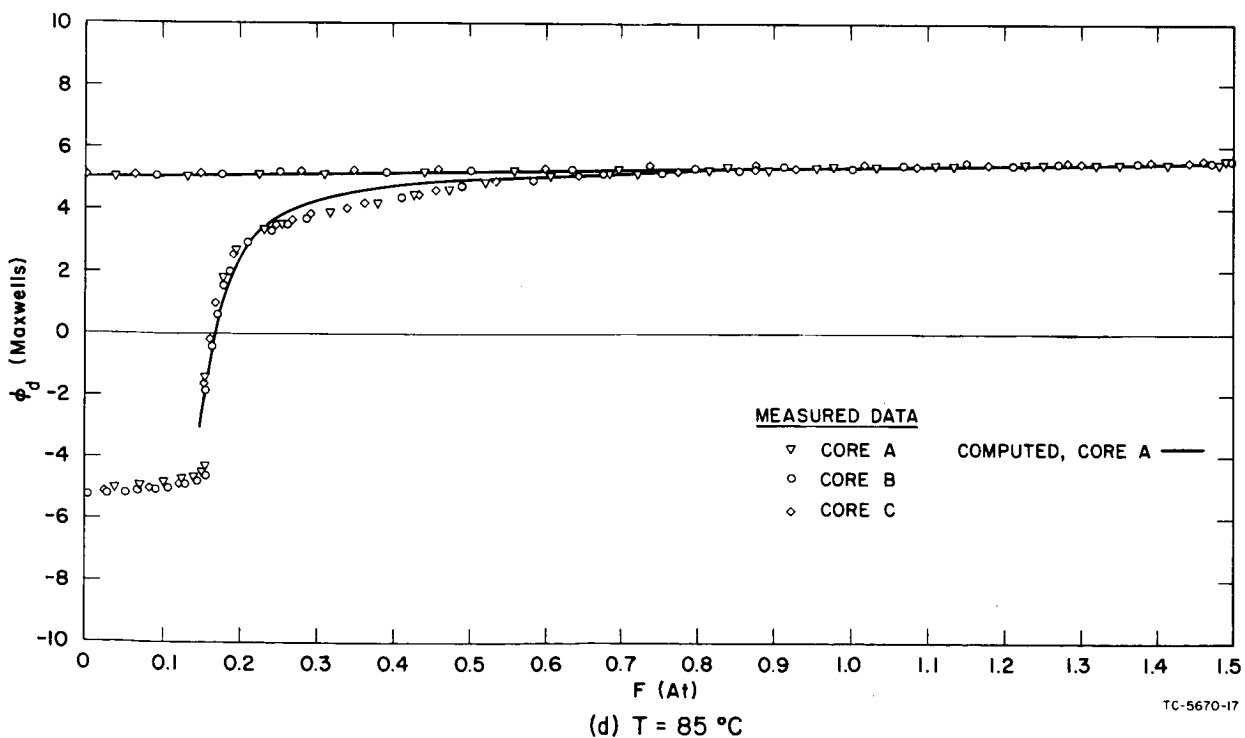
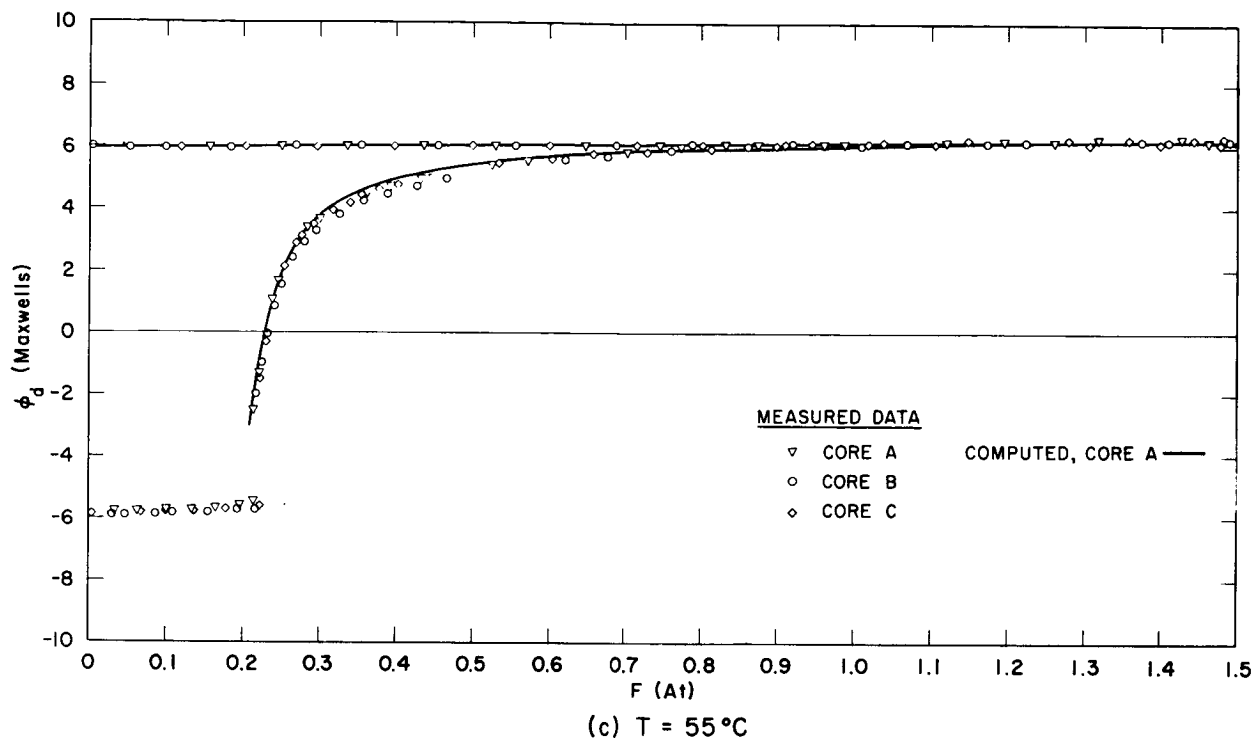


FIG. 36 Concluded

on curve fitting by minimization of $\sum \text{error}^2$, where the error is the difference between ϕ_d computed from Eqs. (82)-(82e) and the measured ϕ_d for a given F value used in the experiment. The experimental data in the positive-saturation region are first used to compute the optimum value of H_a . The rest of the experimental data (excluding the points at negative saturation for $0 \leq F \leq F_d^{\min}$) are then used to compute the optimum values of H_q and H_n . The resulting values of H_a , H_q , and H_n are then used to compute ϕ_d vs. the values of F used in the experiment.

The computer printout includes the values of the parameters determined at each iteration and a table of F , experimental ϕ_d , computed ϕ_d , and the percentage error $[1 - (\phi_{d,\text{comp}}/\phi_{d,\text{exp}})] \cdot 100$.

iv. Results

Computed static $\phi(F)$ curves for Core A, which lie between the curves of the other two cores, are compared with measured static $\phi(F)$ data at $T = -10^\circ\text{C}$, 25°C , 55°C , and 85°C in Fig. 36. It can be seen that except in the region $F_d^{\min} \leq F < F_c$, the agreement is quite satisfactory.

In Fig. 37, the parameters ϕ_r , ϕ_s , H_a , H_q , and H_n of Cores A, B, and C are plotted vs. temperature. Except for H_a , the uniformity of these parameters among the three tested cores is very good. The nonuniformity of H_a indicates that the elastic switching properties of these cores differ from each other both in magnitude and in their change with temperature. Part of this nonuniformity stems from differences in air flux due to variations in winding configuration.

As pointed out in Report 4 (p. 111), the squareness of the static $\phi(F)$ curve may be measured by the ratio H_q/H_n : the smaller H_q/H_n is, the sharper is the $\phi(F)$ wing, and so the more square is the $\phi(F)$ curve. The ratio H_q/H_n is around 1.16 throughout the temperature range. This is in agreement with the results of Core K-1 (which is of the same type as Cores A, B, and C) in Report 4, Fig. 39.

c. Dynamic Core Parameters

i. Experiment

The dynamic parameters are obtained from the measurement of the $\dot{\phi}_p(F)$ curve. The experiment and measurement procedure were described in detail in Report 2, pp. 151-152 and in Report 3, p. 83.

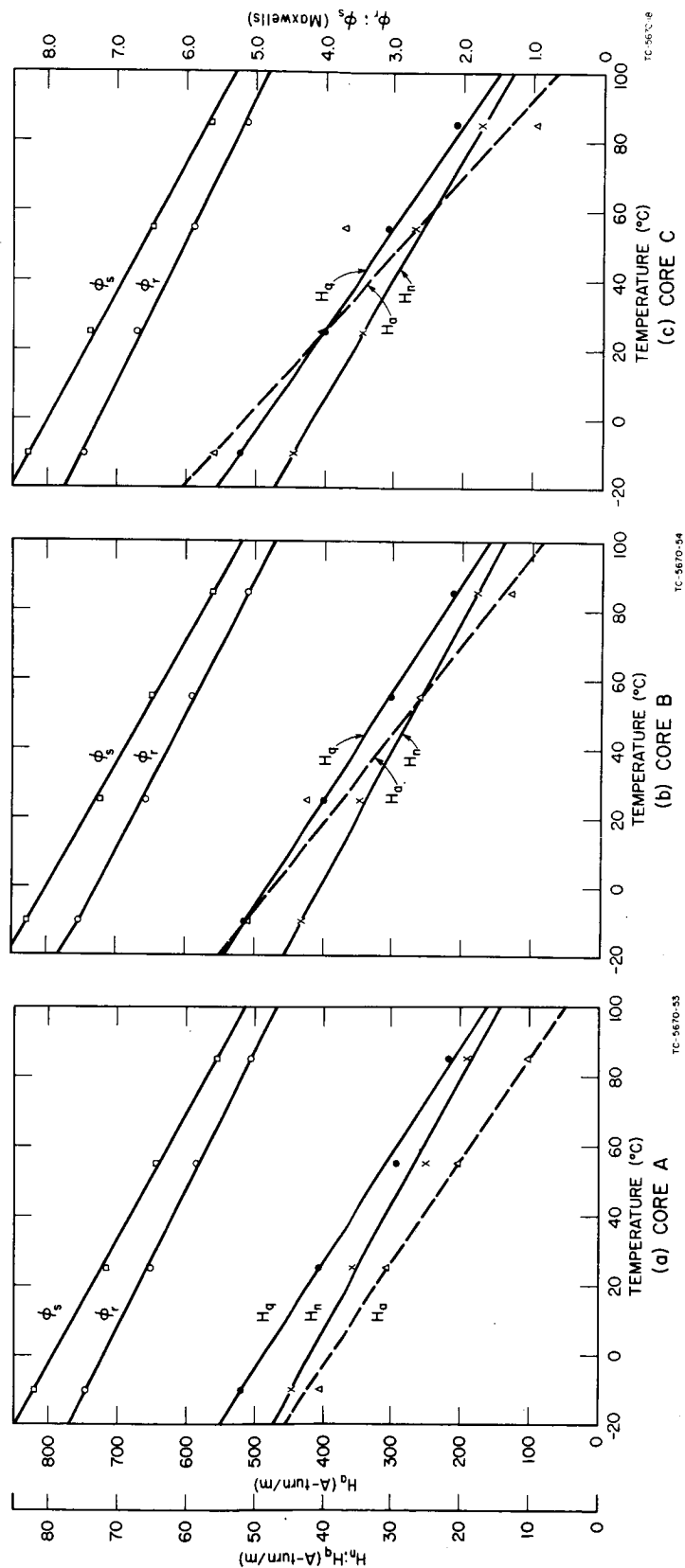


FIG. 37 STATIC $\phi(F)$ PARAMETERS vs. TEMPERATURE. Core Type - Lockheed 100SC1.

Basically, the core is first cleared by a negative CLEAR pulse, a positive CLEAR pulse, and a negative CLEAR pulse. After clearing, the core is set by a positive SET pulse of short rise time and constant amplitude F , and the peak of the main $\dot{\phi}$, $\dot{\phi}_p$, is recorded.

Three different current pulsers were used in this experiment:

- (1) The negative CLEAR pulse was generated by paralleling six vacuum-tube current drivers (Digital Equipment Corp., Model 50), and had a $0.1 \mu\text{s}$ rise time, a $30 \mu\text{s}$ width, and a 5A amplitude; it was applied to a two-turn winding.
- (2) The positive CLEAR pulse was generated by paralleling four transistor current drivers (Digital Equipment Corp., Model 62), and had a $0.1 \mu\text{s}$ rise time, a $35 \mu\text{s}$ width, and a 2A amplitude; it was applied to a two-turn winding.
- (3) The SET pulse was generated by a vacuum-tube driver (Hewlett-Packard, Model 214A), and had a 20 ns rise time, a $500 \mu\text{s}$ width, and a variable amplitude; it was applied to a two-turn winding.

ii. Measured Data

Measured $\dot{\phi}_p(F)$ data for Cores A and B at $T = -10^\circ\text{C}$, 25°C , 55°C , and 85°C are shown in Fig. 38. The uniformity of these curves is good. The solid-line curves are computed $\dot{\phi}_p(F)$ curves of Core A, which will be discussed later.

The measured data were transferred to punched cards, each card containing one $(\dot{\phi}_p; F)$ point.

iii. Computation

We have seen in Sec. I-A-4-c-ii, p. 25, that the curve fitting of $\dot{\phi}_p(F)$ for $F \geq F_d^{\min}$ is divided into three regions: Region I, $F_d^{\min} \leq F \leq F_{dB}$; Region II, $F_{dB} \leq F \leq F_B$; and Region III, $F_B \leq F$. Nine parameters are used in Eqs. (81): λ_d , ν_d , F_{dB} , λ , F_0'' , ν , F_B , ρ_p , and F_0 . However, in order to achieve a continuity of $\dot{\phi}_p(F)$, four constraints are imposed on these parameters by equating $\dot{\phi}_p$ and $\dot{\phi}_p' = d\dot{\phi}_p/dF$ at the boundary $F = F_{dB}$ between Regions I and II and at the boundary $F = F_B$ between Regions II and III. Therefore, only five parameters need to be determined. These were chosen to be F_{dB} , λ , F_0'' , ν , and F_B .

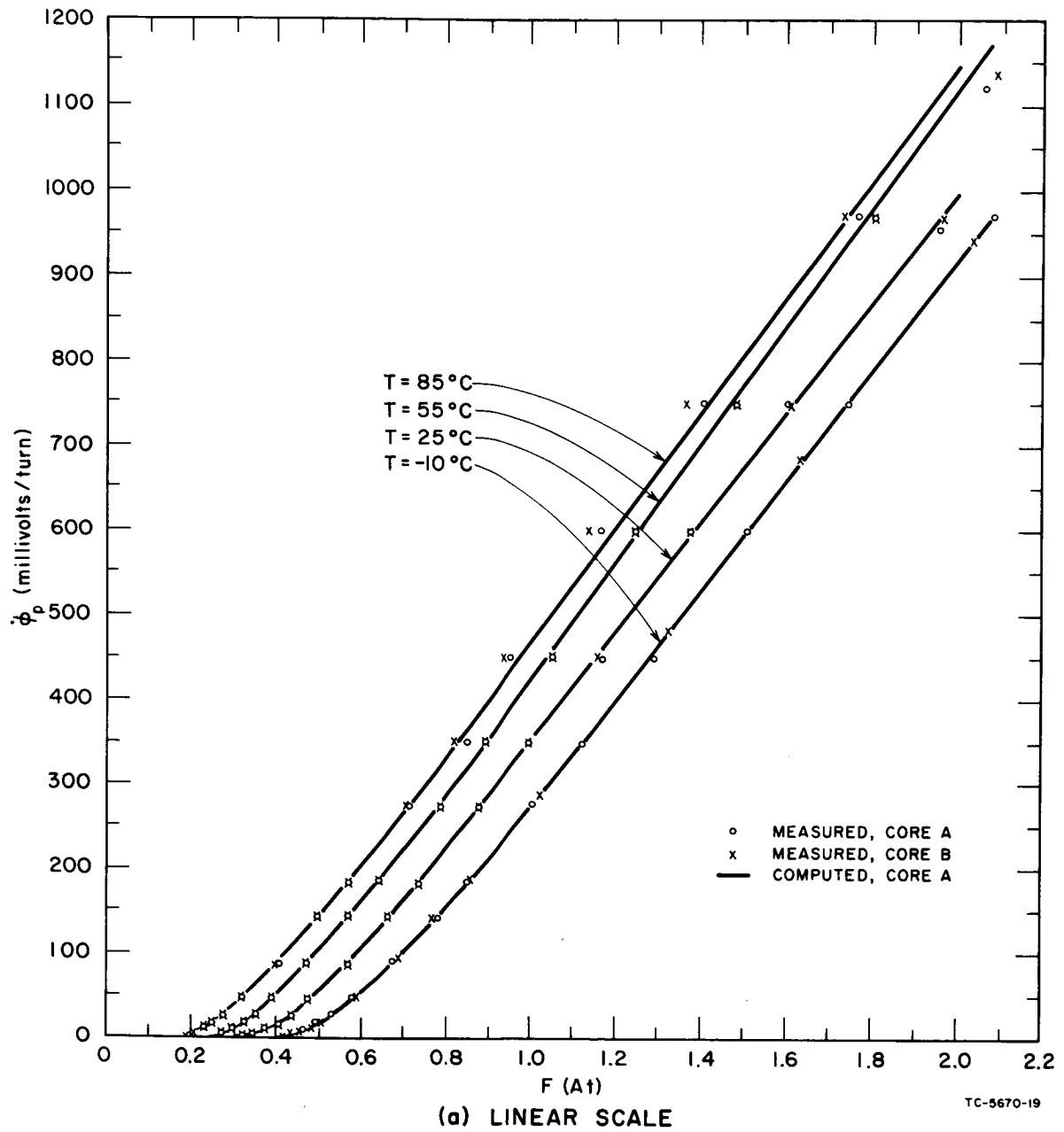
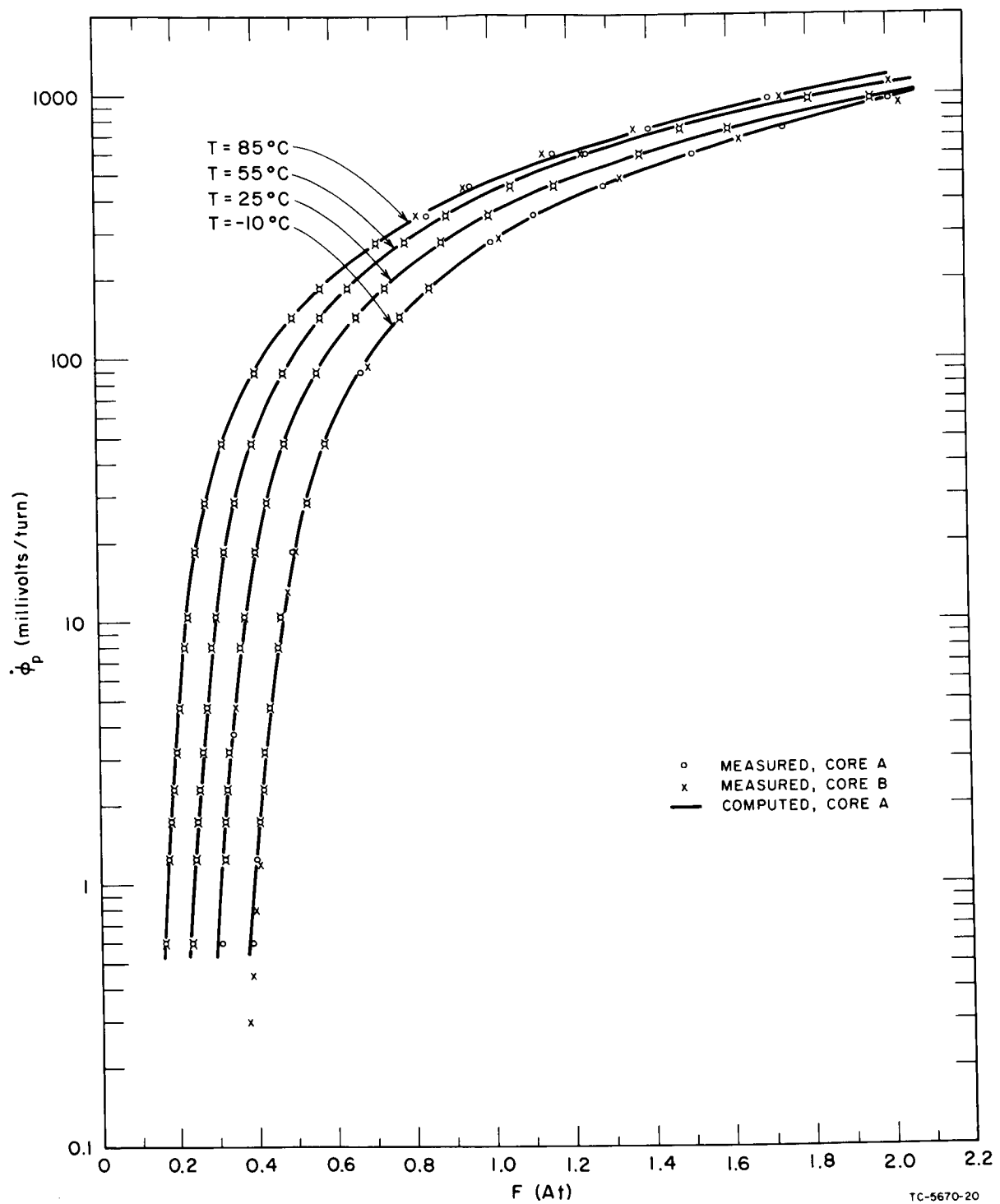


FIG. 38 MEASURED AND COMPUTED $\dot{\phi}_p(F)$ CURVES vs. TEMPERATURE.
Core Type - Lockheed 100SC1.



(b) SEMILOG SCALE

FIG. 38 Concluded

A computer program for determination of F_{dB} , λ , F_0'' , ν , and F_B from measured $\dot{\phi}_p(F)$ data is given in Appendix C. The program is based on least-mean-square curve fitting of Eqs. (81) to the measured data. Initially, the parameter values are guessed. The data of Region II are then used to compute λ , F_0'' , and ν , and the data of Region III are used to compute F_B . If the new value of F_B requires data transfer between the two regions, the above computation is repeated until no such transfer is necessary. A similar procedure was first attempted in determination of F_{dB} . This attempt failed (F_{dB} was too large) because of the inadequacy of Region I curve fitting. Since Regions II and III are much more important than Region I, this procedure was given up and it was assumed that $F_{dB} = 1.1F_0''$. Such an assumption is tolerable because the value of F_{dB} is not crucial at all (similarly, the value of F_B is not crucial). However, the values of λ_d and ν_d were based on the constraints $\dot{\phi}_{p(I)} = \dot{\phi}_{p(II)}$ and $\dot{\phi}'_{p(I)} = \dot{\phi}'_{p(II)}$ at $F = F_{dB}$.

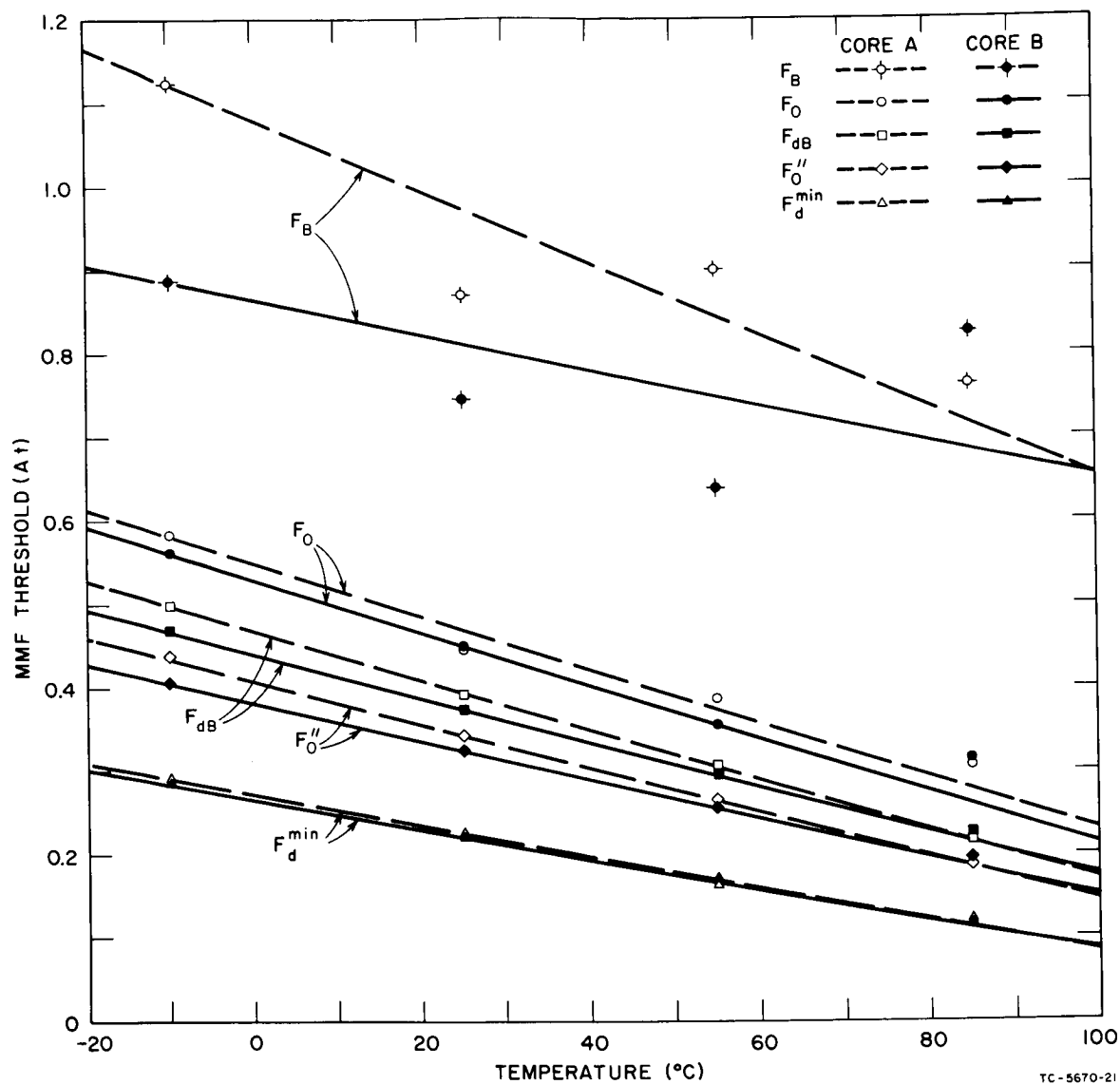
The resulting values of the parameters are used to compute $\dot{\phi}_p$ vs. the F values used in the experiment. The computer output includes the values of the parameters determined at each iteration, and also a table of F , $\dot{\phi}_{p,exp}$, $\dot{\phi}_{p,comp}$, and the percentage error $[1 - (\dot{\phi}_{p,comp}/\dot{\phi}_{p,exp})] \cdot 100$.

iv. Results

A comparison between computed and experimental $\dot{\phi}_p(F)$ of Core A at $T = -10^\circ\text{C}$, 25°C , 55°C , and 85°C is made in Fig. 38(a). The computed $\dot{\phi}_p(F)$ curve of Core B is not shown because it is too close to that of Core A to be distinguishable graphically.

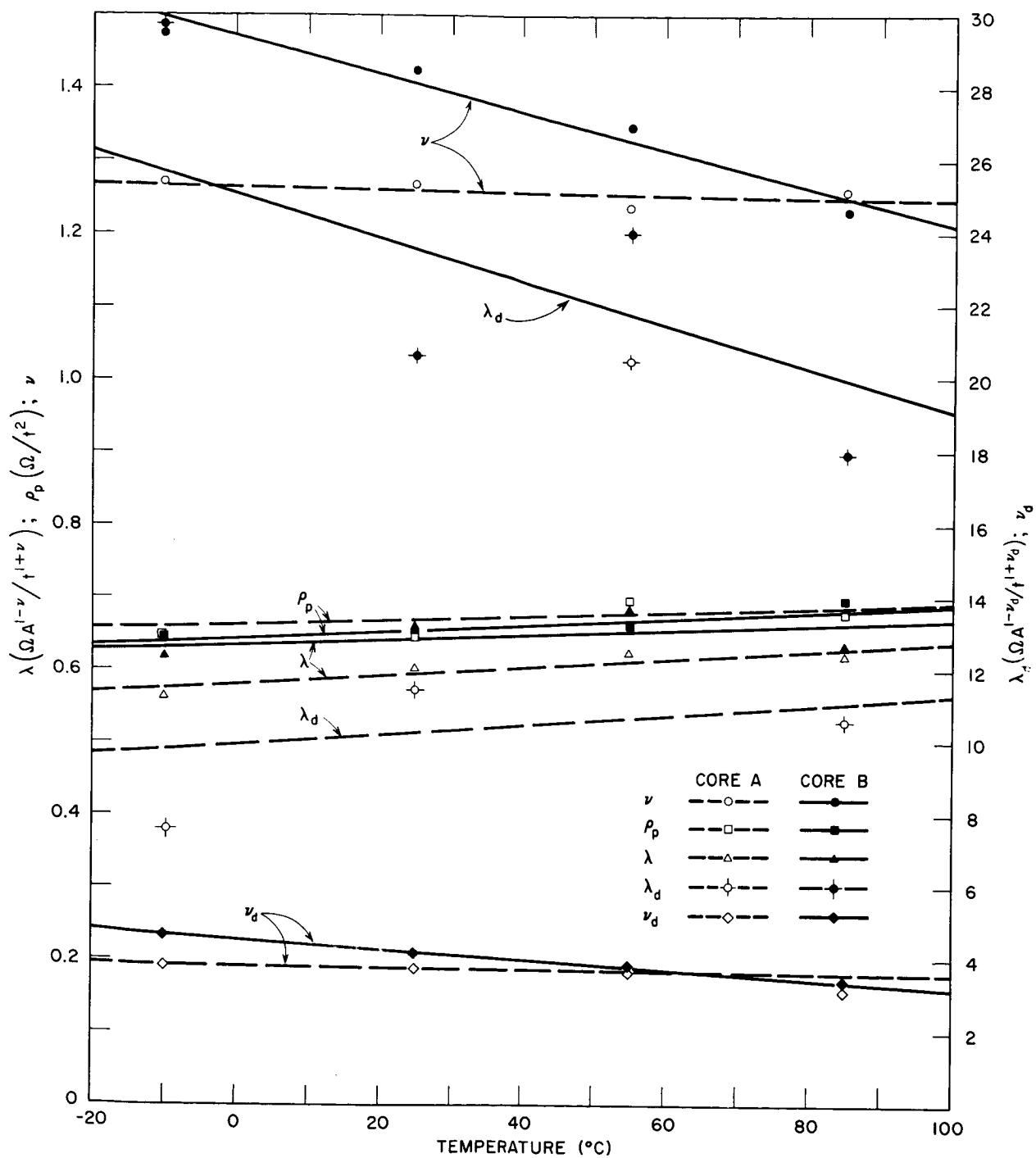
The linear scale in Fig. 38(a) prohibits a meaningful resolution for the experimental and the computed $\dot{\phi}_p(F)$ at low F values. In order to increase this resolution, the experimental $\dot{\phi}_p(F)$ of Cores A and B and the computed $\dot{\phi}_p(F)$ of Core A are redrawn in Fig. 38(b) using a semilog scale.

The threshold parameters F_d^{min} , F_0'' , F_{dB} , F_0 , and F_B of Cores A and B are plotted vs. temperature in Fig. 39(a). Except for the plot of F_B , these plots are close to each other. The rest of the dynamic parameters of Cores A and B are plotted vs. temperature in Fig. 39(b). These plots are very close for ν_d and ρ_p , are close enough for ν and λ , but have a very poor uniformity for λ_d .



(a) MMF-THRESHOLD PARAMETERS

FIG. 39 $\dot{\phi}_p(F)$ PARAMETERS vs. TEMPERATURE. Core Type - Lockheed 100SC1.



(b) PARAMETERS ν_d , λ_d , ν , λ , AND ρ_p

TC-5670-22

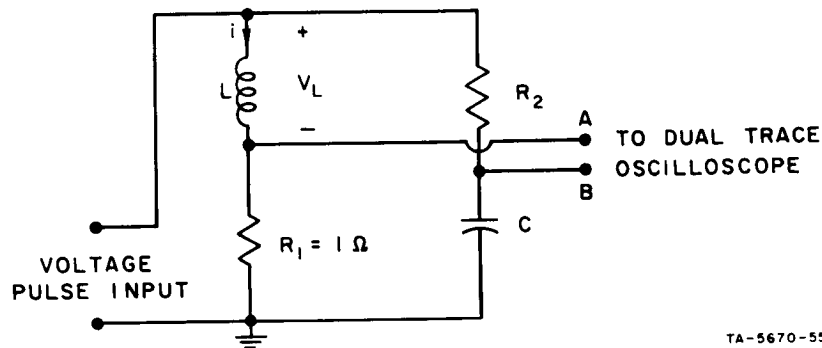
FIG. 39 Concluded

2. Inductor Parameters

Inductors $L_{(0)}$, $L_{(1)}$, and $L_{(2)}$ (see Fig. 25) were tested in order to determine their parameters.

a. Experiment

The circuit for measuring the parameters of Inductor L is shown in Fig. 40. A one-ohm resistance R_1 was added in series with L for measurement of the current i through L . The flux linkage $\psi = \int V_L dt$, where V_L is the voltage across L , was measured by means of the R_2 - C integrator.



TA-5670-55

FIG. 40 A CIRCUIT FOR MEASUREMENT OF THE PARAMETERS OF A NONLINEAR INDUCTOR

Using a dual-trace oscilloscope (Tektronix Model 541 with Type CA plug-in unit), the waveforms $i(t)$ and $\psi(t)$ were superimposed and photographed. Such oscillograms were obtained for each of the three inductors at $T = -10^\circ\text{C}$, 25°C , 55°C , and 85°C .

b. Measured Data

Typical $i(t)$ and $\psi(t)$ oscillograms [for Inductor $L_{(1)}$ at $T = 25^\circ\text{C}$] are shown in Fig. 41.

The values of $i(t)$ and $\psi(t)$ were read from each oscillogram at fixed time intervals on an OSCAR Model-J Machine. The data were punched on cards.

c. Computation

Appendix D gives a computer program for least-mean-square curve fitting of Eq. (83) to the experimental ψ vs. i . Each data point was corrected for the voltage across the one-ohm measuring resistance and for the integrator decay. The computer output includes the values of ψ_{sat} , I_{con} , and L_0 determined at each iteration, and a table containing the experimental and computed ψ and the incremental inductance

$$L = \frac{\Delta\psi}{\Delta i} \quad (111)$$

d. Results

Machine-plotted results of measured and computed incremental inductance L vs. current i for Inductors $L_{(0)}$, $L_{(1)}$, and $L_{(2)}$ at $T = -10^\circ\text{C}$, 25°C , 55°C , and 85°C are shown in Fig. 42. The dispersion of the experimental data is primarily due to inaccuracy in data reading.

Plots of the parameters ψ_{sat} , L_0 , and I_{con} vs. temperature for the three tested inductors are shown in Fig. 43. Whereas ψ_{sat} and I_{con} drop slightly with temperature, L_0 remains essentially constant as the temperature varies.

3. Diode Parameters

a. Forward Static Parameters

i. Experiment

The forward voltage-current characteristics of a diode are determined simply by measuring the current through and the voltage across the conducting diode. Pulses, rather than direct current, must be applied in order to prevent the generation of excessive heat at the high current levels.

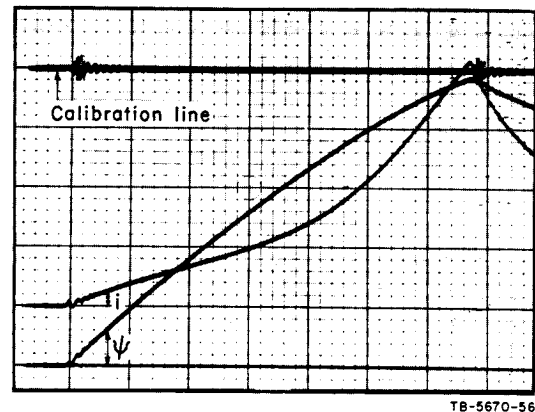


FIG. 41 EXPERIMENTAL $i(t)$ AND $\psi(t)$ OSCILLOGRAMS OF A NONLINEAR INDUCTOR. i scale = 0.1 A/major div.; ψ scale = 10.26 Vμs/major div.; t scale = 0.5 μs/major div.

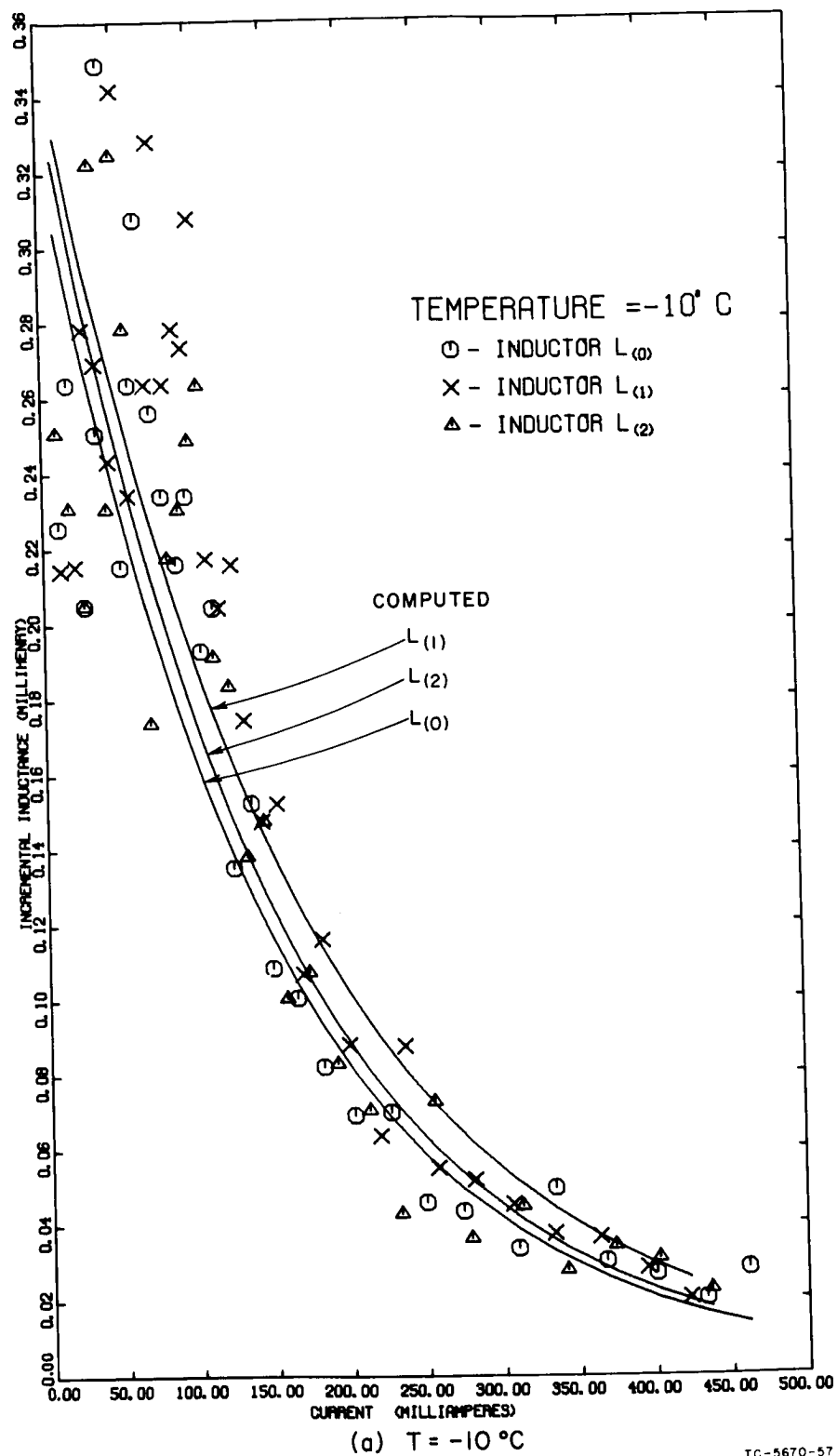


FIG. 42 EXPERIMENTAL AND COMPUTED INCREMENTAL INDUCTANCE vs. CURRENT OF NONLINEAR INDUCTORS

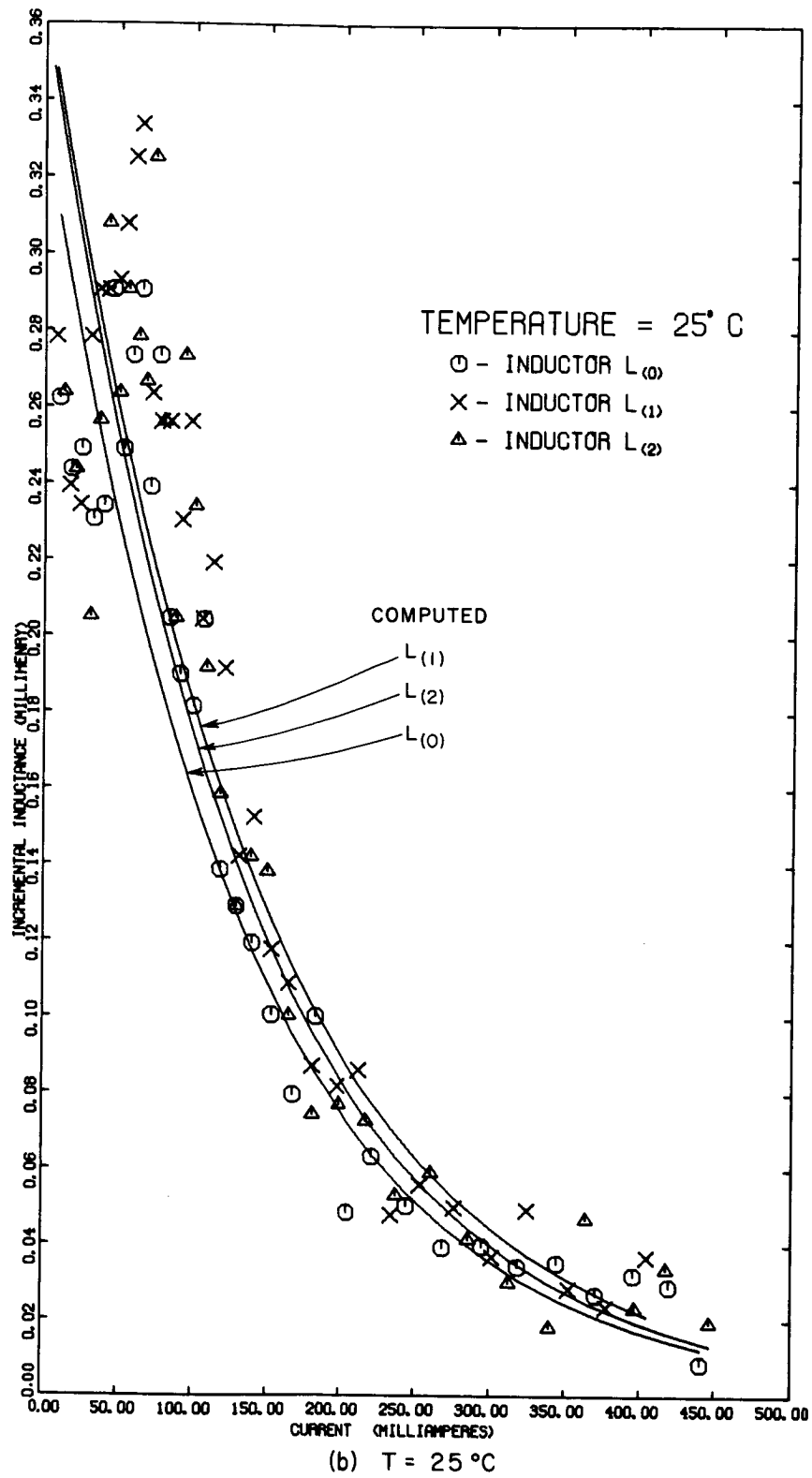
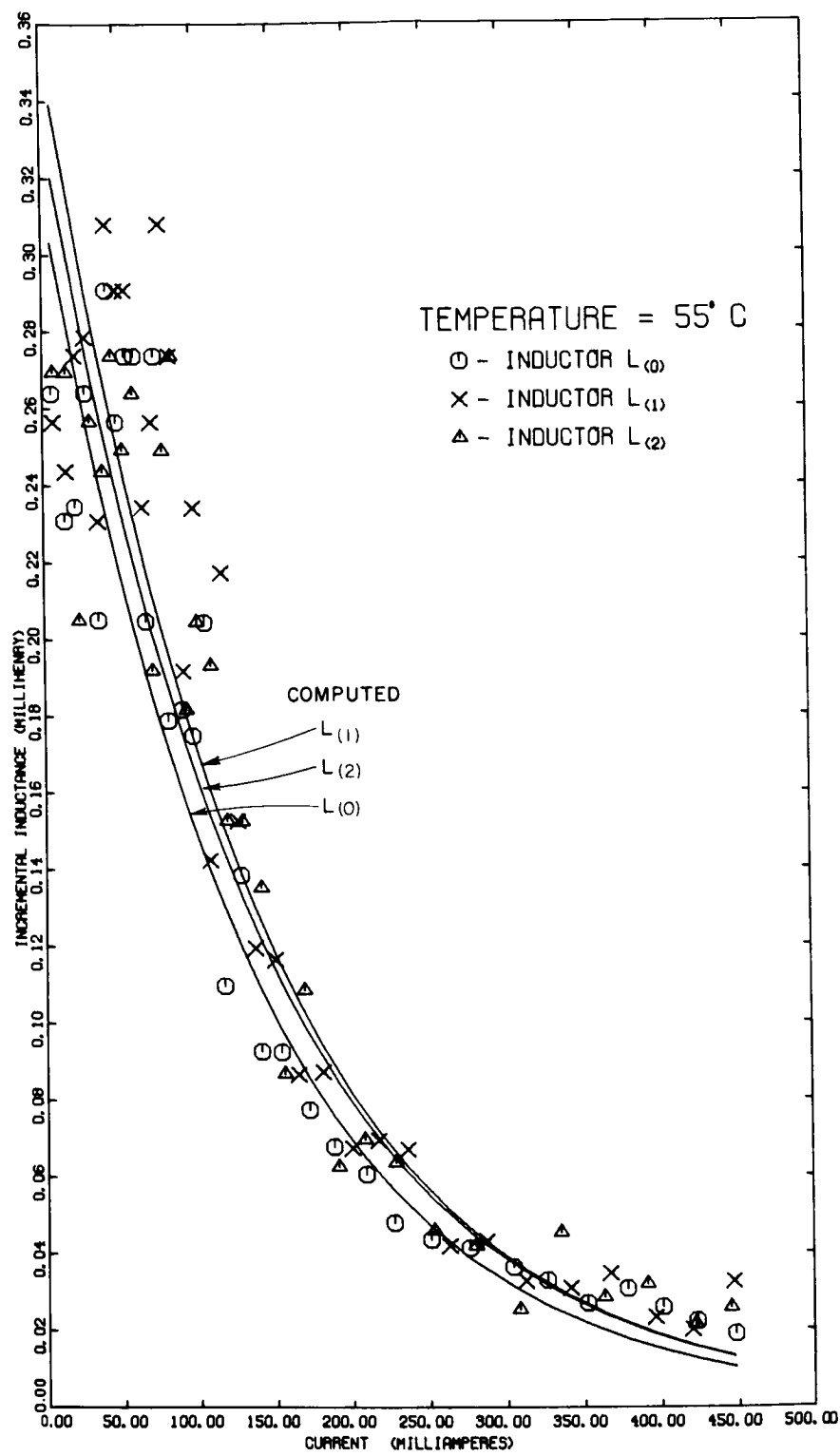
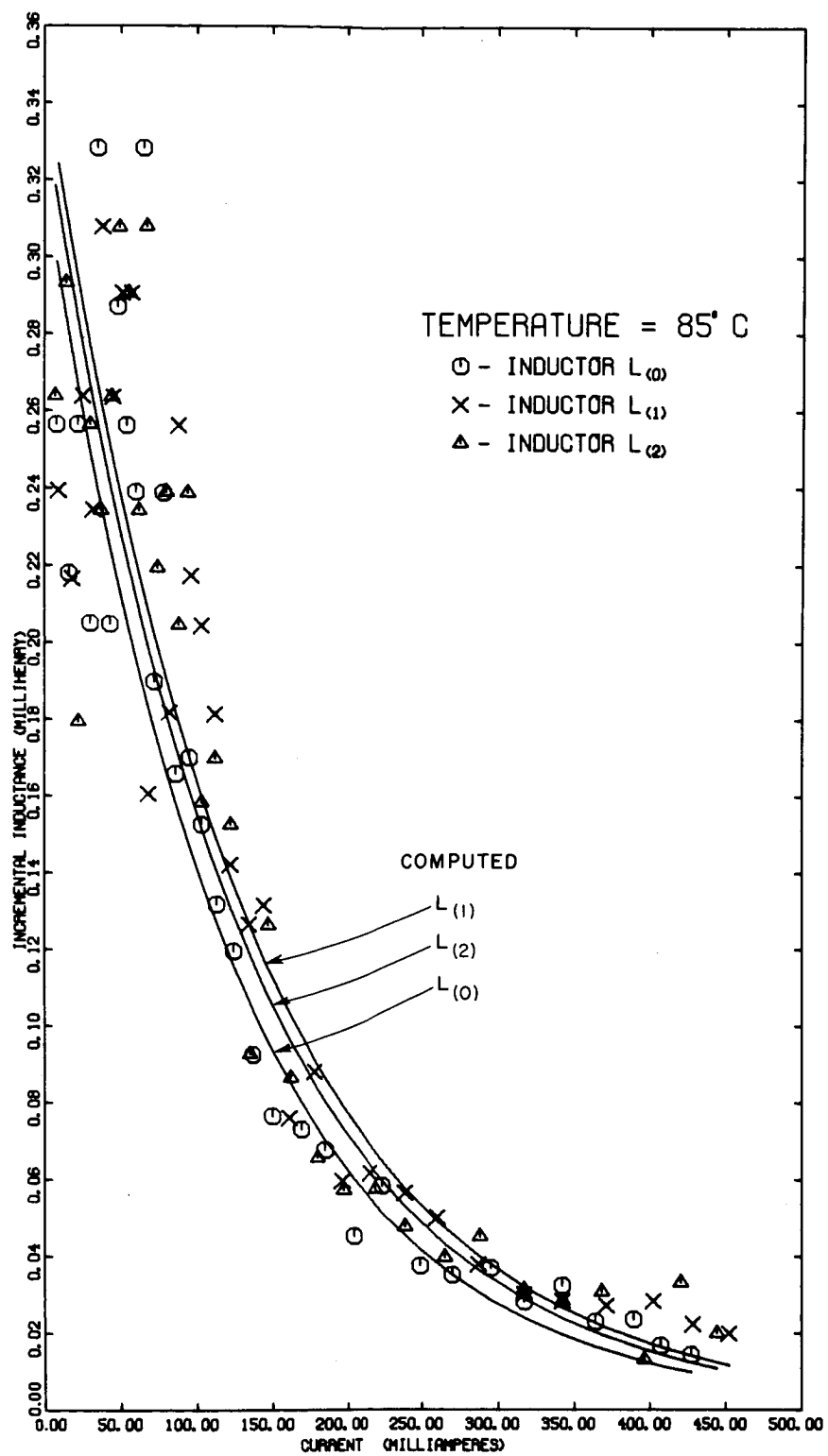


FIG. 42 Continued



(c) $T = 55^{\circ}\text{C}$

FIG. 42 Continued



(d) T = 85 °C

TC-5670-60

FIG. 42 Concluded

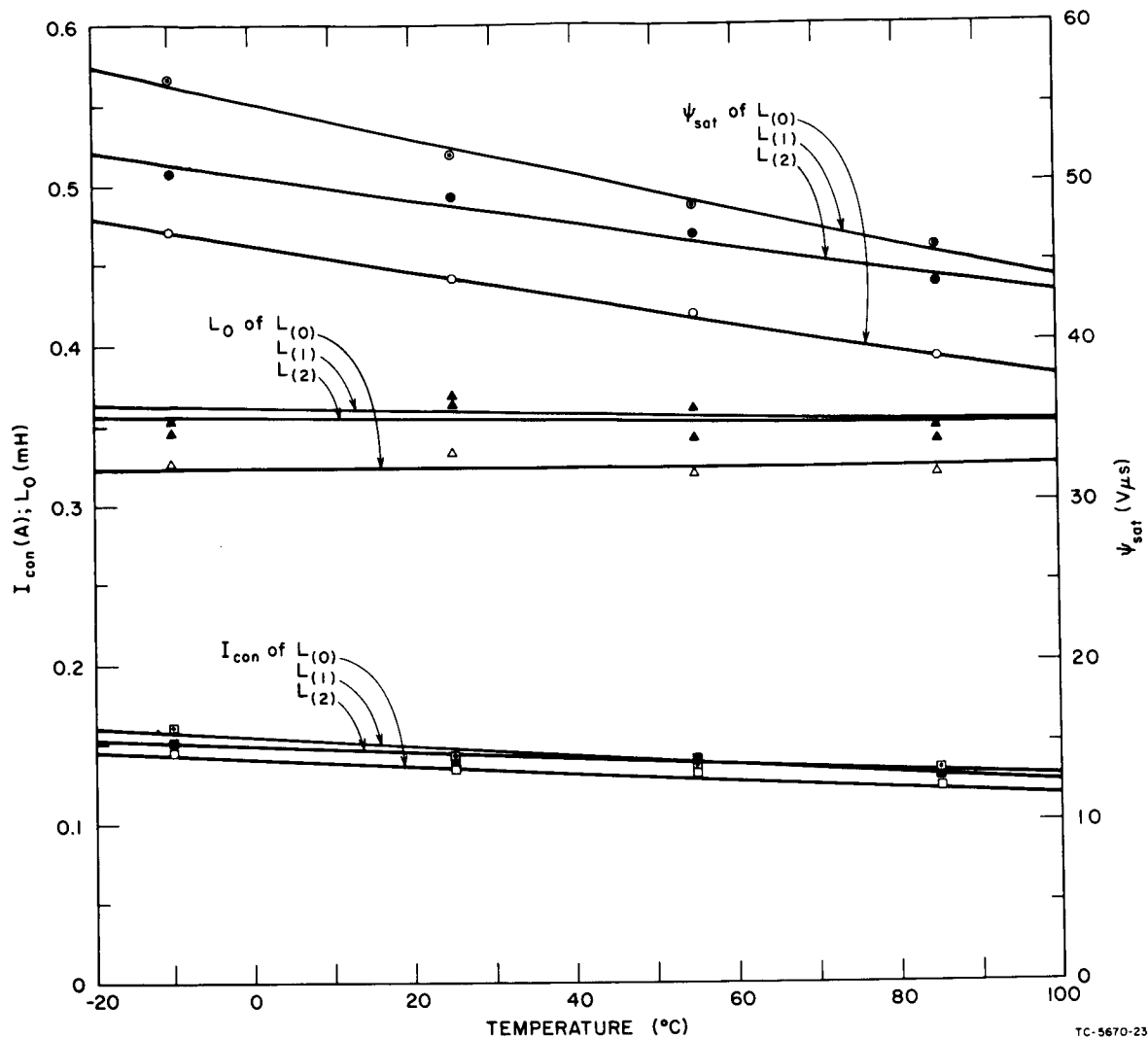
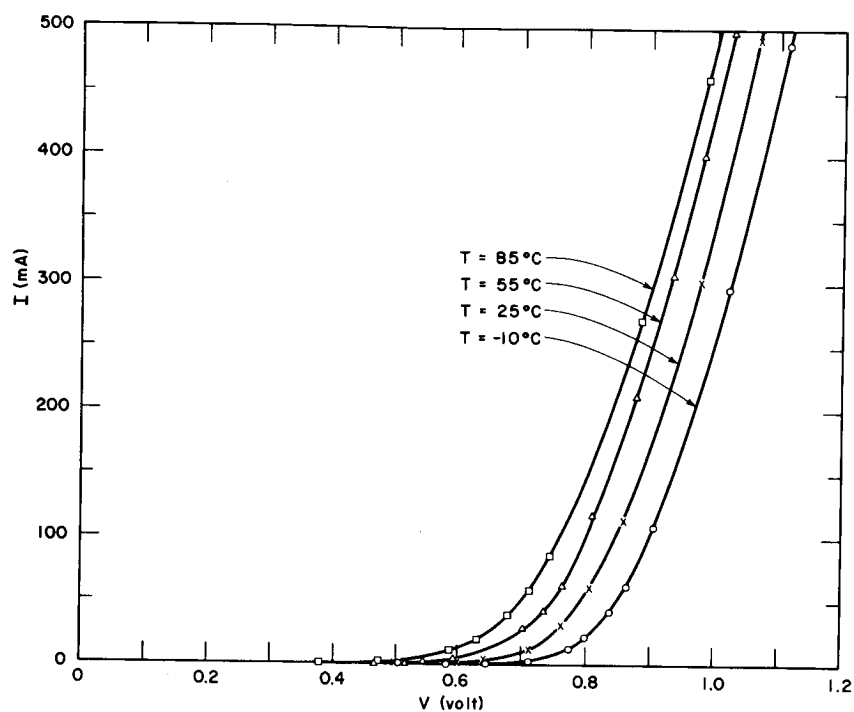


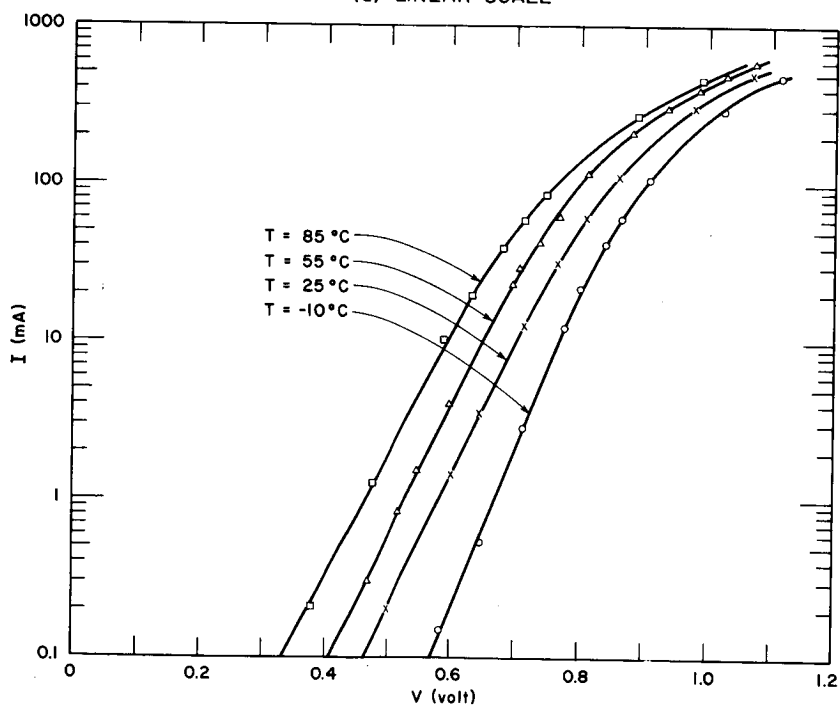
FIG. 43 NONLINEAR-INDUCTOR PARAMETERS vs. TEMPERATURE

ii. Measured Data

Measured forward V - I characteristics of the diode FD643 [Diode $d_{1(2)}$ in Fig. 25] are shown in Fig. 44(a) for $T = -10^\circ\text{C}$, 25°C , 55°C , and 85°C . Since the resolution for low values of current is low, the data are redrawn in Fig. 44(b) on a semilog scale. The solid lines in both parts of Fig. 44 are computed forward V - I characteristics, and will be discussed later.



(a) LINEAR SCALE



(b) SEMILOG SCALE

TD-5670-24

FIG. 44 MEASURED (Data Points) AND COMPUTED (Solid Curve) FORWARD V-I CHARACTERISTICS vs. TEMPERATURE OF AN FD643 DIODE

The measured data were punched on cards. Almost identical results were obtained for Diode $d_{2(2)}$ of Fig. 25.

iii. Computation

Appendix E gives a computer program for least-mean-square curve fitting of Eq. (86) to the measured forward V vs. I data. The computer output includes the parameter values determined at each iteration and a table containing I , experimental V , computed V , and the percentage error $[1 - (V_{\text{comp}}/V_{\text{exp}})] \cdot 100$.

iv. Results

Computed forward V vs. I of the tested diode [FD643 type; Diode $d_{1(2)}$ in Fig. 25] are plotted on linear and semilog scale in Fig. 44 for four temperature values: -10°C , 25°C , 55°C , and 85°C . The agreement between the computed and measured V for given I values is within one percent.

Static forward V - I parameters are plotted vs. temperature in Fig. 45. From the average plot of θ_{m_d} vs. T and from Eq. (85a) it is found that on the average, $m_d = 1.86$.

b. Reverse Static Parameter

i. Experiment

The leakage current V/R_{ℓ_d} was measured by varying a reverse-biased V and measuring I with a picoammeter (Keithley, Model 410).

ii. Measured Data

A typical reverse V - I characteristic of Diode $d_{1(2)}$ at $T = 25^\circ\text{C}$ is shown in Fig. 46.

iii. Results

From the slope of the reverse V - I characteristic of Diode $d_{1(2)}$ in Fig. 46 it is concluded that $R_{\ell_d} = 6.05 \cdot 10^9 \Omega$ at $T = 25^\circ\text{C}$. Values of R_{ℓ_d} at $T = -10^\circ\text{C}$ and $T = 85^\circ\text{C}$ were obtained in a similar way. A plot of R_{ℓ_d} vs. temperature using a semilog scale is a straight line, as shown in Fig. 47. Similar plots for R_{ℓ_e} and R_{ℓ_c} of a transistor will be discussed later.

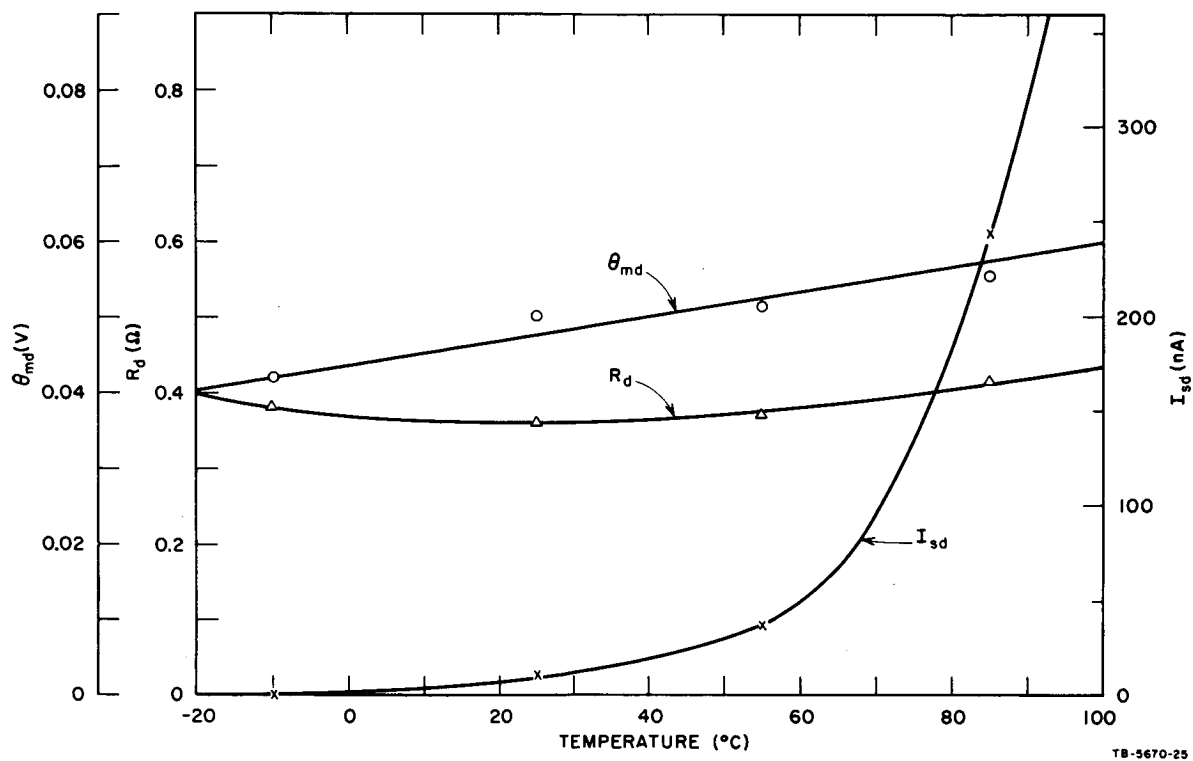


FIG. 45 STATIC FORWARD V-I PARAMETERS vs. TEMPERATURE OF AN FD643 DIODE

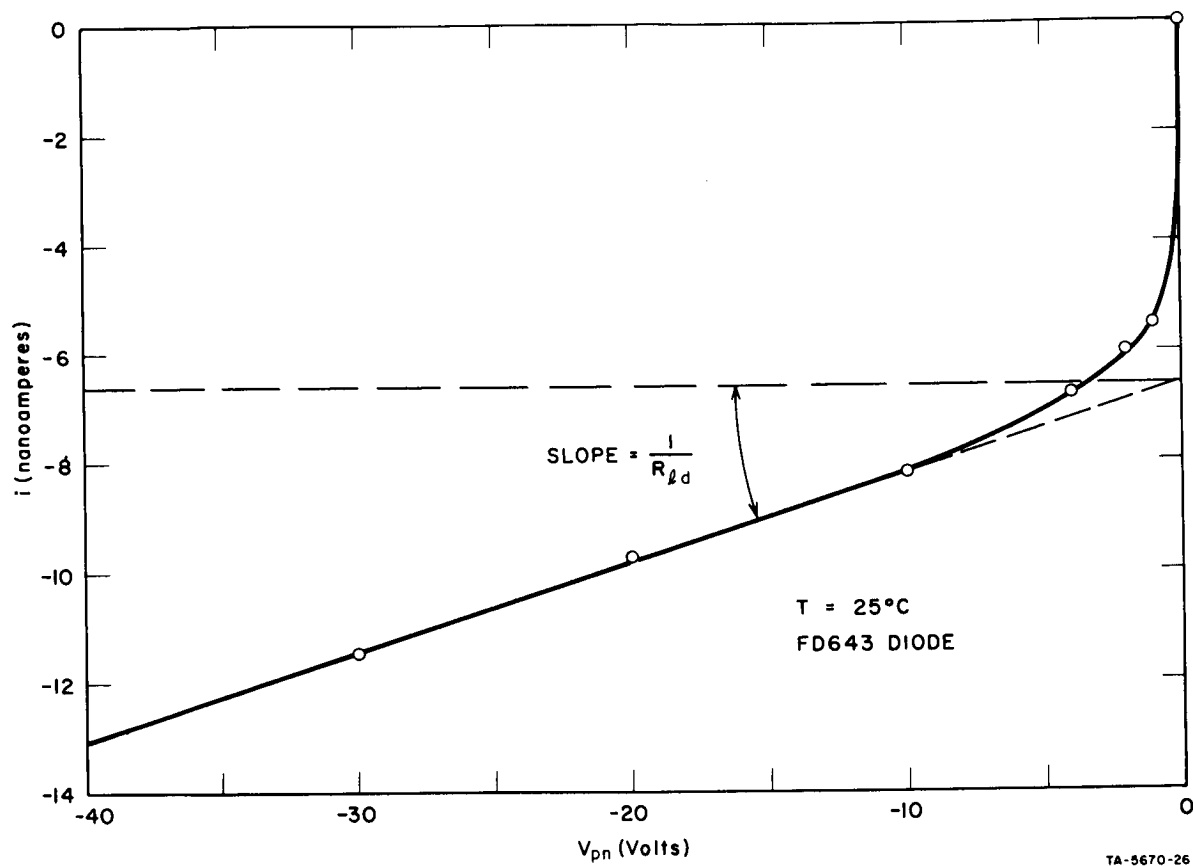


FIG. 46 REVERSE CHARACTERISTIC OF AN FD643 DIODE

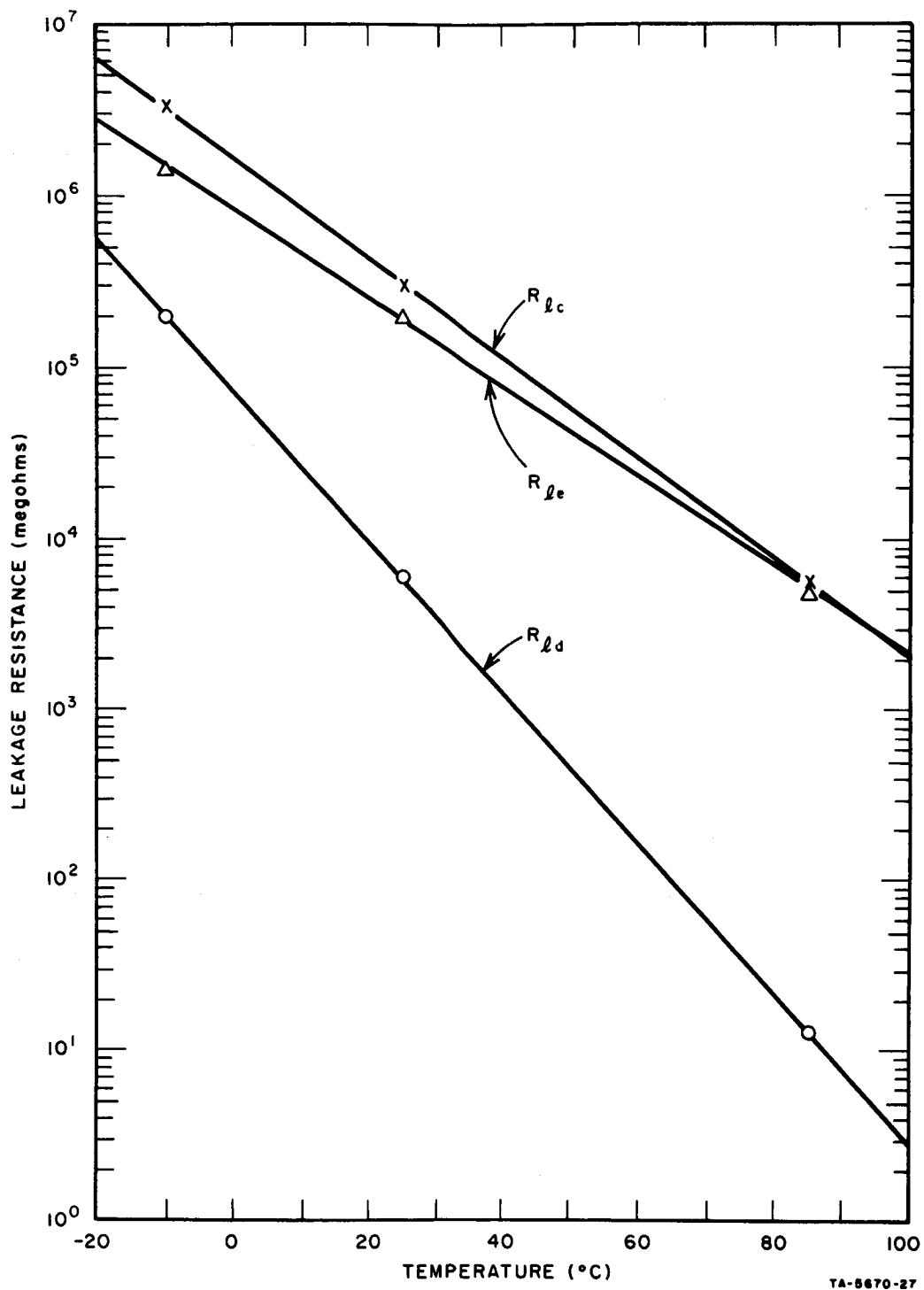


FIG. 47 LEAKAGE RESISTANCES R_{ld} OF AN FD643 DIODE AND R_{le} AND R_{lc} OF A 2N956 TRANSISTOR vs. TEMPERATURE

c. Dynamic Parameters

i. Experiment

The experiment for measuring the junction-capacitance C_{jd} vs. reverse-bias voltage V , and the diffusion-capacitance coefficient, k_d , is the same as the one for base-emitter or base-collector junction of a transistor; it is described in Sec. II-D-4-b, p. 127.

ii. Measured Data

Measured C_{jd} vs. reverse-biased V could not be fit to Eq. (88). The value of C_{j0d} was approximately 1.5 pF. As C_{jd} is decreased below 1 pF, the stray capacitance is of the same order of magnitude as C_{jd} . This may explain why Eq. (88) could not be fit to the experimental data.

The diffusion-capacitance constant k_d was not measured; the reason is given below.

iii. Results

The value of C_{jd} was found to be of the order of 1 pF. Inclusion of such a low value of capacitance in the diode model may do more harm than good. If $V_d < 0$ and C_{jd} is very small, then \dot{V}_d [Eq. (90)] may become spuriously high and cause a computational divergence. On the other hand, if convergence is reached, C_{jd} is too small to have any appreciable effect. For these reasons it was decided to neglect C_{jd} in the model. For simplicity and since the diode capacitance is not crucial to the circuit operation, it was decided to neglect the diffusion capacitance C_{dd} as well.

4. Transistor Parameters

The static and dynamic parameters of Transistor $T_{(2)}$ in Fig. 25 (Fairchild, npn transistor Type 2N956) were determined at $T = -10^\circ\text{C}$, 25°C , and 85°C . The experiments and the computation procedures for determination of these parameters are described next.

a. Static Parameters

i. Experiment

The static parameters are I_{se} , θ_{me} , R_e , β_i , and R_{ℓ_e} for the base-emitter junction, and I_{sc} , θ_{mc} , R_c , β_n , and R_{ℓ_c} for the base-collector junction; the base resistance, R_b , is common to both. By reverse biasing one junction, the other junction may be tested as a diode. The measurement associated with determination of the parameters I_s , θ_m , R , and β of each junction may be obtained by forward biasing that junction; however, the current injected into the reverse-biased junction must be accounted for. For measurement of the leakage resistances R_{ℓ_e} and R_{ℓ_c} , both junctions are reverse-biased. Let us examine the relations between voltages and currents in each case separately.

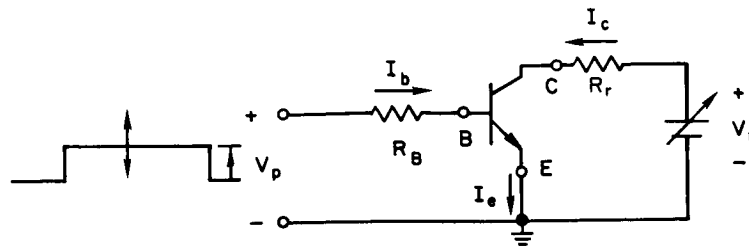
Active-Region Experiment—A measurement circuit for a transistor in the active region (emitter forward-biased, collector reverse-biased) is shown in Fig. 48(a). Capital letters designate dc values. The base-emitter junction is forward-biased by a voltage pulse of about 100 μ s width and variable amplitude V_p . The use of a pulse, rather than a direct voltage, is to prevent the generation of excessive heat, which will change the parameter values (see the effect of temperature on the static parameters of a diode, Fig. 45). The base-collector junction is reverse-biased by a dc or pulse source, whose amplitude V_r is high enough to keep the collector reverse-biased, yet low enough to avoid excessive heating. External resistances R_b and R_r serve to measure I_b and I_c , respectively.

Since the transistor is in a static state of the active region, the equivalent circuit of Fig. 33 is simplified to the one shown in Fig. 48(b).^{23,24} Following Eq. (91), and since $I_e = I_b + I_c$,

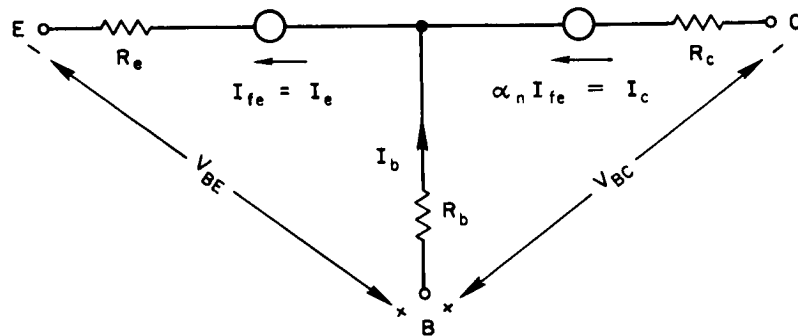
$$V_{BE} = I_b R_b + (I_b + I_c) R_e + \theta_{me} \ln \left(1 + \frac{I_b + I_c}{I_{se}} \right) \quad (112)$$

Also,

$$\beta_n = \frac{I_c}{I_b} \quad (113)$$



(a) MEASUREMENT CIRCUIT



(b) EQUIVALENT CIRCUIT OF AN NPN TRANSISTOR IN THE ACTIVE REGION

TA-5670-61

FIG. 48 DETERMINATION OF BASE-EMITTER FORWARD STATIC CHARACTERISTICS

Inverse-Region Experiment—The measurement circuit is similar to the one in Fig. 48(a), except that the functions of the emitter and collector are interchanged: R_r is in series with the emitter, the emitter is reverse-biased by V_r , and the collector is forward-biased by the voltage pulse of amplitude V_p . The transistor is in a static state of the inverse region. The equivalent circuit is identical with the one in Fig. 48(b), except that $I_c = -I_{fc}$ and $I_e = -\alpha_i I_{fc}$. Following Eq. (98), and since $I_{fc} = -I_c = I_b - I_e$,

$$V_{BC} = I_b R_b + (I_b - I_e) R_c + \theta_{mc} \ln \left(1 + \frac{I_b - I_e}{I_{sc}} \right) \quad (114)$$

It is likely that $I_b R_b \gg |I_e| R_c$; if this is the case, then

$$V_{BC} \approx I_b (R_b + R_c) + \theta_{mc} \ln \left(1 + \frac{I_b - I_e}{I_{sc}} \right) \quad (115)$$

Also,

$$\beta_i = \frac{I_e}{I_b} \quad (116)$$

Cutoff-Region Experiment—In order to determine the leakage resistance R_{ℓ_e} , the collector is reverse-biased by, say, 2 volts, and the emitter is reverse-biased by a direct voltage whose amplitude V is varied, and the reverse current and V are measured. Care must be taken to prevent a thermal runaway. This measurement is repeated with the emitter and collector interchanging function in order to determine R_{ℓ_c} .

ii. Data Measurement

$V_{BE}(I_b, I_c)$ Data—Using the measurement circuit in Fig. 48(a), V_r was adjusted to keep $V_{CB} = 2$ volts. Varying the amplitude V_p of the voltage pulse, the voltages V_p , V_{BE} , and V_{CE} were measured. Given V_p , V_r , V_{BE} , V_{CE} , R_B , and R_r , the base and collector currents can be determined from the relations

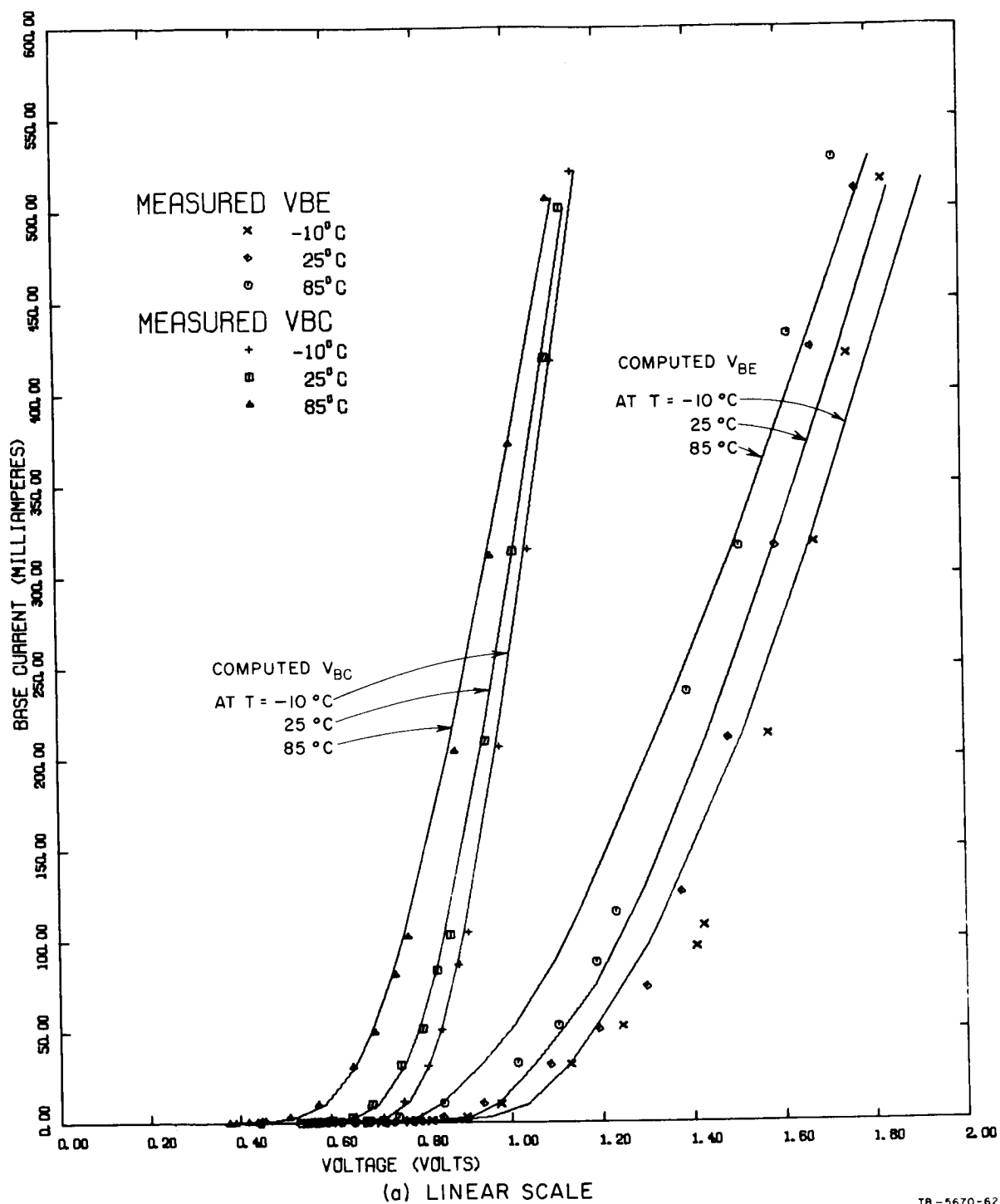
$$I_b = \frac{V_p - V_{BE}}{R_B} \quad (117)$$

and

$$I_c = \frac{V_r - V_{CE}}{R_r} \quad (118)$$

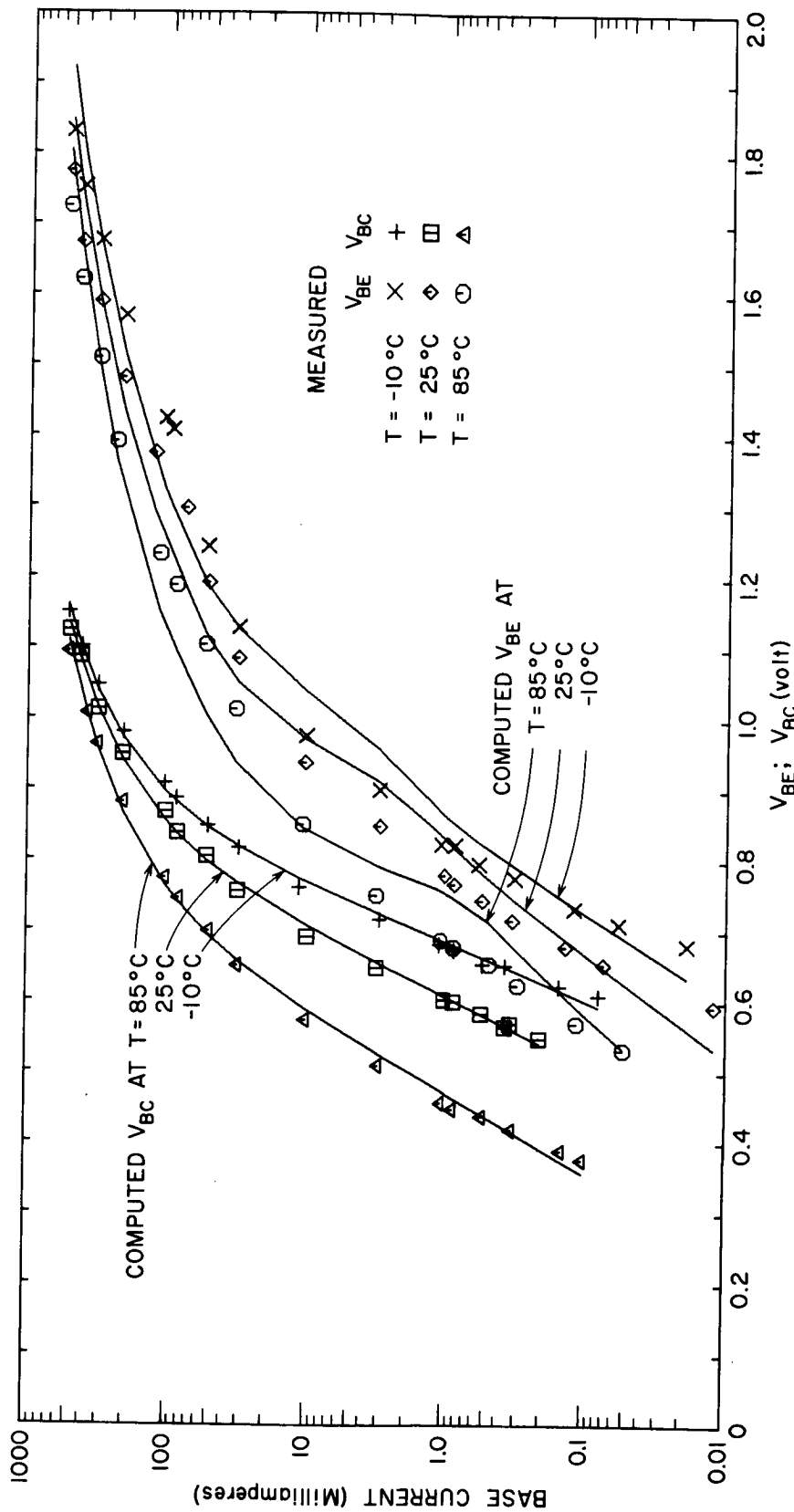
The data of V_{BE} vs. I_b and I_c will be curve-fitted by Eq. (112) in order to determine R_b , R_c , θ_{mc} , and I_{sc} . The data of I_b and I_c will also be used to determine β_n vs. I_c , Eq. (113).

Measured I_b vs. V_{BE} at $T = -10^\circ\text{C}$, 25°C , and 85°C are shown in Fig. 49(a) using a linear scale, and in Fig. 49(b) using a semilog scale. The computed solid lines will be discussed later.



TB-5670-62

FIG. 49 MEASURED AND COMPUTED BASE CURRENT vs. BASE-EMITTER AND BASE-COLLECTOR VOLTAGES OF A 2N956 TRANSISTOR



(b) SEMILOG SCALE

FIG. 49 Concluded

$V_{BC}(I_b, I_c)$ Data—The above experiment for determination of $V_{BE}(I_b, I_c)$ was repeated, except that the functions of the emitter and collector were interchanged. The data of V_{BC} vs. I_b and I_c will be curve-fitted by Eq. (115) in order to determine $R_b + R_c$, θ_{mc} , and I_{sc} . In addition, α_i vs. I_c will be obtained from these data and Eq. (116).

Measured I_b vs. V_{BC} at $T = -10^\circ\text{C}$, 25°C , and 85°C are shown in Fig. 49(a) using a linear scale, and in Fig. 49(b) using a semilog scale. The computed solid line will be discussed later.

iii. Computation

It is desired to determine the static forward parameters by least-mean-square fitting of Eq. (112) to the measured $V_{BE}(I_b, I_c)$ data, and Eq. (114) to the measured $V_{BC}(I_b, I_c)$ data. We have encountered a difficulty with this method: Since $I_b R_b \gg |I_c| R_c$, Eq. (114) is reduced to Eq. (115), and the latter may be used to solve for the sum

$$R_{bc} = R_b + R_c, \quad (119)$$

rather than for R_b and R_c individually. If the value of R_b obtained by fitting Eq. (112) to the measured $V_{BE}(I_b, I_c)$ data is smaller than R_{bc} , then all is well. However, because of fitting error, this was not the case. This difficulty was overcome by assuming that either $R_c = 0$ (Case a) or $R_b = 0$ (Case b), and computing the parameters in the following order:

- (1) By least-mean-square fitting of Eq. (115) to the $V_{BC}(I_b, I_c)$ data, optimum values of R_{bc} , θ_{mc} , and I_{sc} are determined.
- (2) Assuming that $R_c = 0$ (Case a), the values of R_b , θ_{me} , and I_{se} are determined by least-mean-square fitting of Eq. (112) to the $V_{BE}(I_b, I_c)$ data.
- (3) If $R_b \leq R_{bc}$, then the values of R_b , θ_{me} , and I_{se} computed in Step (2) are accepted, and the computation is terminated. Otherwise, it is assumed that $R_c = 0$ and $R_b = R_{bc}$ (Case b), and the values of R_c , θ_{mc} , and I_{sc} are recomputed by least-mean-square fitting of Eq. (112) to the $V_{BE}(I_b, I_c)$ data.

On the basis of these steps, a computer program for determination of θ_{me} , I_{se} , R_e , θ_{mc} , I_{sc} , R_c , and R_b from the measured $V_{BC}(I_b, I_e)$ and $V_{BE}(I_b, I_c)$ data was written, and is given in Appendix F.

The computer output first lists R_{bc} , θ_{mc} , and I_{sc} at each iteration, and a table containing I_e , I_b , β_i , experimental V_{BC} , computed V_{BC} , and the percentage error $[1 - (V_{BC,comp}/V_{BC,exp})] \cdot 100$. This is followed by listing R_b , R_e , θ_{me} , and I_{se} at each iteration, and a table containing I_c , I_b , β_n , experimental V_{BE} , computed V_{BE} , and the percentage error $[1 - (V_{BE,comp}/V_{BE,exp})] \cdot 100$.

iv. Results

Machine-plotted experimental and computed I_b vs. V_{BE} and V_{BC} at $T = -10^\circ\text{C}$, 25°C , and 85°C are compared with measured data in Fig. 49. The agreement for I_b vs. V_{BC} is better than for I_b vs. V_{BE} , probably because the effect of I_c in the latter is more appreciable than the effect of I_e in the former. The computation resulted in $R_c = 0$ (Case b).

The effect of temperature on the forward static parameters of the transistor are shown in Fig. 50.

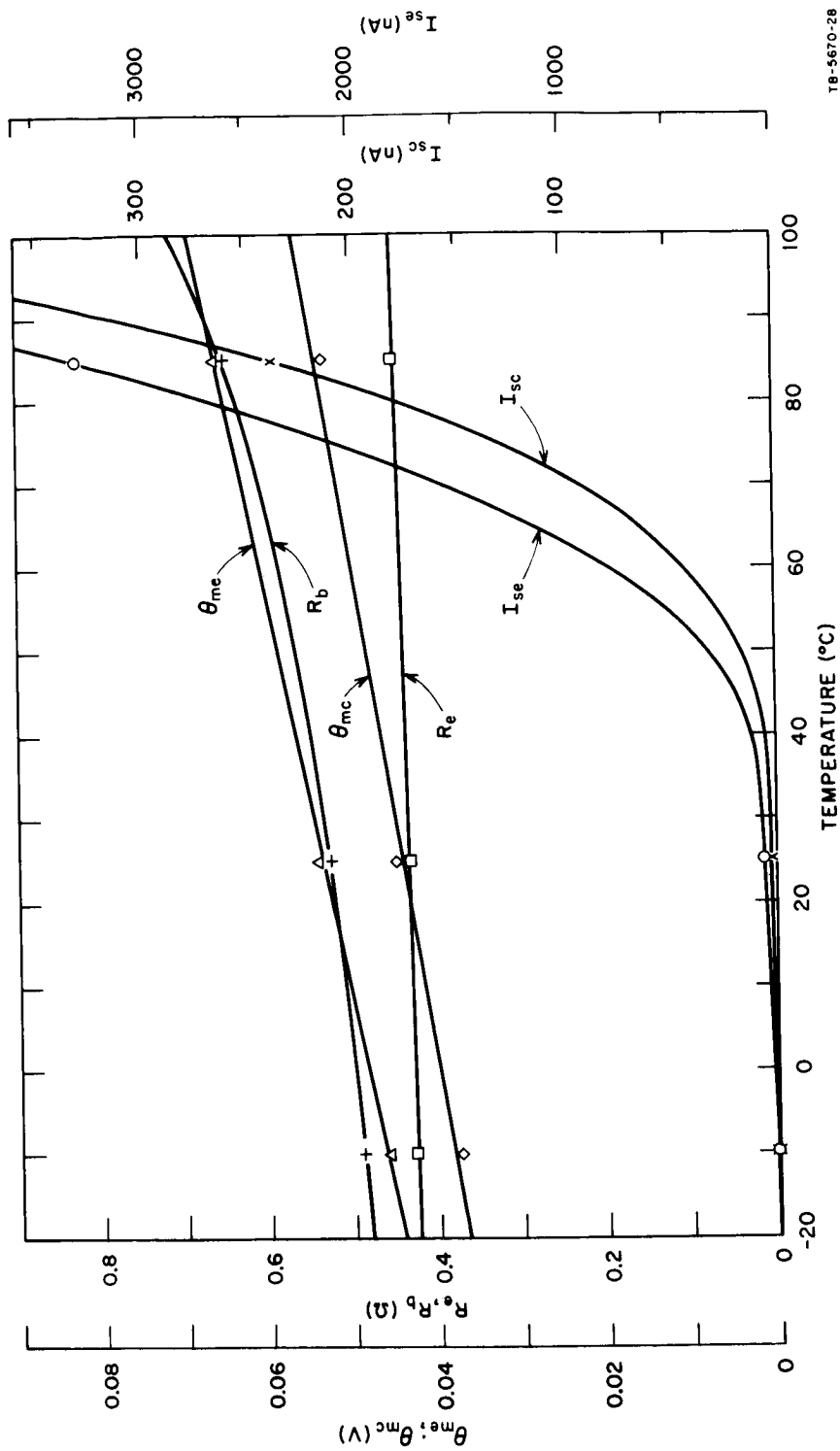
Plots of measured β_n vs. I_c and β_i vs. I_e are shown in Figs. 51 and 52, respectively, for $T = -10^\circ\text{C}$, 25°C , and 85°C .

From the slopes of reverse $V(I)$ data, it was found that $R_{\ell_c} = 3.23 \cdot 10^6$, $3.0 \cdot 10^5$, and $5.48 \cdot 10^3$ megohms and $R_{\ell_e} = 1.43 \cdot 10^6$, $2.0 \cdot 10^5$, and $5.0 \cdot 10^3$ megohms for $T = -10^\circ\text{C}$, 25°C , and 85°C , respectively (see Fig. 47).

b. Dynamic Parameters

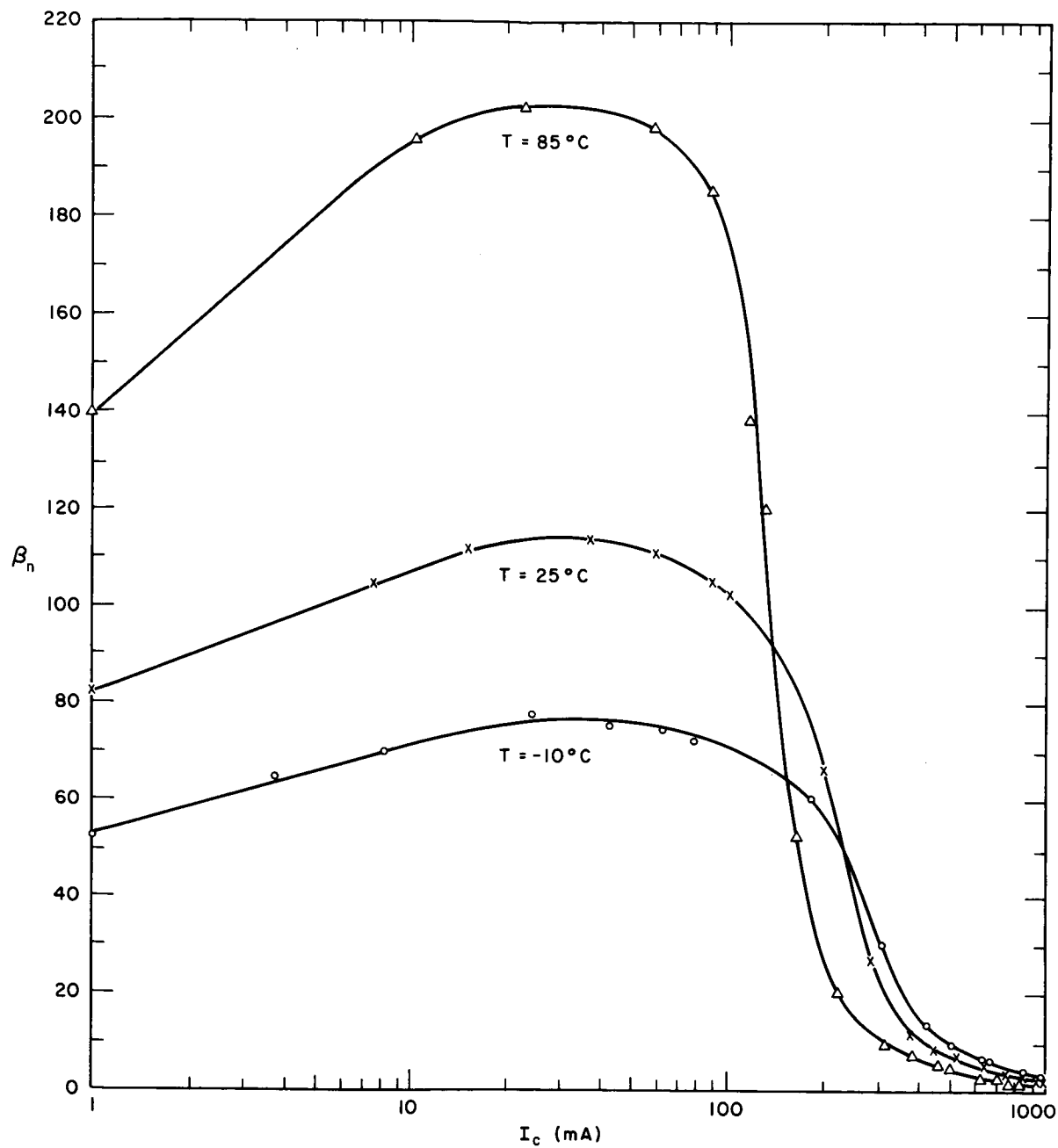
The dynamic parameters are those required to calculate the base-emitter and base-collector diffusion capacitances, C_{de} and C_{dc} , and the junction capacitances, C_{je} and C_{jc} . Referring to Eqs. (93), (94), (100), and (101), these parameters are k_e , C_{j0e} , $V_{\phi e}$, N_e , k_c , C_{j0c} , $V_{\phi c}$, and N_c .

Consider first the base-emitter capacitances. Since C_{de} and C_{je} are in parallel (see Fig. 33), one capacitance can be measured directly only if the other is negligible. Fortunately, each of these conditions can be achieved quite simply. If the emitter junction is



1B-5670-28

FIG. 50 STATIC FORWARD PARAMETERS vs. TEMPERATURE OF A 2N956 TRANSISTOR



TC-5670-29

FIG. 51 MEASURED β_n vs. I_c OF A 2N956 TRANSISTOR

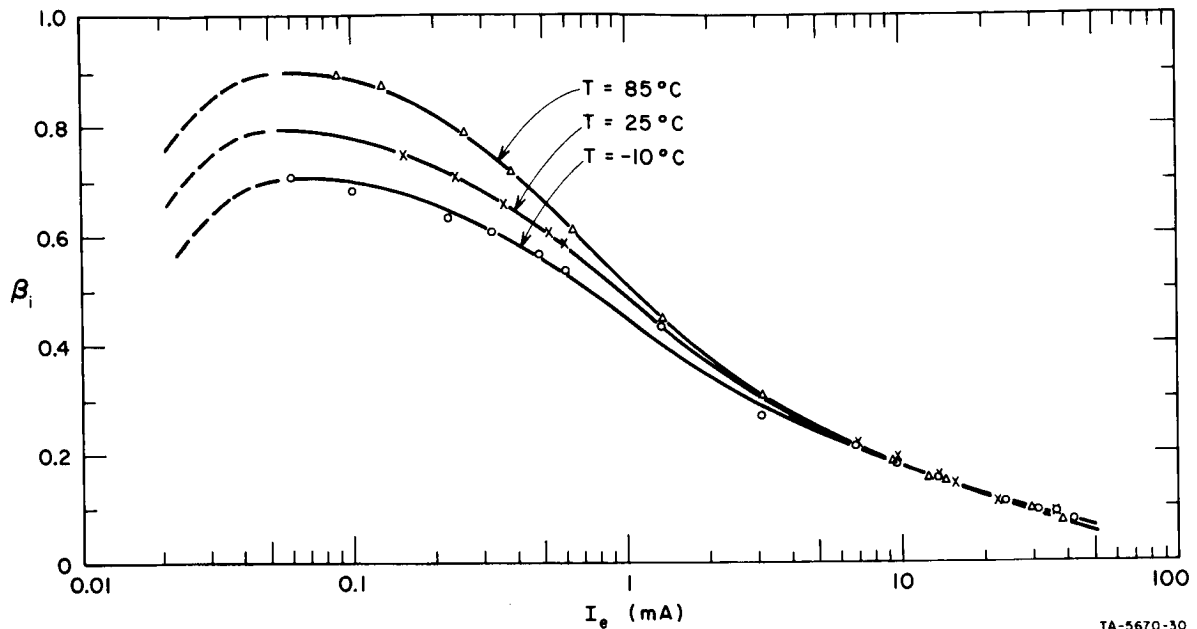


FIG. 52 MEASURED β_i vs. I_e OF A 2N956 TRANSISTOR

reverse biased ($V_e < 0$), then, following Eq. (93), C_{de} is negligible. On the other hand, if the emitter junction is forward biased ($V_e > 0$), then $C_{je} \ll C_{de}$ because the total emitter current is dominated by injected minority-carrier currents^{22,23} (see p. 86). The base-emitter dynamic parameters are thus determined in the following sequence: First, the emitter is reverse biased (cutoff region), and C_{je} is measured vs. V_e . Second, the measured $C_{je}(V_e)$ data are used to determine the values of C_{j0e} , $V_{\phi e}$, and N_e . Third, the emitter is forward biased (active region) at a fixed, positive value of V_e , and the transient waveform of $i_c(t)$ in response to a small step change in base current is recorded. Fourth, k_e is computed on the basis of the effect of the emitter-base capacitance on the time constant of $i_c(t)$.

Similar conditions and a similar method hold for the measurements of C_{je} and C_{de} .

i. Measurement of Reverse-Biased $C_{je}(V_e)$ and $C_{je}(V_e)$

The circuit used for measuring C_{je} vs. V_e is shown in Fig. 53. The collector was kept reverse-biased by a voltage source of amplitude $V_r = 2$ volts. The emitter was kept reverse-biased by a voltage

source of variable amplitude V . The three 1-megohm resistors were added for isolation of the transistor from the biasing voltage sources.

While V was varied, the base-emitter capacitance was measured directly with a capacitance meter (Tektronix Inc., Type 130 L-C Meter). The peak-to-peak signal voltage of the capacitance should be as low as possible. Since $V \approx V_e$ and $C_{je} \gg C_{de}$, the measured data obtained are essentially C_{je} vs. V_e .

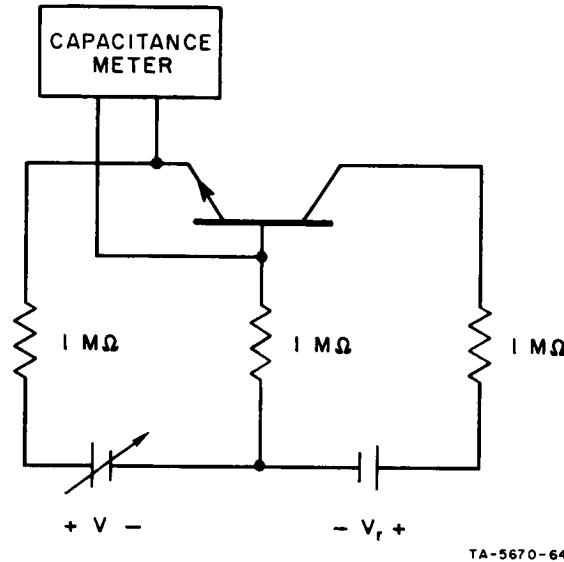


FIG. 53 A CIRCUIT FOR MEASURING C_{je} vs. V_e

The measurement of C_{jc} vs. V_c was performed in the same manner as above, except that functions of the collector and emitter were interchanged.

Measured data of C_{je} vs. V_e and C_{jc} vs. V_c are plotted in Fig. 54 for $T = -10^\circ\text{C}$, 25°C , and 85°C .

ii. Determination of the parameters of C_{je} and C_{jc}

A computer program for least-mean-square curve fitting of Eqs. (94) and (101) to the measured data has not been written yet. Consequently, the parameters of C_{je} and C_{jc} were determined manually.

Determination of C_{j0e} , $V_{\phi e}$, and N_e is described first. The measured C_{je} vs. V_e data at each temperature in Fig. 54 were extrapolated to the $V_e = 0$ axis in order to obtain C_{j0e} . The accuracy of such

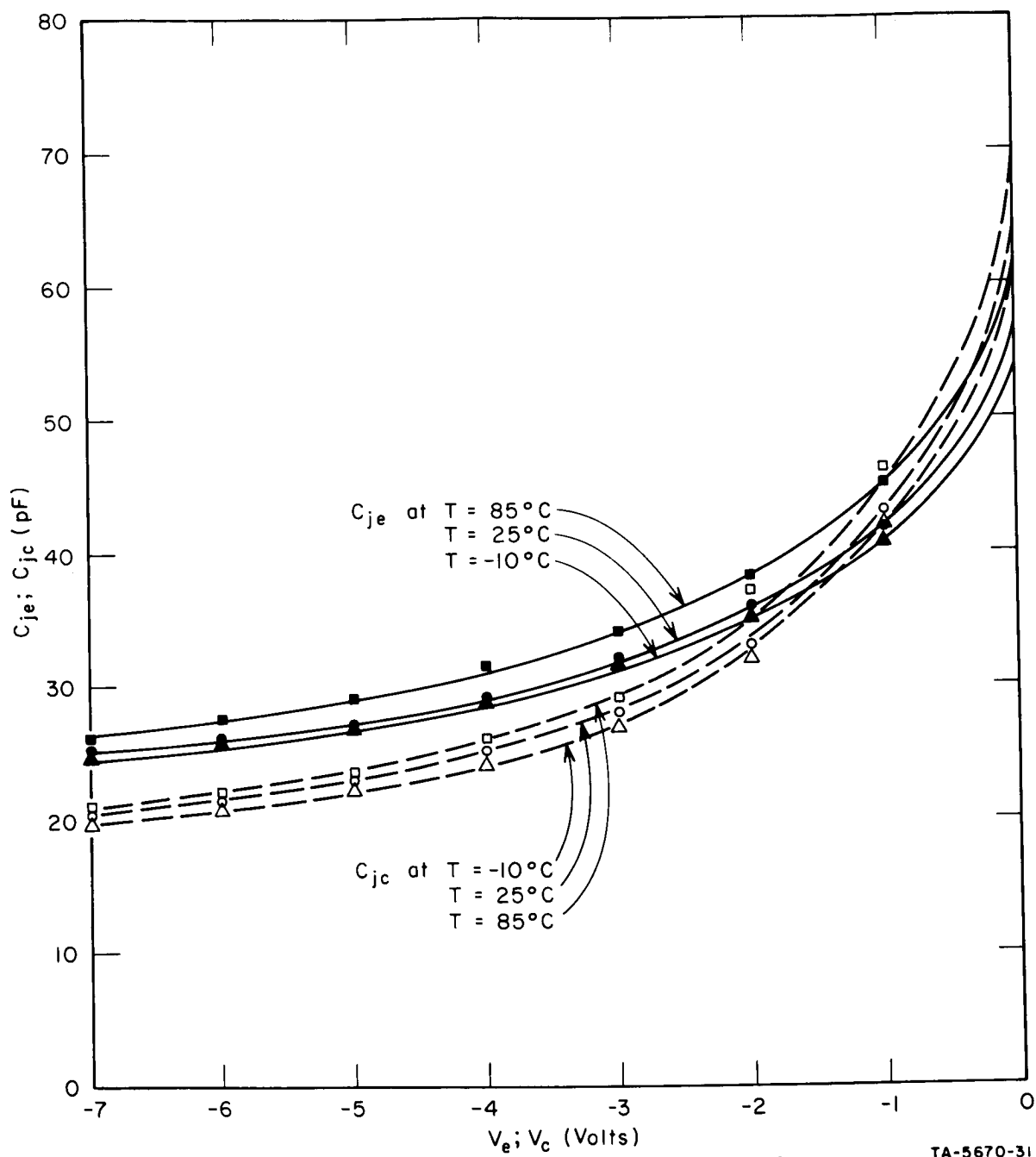


FIG. 54 MEASURED JUNCTION CAPACITANCES vs. VOLTAGE AND TEMPERATURE OF A 2N956 TRANSISTOR

an extrapolation suffers from the nonlinearity of C_{je} vs. V_e . This drawback may be overcome in two ways: first, by using a capacitance meter with a low peak-to-peak signal voltage (e.g., 0.1 volt), thus obtaining reliable data close to the $V_e = 0$ axis, and second, by iterative determination of C_{j0e} , $V_{\phi e}$, and N_e and a linear extrapolation of $(1/C_{je})^{1/N_e}$ vs. V_e .²³

The values of $V_{\phi e}$ and N_e were determined next. Physically, $V_{\phi e}$ increases linearly with temperature T .²² However, for simplicity, $V_{\phi e}$ was assumed to be invariant with T . After trying several values of $V_{\phi e}$ below 1 volt, it was found that reasonable N_e values (between 1/3 and 1/2) were obtained for all temperatures if $V_{\phi e} = 0.6$ volt.

A similar procedure was used to determine C_{j0c} , $V_{\phi c}$, and N_c from the measured C_{jc} vs. V_c data. A value of $V_{\phi c} = 0.7$ volt was found to yield reasonable N_c values for all temperatures.

The resulting values of C_{j0e} , $V_{\phi e}$, N_e , C_{j0c} , $V_{\phi c}$, and N_c vs. temperature are quite linear, as shown in Fig. 55. The inaccuracy of these results is mainly due to the assumption that $V_{\phi e}$ and $V_{\phi c}$ do not vary with T . An alternative way to determine these parameters, which is physically more rigorous, is to assume that N_e and N_c are invariant with T , and to obtain linear increases of $V_{\phi e}$ and $V_{\phi c}$ with T .

iii. Measurement of $i_c(t)$ and $i_e(t)$ time constants

The circuit for measuring the $i_c(t)$ time constant is considered first and is shown in Fig. 56(a). The collector was reverse-biased by a direct voltage of amplitude $V_r = 3$ volts. A rectangular bias base current, I_b , was generated by a voltage-pulse source in series with a high resistance, $R_B = 10$ k Ω . The transistor was thus in the active region. The bias voltage was adjusted so that I_c was equal to the value for which β_n is maximum (i.e., $I_c \approx 40$ mA, Fig. 51). A rectangular current pulse of amplitude ΔI_b much smaller than I_b was superimposed in the middle of the bias base-current pulse. The waveforms of the bias and the incremental base currents and the waveform of the resulting collector current are shown in Fig. 56(b). The effective time constant τ_c associated with the response of $i_c(t)$ to ΔI_b was measured. This was repeated at three temperature values: -10°C , 25°C , and 85°C .

Measurements of τ_e associated with the response of $i_e(t)$ to ΔI_b were performed in the same manner as described above, except that the emitter and the collector interchanged functions.

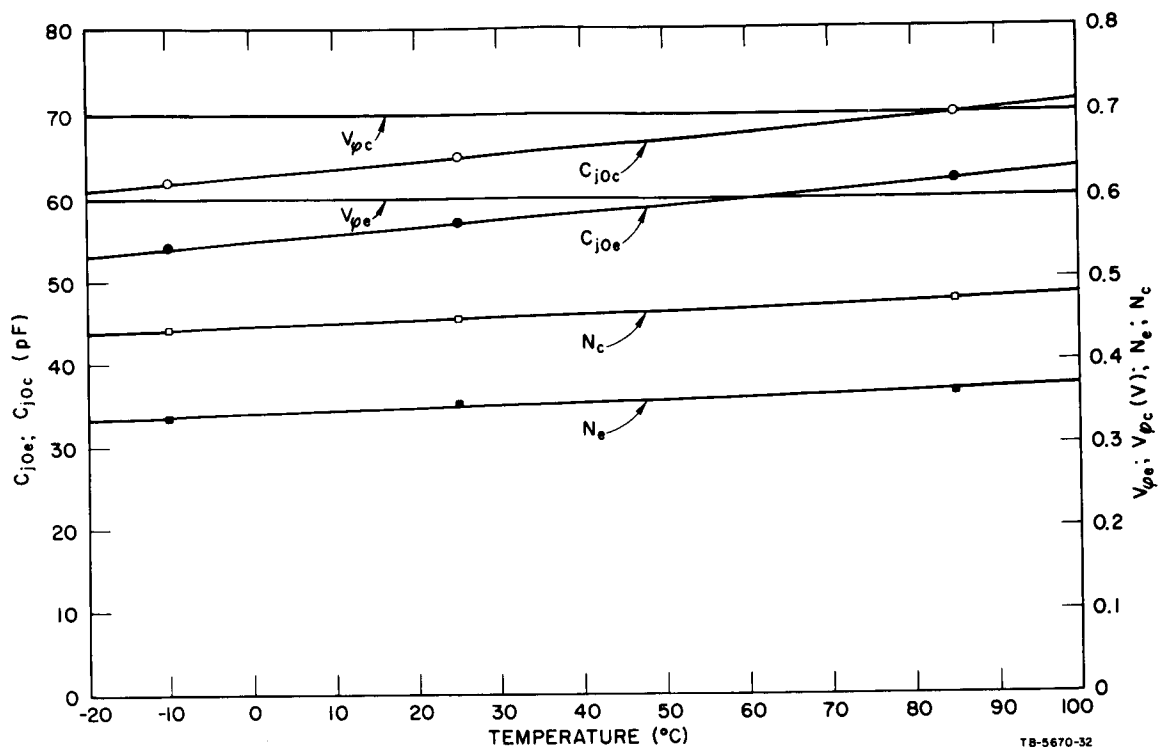


FIG. 55 PARAMETERS OF EMITTER AND COLLECTOR JUNCTION CAPACITANCES vs. TEMPERATURE OF A 2N956 TRANSISTOR

iv. Computation of k_e and k_c

Computation of k_e is discussed first. The equivalent circuit of the measurement circuit in Fig. 56(a) is shown in Fig. 56(c). Those elements in Fig. 33 which have a negligible effect on the transistor behavior in the active region have been omitted in Fig. 56(c).

By inspection of Fig. 56(c), the emitter and collector currents are

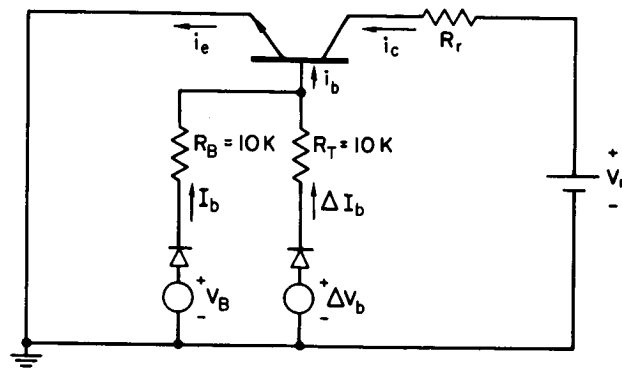
$$i_e = i_{fe} + (C_{de} + C_{je})\dot{V}_e \quad (120)$$

and

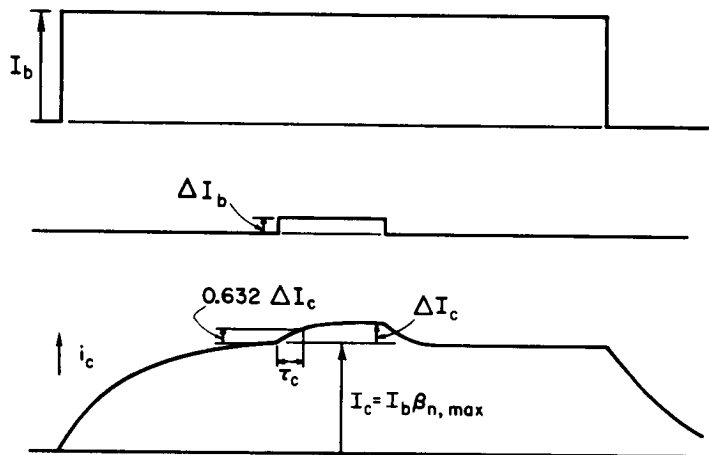
$$i_c = \alpha_n i_{fe} - C_{jc}\dot{V}_c \quad (121)$$

where

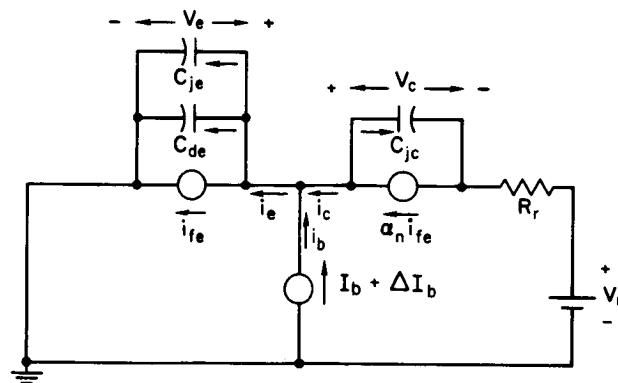
$$i_{fe} = I_{se} \left(e^{V_e / \theta_{ne}} - 1 \right) \quad (122)$$



(a) MEASUREMENT CIRCUIT



(b) BASE AND COLLECTOR CURRENT WAVEFORMS



(c) EQUIVALENT CIRCUIT

TS-5670-65

FIG. 56 A MEASUREMENT CIRCUIT FOR DETERMINATION OF EMITTER DIFFUSION CAPACITANCE

Differentiating Eq. (122) with respect to time and substituting

$$I_{se} e^{V_e / \theta_{me}} = C_{de} / k_e$$

from Eq. (93) gives

$$\dot{V}_e = \frac{\theta_{me} k_e}{C_{de}} \frac{di_{fe}}{dt} \quad (123)$$

Substituting Eq. (123) into Eq. (120) gives

$$i_e = i_{fe} + \left(1 + \frac{C_{je}}{C_{de}}\right) \theta_{me} k_e \frac{di_{fe}}{dt} \quad (124)$$

Since the emitter junction is forward biased ($V_e > 0$), the emitter current is dominated by the minority-carrier currents that are injected across the space-charge layer into the neutral emitter and base regions,²² and we may assume that $C_{je} \ll C_{de}$ (see pp. 127 and 130). The larger V_e is, the more justified is this assumption. Thus, Eq. (124) may be simplified to

$$i_e \approx i_{fe} + k_e \theta_{me} \frac{di_{fe}}{dt} \quad (125)$$

Substitution of Eqs. (121) and (125) into $i_b = i_e - i_c$ gives

$$i_b \approx (1 - \alpha_n) i_{fe} + k_e \theta_{me} \frac{di_{fe}}{dt} + C_{jc} \dot{V}_c \quad (126)$$

By inspection of Fig. 56(a),

$$V_c = i_c R_r - V_r + \Delta V_b - R_T \Delta I_b \quad (127)$$

Hence,

$$\dot{V}_c = R_r \frac{di_c}{dt} \quad (128)$$

and Eq. (121) becomes

$$i_{fe} = \frac{1}{\alpha_n} \left(i_c + R_r C_{jc} \frac{di_c}{dt} \right) \quad (129)$$

Substitution of \dot{V}_c [Eq. (128)], i_{fe} [Eq. (129)], and di_{fe}/dt from Eq. (129) into Eq. (126) yields a solution of $i_c(t)$ which is too complex to be correlated with the experimental $i_c(t)$ waveform. Furthermore, R_r may be made very small by using a current probe in order to observe the $i_c(t)$ waveform. Hence, the effect of the component $C_{jc} \dot{V}_c$ on i_{fe} may be neglected, and we may substitute $i_{fe} \approx i_c/\alpha_n$ and $di_{fe}/dt \approx (di_c/dt)/\alpha_n$ into Eq. (126). By the additional substitution of Eq. (128), Eq. (126) is reduced to

$$i_b \approx \frac{1 - \alpha_n}{\alpha_n} i_c + \left(\frac{k_e \theta_{me}}{\alpha_n} + R_r C_{jc} \right) \frac{di_c}{dt} \quad (130)$$

Initially (when the step ΔI_b is applied), $i_b = I_b$, and so $i_{c(0)} = \beta_n I_b$, where $\beta_n = \alpha_n/(1 - \alpha_n)$. The solution of Eq. (130) is, therefore,

$$i_c \approx \beta_n I_b + \beta_n \Delta I_b (1 - e^{-t/\tau_c}) \quad (131)$$

where

$$\tau_c = \beta_n \left(\frac{k_e \theta_{me}}{\alpha_n} + R_r C_{jc} \right) \quad (132)$$

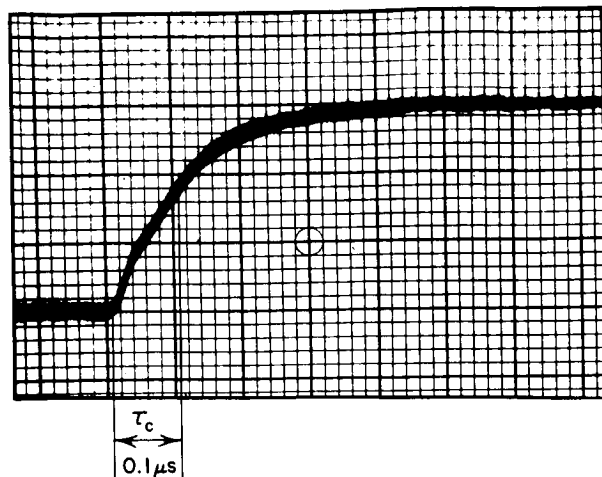
Referring to Fig. 56(b), τ_c was determined experimentally at the I_c value for which β_n is maximum. Hence,

$$\alpha_n = \beta_{n, \max} / (\beta_{n, \max} + 1) \approx 1 \quad ,$$

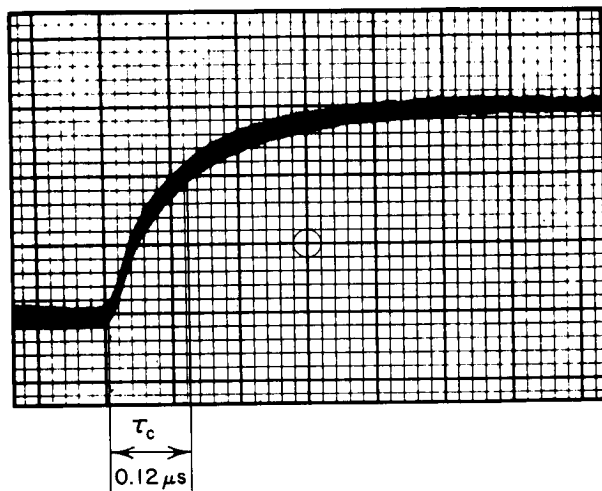
and

$$k_e \approx \left(\frac{\tau_c}{\beta_{n, \max}} - R_r C_{jc} \right) \frac{1}{\theta_{me}} \quad (133)$$

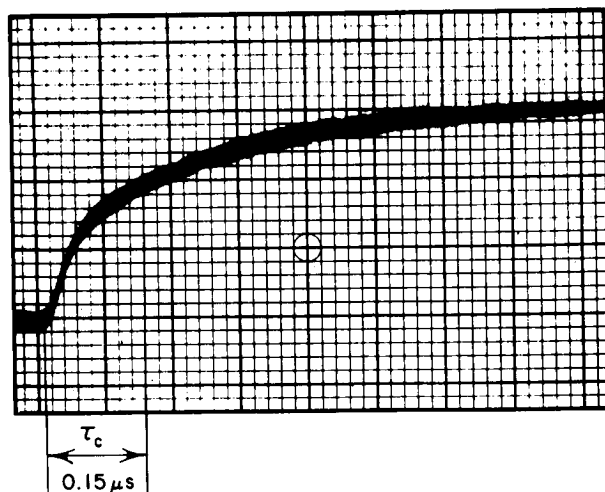
Oscillograms of $i_c(t)$ transient waveforms in response to ΔI_b at $T = -10^\circ\text{C}$, 25°C , and 85°C are shown in Fig. 57. These waveforms are not exactly exponential, since Eq. (131) is only an approximation. At $T = -10^\circ\text{C}$, for example, $\tau_c = 0.1 \mu\text{s}$, $\beta_{n, \max} = 76.5$, $\theta_{me} = 0.0459\text{V}$, and



(a) $T = -10^{\circ}\text{C}$



(b) $T = 25^{\circ}\text{C}$



(c) $T = 85^{\circ}\text{C}$

TD-5670-66

FIG. 57 TRANSIENT WAVEFORMS OF COLLECTOR CURRENT IN RESPONSE TO A SMALL STEP CHANGE IN BASE CURRENT OF A 2N956 TRANSISTOR IN THE ACTIVE REGION. $I_c = 40\text{mA}$; $\Delta I_c = 3\text{mA}$; $R_r \approx 0$; time scale = $0.1\text{ }\mu\text{s}$ /major div.; i_c scale = 1mA /major div.

$C_{j0e} = 54$ pF; hence, following Eq. (133), $k_e \approx 28.5$ nF/A. Similarly, it was found that $k_e = 19.3$ and 13.9 nF/A for $T = 25^\circ\text{C}$ and 85°C , respectively.

Determination of k_c was obtained in the same way as that of k_e , except that emitter and collector functions were interchanged.

Resulting values of k_e and k_c vs. temperature are shown in Fig. 58. In the absence of more than three points for each case, the dashed lines should be considered as rough guesses only. However, it may be concluded from these data that for this 2N956 transistor, k_c is about 6,000 (at $T = -10^\circ\text{C}$) to 12,000 (at $T = 85^\circ\text{C}$) times larger than k_e , and that an increase in temperature causes k_e to decrease much more than k_c .

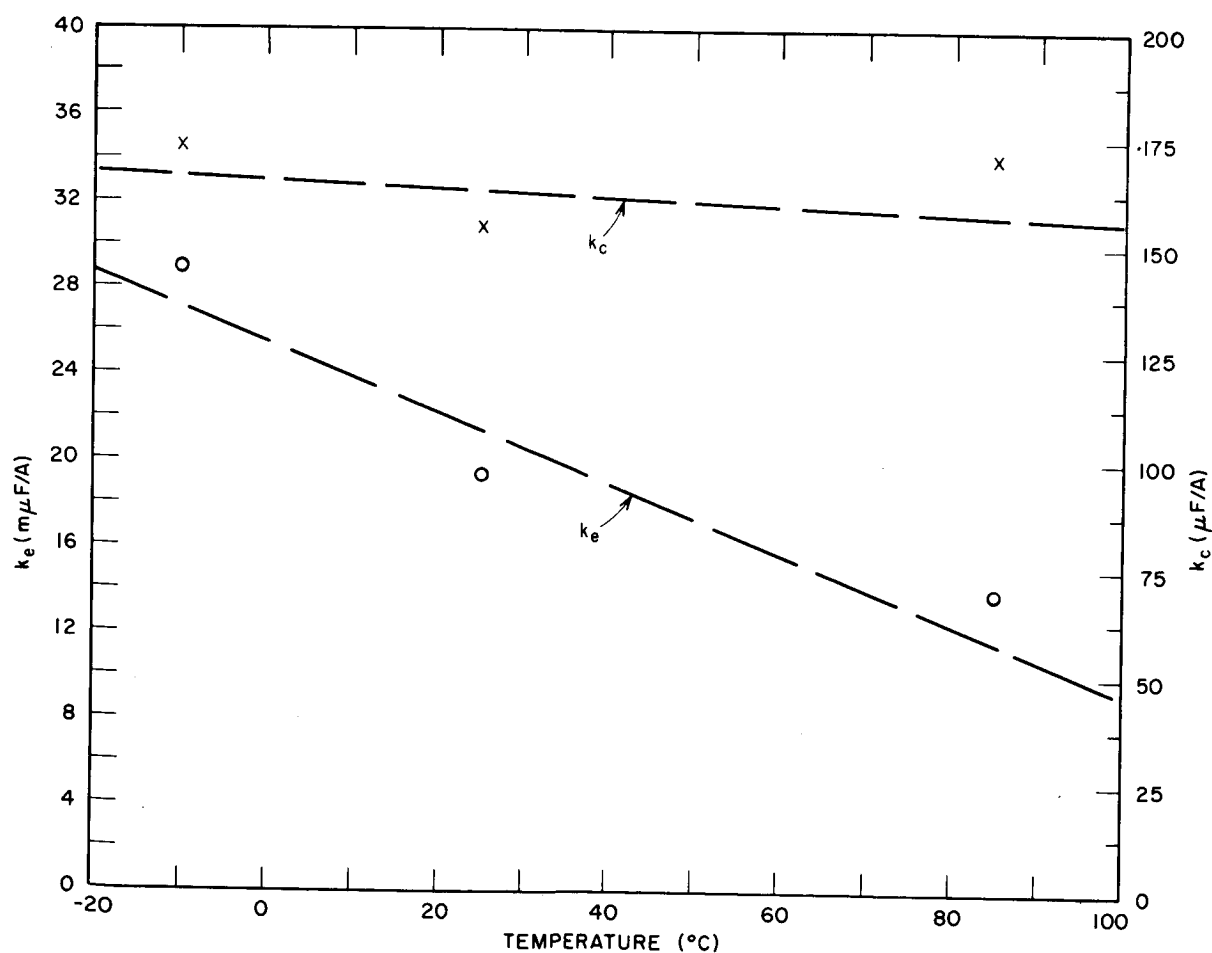


FIG. 58 DIFFUSION-CAPACITANCE PARAMETERS k_e AND k_c vs. TEMPERATURE OF A 2N956 TRANSISTOR

5. Summary

The experiments, the data measurement, and the computation methods associated with determination of the parameter values of the various devices in the binary counter have been described in the preceding sections. The resulting parameter values of the cores, resistors, inductors, diode, and transistor at $T = -10^\circ\text{C}$, 25°C , and 85°C are summarized in Table III. (Cores 1 and 2 were referred to as Cores A and B, respectively, in Sec. II-D-1.) These values will be used in the computer analysis, which is our next topic. The sign-S column will be discussed later.

E. Computer Analysis

The development of a computer program for analyzing the four modes of operation of the binary counter will now be described. This program is an extension of the computer analysis of Mode I only in Report 4. The computed results will be compared with experimental data in each of the four modes of operation, under three conditions: $T = 25^\circ\text{C}$ and $V_s = 28$ volts (nominal), $T = -10^\circ\text{C}$ and $V_s = 15$ volts (extreme low), and $T = 85^\circ\text{C}$ and $V_s = 50$ volts (extreme high).

1. Circuit Equations

The basic circuit equations for Mode I of operation were derived in Report 4, pp. 56-61. These equations will now be extended into a general form, and thus be applicable in any mode of operation. We shall derive these circuit equations for the second stage of the binary counter. For this reason, the time variables of the second stage only are designated in Fig. 25, p. 69.

By inspection of Fig. 25, the net MMFs acting on Cores 1 and 2 are

$$F_1 = N_{s1}i_s + N_{B1}i_d + N_{c1}i_c - N_{CL}i_{CL} \quad (134)$$

and

$$F_2 = N_{s2}i_s - N_{B2}i_d - N_{c2}i_c \quad (135)$$

Table III
 DEVICE PARAMETER VALUES (IN MKS UNITS) *vs.* TEMPERATURE AND THE SIGN *S*
 OF A CHANGE IN THE PARAMETER VALUE WHICH INCREASES $V_{s, \min}$
 OF A CORE-DIODE-TRANSISTOR BINARY COUNTER

DEVICE		PARAMETER VALUE			<i>S</i>
		$T = -10^{\circ}\text{C}$	$T = 25^{\circ}\text{C}$	$T = 85^{\circ}\text{C}$	
Core 1	l_{i1}	$5.59 \cdot 10^{-3}$	$5.59 \cdot 10^{-3}$	$5.59 \cdot 10^{-3}$	+
	l_{o1}	$7.98 \cdot 10^{-3}$	$7.98 \cdot 10^{-3}$	$7.98 \cdot 10^{-3}$	+
	ϕ_{r1}	$7.47 \cdot 10^{-8}$	$6.52 \cdot 10^{-8}$	$5.065 \cdot 10^{-8}$	-
	ϕ_{s1}	$8.217 \cdot 10^{-8}$	$7.17 \cdot 10^{-8}$	$5.5715 \cdot 10^{-8}$	-
	H_{a1}	405.096	306.885	101.516	+
	H_{q1}	52.094	40.809	21.718	+
	H_{n1}	44.847	36.003	18.839	+
	λ_{d1}	7.7657	11.4541	10.6233	-
	ν_{d1}	3.8851	3.7095	3.1159	-
	F_{dB1}	0.5000	0.3917	0.2168	+
	F''_{01}	0.4348	0.3406	0.1885	+
	λ_1	0.5618	0.6023	0.6196	-
	ν_1	1.2689	1.2667	1.2583	-
	F_{B1}	1.1261	0.8701	0.7660	+
	F_{01}	0.5813	0.4521	0.3071	+
	ρ_{p1}	0.6455	0.6439	0.6765	-
Core 2	l_{i2}	$5.59 \cdot 10^{-3}$	$5.59 \cdot 10^{-3}$	$5.59 \cdot 10^{-3}$	+
	l_{o2}	$7.98 \cdot 10^{-3}$	$7.98 \cdot 10^{-3}$	$7.98 \cdot 10^{-3}$	+
	ϕ_{r2}	$7.525 \cdot 10^{-8}$	$6.555 \cdot 10^{-8}$	$5.095 \cdot 10^{-8}$	-
	ϕ_{s2}	$8.2775 \cdot 10^{-8}$	$7.2105 \cdot 10^{-8}$	$5.6045 \cdot 10^{-8}$	-
	H_{a2}	509.094	422.415	127.337	+
	H_{q2}	51.302	39.986	21.157	+
	H_{n2}	43.118	34.642	17.817	+
	λ_{d2}	29.64	20.62	17.95	-
	ν_{d2}	4.70	4.05	3.41	-
	F_{dB2}	0.4691	0.3714	0.2228	+
	F''_{02}	0.4079	0.3230	0.1937	+
	λ_2	0.6148	0.6594	0.6301	-
	ν_2	1.4762	1.4223	1.2312	-
	F_{B2}	0.8883	0.7474	0.8254	+
	F_{02}	0.5629	0.4490	0.3124	+
	ρ_{p2}	0.6401	0.6531	0.6976	-
Windings	N_{s1}	11	11	11	+
	N_{s2}	12	12	12	-
	N_{B1}	16	16	16	-
	N_{B2}	20	20	20	-
	N_{c1}	12	12	12	+
	N_{c2}	12	12	12	-
	N_{CL}	5	5	5	-

Table III (Concluded)

DEVICE	PARAMETER VALUE			S	
	$T = -10^{\circ}\text{C}$	$T = 25^{\circ}\text{C}$	$T = 85^{\circ}\text{C}$		
Resistors	$R_{1(0)}$	104.75	104.3	105.75	0
	$R_{1(1)}$	104.75	104.3	105.75	0
	$R_{1(2)}$	105.0	104.7	106.3	0
	R_2	206.4	205.3	208.1	-
	R_3	0.293	0.340	0.420	0
	R_4	0.457	0.530	0.655	+
Inductors	$L_{0(0)}$	$0.3260 \cdot 10^{-3}$	$0.3311 \cdot 10^{-3}$	$0.3190 \cdot 10^{-3}$	0
	$I_{con(0)}$	0.1451	0.1340	0.1224	0
	$L_{0(1)}$	$0.3529 \cdot 10^{-3}$	$0.3655 \cdot 10^{-3}$	$0.3469 \cdot 10^{-3}$	0
	$I_{con(1)}$	0.1607	0.1419	0.1331	0
	$L_{0(2)}$	$0.3442 \cdot 10^{-3}$	$0.3614 \cdot 10^{-3}$	$0.3362 \cdot 10^{-3}$	0
	$I_{con(2)}$	0.1469	0.1356	0.1292	0
Diode	I_{sd}	$0.1307 \cdot 10^{-9}$	$9.7465 \cdot 10^{-9}$	$242.2 \cdot 10^{-9}$	+
	θ_{md}	0.0420	0.0502	0.0553	-
	$R_{\rho d}$	$200 \cdot 10^9$	$6.05 \cdot 10^9$	$0.0125 \cdot 10^9$	-
	R_d	0.382	0.360	0.415	-
Transistor	I_{se}	$1.01 \cdot 10^{-9}$	$54.01 \cdot 10^{-9}$	$3317.78 \cdot 10^{-9}$	-
	θ_{me}	0.0459	0.0543	0.0659	+
	C_{j0e}	$54.0 \cdot 10^{-12}$	$57.0 \cdot 10^{-12}$	$62.0 \cdot 10^{-12}$	-
	$V_{\phi e}$	0.6	0.6	0.6	+
	N_e	0.334	0.351	0.364	+
	k_e	$28.446 \cdot 10^{-9}$	$19.343 \cdot 10^{-9}$	$13.888 \cdot 10^{-9}$	-
	$R_{\rho e}$	$1430 \cdot 10^9$	$200 \cdot 10^9$	$5.0 \cdot 10^9$	-
	R_e	0.429	0.430	0.450	+
	I_{sc}	$0.0183 \cdot 10^{-9}$	$2.1964 \cdot 10^{-9}$	$237.6442 \cdot 10^{-9}$	+
	θ_{mc}	0.0375	0.0450	0.0531	-
	C_{j0c}	$62.0 \cdot 10^{-12}$	$65.0 \cdot 10^{-12}$	$70.0 \cdot 10^{-12}$	-
	$V_{\phi c}$	0.7	0.7	0.7	-
	N_c	0.442	0.452	0.475	+
	k_c	$1.729 \cdot 10^{-4}$	$1.543 \cdot 10^{-4}$	$1.706 \cdot 10^{-4}$	-
	$R_{\rho c}$	$3230 \cdot 10^9$	$300 \cdot 10^9$	$5.48 \cdot 10^9$	-
	R_c	0.000	0.000	0.000	+
	R_b	0.490	0.527	0.652	+

The core model to be applied is expressed in Eqs. (78) through (82). Following Eq. (78), the $\dot{\phi}$ of each core is composed of an elastic component $\dot{\phi}_\epsilon$, and an inelastic component $\dot{\phi}_{inel}$; thus,

$$\dot{\phi}_1 = \dot{\phi}_{\epsilon 1} + \dot{\phi}_{inel}(F_1, \phi_1) \quad (136)$$

$$\dot{\phi}_2 = \dot{\phi}_{\epsilon 2} + \dot{\phi}_{inel}(F_2, \phi_2) \quad , \quad (137)$$

where, following Eq. (79), $\dot{\phi}_{\epsilon 1} = \epsilon \dot{F}_1$ and $\dot{\phi}_{\epsilon 2} = \epsilon \dot{F}_2$, and where $\dot{\phi}_{inel}(F_1, \phi_1)$ and $\dot{\phi}_{inel}(F_2, \phi_2)$ are each evaluated by the use of Eqs. (80) through (82).

By inspection of the loops containing inductors in Fig. 25, each of the drive currents i_L , i_{CL} , and i_c may be described by a general loop equation,

$$V = N\dot{\phi} + R_1 i + L \frac{di}{dt} + V_L \quad , \quad (138)$$

in which i , V , $N\dot{\phi}$, R_1 , L , and V_L corresponding to each drive current are given in Table IV. Since the voltage across Diode $d_{2(2)}$ is much smaller than any other term in the corresponding loop equation, it need not be exact and is approximated by $i_L R_d + 0.6$ volt. For the same reason, the sum of the voltages across Core D and the collector and emitter of Transistor $T_{(0)}$ is approximated by 1.0 volt. These approximations will simplify the computer analysis without damaging the accuracy of the computed results.

Table IV
VALUES OR EXPRESSIONS FOR THE TERMS IN THE GENERAL
LOOP EQUATION CORRESPONDING TO EACH DRIVE CURRENT

i	V	$N\dot{\phi}$	R_1	L	V_L
i_L	0	$N_{s1}\dot{\phi}_1 + N_{s2}\dot{\phi}_2$	$R_{1(1)} + R_d$	$L_{(1)}$	$0.6 + i_s R_3$
i_{CL}	V_s	$-N_{CL}\dot{\phi}_1$	$R_{1(0)}$	$L_{(0)}$	1.0
i_c	V_s	$N_{c1}\dot{\phi}_1 - N_{c2}\dot{\phi}_2$	$R_{1(2)}$	$L_{(2)}$	V_{CE}

The values of $L_{(0)}$, $L_{(1)}$, and $L_{(2)}$, which are to be used in Eq. (138), are determined as functions of i_{CL} , i_L , and i_c , respectively, by using the nonlinear inductor model, Eq. (84).

There are two more loop equations associated with the second stage, which apply to all four modes of operation:

$$f = N_{B2}\dot{\phi}_2 - N_{B1}\dot{\phi}_1 - V_{pn} - i_d R_4 = 0 \quad (139)$$

and

$$g = N_{s2}\dot{\phi}_2 + N_{s1}\dot{\phi}_1 + i_s R_3 - R_2(i_L - i_s) = 0 \quad (140)$$

The voltage V_{pn} appears across Diode $d_{1(2)}$ in parallel with the base and emitter of Transistor $T_{(2)}$. In Modes I, II, and IV, and in the beginning of Mode III, $V_{pn} > 0$, and so the transistor is cut off while the diode is conducting; hence, V_{pn} is evaluated by ignoring the transistor and considering the forward characteristics of the diode [Eqs. (85) through (90)]. On the other hand, in Mode III (except in the beginning), $V_{pn} < 0$, and so the diode is reverse-biased while the transistor is either in the active region or in saturation; hence, V_{pn} is evaluated by ignoring the diode and considering the transistor model [Eqs. (91) through (108)].

Equations (134) through (140) plus the core, inductor, diode, and transistor models [Eqs. (79) through (108)] will be used to obtain the numerical solution of all the time variables. This solution employs a simple predictor-corrector integration method and the Newton-Raphson method for the transcendental solution of Eqs. (139) and (140). The applications of both methods are discussed next.

2. Computation Methods

a. A Simple Predictor-Corrector Integration Method

In the circuit analysis above, eight variables have been expressed in a differential form: ϕ_1 and ϕ_2 [Eq. (80)]; i_L , i_{CL} , and i_c [Eq. (138) and Table IV]; V_d [Eq. (90)]; V_e [Eq. (96)]; and V_c [Eq. (103)]. The differential equation describing each of these time variables is nonlinear, and will therefore be solved numerically. It was concluded in Report 4 (pp. 68-70) that for this circuit, the results obtained by using a simple predictor-corrector integration method (Report 4, p. 61) are

essentially identical with the results obtained by using the more sophisticated Runge-Kutta and Adams methods (Report 4, p. 67). Following this conclusion, we shall use the former.

Letting y stand for $\phi_1, \phi_2, i_L, i_{CL}, i_c, V_d, V_e$, and V_c at time t , assume that $y_{(-2)}, y_{(-1)}$, and $\dot{y}_{(-1)}$ are known, where the subscripts (-2) and (-1) indicate values at times $(t - 2\Delta t)$ and $(t - \Delta t)$, respectively, and Δt is a short time increment. First, y is predicted from the integration formula

$$y = y_{(-2)} + 2\Delta t \dot{y}_{(-1)} \quad (141)$$

A correction for y is then obtained, using the differential equation

$$\dot{y} = f(y) \quad (142)$$

and the integration formula

$$y = y_{(-1)} + 0.5\Delta t [\dot{y} + \dot{y}_{(-1)}] \quad (143)$$

The various time variables depend on one another. Therefore, after Eq. (141) is applied to each variable, the iterative computation of these variables should be performed sequentially in a *loop*, until a general convergence is achieved. Within each computation cycle of this major loop, one may be tempted to iterate Eqs. (142) and (143) in a minor loop until convergence is achieved for one variable, before proceeding to do the same for another. Compared with the method of computation where no minor-loop convergence of one variable at a time is allowed, this method is not only more costly, but may also result in a wrong convergence of an individual variable. Such a danger exists if the values of the other variables are not close to their true values. In conclusion, following the application of Eq. (141) to all variables, Eqs. (142) and (143) will be applied to each variable only once within each computation cycle. The computation cycle will be repeated until convergence is reached for the entire system of time variables.

In order to achieve convergence, $\Delta t \dot{y}$ should be much smaller than y ; hence, Δt should be much smaller than $|y/f(y)|$. It turns out that a reasonable value of Δt (from the point of view of computation

cost) satisfies this condition for all variables, except V_d . Substituting Eq. (85) into Eq. (90), and since $V_d/R_{\ell d} \ll i$ and $e^{V_d/\theta_{md}} \gg 1$, we obtain

$$\dot{V}_d \approx \frac{i - I_{sd} e^{V_d/\theta_{md}}}{C_{dd} + C_{jd}}, \quad (144)$$

where C_{dd} and C_{jd} are expressed in Eqs. (87) and (88) as functions of V_d . Hence, Δt should be much smaller than $(C_{dd} + C_{jd})V_d / |i - I_{sd} e^{V_d/\theta_{md}}|$. The total capacitance $(C_{dd} + C_{jd})$ of a d_1 diode used in this binary-counter circuit was found to be very small (around 1 pF). Consequently, the Δt required to achieve convergence is small enough to increase the cost of computation appreciably. Since such a small capacitance has a negligible effect on V_d and i_d and since $i_d \gg V_d/R_{\ell d}$, Eqs. (89) and (90), when applied to a d_1 diode, are reduced to

$$V_{pn} = i_d R_d + \theta_{md} \ln \left(1 + \frac{i_d}{I_{sd}} \right). \quad (145)$$

As expected, Eq. (145) is essentially identical with Eq. (86), which describes the static V - I characteristic of a diode. In conclusion, the value of V_{pn} in Eq. (139) will be computed from Eq. (145) in Modes I, II, and IV and in the beginning of Mode III, whereas in Mode III (except the beginning), V_{pn} will be computed by applying Eqs. (142) and (143) to the dynamic model of the transistor, Eqs. (91) through (108).

b. Newton-Raphson Method for Transcendental Solution of Currents

As described above, each of the integrable time variables (ϕ_1 , ϕ_2 , i_L , i_{CL} , i_c , V_d , V_e , and V_c) is predicted initially by using Eq. (141), and then corrected by applying Eqs. (142) and (143) once in every cycle of computation. Substituting these values into Eqs. (134) through (138), Eqs. (139) and (140) become two transcendental equations with currents i_d and i_s as unknowns. These will be solved by the use of Newton-Raphson method of successive approximation.²⁵ At the end of each computation cycle, corrections δi_d and δi_s are added to the values of i_d and i_s , respectively, of the previous computation cycle (see Report 4, p. 60), where

$$\delta i_d = \frac{1}{D} \left(-f \frac{\partial g}{\partial i_s} + g \frac{\partial f}{\partial i_s} \right) \quad (146)$$

and

$$\delta i_s = \frac{1}{D} \left(f \frac{\partial g}{\partial i_d} - g \frac{\partial f}{\partial i_d} \right) , \quad (147)$$

and where

$$D = \left(\frac{\partial f}{\partial i_d} \right) \left(\frac{\partial g}{\partial i_s} \right) - \left(\frac{\partial f}{\partial i_s} \right) \left(\frac{\partial g}{\partial i_d} \right) . \quad (148)$$

If f (or g) is oscillatory, the correction for i_d (or i_s) is $0.5\delta i_d$ (or $0.5\delta i_s$).

Differentiation of Eqs. (134) through (137), (139), and (140) with respect to i_d and i_s gives

$$\frac{\partial f}{\partial i_d} = -(N_{B2}^2 \dot{\phi}'_2 + N_{B1}^2 \dot{\phi}'_1 + R_4 + V'_{pn}) , \quad (149)$$

$$\frac{\partial g}{\partial i_s} = N_{s2}^2 \dot{\phi}'_2 + N_{s1}^2 \dot{\phi}'_1 + R_2 + R_3 , \quad (150)$$

and

$$\frac{\partial f}{\partial i_s} = - \frac{\partial g}{\partial i_d} = N_{s2} N_{B2} \dot{\phi}'_2 - N_{s1} N_{B1} \dot{\phi}'_1 , \quad (151)$$

where $\dot{\phi}'_1 = d\dot{\phi}_1/dF_1$, $\dot{\phi}'_2 = d\dot{\phi}_2/dF_2$, and $V'_{pn} = dV_{pn}/di_d$.

Let us consider $\dot{\phi}'_1$ and $\dot{\phi}'_2$ first. Following Eq. (78),

$$\dot{\phi}' = \dot{\phi}'_\epsilon + \dot{\phi}'_{ine1} , \quad (152)$$

where $\dot{\phi}'_\epsilon = d\dot{\phi}_\epsilon/dF$ and $\dot{\phi}'_{ine1} = d\dot{\phi}_{ine1}/dF$. Approximating \dot{F} by $[F - F_{(-1)}]/\Delta t$, the derivative of Eq. (79) with respect to F becomes

$$\dot{\phi}'_\epsilon \approx \frac{\epsilon}{\Delta t} , \quad (153)$$

where $\epsilon = \epsilon(F)$ [Eq. (79a)]. Differentiating Eq. (80) with respect to F , we get

$$\dot{\phi}'_{inel} = \left[1 - \left(\frac{2\phi + \phi_s - \phi_d}{\phi_s + \phi_d} \right)^2 \right] \dot{\phi}'_p + 4\dot{\phi}_p \frac{(2\phi + \phi_s - \phi_d)(\phi + \phi_s)}{(\phi_s + \phi_d)^3} \phi'_d, \quad (154)$$

where $\dot{\phi}'_p = d\dot{\phi}_p/dF$ and $\phi'_d = d\phi_d/dF$; thus, following Eq. (81),

$$\dot{\phi}'_p = \begin{cases} 0 & \text{if } 0 \leq F \leq F_d^{\min} \\ \lambda_d \nu_d (F - F_d^{\min})^{\nu_d - 1} & \text{if } F_d^{\min} \leq F \leq F_{dB} \\ \lambda \nu (F - F_0'')^{\nu - 1} & \text{if } F_{dB} \leq F \leq F_B \\ \rho_p & \text{if } F_B \leq F \end{cases} \quad (155)$$

and, following Eq. (82),

$$\phi'_d = \begin{cases} V_1 \left[\ln \left(\frac{F - H_a l_o}{F - H_a l_i} \right) + F \left(\frac{1}{F - H_a l_o} - \frac{1}{F - H_a l_i} \right) \right] & \text{if } F \leq F_d^{\min} \\ V_2 \left\{ \frac{1}{H_d^{\min}} + \left(\frac{1}{H_n} - \frac{1}{H_q} \right) \left[\ln \left(\frac{F \left(1 - \frac{H_n}{H_d^{\min}} \right)}{F - H_n l_i} \right) - \frac{H_n l_i}{F - H_n l_i} \right] \right\} & \text{if } F_d^{\min} \leq F \leq H_d^{\min} l_o \\ V_2 \left(\frac{1}{H_n} - \frac{1}{H_q} \right) \left[\ln \left(\frac{F - H_n l_o}{F - H_n l_i} \right) + F \frac{H_n (l_o - l_i)}{(F - H_n l_o)(F - H_n l_i)} \right] & \text{if } H_d^{\min} l_o \leq F \end{cases} \quad (156)$$

The expressions for V'_{pn} are considered next. As explained previously, in Modes I, II, and IV and in the beginning of Mode III, V_{pn} is expressed by Eq. (145), and so its derivative with respect to i_d is simply

$$V'_{pn} \equiv \frac{dV_{pn}}{di_d} = R_d + \frac{\theta_{nd}}{i_d + I_{sd}}. \quad (157)$$

During Mode III (except the beginning) determination of V_{pn} , and thus also of V'_{pn} , is more complex. Differentiating the combination of Eqs. (95) and (97) with respect to i_b , and substituting $i_b = i_e - i_c$, we get

$$V'_{BE} \equiv \frac{dV_{BE}}{di_b} = V'_{pn} = R_b + \frac{1 + R_e \frac{di_e}{dV_e}}{\frac{di_e}{dV_e} - \frac{di_c}{dV_e}}. \quad (158)$$

Note that $V'_{pn} = V'_{BE}$ because $V_{BE} = -V_{pn}$ and $i_b = -i_d$. The expression for di_e/dV_e is derived by substituting Eqs. (91), (93), (94), and (98) into Eq. (96) and differentiating the latter with respect to V_e . Substituting the approximations

$$\frac{d\dot{V}_e}{dV_e} = \frac{\ddot{V}_e}{\dot{V}_e} \approx \frac{1}{\Delta t} \left[1 - \frac{\dot{V}_e(-1)}{\dot{V}_e} \right]$$

and

$$\frac{dV_c}{dV_e} \approx \frac{\Delta V_c}{\Delta V_e} = \frac{V_c - V_c(-1)}{V_e - V_e(-1)}$$

into the resulting expression for di_e/dV_e , the latter becomes

$$\frac{di_e}{dV_e} \approx i'_e - \frac{\alpha_i I_{sc} e^{V_c/\theta_{mc}}}{\theta_{mc}} \left[\frac{V_c - V_c(-1)}{V_e - V_e(-1)} \right] \quad (159)$$

where

$$i'_e = \frac{I_{se} e^{V_e/\theta_{me}}}{\theta_{me}} + \frac{1}{R_{le}} + \frac{(C_{de} + C_{je})}{\Delta t} \left[1 - \frac{\dot{V}_e(-1)}{\dot{V}_e} \right] + \dot{V}_e \left(\frac{k_e I_{se} e^{V_e/\theta_{me}}}{\theta_{me}} + \frac{N_e C_{je}}{V_{\phi e} - V_e} \right). \quad (160)$$

Applying similar substitution, differentiation, and approximation to the collector junction, Eqs. (98) through (104) and Eq. (91), result in

$$\frac{di_c}{dV_e} \approx \frac{\alpha_n I_{se} e^{V_e/\theta_{me}}}{\theta_{me}} - i'_c \frac{V_c - V_c(-1)}{V_e - V_e(-1)}, \quad (161)$$

where

$$i'_c = \frac{I_{sc} e^{V_c / \theta_{mc}}}{\theta_{mc}} + \frac{1}{R_{\ell_c}} + \frac{C_{dc} + C_{jc}}{\Delta t} \left[1 - \frac{\dot{V}_c (-1)}{\dot{V}_c} \right] + \dot{V}_c \left(\frac{k_c I_{sc} e^{V_c / \theta_{mc}}}{\theta_{mc}} + \frac{N_c C_{jc}}{V_{\psi_c} - V_c} \right). \quad (162)$$

3. Computer Program

The development of a computer program for analyzing the four modes of operation of the core-diode-transistor binary counter was based on the circuit equations in Sec. E-1 and on the computation methods in Sec. E-2. The program is given in Appendix G. We shall first describe the features of this program, then outline its organization, and finally outline the computation steps at each time increment.

a. Program Features

The core and circuit parameters are read in from a deck of input-data cards which corresponds to a fixed temperature and a specific performance feature. Card decks for different temperature values differ from each other primarily in having different nominal parameter values (see Table III). Usually, evaluation of a specific performance feature is the main objective of the computer analysis. For example, the performance feature may be the minimum supply voltage $V_{s, \min}$, the maximum supply voltage $V_{s, \max}$, the maximum operation speed, etc. In the program shown in Appendix G, $V_{s, \min}$ is the performance feature. This choice is based on the experimental observation that $V_{s, \min}$ is determined by a failure in circuit performance (see Fig. 27), whereas $V_{s, \max}$ is determined by V_{CE} exceeding the specified $V_{CE, \max}$ of the transistor, rather than by operation failure (see Fig. 29).

Each of the input-data cards corresponds to a single parameter, and includes the following: the nominal value P_n at the given temperature; the maximum percentage deviation from the nominal value d_{\max} (due to manufacturing nonuniformity, aging, etc.); and the sign S of a change in the parameter value which causes a specific circuit-performance feature to become worse. The value P of each parameter to be used in the analysis is then computed from the relation

$$P = P_n \left(1 + S \frac{d_{\max}}{100} \right). \quad (163)$$

Since every parameter is assigned its worst value, a worst-case analysis is thus likely to be achieved. Only a slight change in the computer program will be required in future if a different method guaranteeing a worst-case analysis is developed. The values of P_n , d_{\max} , and S are printed out at the outset of the computation.

After setting the core and circuit parameters, the initial values of the time variables in Mode I must be established before running the computation through the four modes of operation. These initial values are zero for all time variables, except for ϕ_1 and ϕ_2 and for the fact that $V_{CE} = -V_c = V_s$. Referring to Fig. 25, N_{CL} is considerably smaller than N_{c2} because N_{CL} is limited by flux unsetting during Mode II (see Fig. 29), whereas no such limitation is imposed on N_{c2} . In fact, referring to Table III, $N_{c2} = 12$ and $N_{CL} = 5$. As a result of this condition, the MMF pulse $N_{c2}i_c$ is capable of switching Core 2 to essentially negative saturation for $V_s \geq V_{s,\min}$; in contrast, the MMF pulse $N_{CL}i_{CL}$ is not large enough to switch Core 1 to negative saturation if V_s is around $V_{s,\min}$. Consequently, whereas the initial value of ϕ_2 , ϕ_{20I} , may be assumed to be $-\phi_r$, the initial value of ϕ_1 , ϕ_{10I} , must be computed. Referring to Fig. 27, if the composite duration of the i_{CL} pulses during Modes II-1 and II-2 were long enough to complete switching to a point on the static $\phi_d(F)$ curve of Core 1, then ϕ_{10I} could be evaluated transcendently by using Eq. (82). This, however, is not the case for two reasons: First, the lower the value of V_s is, the lower is the amplitude of i_{CL} , and so the longer is the required pulse duration for complete switching. Second, as explained in Fig. 28, lowering V_s causes the duration of Submode III-B, T_{III-B} , to shorten, and as a result the duration of the i_c pulse becomes shorter. Fortunately, exact determination of ϕ_{10I} for any value of V_s can be achieved quite simply by adding a computation run through preliminary Modes IV-1 and IV-2, to be referred to as Modes 0-1 and 0-2, before the computation of Modes I-IV is begun. Assuming that initially (beginning of the preliminary Mode 0-1) $\phi_1 = \phi_r$ and $\phi_2 = -\phi_r$, the time variables during Mode 0-1 and Mode 0-2 are computed; the final values of ϕ_1 and ϕ_2 , then, serve as the initial values, ϕ_{10I} and ϕ_{20I} , of Mode I.

After establishing the initial conditions of Mode I, computation of the time variables *vs.* time proceeds along Modes I, II-1, II-2, III, IV-1, and IV-2. The final ϕ_1 and ϕ_2 values of one mode become the initial ϕ_1 and ϕ_2 values of the following mode. The time increment Δt is not constant, but rather dependent on the convergence conditions. Generally, Δt

in Modes II and IV is longer than Δt in Mode I, and the latter is longer than Δt in Mode III. Furthermore, Δt within a given mode may be changed according to the convergence condition.

At each time increment Δt , the time variables are solved for by applying the computation methods of Eqs. (141) through (162) to the basic circuit equations, Eqs. (134) through (140), and the device models, Eqs. (79) through (108). This numerical solution is carried out within a PROCEDURE called INCREMENT, which may be regarded as the heart of the entire program.

The main program includes the instructions for reading in the input-data cards and setting the value of V_s . It also includes the framework for the computation in each mode, in which instructions are given for establishing the initial conditions, establishing Δt , calling PROCEDURE INCREMENT, printing circuit-failure messages, and switching to the next mode.

The value of $V_{s,\min}$ for a given temperature and performance feature is determined by the computer in the following manner: a low value of V_s is set, and the computation for successive modes is performed. If there is a failure in Mode III because the transistor either turns off in Submode III-C or does not turn on at all, the computation with the assumed V_s terminates, V_s is increased by ΔV_s , and a new computation is performed from the beginning. This computation is repeated until the transistor stays on properly during Mode III, in which case the computation in Modes IV-1 and IV-2 is completed; the corresponding V_s value is regarded as $V_{s,\min}$. A similar algorithm can be built into the program in order to compute $V_{s,\max}$.

b. Program Outline

The computer-analysis program of the core-diode-transistor binary counter is given in Appendix G. The outline of this program is as follows:

(1) Declare

(A) the global identifiers

(B) the lists:

LIST2 (temperature, V_s , I_L , and T_r)

LIST3 (time variables).

(C) the formats:

FMT2 (for LIST2);

FMT3 (for LIST3);

FMT4 (heading for output time variables);

FMT5 ("Mode");

FLAG1 ("spurious transistor turn-on");

FLAG2 ("spurious transistor turn-off");

FLAG3 ("Maximum collector-emitter voltage exceeded");

FLAG4 ("No transistor turn-on in Mode 3").

(2) Declare the PROCEDUREs whose names and functions are as follows:

TRANSFER (N, A, B)

Transfer the values of N identifiers from Array A to Array B .

PRINTOUT

Print output variables (LIST3) every n th Δt .
At the end of a page, print computation time, skip page, and print output heading (FMT4).
Fill PLOT arrays with the values of time variables and time, each multiplied by its own scale factor, every m th Δt (m differs among modes).

PRINTHEAD

On a new page print Mode number, output heading (FMT4), and initial values of output variables (LIST3).

INTERPOL (POINTS, ICC, BET, COEF)

Compute the coefficients of a third-degree polynomial for every four experimental points of β_n vs. I_c (or β_i vs. I_c), which are to be used in the interpolation of β_n (or β_i).

BETA (IC, P, COEF, ICC, BET, POINTS)

Interpolate β_n for given I_c (or β_i for given I_c).

PHIDOTE (F, FMI, EPS, PHIDOTEPR)

Compute $\dot{\phi}_\epsilon = \epsilon [F - F_{(-1)}] / \Delta t$ and $\dot{\phi}'_\epsilon = \epsilon / \Delta t$.

PHIDOT (F, PHI, LI, LO, PHIR, PHIS, HA, HQ, HTH, HN,
LAMBDA, NUD, FDB, FOPP, LAMBDA, NU, FB, FO, ROP,
F12, F23, V1, V2, PHIDOTPRIME)

For given F and ϕ (both of arbitrary sign),
compute $\dot{\phi}_d$ [Eq. (82)]; $\dot{\phi}'_d$ [Eq. (156)];
 $\dot{\phi}_p$ [Eq. (81)]; $\dot{\phi}'_p$ [Eq. (155)]; $\dot{\phi}_{inel}$ [Eq. (80)];
and $\dot{\phi}'_{inel}$ [Eq. (154)]. If $\phi \geq \phi_d$, then
 $\dot{\phi}_{inel} = 0$ and $\dot{\phi}'_{inel} = 0$.

I (V, VL, II, IML, IDOTMI, NPHIDOT, R1, LO, ICON, IDOT)

For a loop that includes a nonlinear inductance,
compute once (no iteration) L [Eq. (84)];
 di/dt [Eq. (138)]; and i [Eq. (143)]. i cannot
be negative.

V (I, VJ, VMI, VDOTMI, IS, THETAM, CJO, VCPOT, N, K,
RL, CJ, CD, ISF, VDOT, IPR)

For given current i and voltage V of a base-
emitter (or base-collector) junction, compute
 $I_s e^{V/\theta_m}$; C_j [Eq. (94) or Eq. (101)]; C_d
[Eq. (93) or Eq. (100)]; \dot{V} [Eq. (96) or
Eq. (103)]. Correct V [Eq. (143)] and $I_s e^{V/\theta_m}$,
and compute i' [Eq. (160) or Eq. (162)].

INCREMENT*

Compute every time variable y and its derivative \dot{y}
at a given time increment from the values of
 $y_{(-1)}$, $\dot{y}_{(-1)}$, and $y_{(-2)}$ and the circuit equations
[Eqs. (134) through (140)] by applying the device
models [Eqs. (79) through (108)], the predictor-
corrector integration method [Eqs. (141) through
(143)], and the Newton-Raphson iterative method
[Eqs. (146) through (151)].

(3) Proceed with the MAIN PROGRAM:

(A) Read in the deck of input-data cards correspond-
ing to given temperature and performance feature.
(Each card contains the data for one parameter:

* The computation steps are outlined in Sec. II-E-3-c, p. 159.

nominal value, maximum percentage deviation, and worst-case differential sign.) Compute the worst-case parameter value [Eq. (163)].

- (B) Print the above data in a table, and verify by listing the corresponding global parameters and their values.
- (C) Compute the following auxiliary parameters for each of the two cores: H_s [Eq. (82e)]; H_d^{\min} [Eq. (82d)]; F_d^{\min} [Eq. (82c)]; $F_{23} = H_d^{\min} l_o$; V_1 [Eq. (82a)]; V_2 [Eq. (82b)]; and ϵ [Eq. (79a)].
- (D) For each specified value of V_s , perform the following all-mode computation:
 1. Determine T_r , I_L , and the maximum slope of $i_L(t)$.
 2. Compute average values for i_s and $\dot{\phi}_1$ in Mode I, using the relations (see Report 4, p. 62)

$$I_s = \left(\frac{V_s}{R_1} \right) \frac{R_2}{R_2 + 0.6\rho_{p1}(N_{s1}^2 + N_{s2}^2)} \quad (164)$$

and

$$\overline{\phi_{12}} = \left| \frac{0.6\rho_{p1}N_{B2}[(N_{s1}N_{B2} + N_{s2}N_{B1})I_s - (N_{B1} + N_{B2})F_0'] - 0.7N_{B1}}{N_{B1}^2 + N_{B2}^2} \right| \quad (165)$$

Establish a "negligible value"

$$NV = 0.001\dot{\phi}_{12} \quad (166)$$

for $\dot{\phi}_1$ and $\dot{\phi}_2$.

3. Establish and print the values of the time variables after the completion of each of the modes:
 - (i) Subtract $\Delta\phi_\epsilon(F_1)$ from ϕ_1 and $\Delta\phi_{\epsilon2}(F_2)$ from ϕ_2 , where, following Eqs. (79a) and (82a) [see Eq. (30) in Report 1 (p. 19)],

$$\Delta\phi_\epsilon = FV_1 \ln \left(\frac{H_a l_o + |F|}{H_a l_i + |F|} \right) \quad (167)$$

Make sure that final $|\phi_1| \leq \phi_{r1}$
and final $|\phi_2| \leq \phi_{r2}$.

(ii) Set $V_{CE} = -V_c = V_s$.

(iii) Set all other variables to zero.

4. Perform the computation steps outlined next for each mode of operation in the following order: Mode 0 (repeated twice); Mode I; Mode II (repeated twice), Mode III; Mode IV (repeated twice):

Mode 0

- (i) Set the initial flux levels $\phi_1 = \phi_r$ and $\phi_2 = -\phi_r$ for Mode 0-1 only.
- (ii) Compute approximate switching time, $\tau_s = 2\phi_{r1}N_{B1}/0.7$.
- (iii) Set $\Delta t = \tau_s/150$.
- (iv) Call PRINthead PROCEDURE.
- (v) For every Δt until termination:
Set $t = t_{(-1)} + \Delta t$.
Call INCREMENT PROCEDURE.
Call PRINTOUT PROCEDURE.
- (vi) Terminate Mode 0 when $\dot{\phi}_1$ and $\dot{\phi}_2$ are negligible (i.e., $|\dot{\phi}_1| < NV$ and $|\dot{\phi}_2| < NV$) for 30 Δt 's or if $\dot{\phi}_1$ and $\dot{\phi}_2$ are negligible at least once and $\phi_1 < -0.1\phi_{r1}$.

Mode I

- (i) Compute approximate switching time, $\tau_s = 2\phi_{r1}/\dot{\phi}_{12}$.
- (ii) Call PRINthead PROCEDURE.
- (iii) For every Δt until termination:

$$\text{Set } \Delta t = \begin{cases} \tau_s/300 & \text{if } t < T_r \\ \tau_s/60 & \text{if } t \geq T_r \text{ and } |\dot{\phi}_1|, |\dot{\phi}_2| > 20NV \\ \tau_s/30 & \text{otherwise} \end{cases}$$

Set $t = t_{(-1)} + \Delta t$.

Call INCREMENT PROCEDURE.

If $V_{CE} > V_{CE, \max}$ print FLAG3.

Call PRINTOUT PROCEDURE.

If $V_{CE} < 1.0$ volt, print FLAG1.

- (iv) Terminate Mode I when $\dot{\phi}_1$ and $\dot{\phi}_2$ are negligible for 30 Δt 's or at least once
and $\phi_1 > -0.9\phi_{r1}$.

Mode II

- (i) Compute approximate switching time,
 $\tau_s = 2\phi_{r1}N_{B1}/0.7$.
- (ii) Set $\Delta t = \tau_s/150$.
- (iii) Call PRINthead PROCEDURE.
- (iv) For every Δt until termination:
Set $t = t_{(-1)} + \Delta t$.
Call INCREMENT PROCEDURE.
Call PRINTOUT PROCEDURE.
- (v) Terminate Mode II when $\dot{\phi}_1$ and $\dot{\phi}_2$ are negligible for 30 Δt 's or at least once
and $\phi_1 < -0.1\phi_{r1}$.

Mode III

- (i) Compute approximate switching time,
 $\tau_s = 2\phi_{r1}/\dot{\phi}_{12}$.
- (ii) Call PROCEDURE INTERPOL twice,
once for β_n vs. I_c and once for β_i vs. I_e .
- (iii) Call PRINthead PROCEDURE.
- (iv) For every Δt until termination:
- $$\text{Set } \Delta t = \begin{cases} \tau_s/300 & \text{if } t < 2T_r \text{ or} \\ & (\phi_1 > \phi_{r1} \text{ and } \phi_2 > 0.8\phi_{r2}) \text{ or} \\ & (\phi_1 > \phi_{r1} \text{ and } \phi_2 < -\phi_{r2}) \\ \tau_s/100 & \text{otherwise.} \end{cases}$$
- Decrease Δt by a factor of, say, 2.5, if convergence may fail.
- Set $t = t_{(-1)} + \Delta t$.

Determine the time T_v when the transistor is on and the diode is off, e.g., when $V_{pn} < -0.1$ volt. While the transistor is on ($t \geq T_v$), call PROCEDURE BETA twice, once for β_n vs. i_c , and once for β_i vs. i_e ; Compute $\alpha_n = \beta_n / (1 + \beta_n)$ and $\alpha_i = \beta_i / (1 + \beta_i)$.

Call INCREMENT PROCEDURE.

If $\phi_2 > 0 < \phi_1$ and $V_{CE} > 5V_s$, then the operation fails due to transistor turn-off; print FLAG2 and terminate the computation for the given V_s value.

Call PRINTOUT PROCEDURE.

- (v) Terminate Mode III when $\dot{\phi}_1$ and $\dot{\phi}_2$ are negligible for 30 Δt 's or at least once and $\phi_1 > 0 > \phi_2$) or $(\phi_1 > \phi_{r1}$ and $\phi_2 < -1.2\phi_{r2}$) or $(\phi_1 \geq \phi_{r1}$ and $\phi_2 < -\phi_{r2}$ and $V_{CE} > V_s)$ or $(i_c \leq 1 \text{ mA and } \phi_1 > 0 > \phi_2)$.

If there is no transistor turn-on in Mode III, print FLAG4 and terminate the computation for the given V_s value.

Mode IV

- (i) Compute approximate switching time,

$$\tau_s = 2\phi_{r1}N_{B1}/0.7.$$
- (ii) Set $\Delta t = \tau_s/150$.
- (iii) Call PRINthead PROCEDURE.
- (iv) For every Δt until termination:
 Set $t = t_{(-1)} + \Delta t$.
 Call INCREMENT PROCEDURE.
 Call PRINTOUT PROCEDURE.
- (v) Terminate Mode IV when $\dot{\phi}_1$ and $\dot{\phi}_2$ are negligible for 30 Δt 's or at least once and $\phi_1 < -0.1\phi_{r1}$.
- (E) Repeat the above all-mode computation in Step (D) until four modes are executed without failure.

c. Outline for PROCEDURE INCREMENT

As explained previously, the heart of the computer program is the INCREMENT PROCEDURE, where the computation of the time variables is carried out at each time increment, Δt . The outline of this PROCEDURE is as follows:

(A) Lower the Δt index of the time variables:

1. Set $y_{(-2)}$, $y_{(-1)}$, and $\dot{y}_{(-1)}$ [Eqs. (141) through (143)] equal to the values of $y_{(-1)}$, y , and \dot{y} , respectively, of the previous Δt , where $y = \phi_1, \phi_2, i_L$ (in every mode); i_{CL} (in Modes 0, II, and IV); i_c, V_e, V_c (in Mode III, transistor on).
2. Set $y_{(-2)}$ equal to previous $y_{(-1)}$ for $y = i_d$ and i_s and set $y_{(-1)}$ equal to previous y for $y = i_d, i_s, F_1$, and F_2 .

(B) GUESS:

1. Using Eq. (141), predict the values of $y = \phi_1, \phi_2$ (in every mode); i_{CL} (in Modes 0, II, and IV); i_c, V_e, V_c (in Mode III, transistor on); i_L (in every mode except if $t \leq T_r$ in Mode I or III, in which case compute i_L from experimental i_L vs. t).
2. Using the approximation $y \approx 2y_{(-1)} - y_{(-2)}$, predict the values of $y = i_d$ and i_s .

(C) LOOP:

In each computation cycle, compute the following:

1. F_1 [Eq. (134)] and F_2 [Eq. (135)].
2. $\dot{\phi}_{inel,1}$ and $\dot{\phi}_{e1}$ by evaluation $\epsilon(F_1)$ [Eq. (79a)] and calling PROCEDURES PHIDOT and PHIDOTE for Core 1;

$$\dot{\phi}_1 = \dot{\phi}_{inel,1} + \dot{\phi}_{e1} ; \text{ and}$$

$$\dot{\phi}'_1 = \dot{\phi}'_{inel,1} + \dot{\phi}'_{e1} .$$
3. $\dot{\phi}_{inel,2}$ and $\dot{\phi}_{e2}$, by evaluating $\epsilon(F_2)$ [Eq. (79a)] and calling PROCEDURES PHIDOT and PHIDOTE for Core 2;

$$\dot{\phi}_2 = \dot{\phi}_{inel,2} + \dot{\phi}_{e2} ; \text{ and}$$

$$\dot{\phi}'_2 = \dot{\phi}'_{inel,2} + \dot{\phi}'_{e2} .$$

4. i_L (unless $t \leq T_r$ in Mode I or III), by calling PROCEDURE I [Eq. (138) and Table IV].
5. i_{CL} (in Modes 0, II, and IV), by calling PROCEDURE I [Eq. (138) and Table IV]
(if $t > 4.6 \mu s$, then $V_s = 0$).
6. i_c (if the transistor is on in Mode III), by calling PROCEDURE I [Eq. (138) and Table IV].
7. ϕ_1 and ϕ_2 , Eq. (143).
8. Unless the transistor is on in Mode III:
 V_{pn} [Eq. (145)] and V'_{pn} [Eq. (157)]
assuming ideal reverse-bias characteristics.

If the transistor is on in Mode III:

- (i) $i_b = -i_d$ and $i_e = i_b + i_c$.
- (ii) V_e , by calling PROCEDURE V for the emitter junction.
- (iii) V_c , by calling PROCEDURE V for the collector junction.
- (iv) V_{BE} [Eqs. (95) and (97)].
- (v) V_{CE} [Eq. (106)].
- (vi) di_e/dV_e [Eq. (159)].
- (vii) di_c/dV_e [Eq. (161)].
- (viii) V'_{BE} [Eq. (158)].
- (ix) $V_{pn} = -V_{BE}$ and $V'_{pn} = V'_{BE}$.
9. f and g [Eqs. (139) and (140)].
10. $\partial f / \partial i_d$ [Eq. (149)]; $\partial g / \partial i_s$ [Eq. (150)];
 $\partial f / \partial i_s$ [Eq. (151)]; $\partial g / \partial i_d = -\partial f / \partial i_s$;
 D [Eq. (148)].
11. δi_d [Eq. (146)]; δi_s [Eq. (147)].
12. Add δi_d to i_d of previous computation cycle, but if the sign of f has changed, add only $0.5\delta i_d$; add δi_s to i_s of previous computation cycle, but if the sign of g has changed, add only $0.5\delta i_s$.

- (D) If $|\delta i_d| > 0.0001 |i_d|$ or $|\delta i_s| > 0.0001 |i_s|$, perform the computation cycle under (C) again, provided no more than 19 cycles have been computed.
- (E) If $|\dot{\phi}_1| < NV$ and $|\dot{\phi}_2| < NV$ and $t > \tau_s/2$, then $\dot{\phi}_1$ and $\dot{\phi}_2$ are regarded as negligible (no switching).

4. Experimental and Computed Time-Variable Waveforms

a. Results

The three-stage binary counter (Fig. 25) was run experimentally under a nominal condition of $T = 25^\circ\text{C}$ and $V_s = 28\text{V}$, and under two extreme conditions: $T = -10^\circ\text{C}$ and $V_s = 15\text{V}$ (it was found that at $T = -10^\circ\text{C}$, $V_{s,\min} = 14.9\text{V}$) and $T = 85^\circ\text{C}$ and $V_s = 50\text{V}$ ($V_{s,\max}$ was not reached; the value of $V_s = 50\text{V}$ was limited by the specification of maximum collector-emitter voltage). In each run, oscillograms of the following time variables were photographed:

Mode I: $i_L, i_s, \dot{\phi}_1, \dot{\phi}_2, V_{pn},$ and i_d

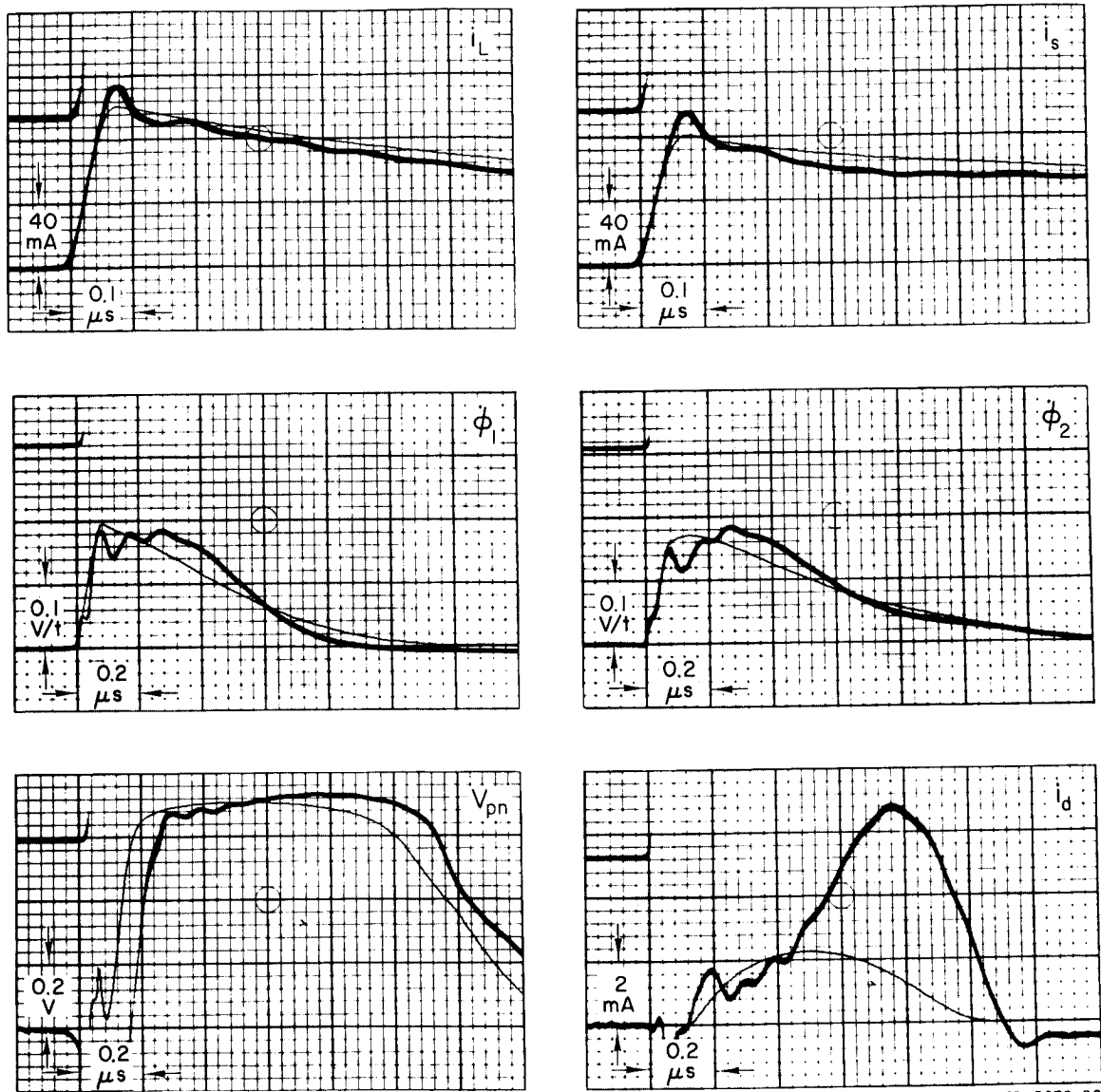
Mode II-1: $i_{CL}, i_s, \dot{\phi}_1, \dot{\phi}_2, V_{pn},$ and i_d

Mode III: $i_L, i_s, \dot{\phi}_1, \dot{\phi}_2, V_{pn}, i_d, V_{CE},$ and i_c

Mode IV-1: $i_{CL}, i_s, \dot{\phi}_1, \dot{\phi}_2, V_{pn},$ and i_d .

For each of the above cases, a computer program was run on a Burroughs B-5500 digital computer, using the core and circuit parameters in Table III and the scale factors of the recorded oscillograms. The computed results, first written on a magnetic tape, were plotted on a CalComp Model 570 plotter.

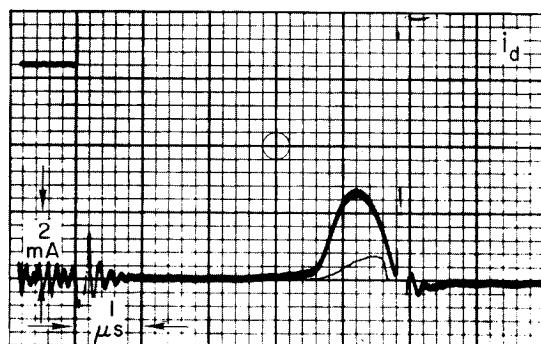
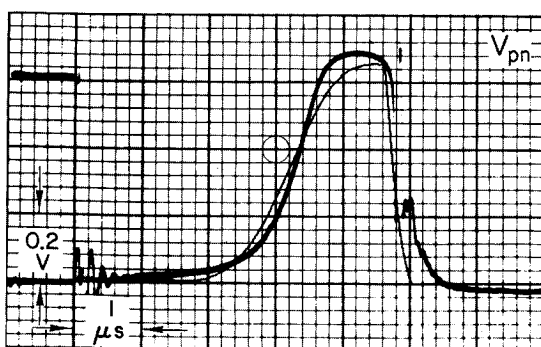
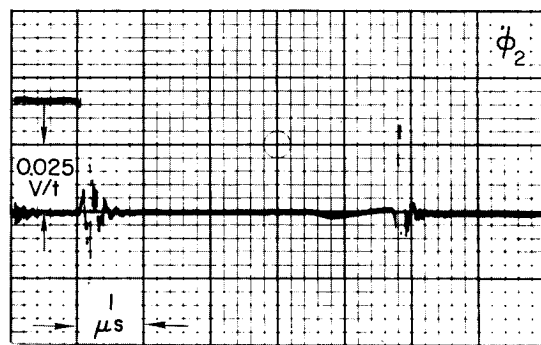
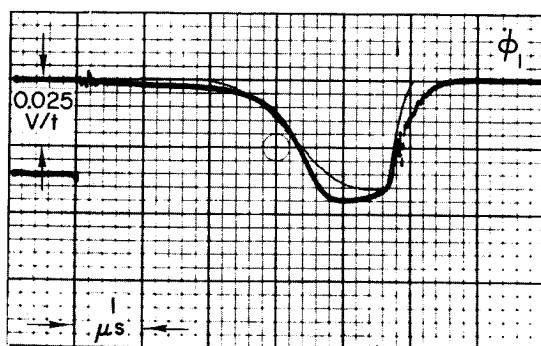
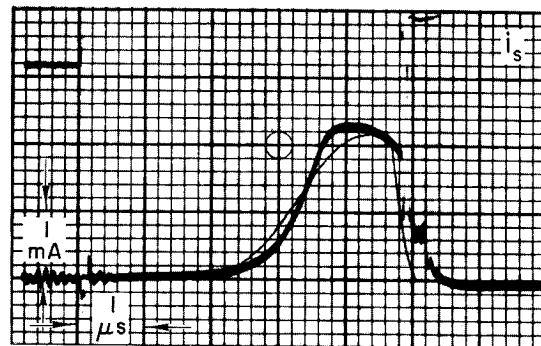
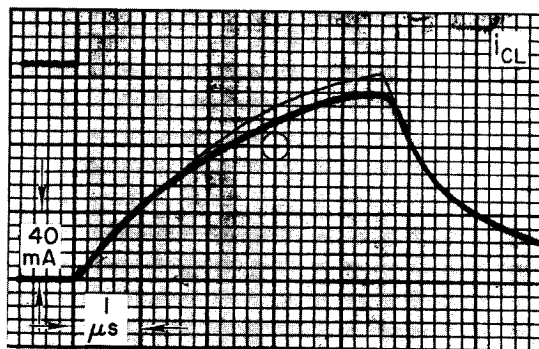
The above-listed experimental oscillograms and the corresponding computed waveforms are compared in Figs. 59, 60, and 61 for the cases of $T = -10^\circ\text{C}$ and $V_s = 15\text{V}$, $T = 25^\circ\text{C}$ and $V_s = 28\text{V}$, and $T = 85^\circ\text{C}$ and $V_s = 50\text{V}$, respectively. In the case of $T = -10^\circ\text{C}$ and $V_s = 15\text{V}$, the computation could not be completed in the four modes of operation because of a transistor turn-off in Submode III-C. (Proper operation was computed for $T = -10^\circ\text{C}$ at $V_s = 16.1\text{V}$, as we shall see later.) In order to be able to compare the experimental and computed waveforms for $T = -10^\circ\text{C}$ and $V_s = 15\text{V}$, the initial value of ϕ_2 in Mode 0-1 was raised from $-\phi_{r2}$ to $-0.8\phi_{r2}$. A marker designating $t = 0$ was photographed together with each oscillogram in Figs. 59, 60, and 61. In each oscillogram, one of the two arrows designating the vertical scale touches the abscissa (time axis).



TD-5670-80

(a) Mode I

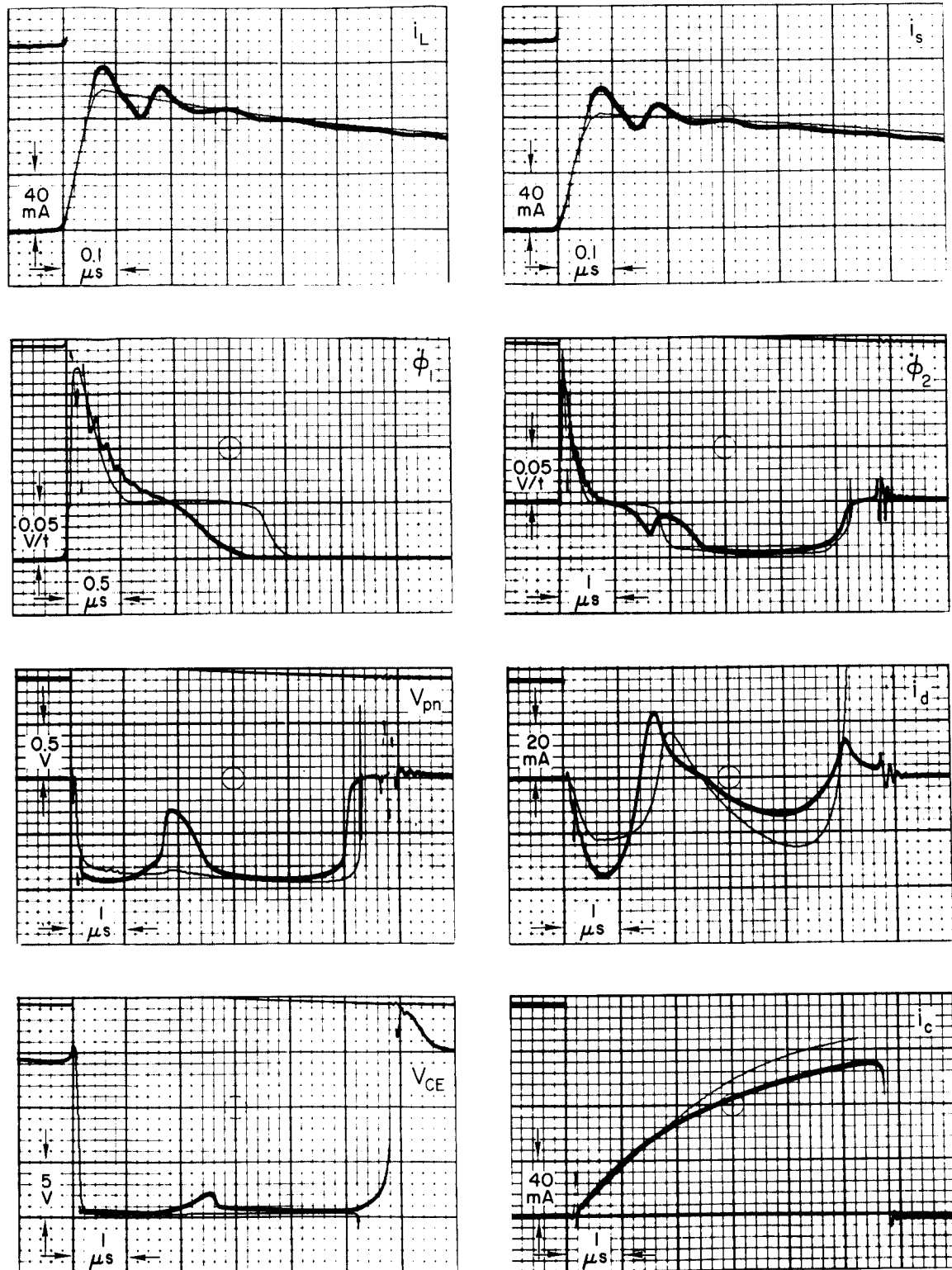
FIG. 59 EXPERIMENTAL (Heavy Line) AND COMPUTED (Light Line) CURRENT AND VOLTAGE WAVEFORMS IN FOUR MODES OF OPERATION OF A CORE-DIODE-TRANSISTOR BINARY COUNTER AT $T = -10^\circ\text{C}$ AND $V_s = 15\text{V}$



TD-5670-81

(b) Mode II

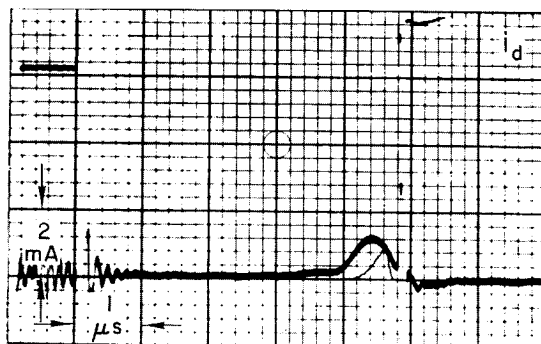
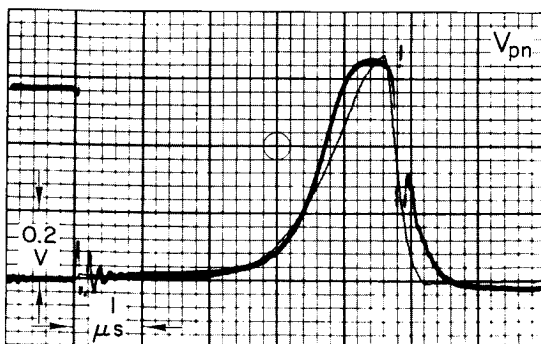
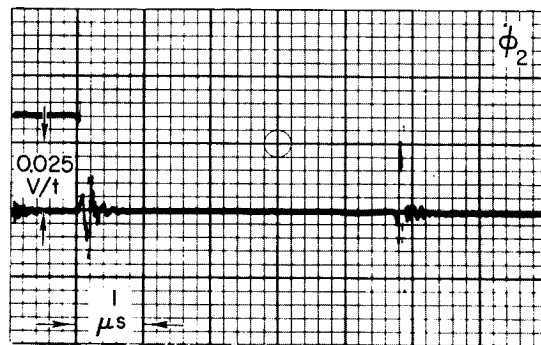
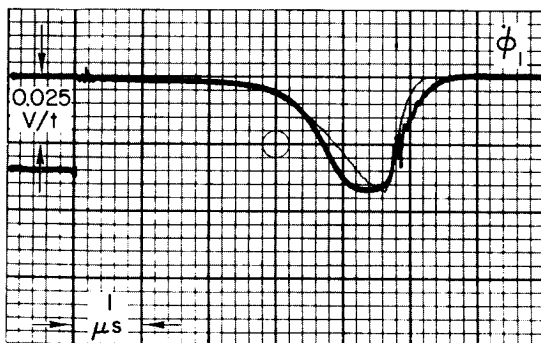
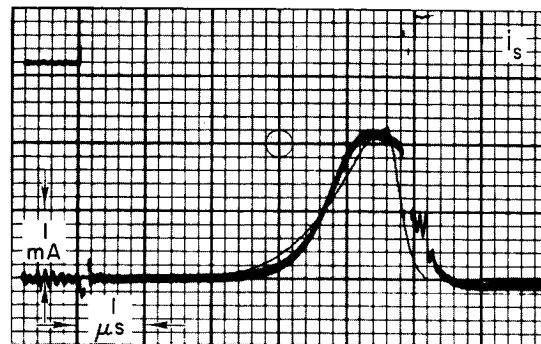
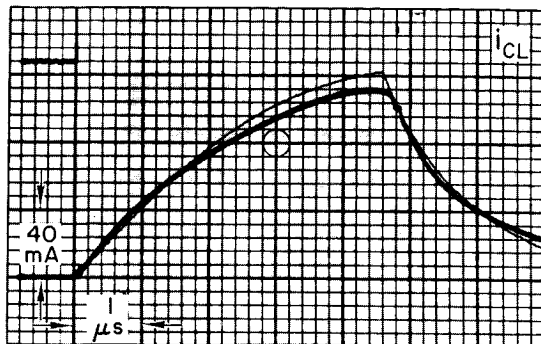
FIG. 59 Continued



TD-5670-82

(c) Mode III

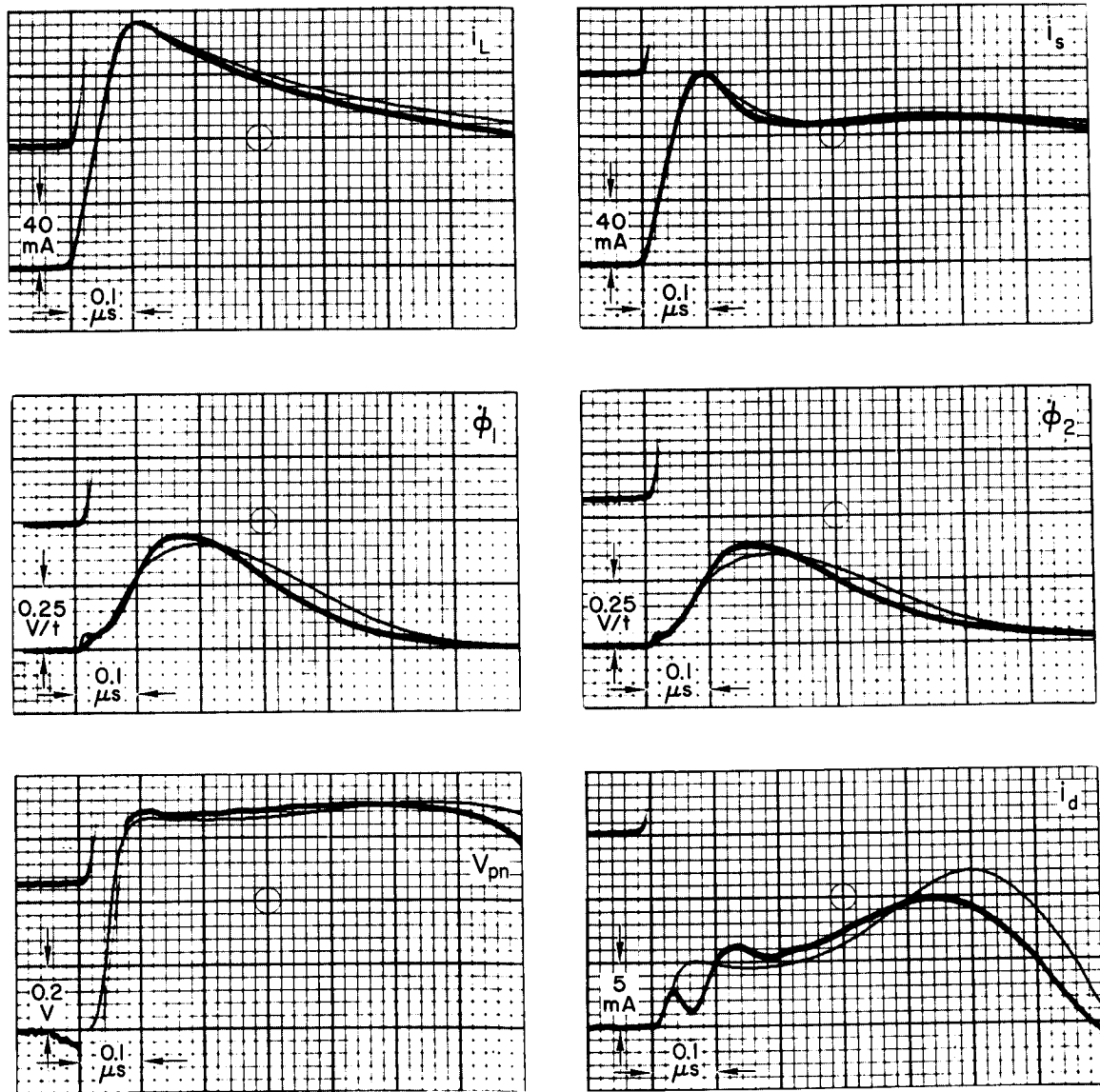
FIG. 59 Continued



(d) Mode IV

TD-5670-83

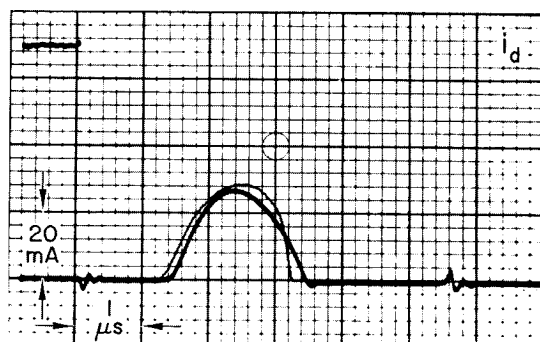
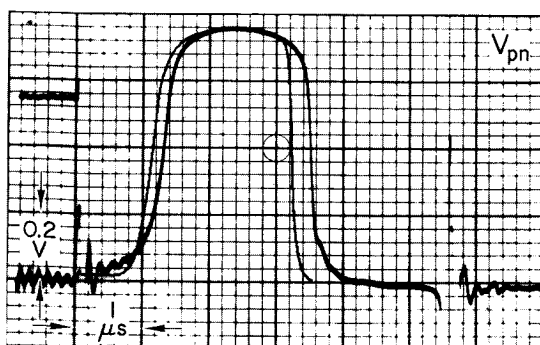
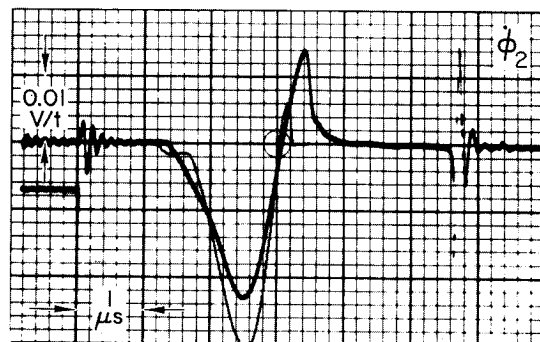
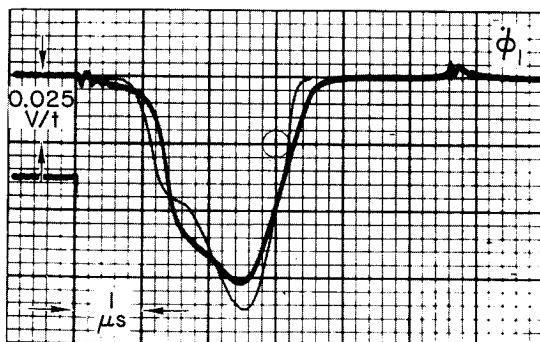
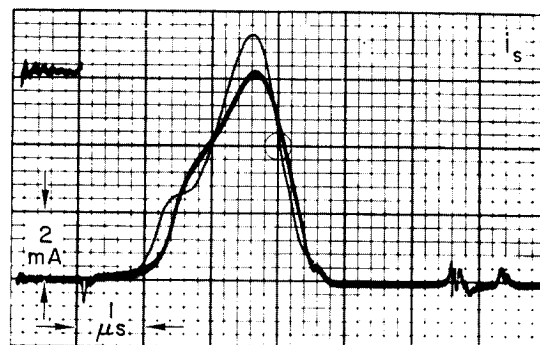
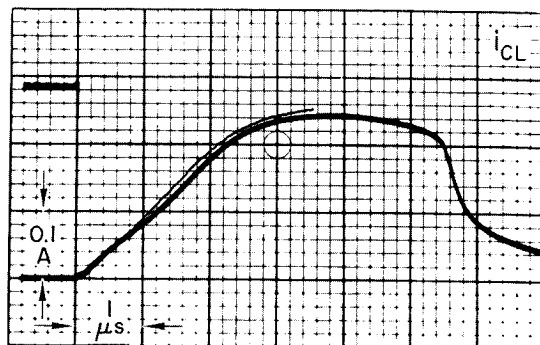
FIG. 59 Concluded



TD-5670-84

(a) Mode 1

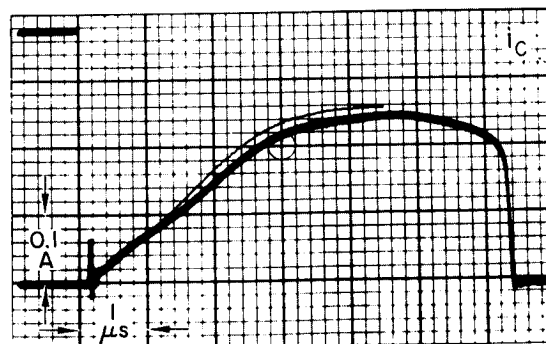
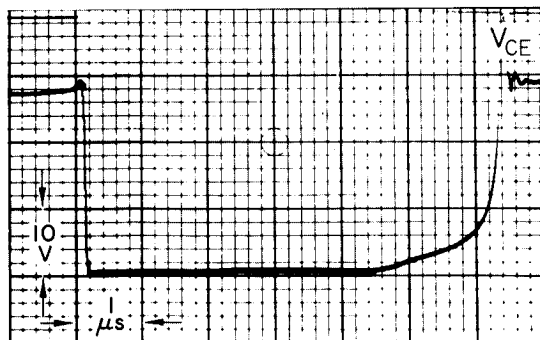
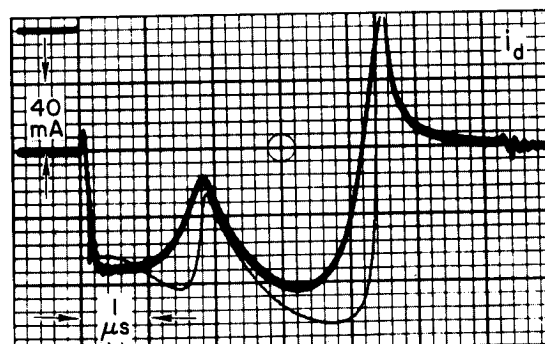
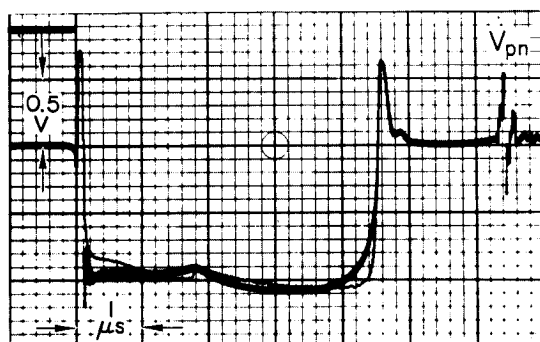
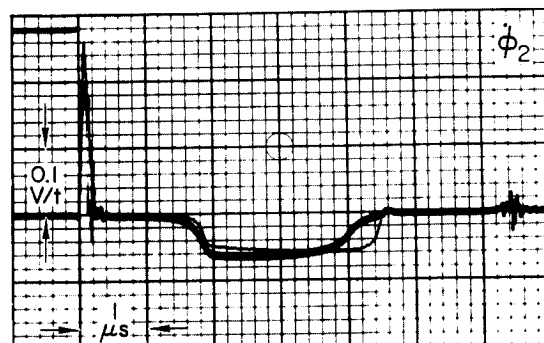
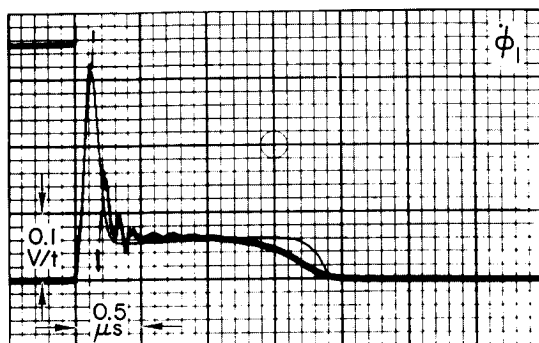
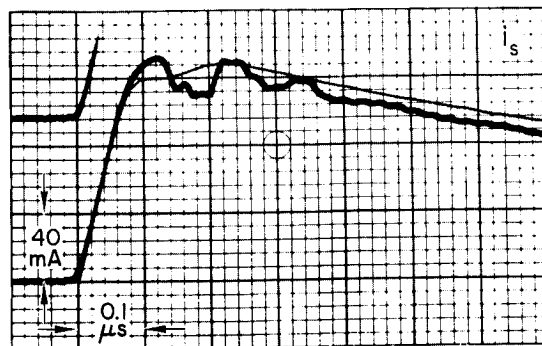
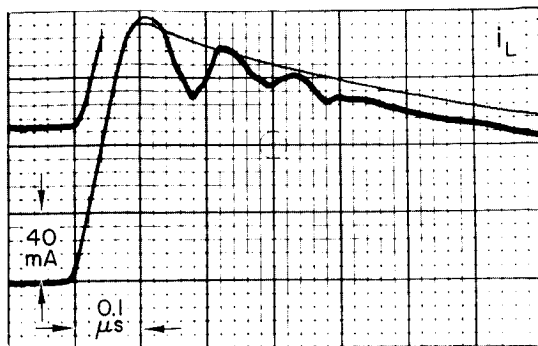
FIG. 60 EXPERIMENTAL (Heavy Line) AND COMPUTED (Light Line) CURRENT AND VOLTAGE WAVEFORMS IN FOUR MODES OF OPERATION OF A CORE-DIODE-TRANSISTOR BINARY COUNTER AT $T = 25^\circ C$ AND $V_s = 28V$



TD-5670-85

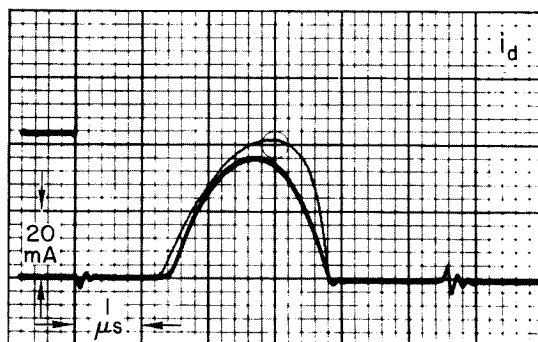
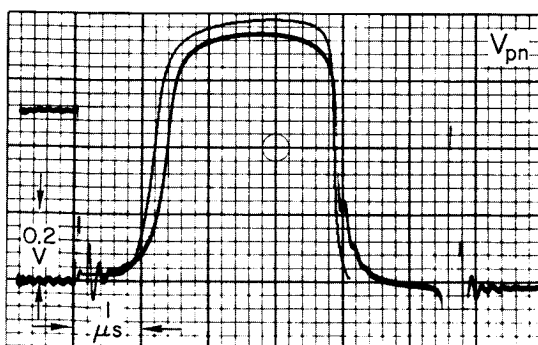
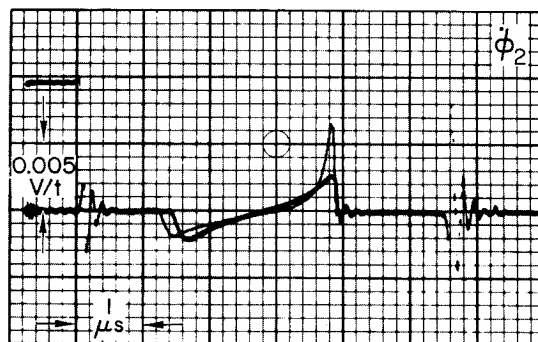
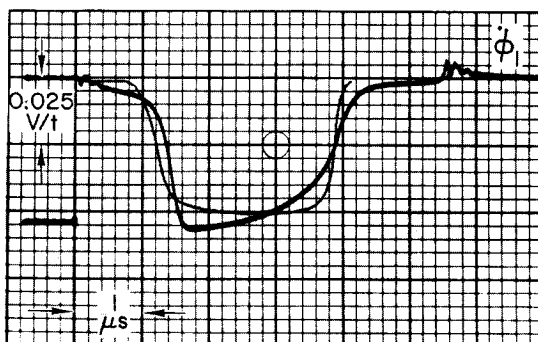
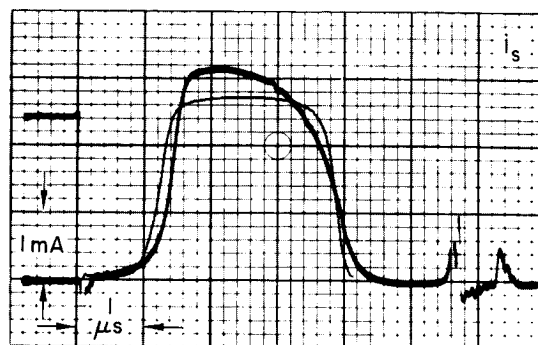
(b) Mode II

FIG. 60 Continued



TD-5670-86

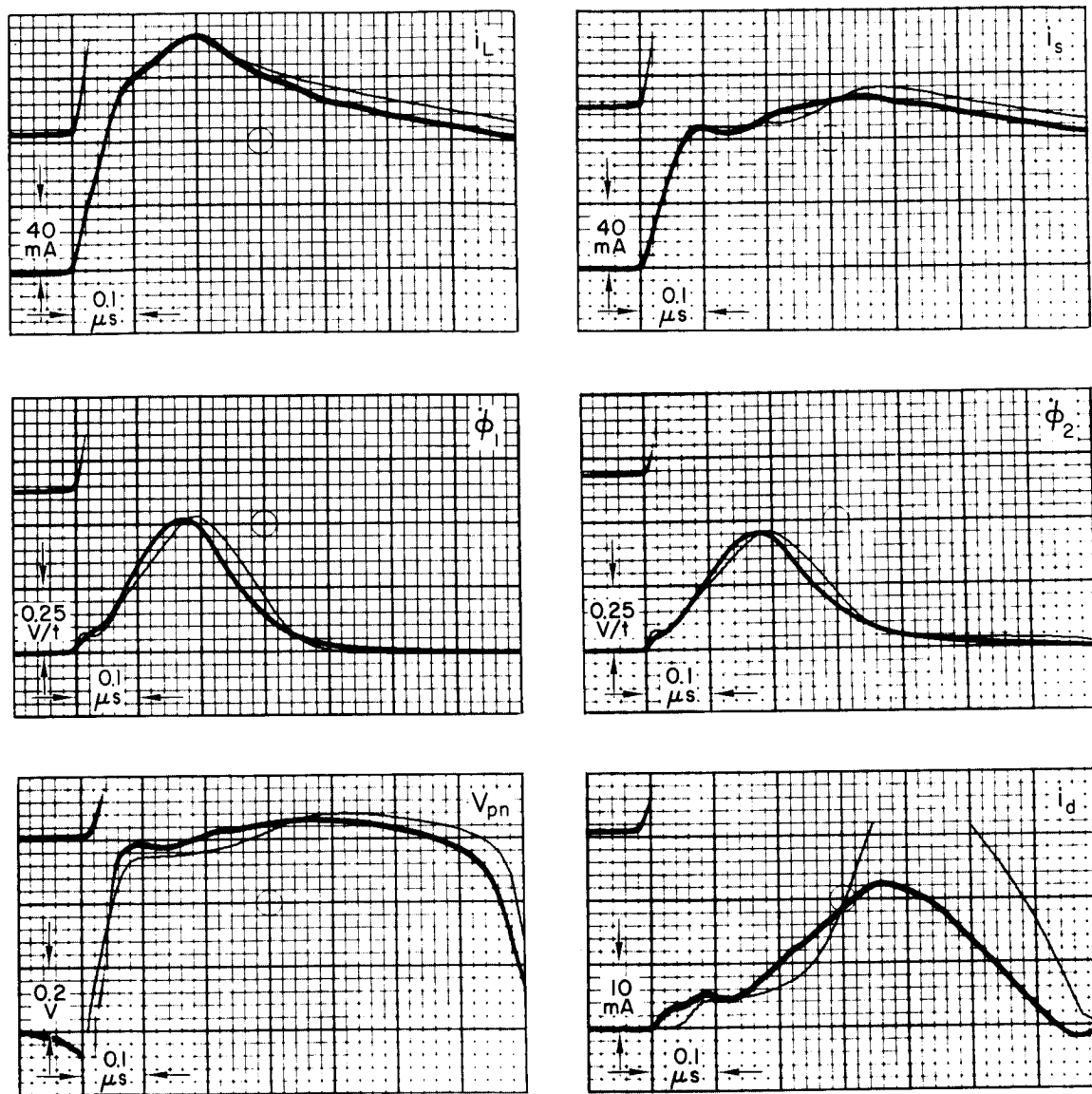
(c) Mode III
FIG. 60 Continued



TD-5670-87

(d) Mode IV

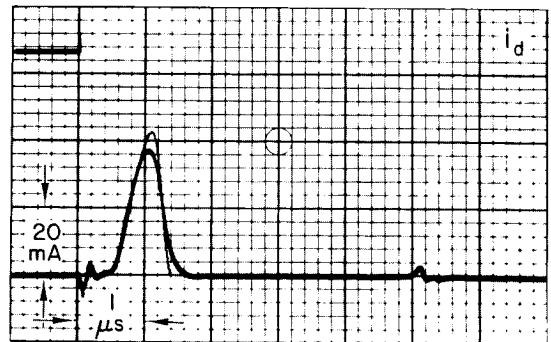
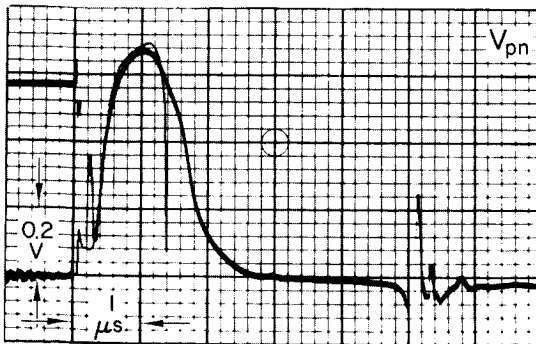
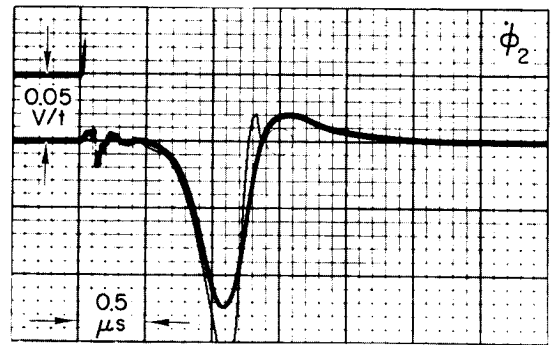
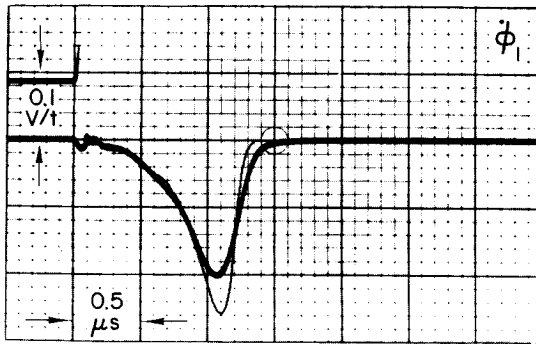
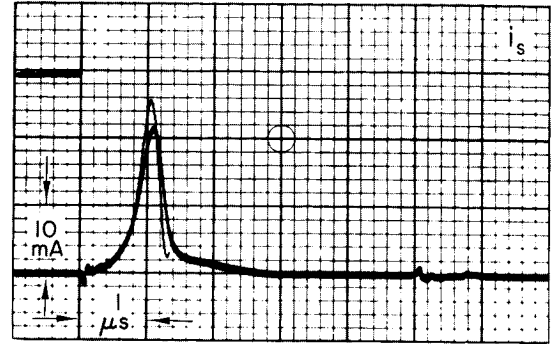
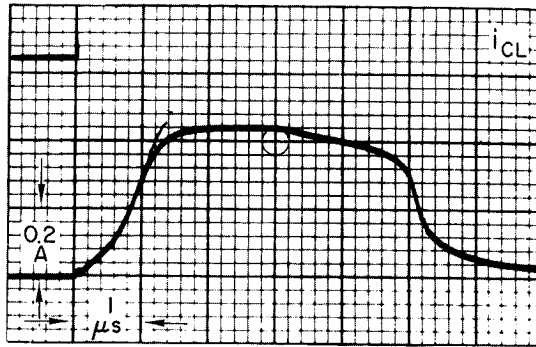
FIG. 60 Concluded



TD-5670-88

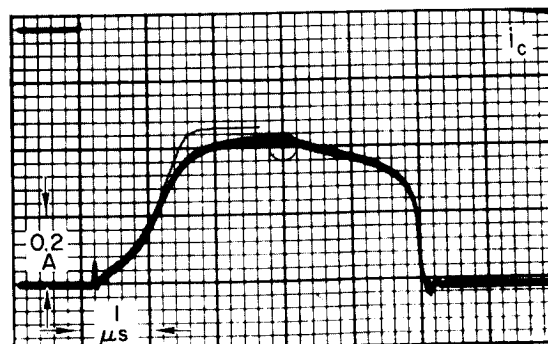
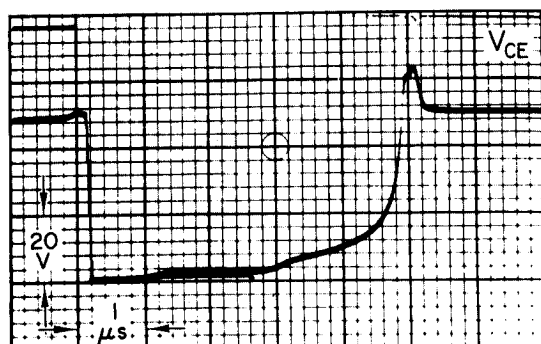
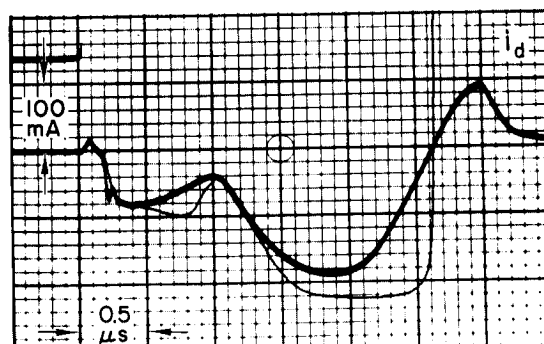
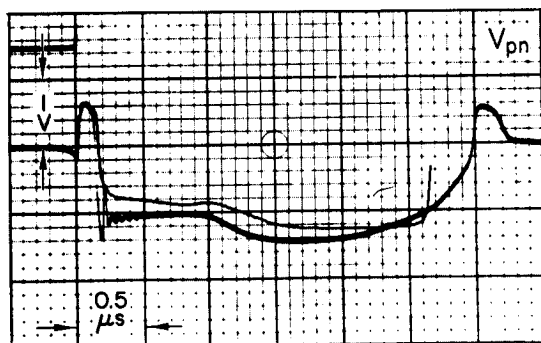
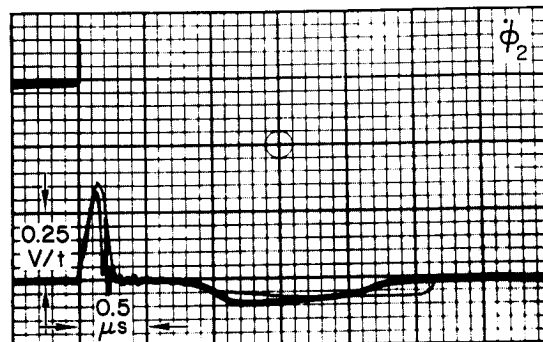
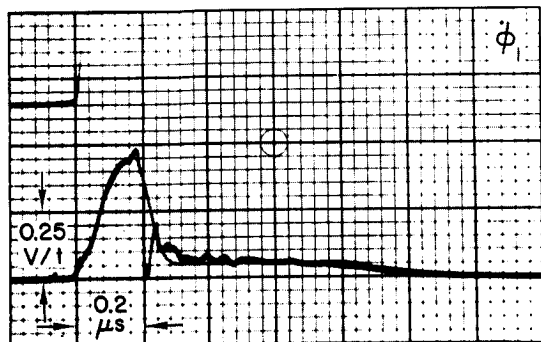
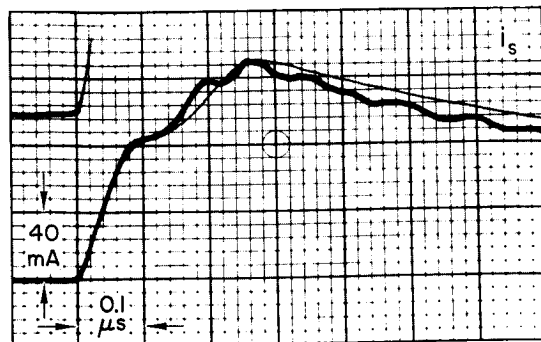
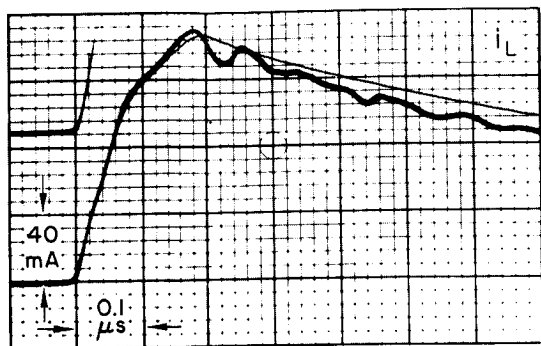
(a) Mode I

FIG. 61 EXPERIMENTAL (Heavy Line) AND COMPUTED (Light Line) CURRENT AND VOLTAGE WAVEFORMS IN FOUR MODES OF OPERATION OF A CORE-DIODE-TRANSISTOR BINARY COUNTER AT $T = 85^{\circ}\text{C}$ AND $V_s = 50\text{V}$



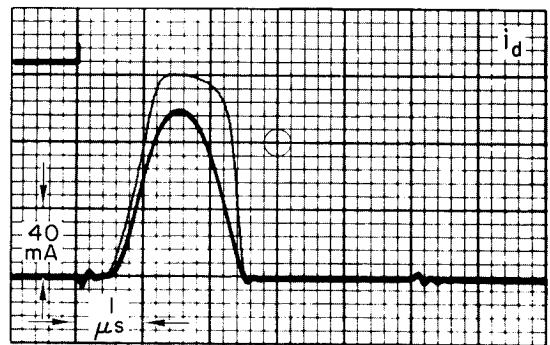
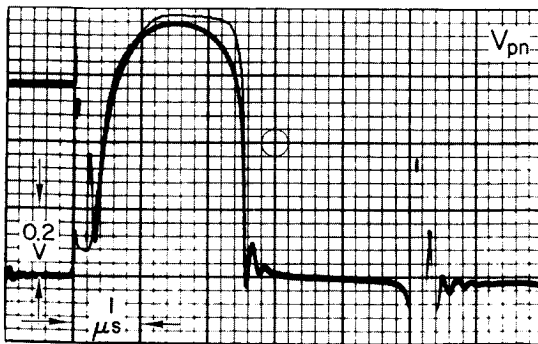
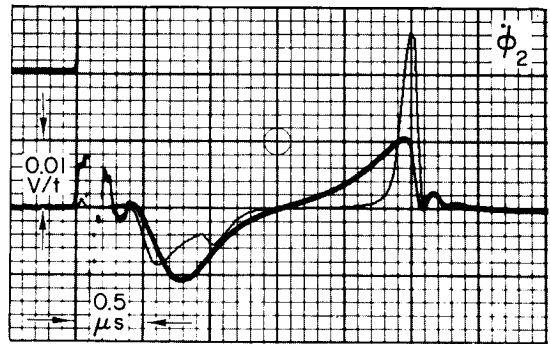
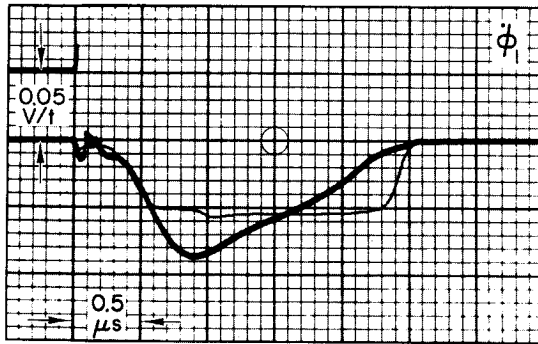
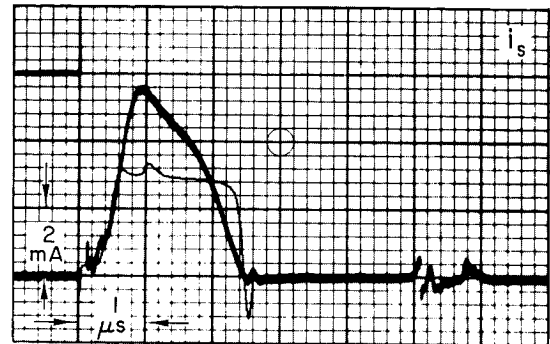
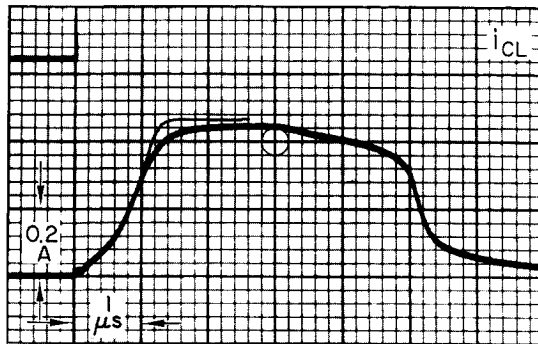
TD-5670-89

(b) Mode II
FIG. 61 Continued



TD-5670-9C

(c) Mode III



TD-5670-91

(d) Mode IV

FIG. 61 Concluded

b. Discussion

i. Comparing Experimental and Computed Results

In general, the agreement between the computed and the experimental waveforms of the time variables in Figs. 59, 60, and 61 is satisfactory. The main sources of disagreement are as follows:

- (1) A difference between the temperature at which the oscillograms were recorded and the temperature at which the device parameters were measured
- (2) Measurement errors
- (3) Inaccuracy in the device models
- (4) Computational errors.

Let us compare the computed and the experimental waveforms in each of Figs. 59, 60, and 61 separately.

Figure 59 ($T = -10^\circ\text{C}$; $V_s = 15\text{V}$)—The disagreements in $i_d(t)$ during Modes I, II, and IV are most noticeable. These are the result of the forward characteristic of the diode (see Fig. 44): If V_{pn} is below the "knee," an error in V_{pn} results in a magnified error in i_d . For example, at $T = -10^\circ\text{C}$, $V_{pn} = 0.6, 0.7$, and 0.8V correspond to $i_d = 0.2, 2$, and 20 mA , respectively [see Fig. 44(b)]. An error of 14.3 percent in V_{pn} is thus magnified to an error of 900 percent in i_d .

The disagreement of $\dot{\phi}_1(t)$ during $1\text{ }\mu\text{s} \lesssim t \lesssim 2\text{ }\mu\text{s}$ in Mode III stems from the inaccuracy in the initial value of ϕ_1 and from the inadequacy of our flux-switching model for switching from a partially set state. (Since V_s is low, $\Delta\phi_1$ during Modes II-1 and II-2 is too small to clear Core 1 close to $-\phi_r$, as is shown in Figs. 27 and 28.) As a result of this disagreement in $\dot{\phi}_1(t)$, there is also a disagreement in $\dot{\phi}_2(t)$ during $1\text{ }\mu\text{s} \lesssim t \lesssim 2\text{ }\mu\text{s}$ in Mode III. Consequently, the dip in the experimental V_{pn} does not appear in the computed V_{pn} .

Figure 60 ($T = 25^\circ\text{C}$; $V_s = 28\text{V}$)—The agreement is much better than in Fig. 59. From the viewpoint of applying this computer-aided analysis to compute $V_{s,\text{min}}$, this is unfortunate: one would prefer a better agreement for the low values of V_s .

Note that the good agreement for the waveforms of i_{CL} in Modes II-1 and IV-1 and i_c in Mode III is due to the nonlinearity of the

inductor model [Eq. (84)]. For V_s values around 15V, this nonlinearity is insignificant because i_{CL} and i_c are low enough to assume that $L \approx L_0$. However, for $V_s \gtrsim 28V$, this nonlinearity is very effective.

Figure 61 ($T = 85^\circ C$; $V_s = 50V$)—The agreement is, in general, not as good as in Fig. 60, but better than in Fig. 59.

The main disagreement occurs during Mode IV for $\dot{\phi}_1(t)$ and $i_s(t)$. This is caused by the error in the loading current of the clamping diode. The causes of this error are not adequately understood.

ii. All-Mode Variations of $\phi_1(F_1)$ and $\phi_2(F_2)$

Machine-plotted variations of $\phi_1(F_1)$ and $\phi_2(F_2)$ during all modes of operation, which were computed by the same computer run that computed the waveforms of the time variables, are shown in Figs. 62, 63, and 64 for the cases of $T = -10^\circ C$ and $V_s = 15V$, $T = 25^\circ C$ and $V_s = 28V$, and $T = 85^\circ C$ and $V_s = 50V$, respectively. Static $\phi(F)$ loops (dashed lines) have been added manually in each case. Since the computed $\phi_2(F_2)$ loop for the case of $T = -10^\circ C$ and $V_s = 15V$ does not close due to the incorrect initial condition of $\phi_2 = -0.8\phi_{r2}$ in Mode I, a dashed line, similar to the one computed for $V_s = 16.1V$, is added in Fig. 62 in order to indicate how the loop would appear had the computed $V_{s,min}$ been equal to or less than 15V.

The variations of $\phi_1(F_1)$ and $\phi_2(F_2)$ are very important in understanding the operation of the binary counter and the causes of its failures. For detailed explanation of this behavior, see Sec. II-B and compare Figs. 62 through 64 with Figs. 27 through 30.

5. Computed $V_{s,min}$ for Various Worst-Case Conditions

Although it is not feasible in practice to build a test circuit with worst-case components, the probability of worst-case occurrence is not zero. Consequently, the main function of the computer-aided analysis is to compute the range of supply voltage using worst-case parameter values. Since the specified maximum allowable V_{CE} voltage (50V) was found to be below $V_{s,max}$, the analysis is limited to computation of $V_{s,min}$, below which the circuit fails to operate properly. (Only a minor change is needed in order to compute $V_{s,max}$.)

The level of confidence in this type of worst-case analysis is based on the agreement between the computed and the experimental waveforms of

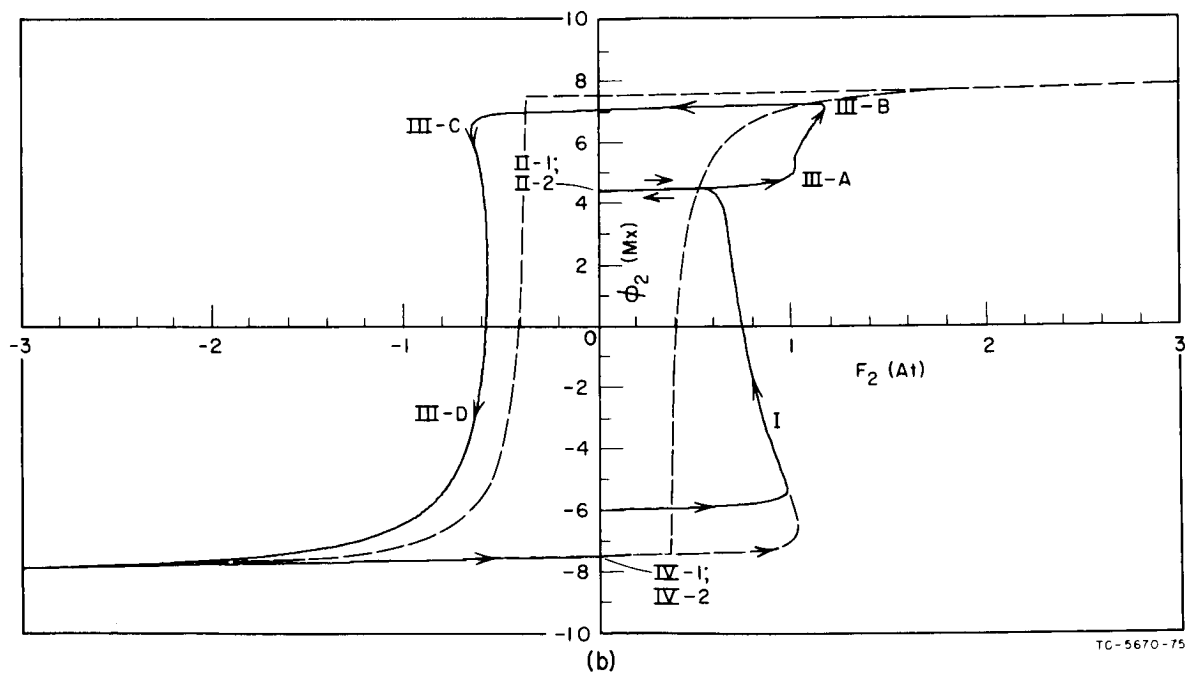
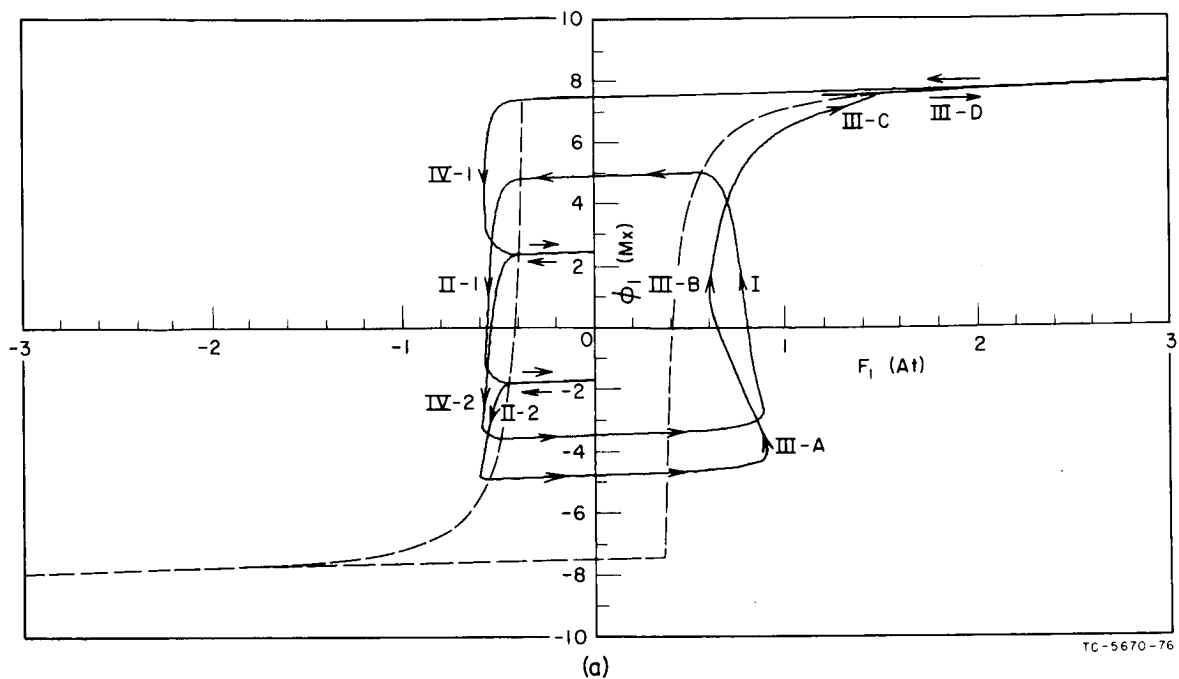


FIG. 62 VARIATIONS OF $\phi_1(F_1)$ AND $\phi_2(F_2)$ DURING FOUR MODES OF OPERATION OF A CORE-DIODE-TRANSISTOR BINARY COUNTER AT $T = -10^\circ\text{C}$ AND $V_s = 15\text{V}$

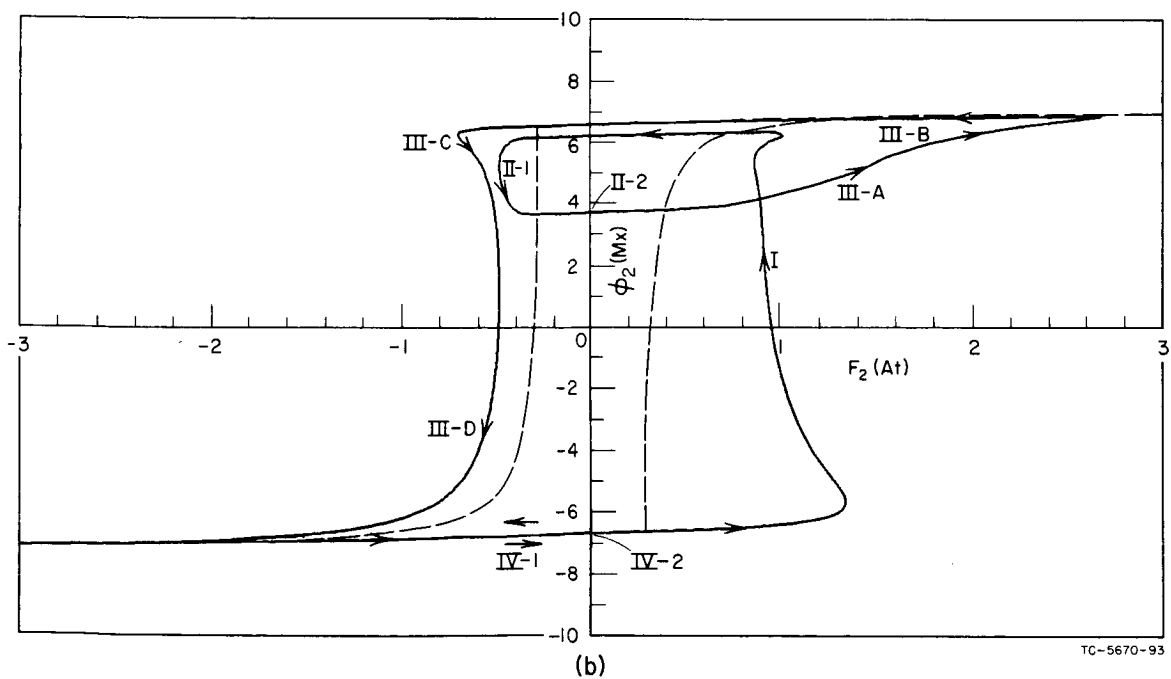
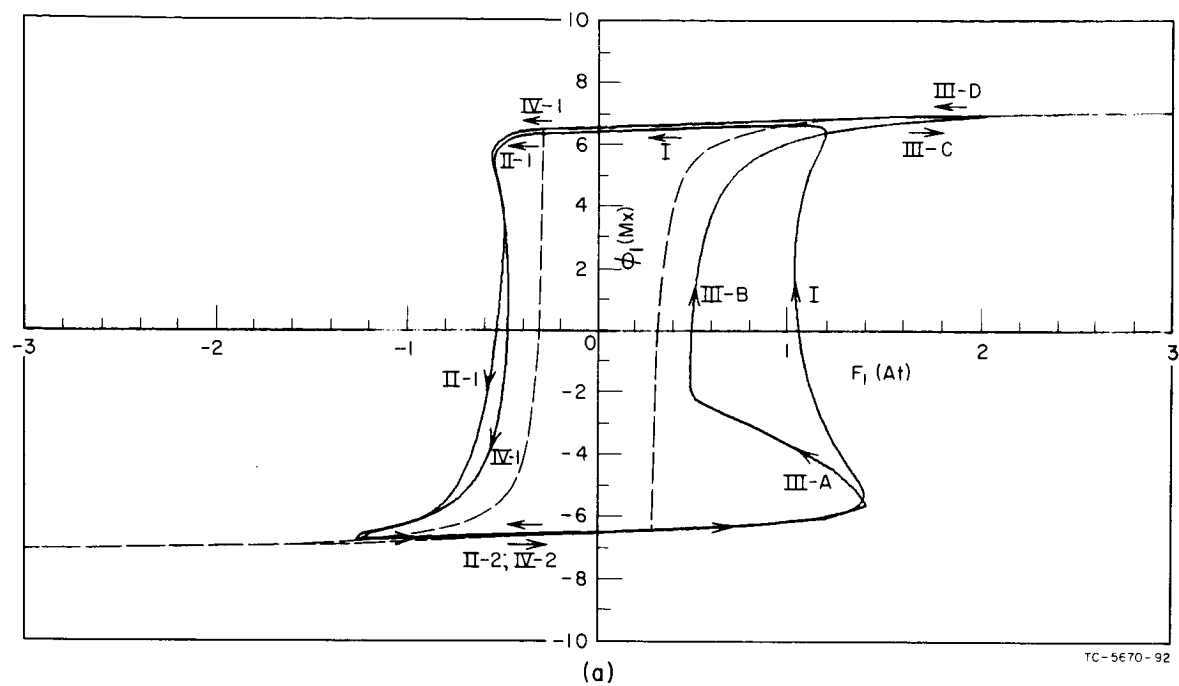


FIG. 63 VARIATIONS OF $\phi_1(F_1)$ AND $\phi_2(F_2)$ DURING FOUR MODES OF OPERATION OF A CORE-DIODE-TRANSISTOR BINARY COUNTER AT $T = 25^\circ\text{C}$ AND $V_s = 28\text{V}$

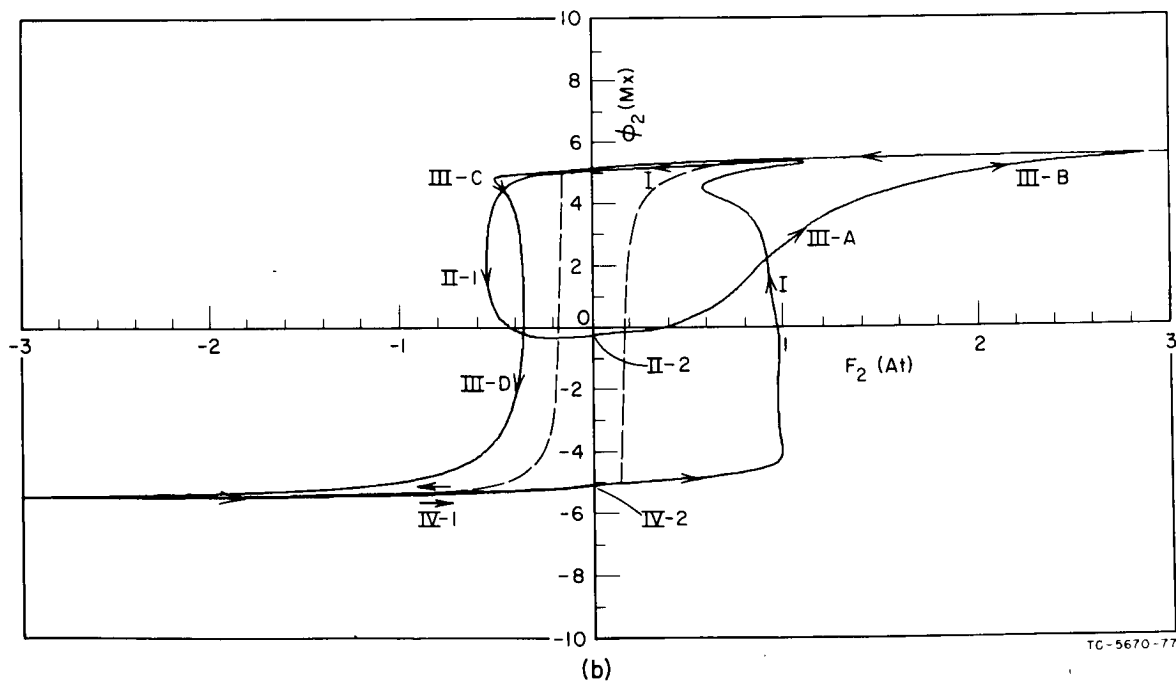
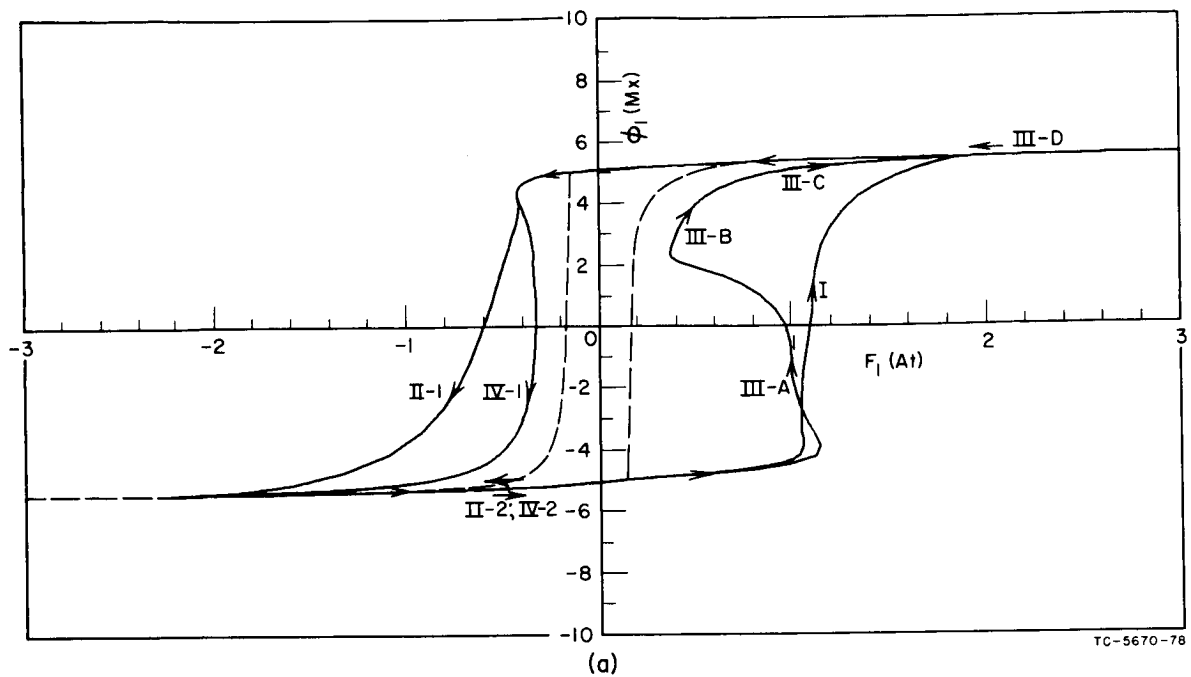


FIG. 64 VARIATIONS OF $\phi_1(F_1)$ AND $\phi_2(F_2)$ DURING FOUR MODES OF OPERATION OF A CORE-DIODE-TRANSISTOR BINARY COUNTER AT $T = 85^\circ\text{C}$ AND $V_s = 50\text{V}$

the time variables, Figs. 59 through 61, and on the agreement between the computed and the measured $V_{s, \min}$, to be discussed next.

a. Computed $V_{s, \min}$ vs. Measured $V_{s, \min}$

Using the actual core and circuit parameter values at $T = -10^\circ\text{C}$, the computer program in Appendix G was run with V_s values starting from 13V and increasing in steps of one volt until a proper four-mode operation was achieved. The results of computation showed that for $V_s = 13\text{V}$, the operation fails because the transistor does not turn on in Mode III, and that for $V_s = 14, 15$, and 16V , the operation fails because the transistor turns off spuriously in Submode III-C. A proper operation was computed for $V_s = 17\text{V}$. A further search between $V_s = 16\text{V}$ and $V_s = 17\text{V}$ resulted in a proper operation for $V_s = 16.1\text{V}$. Limiting the accuracy to 0.1V, we conclude that the result of computation is $V_{s, \min} = 16.1\text{V}$. In comparison, it was found experimentally that at $T = -10^\circ\text{C}$, $V_{s, \min} = 15.0\text{V}$ (the transistor turned off spuriously at $V_s = 14.9\text{V}$). For pessimistic design criteria, this result is fortunate because it is safer to obtain a computed $V_{s, \min}$ higher than the measured $V_{s, \min}$ than vice versa.

In the computer runs described so far, the maximum percentage deviation from the nominal parameter value, d_{\max} , was set to zero. The results of computation with values of d_{\max} larger than zero are described next.

b. Computed Worst-Case $V_{s, \min}$ vs. d_{\max}

The program in Appendix G was run on a Burroughs B5500 digital computer in order to compute $V_{s, \min}$ vs. d_{\max} at $T = -10^\circ\text{C}$. The value P of each core and circuit parameter was determined by using Eq. (163):

$$P = P_n \left(1 + S \frac{d_{\max}}{100} \right),$$

where P_n is the nominal parameter value and S is the sign of a change in P which increases $V_{s, \min}$ (in case P has no effect on $V_{s, \min}$, $S = 0$). Tabulation of S for each parameter is given in Table III. For each d_{\max} value, a search for $V_{s, \min}$ was made in a way similar to the one described above in computing $V_{s, \min}$ for $d_{\max} = 0$.

Using the values $d_{\max} = 5, 10, 15, 20$ and 25 percent, the results of computation were found to be $V_{s,\min} = 16.8, 18.8, 19.8, 21.3$ and $23.3V$, respectively. These results, and the result of $V_{s,\min} = 16.1V$ for $d_{\max} = 0$, are plotted in Fig. 65.

c. Discussion

i. $V_{s,\min}$ vs. d_{\max}

The plot of computed $V_{s,\min}$ vs. d_{\max} in Fig. 65 has an inflection point near $d_{\max} = 7.5$ percent. In view of the complexity of the composite effect of the core and circuit parameters on the transistor turn-off, this result is possible.

The specification of the supply voltage is $V_s = 28 \pm 5.6V$. As shown in Fig. 65, the specified minimum supply voltage of $22.4V$ intersects $V_{s,\min}$ at $d_{\max} = 23$ percent. Hence, in order to assure proper operation within the specified range of V_s , the worst-case variation of parameters should not exceed 23 percent. Considering a safety factor, this parameter variation should be limited to a lower value than 23 percent.

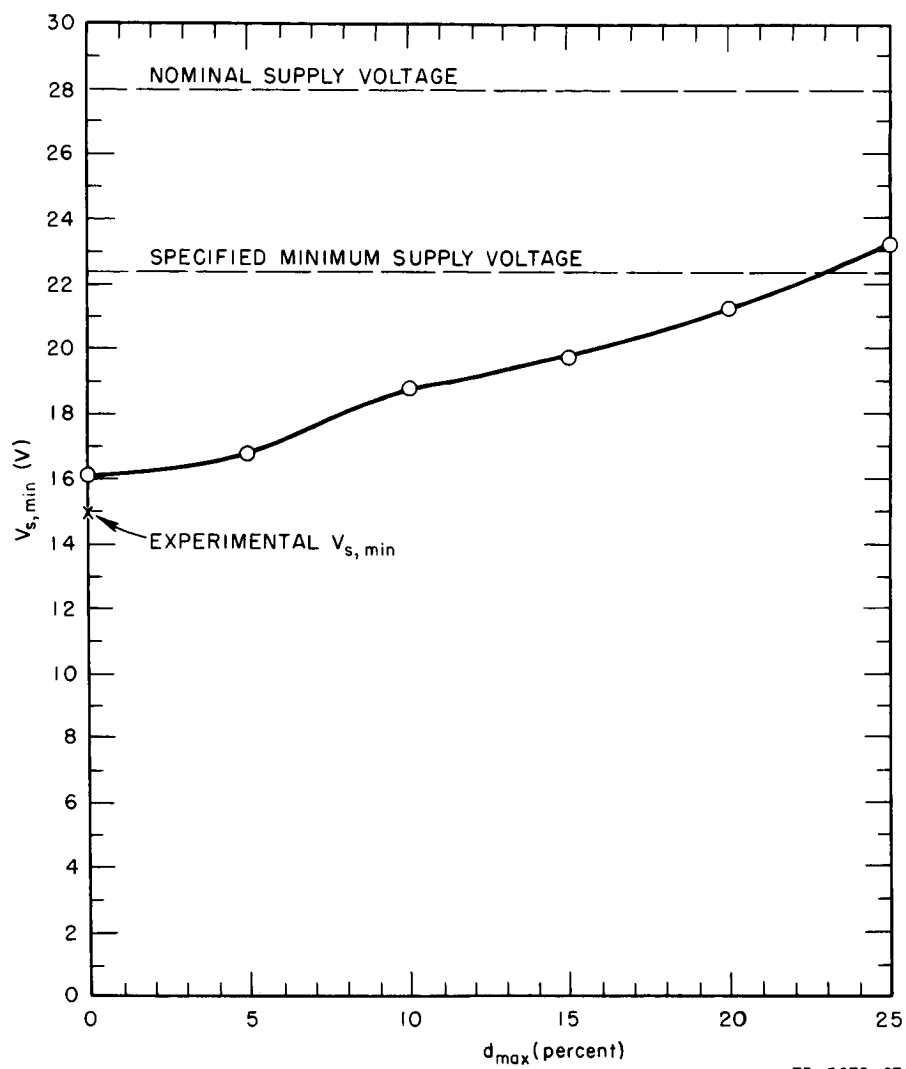
ii. Sign S

The sign S of each of several parameters in Table III was determined experimentally by changing the parameter value and observing the effect of this change on $V_{s,\min}$. Such a test was performed for any parameter whose value can be changed by simply inserting in series or in parallel a similar component, e.g., a resistor, an inductor, a diode, a winding, etc.

The sign S of each of the rest of the parameters could be found by simulating a parameter change on the computer and observing its effect on $V_{s,\min}$. This was not done because of the lack of sufficient funds. Instead, these signs were postulated on the basis of our understanding of the circuit operation and the causes of spurious transistor turn-off in Mode III (see Figs. 27 and 28). It is possible, therefore, that a few of these signs are erroneous.

iii. Flux Changes at $V_s = V_{s,\min}$

The computed flux changes at $V_s = V_{s,\min}$ were examined by inspecting the computer output (time variables vs. t) for all d_{\max} values.



TB-5670-67

FIG. 65 THE EFFECT OF WORST-CASE PARAMETER VARIATION ON COMPUTED $V_{s,min}$

It was found that for all the values of d_{\max} (and, hence, also of ϕ_r), the *initial* value of ϕ_2 is equal to $(0.46 \pm 0.04) \phi_r$ in Mode III (and also in Mode II, since $\Delta\phi_{2\text{II}} \approx 0$) and is equal to $-\phi_r$ in Mode I (and also in Mode IV, since $\Delta\phi_{2\text{IV}} \approx 0$). No such correlation at $V_s = V_{s,\min}$ was found for the initial values of ϕ_1 , except for the initial value $\phi_1 = \phi_r$ in Mode IV.

It was also found that the *final* values of ϕ_1 and ϕ_2 in Mode IV-2 were equal to the *initial* values of ϕ_1 and ϕ_2 , respectively, in Mode I, as they should be. This validates the use of Modes 0-1 and 0-2 in computing the initial values of ϕ_1 and ϕ_2 in Mode I.

6. Conclusions

It is concluded from the agreement between the computed and experimental results (waveforms of time variables and $V_{s,\min}$ for $d_{\max} = 0$) that the results of the computer analysis are reliable. Thus, on the basis of the computed $V_{s,\min}$ vs. d_{\max} , it is concluded that the binary counter stages will operate properly within the specification of $V_s = 28 \pm 5.6$ volts if no parameter variation exceeds 23 percent. As a safety factor, the parameter variation should be limited to a smaller value. These conclusions are based on the analysis of the second stage only. Since the effects of variations of V_s and the core and circuit parameters on this stage are the same as the effects on any other stage [except Stage (1)], these conclusions hold for the entire binary counter, except for Stage (1) and the driver of the binary counter (see Fig. 25).

APPENDIX A

COMPUTER PROGRAM FOR A VOLTAGE DRIVE

VOLTAGE DRIVE.

```

BEGIN REAL LI, LO, PHIR, PHIS, HA, HQ, HN, LAMBDA, FOPP, NU, ROP, FO, 0000000
FB, V1, V2, F12, F23, PHIDOTMAX, T, OMEGA, PSI, ALPH, BETA, TAUS, 0000001
DELT, AF, PHIDPRIME, PHIDOTP, PHIDOTPPRIME, FM2, FM1, FZ, F, PHID, 0000002
CAPT, PHIDOTC, PHIC; 0000003
INTEGER LINES, COUNT; 0000004
INTEGER CT; 0000005
LABEL STARTCORE, QUIT; 0000006
ALPHA CORENAME, TD1, TD2, TD3, TD4, TD5; 0000007
FILE FACT (3, 10), LP 4 (3, 15); 0000008
FORMAT COREPARAMETERS ("CORE ", A6, X4, "LI=", F8.5, X4, "LO=", F8.5, 0000009
X4, "PHIR=", F9.5, X4, "PHIS=", F9.5, X4, "HA=", F9.4, X4, "HQ=", 0000010
F9.4, /, "HN=", F9.4, X4, "LAMBDA=" F7.4, X4, "FOPP=", F7.4, X4, 0000011
"NU=", F7.4, X4, "ROP=", F7.4, X4, "FO=", F7.4, X4, "FB=", F7.4 / / / 0000012
), CKTPARAMETERS (5 A6, X5, "PHIDOTMAX = ", F8.4, X5, "CAPT = ", F9.3 0000013
/ /), FMO (5 F20.6, I6), OUTPUTHEADING (X13, "T", X19, "PHIDOT", X14, "0000014
HI", X17, "F", X19, "PHID", X7, "CT" /); 0000015

REAL PROCEDURE ARCCOS (X1); 0000016
VALUE X1; 0000017
REAL X1; 0000018
BEGIN REAL PIC, MC, X, T, Z, PI2; 0000019
LABEL L1; 0000020
IF ABS (X1) < 1D-6 THEN 0000021
BEGIN ARCCOS + X1 + 1.57079632679; 0000022
GO TO L1 0000023
END; 0000024
PIC + 0; 0000025
MC + 1; 0000026
Z + SIGN (X1); 0000027
X + ABS (X1); 0000028
IF X > 0.92387953231 THEN 0000029
BEGIN X + SQRT ((1 - X) / 2); 0000030
PIC + 1.57079632679; 0000031
MC + - 2 0000032
END ELSE 0000033
BEGIN IF X > 0.70710678119 THEN 0000034
BEGIN X + 2 * (X * 2) - 1; 0000035
PIC + 0.785398163397; 0000036
MC + 0.5 0000037
END; 0000038
END; 0000039
T + X * 2; 0000040
ARCCOS + ((0.364541120348 - 4.22649415434 / (T - 8.66648256098 - 0000041
6.1228848016 / (T - 3.2316720226 - 0.312873861283 / (T - 0000042
1.63902626905 - 0.0268477822258 / (T - 1.16535753774)))) * MC * X 0000043
+ PIC) * Z + 1.57079632679; 0000044
L1; 0000045
END ARCCOS (X1); 0000046

REAL PROCEDURE MMF (PHIDOT, PHI, AF, PHID); 0000047
VALUE PHIDOT, PHI, AF; 0000048
REAL PHIDOT, PHI, PHID, AF; 0000049
BEGIN REAL G, GPR, F, P1, P2; 0000050
LABEL LOOP; 0000051
F + AF; 0000052
CT + 0; 0000053
LOOP: CT + CT + 1; 0000054
COMMENT: COMPUTE PHID AND PHIDPRIME VS. F; 0000055
IF F ≤ F12 THEN 0000056
BEGIN PHID + V1 * F * LN ((F - HA * LO) / (F - HA * LI)) - PHIR; 0000057

```

```

      PHIDPRIME + V1 * (LN ((F - HA * LO) / (F - HA * LI)) + F * (1 /
      (F - HA * LO) - 1 / (F - HA * LI)))
END;
IF F12 < F AND F ≤ F23 THEN
  BEGIN PHID + V2 * (F / HQ - LI + F * (1 / HN - 1 / HQ) * LN ((1 -
    HN / HQ) / (1 - HN * LI / F))) - PHIR;
    PHIDPRIME + V2 * (1 / HQ + (1 / HN - 1 / HQ) * (LN (F * (1 - HN
    / HQ) / (F - HN * LI)) - HN * LI / (F - HN * LI)))
  END;
IF F23 < F THEN
  BEGIN PHID + V2 * (LO - LI + F * (1 / HN - 1 / HQ) * LN ((F - HN *
    LO) / (F - HN * LI))) - PHIR;
    PHIDPRIME + V2 * (1 / HN - 1 / HQ) * (LN ((F - HN * LO) / (F -
    HN * LI)) + F * HN * (LO - LI) / ((F - HN * LO) * (F - HN * LI)
    ))
  END;
COMMENT: COMPUTE PHIDOTP AND PHIDOTPPRIME VS. F;
IF F ≤ FOPP THEN
  BEGIN PHIDOTP + 0;
    PHIDOTPPRIME + 0
  END;
IF FOPP < F AND F ≤ FB THEN
  BEGIN PHIDOTP + LAMBDA * (F - FOPP) * NU;
    PHIDOTPPRIME + LAMBDA * NU * (F - FOPP) * (NU - 1)
  END;
IF FB < F THEN
  BEGIN PHIDOTP + ROP * (F - F0);
    PHIDOTPPRIME + ROP
  END;
P1 + 2 * PHI + PHIS - PHID;
P2 + PHIS + PHID;
G + PHIDOTP * (1.0 - (P1 / P2) * 2) - PHIDOT;
GPR + PHIDOTPPRIME * (1.0 - (P1 / P2) * 2) + 4 * PHIDOTP *
PHIDPRIME * P1 * (PHI + PHIS) / (P2 * 3);
F + F - G / GPR;
IF ABS (G / GPR) > ABS (.0001 * F) AND CT < 20 THEN GO TO LOOP;
MMF + F;
END MMF;

STARTCORE: READ (FACT, /, CORENAME, LI, LO, PHIR, PHIS, HA, HQ, HN,
LAMBDA, FOPP, NU, ROP, F0, FB) [QUIT];
V1 + (PHIS - PHIR) / ((LO - LI) * HA);
V2 + (PHIS + PHIR) * HQ / ((LO - LI) * HN);
F12 + HQ * LI;
F23 + HQ * LO;
BEGIN LABEL SWITCHING;
  COMMENT INSERT VOLTAGE DRIVE PACKAGE HERE;
  COMMENT PHIDOT = PHIDOTMAX * SIN(OMEGA * T);
  REAL PROCEDURE PHIDOT (T);
    VALUE T;
    REAL T;
    BEGIN REAL PHDT;
      IF T ≤ CAPT THEN PHDT + PHIDOTMAX * SIN (OMEGA * T) ELSE PHDT +
      0.0;
      PHIDOT + PHDT;
    END PHIDOT;
    REAL PROCEDURE PHI (T);
      VALUE T;
      REAL T;
      BEGIN REAL PH;
        IF T ≤ CAPT THEN PH + - PHIR + PHIDOTMAX * (1.0 - COS (OMEGA *
        T)) / OMEGA ELSE PH + PHI (CAPT);
        PHI + PH;
      END PHI;
      TD1 + " SIN";
      TD2 + "US0IDA";

```

TD3 + "L VOLT";	0000123
TD4 + "AGE DR";	0000124
TD5 + "IVE ";	0000125
FOR PHIDOTMAX + .05 DO FOR CAPT + 3. x @-6 DO	0000126
BEGIN OMEGA + 3.14159 / CAPT;	0000127
IF PHIDOTMAX ≤ PHIR × OMEGA THEN TAUS + CAPT ELSE TAUS + ARCCOS	0000128
(1.0 - 2 × PHIR × OMEGA / PHIDOTMAX) / OMEGA;	0000129
FZ + 1.01 × FOPP;	0000130
COMMENT END OF PACKAGE;	0000131
DELT + 0.002 × TAUS;	0000132
WRITE (LP [PAGE]);	0000133
WRITE (LP, CKTPARAMETERS, TD1, TD2, TD3, TD4, TD5, PHIDOTMAX,	0000134
CAPT × @6);	0000135
WRITE (LP, COREPARAMETERS, CORENAME, LI × @3, LO × @3, PHIR ×	0000136
@8, PHIS × @8, HA, HQ, HN, LAMBDA, FOPP, NU, ROP, FO, FB);	0000137
WRITE (LP, OUTPUTHEADING);	0000138
T + 0.0;	0000139
COUNT + 0;	0000140
PHID + PHIC + - PHIR;	0000141
FM2 + FM1 + F + FZ;	0000142
WRITE (LP, FMO, T × @6, PHIDOTC, PHIC × @8, F, PHID × @8);	0000143
LINES + 1;	0000144
SWITCHING: T + T + DELT;	0000145
COUNT + COUNT + 1;	0000146
PHIDOTC + PHIDOT (T);	0000147
PHIC + PHI (T);	0000148
AF + 2 × FM1 - FM2;	0000149
F + MMF (PHIDOTC, PHIC, AF, PHID);	0000150
FM2 + FM1;	0000151
FM1 + F;	0000152
IF PHIC > PHID OR F > 5 × FOPP THEN PHIDOTC + 0.0;	0000153
IF COUNT MOD 10 = 0 OR PHIDOTC = 0.0 THEN	0000154
BEGIN IF LINES MOD 50 = 0 THEN	0000155
BEGIN WRITE (LP [PAGE]);	0000156
LINES + LINES + 2;	0000157
WRITE (LP, OUTPUTHEADING);	0000158
END;	0000159
WRITE (LP, FMO, T × @6, PHIDOTC, PHIC × @8, F, PHID × @8, CT	0000160
);	0000161
LINES + LINES + 1;	0000162
END;	0000163
IF PHIDOTC ≠ 0.0 THEN GO TO SWITCHING;	0000164
END;	0000165
END;	0000166
GO TO STARTCORE;	0000167
QUIT: END.	0000168

PRECEDING PAGE BLANK NOT FILMED.

APPENDIX B

COMPUTER PROGRAM FOR STATIC $\phi(F)$ PARAMETERS

```

STATIC PHI(F) PARAMETERS.
BEGIN FILE IN BCR (2, 10);
FILE OUT BP 4 (2, 15);
INTEGER N;
LABEL DONE, AGAIN;
AGAIN: READ (BCR, /, N) [DONE];
BEGIN REAL PHIS, PHIR, LO, LI, HA, HALO, HALI, LL, LOHALO, LIHALI,
LNHA, DIFTERM, ETERM, FN, FNPR, INITHA, ERR;
REAL HQ, HN, L, HN2, DR, DR2, DRH, LNH, FLI, FLO, LNF, FI, SQE;
INTEGER I, S1, S2, S3, S4, CTS, TEMP;
ALPHA CORE;
ARRAY F, FNQ, PHID, PHIDNQ, PHI, PHIDO, E [0 : N], PHIQ [0 : N, 0
: 2], DPH [0 : 2], COV [0 : 2, 0 : 2];
LABEL QUIT, ITER8, ALL, ITER82;
LABEL SECOND;
FORMAT NEWT (4 E15.6, X20, I3), CORENAME (X25, "CALCULATION OF HA,
N AND HQ FOR CORE", A6, " AT ", I4, " DEGREES CENTIGRADE" /), FMTA (
X9, "PHIS", X14, "PHIR", X17, "LO", X16, "LI", X11, "EST. HA", X10
, "EST. HN", X9, "EST. HQ" /), FMTB (/ / / /, "DATA INDEX", X7,
"F", X15, "PHID", X11, "CALC. PHID", X14, "ERROR" /), FMTC (/ / /
/ /, X7, "HA", X12, "FN", X12, "FNPR", X12, "ERR", X27, "CTS" /),
FMTD (/ / /, X6, "HN", X10, "HQ", X9, "CTS" /), FMTE (/ / /, X10, "F
", X13, "PHI" /), DATA (2 E18.6, 2 F17.6, 3 F16.3), DATB (2 E15.5, I2)
, DATC (I5, 3 E18.4, F18.2, "%"), TIMER (/ "RUN TIME =", F6.3, "SEC
NDS, I/O TIME =", F6.3, "SECONDS"), SOLN2 (/ / /, X20, "THE BEST VALUES
FOUND ARE HN=", F11.6, X5, "HQ=", F11.6), SOLN (/ / / /, X20, "THE BEST
VALUE OF HA IS ", F11.6);
COMMENT: LINEARSYSTEM II, B5500 VERSION, 5 / 19 / 65;
DEFINE LP = BP #;
COMMENT GLOBAL ARRAYS;
ARRAY PS, SCALES, RES, DXS [0 : 17];

PROCEDURE DECOMPOSE (N, A);
VALUE N;
INTEGER N;
ARRAY A [0, 0];
COMMENT SUBSCRIPTS FROM 1 TO N;
COMMENT USES GLOBAL ARRAYS PS AND SCALES;
COMMENT DECOMPOSES A INTO TRIANGULAR L AND U SO THAT LxU = A. STORE
S L-I AND U OVER A. PS IS PIVOT VECTOR;
BEGIN INTEGER I, J, M, PIV;
REAL SCALE, PIVOT, SIZE, MULT;
FORMAT FMTI2A (/, "*** SINGULAR MATRIX ***", /);
PROCEDURE ELIM (J1, J2, MULT, AI, AM);
VALUE J1, J2, MULT;
INTEGER J1, J2;
REAL MULT;
REAL ARRAY AI, AM [0];
COMMENT DOES ONE ROW'S WORTH OF GAUSSIAN ELIMINATION;
BEGIN INTEGER J;
FOR J = J1 STEP 1 UNTIL J2 DO AI [J] = AI [J] - MULT * AM [J]
J;
END ELIM;
COMMENT FIND SCALE FACTORS AND INITIALIZE PIVOT VECTOR;
FOR I = 1 STEP 1 UNTIL N DO
BEGIN PS [I] = 1;
SCALE = 0;
FOR J = 1 STEP 1 UNTIL N DO IF ABS (A [I, J]) > SCALE THEN
SCALE = ABS (A [I, J]);
IF SCALE = 0 THEN WRITE (LP, FMTI2A);
SCALES [I] = 1 / SCALE;

```

END;	0000059
COMMENT GAUSSIAN ELIMINATION WITH PARTIAL PIVOTING;	0000060
FOR M + 1 STEP 1 UNTIL N DO	0000061
BEGIN PIVOT + 0;	0000062
FOR I + M STEP 1 UNTIL N DO	0000063
BEGIN SIZE + ABS (A [PS [I], M]) * SCALES [PS [I]];	0000064
IF SIZE > PIVOT THEN	0000065
BEGIN PIVOT + SIZE;	0000066
PIV + I	0000067
END;	0000068
END;	0000069
IF PIV ≠ M THEN	0000070
BEGIN J + PS [M];	0000071
PS [M] + PS [PIV];	0000072
PS [PIV] + J	0000073
END;	0000074
PIVOT + A [PS [M], M];	0000075
IF PIVOT = 0 THEN WRITE (LP, FMTI2A);	0000076
FOR I + M + 1 STEP 1 UNTIL N DO	0000077
BEGIN A [PS [I], M] + MULT + A [PS [I], M] / PIVOT;	0000078
IF MULT ≠ 0 THEN ELIM (M + 1, N, MULT, A [PS [I], *], A [0000079
PS [M], *]);	0000080
END I;	0000081
END M;	0000082
END DECOMPOSE;	0000083
PROCEDURE SOLVE (N, LU, B, X);	0000084
VALUE N;	0000085
INTEGER N;	0000086
REAL ARRAY LU [0, 0];	0000087
REAL ARRAY B, X [0];	0000088
COMMENT GLOBAL ARRAY PS;	0000089
COMMENT SOLVES AX = B USING LU FROM DECOMPOSE;	0000090
BEGIN INTEGER I;	0000091
REAL PROCEDURE DOTPROD (J1, J2, X, Y);	0000092
VALUE J1, J2;	0000093
INTEGER J1, J2;	0000094
REAL ARRAY X, Y [0];	0000095
BEGIN INTEGER J;	0000096
REAL SUM;	0000097
SUM + 0;	0000098
FOR J + J1 STEP 1 UNTIL J2 DO SUM + SUM + X [J] * Y [J];	0000099
DOTPROD + SUM;	0000100
END DOTPROD;	0000101
FOR I + 1 STEP 1 UNTIL N DO X [I] + B [PS [I]] - DOTPROD (1, I	0000102
- 1, LU [PS [I], *], X);	0000103
FOR I + N STEP - 1 UNTIL 1 DO X [I] + (X [I] - DOTPROD (I + 1,	0000104
N, LU [PS [I], *], X)) / LU [PS [I], I];	0000105
END SOLVE;	0000106
PROCEDURE FIT (N, M, Y, X, B, SQE, E, COV, SINGULAR);	0000107
VALUE N, M, X, Y;	0000108
INTEGER N, M;	0000109
REAL SQE;	0000110
ARRAY Y [0], X [0, 0], B [0], E [0], COV [0, 0];	0000111
LABEL SINGULAR;	0000112
BEGIN COMMENT LEAST SQUARE SOLUTION OF Y = X*B + E, IF X[M,N] HAS	R0000113
ANK M. M = NUMBER OF VARIABLES N = OBSERVATIONS;	0000114
INTEGER I, J, K, L;	0000115
REAL S;	0000116
ARRAY A, XY [0 : M], XT [0 : M, 0 : N];	0000117
REAL PROCEDURE PRODUCT (X, Y, N);	0000118
VALUE X, Y, N;	0000119
INTEGER N;	0000120
ARRAY X, Y [0];	0000121
BEGIN REAL S;	0000122

INTEGER J;	0000123
S = 0.0;	0000124
FOR J = 1 STEP 1 UNTIL N DO S = S + X [J] * Y [J];	0000125
PRODUCT = S;	0000126
END PRODUCT;	0000127
FOR I = 1 STEP 1 UNTIL M DO FOR J = 1 STEP 1 UNTIL N DO XT [I,	0000128
J] = X [J, I];	0000129
FOR K = 1 STEP 1 UNTIL M DO FOR J = 1 STEP 1 UNTIL K DO COV [J,	0000130
K] = COV [K, J] + PRODUCT (XT [K, *], XT [J, *], N);	0000131
FOR K = 1 STEP 1 UNTIL M DO XY [K] = PRODUCT (XT [K, *], Y, N);	0000132
DECOMPOSE (M, COV);	0000133
SOLVE (M, COV, XY, B);	0000134
FOR J = 1 STEP 1 UNTIL N DO E [J] = Y [J] - PRODUCT (X [J, *],	0000135
B, M);	0000136
FOR K = 1 STEP 1 UNTIL M DO XY [K] = PRODUCT (XT [K, *], E, N);	0000137
SOLVE (M, COV, XY, A);	0000138
FOR J = 1 STEP 1 UNTIL M DO B [J] = B [J] + A [J];	0000139
SQE = 0.0;	0000140
FOR J = 1 STEP 1 UNTIL N DO	0000141
BEGIN E [J] = E [J] - PRODUCT (X [J, *], A, M);	0000142
SQE = SQE + E [J] * 2;	0000143
END;	0000144
END FIT;	0000145
S2 = 80;	0000146
READ (BCR, /, CORE, TEMP);	0000147
READ (BCR, /, PHIS, PHIR, LO, LI, HA);	0000148
FOR I = 1 STEP 1 WHILE I < S2 DO	0000149
BEGIN READ (BCR, /, F [I], PHID [I]);	0000150
IF F [I] = 0 THEN S2 = I;	0000151
F [I] = - F [I] * 2 * Q-4;	0000152
PHID [I] = - PHID [I] * 5 * Q-11;	0000153
END;	0000154
FOR I = 1 STEP 1 UNTIL N DO	0000155
BEGIN READ (BCR, /, FNQ [I], PHIDNQ [I]) [ALL];	0000156
FNQ [I] = 2 * FNQ [I] * Q-4;	0000157
PHIDNQ [I] = PHIDNQ [I] * 5 * Q-11;	0000158
END;	0000159
ALL: N = I - 1;	0000160
HQ = FNQ [1] / LI;	0000161
HN = .85 * HQ;	0000162
CTS = 0;	0000163
WRITE (BP [DBL], CORENAME, CORE, TEMP);	0000164
WRITE (BP, FMTA);	0000165
WRITE (BP, DATA, PHIS, PHIR, LO, LI, HA, HN, HQ);	0000166
LL = (PHIS - PHIR) / (LO - LI);	0000167
L = (PHIS + PHIR) / (LO - LI);	0000168
S1 = 1;	0000169
S4 = N;	0000170
FOR I = 1 STEP 1 WHILE FNQ [I] < FNQ [1] * LO / LI DO S3 = I;	0000171
IF S2 < 1 THEN GO TO SECOND;	0000172
WRITE (BP, FMTC);	0000173
ITER8: FN = 0;	0000174
FNPR = 0;	0000175
ERR = 0;	0000176
IF CTS = 20 THEN	0000177
BEGIN CTS = 0;	0000178
GO TO ITER8;	0000179
END;	0000180
CTS = CTS + 1;	0000181
FOR I = S1 STEP 1 UNTIL S2 DO	0000182
BEGIN HALO = F [I] - HA * LI;	0000183
HALI = F [I] - HA * LI;	0000184
LOHALO = LO / HALO;	0000185
LIHALI = LI / HALI;	0000186
LNHA = LN (HALO / HALI);	0000187

DIFTERM + LIHALI - LOHALO - LNHA / HA;	0000188
ETERM + F [I] * (LL * F [I] * LNHA / HA - PHIR - PHID [I]);	0000189
FN + FN + ETERM * DIFTERM;	0000190
FNPR + FNPR + ETERM * (LIHALI * 2 - LOHALO * 2 - DIFTERM / HA)	0000191
+ LL * F [I] * 2 * DIFTERM * 2 / HA;	0000192
ERR + ERR + (LL * F [I] * LNHA / HA - PHIR - PHID [I]) * 2;	0000193
PHI [I] + LL * F [I] * LNHA / HA - PHIR;	0000194
END SUMFN;	0000195
HA + HA - FN / FNPR;	0000196
ERR + SQRT (ERR);	0000197
WRITE (BP, NEWT, HA, FN, FNPR, ERR, CTS);	0000198
IF ABS (FN / FNPR) > .001 * ABS (HA) THEN GO TO ITER8;	0000199
WRITE (BP [DBL], SOLN, HA);	0000200
WRITE (BP, FMTB);	0000201
FOR I + 1 STEP 1 UNTIL S2 DO WRITE (BP, DATC, I, F [I], PHID [I],	0000202
PHI [I], 100.0 * (PHID [I] - PHI [I]) / PHID [I]);	0000203
SECOND: WRITE (BP, FMTD);	0000204
CTS + 0;	0000205
ITER8: CTS + CTS + 1;	0000206
FOR I + 1 STEP 1 UNTIL S4 DO IF FNQ [I] ≤ HQ * LO THEN S3 + I;	0000207
DR + 1 / HN - 1 / HQ;	0000208
HN2 + HN * HN;	0000209
DR2 + 1 / HQ - 2 / HN;	0000210
DRH + 1 - HN / HQ;	0000211
FOR I + 1 STEP 1 UNTIL S4 DO	0000212
BEGIN FI + FNQ [I];	0000213
FLI + FI - HN * LI;	0000214
FLO + FI - HN * LO;	0000215
IF I ≤ S3 THEN	0000216
BEGIN LNH + LN (DRH / (1 - HN * LI / FI));	0000217
PHID0 [I] + - L * HQ * (FI / HQ - LI + FI * DR * LNH) / HN +	0000218
PHIR + PHIDN [I];	0000219
PHIQ [I, 1] + L * (FI / HQ - LI + FI * LNH / HN) / HN;	0000220
PHIQ [I, 2] + L * HQ * (LI + FI * (- 1 / HQ + DR2 * LNH - ((0000221
FI - HQ * LI) / FLI) / HQ)) / HN2;	0000222
END;	0000223
IF S3 < I AND I ≤ S4 THEN	0000224
BEGIN LNF + LN (FLO / FLI);	0000225
PHID0 [I] + - L * HQ * (LO - LI + FI * DR * LNF) / HN + PHIR	0000226
+ PHIDN [I];	0000227
PHIQ [I, 1] + L * (LO - LI + FI * LNF / HN) / HN;	0000228
PHIQ [I, 2] + L * HQ * ((LI - LO) * (1 + FI * 2 * DRH / (FLI	0000229
* FLO)) + FI * DR2 * LNF) / HN2;	0000230
END;	0000231
END;	0000232
FIT (S4, 2, PHID0, PHIQ, DPH, SQE, E, COV, QUIT);	0000233
HQ + HQ + DPH [1];	0000234
HN + HN + DPH [2];	0000235
WRITE (BP, DATB, HN, HQ, CTS);	0000236
IF (ABS (DPH [1]) > .001 * HQ OR ABS (DPH [2]) > .001 * HN) AND	0000237
CTS < 20 THEN GO TO ITER8;	0000238
DR + 1 / HN - 1 / HQ;	0000239
FOR I + 1 STEP 1 UNTIL S4 DO	0000240
BEGIN FI + FNQ [I];	0000241
IF I ≤ S3 THEN PHI [I] + L * HQ * (FI / HQ - LI + FI * DR * LN (0000242
(1 - HN / HQ) / (1 - HN * LI / FI))) / HN - PHIR ELSE PHI [I] +	0000243
L * HQ * (LO - LI + FI * DR * LN ((FI - HN * LO) / (FI - HN *	0000244
LI))) / HN - PHIR;	0000245
END;	0000246
WRITE (BP, SOLN2, HN, HQ);	0000247
WRITE (BP, FMTB);	0000248
FOR I + 1 STEP 1 UNTIL N DO WRITE (BP, DATC, I, FNQ [I], PHIDN [I	0000249
], PHI [I], 100.0 * (PHIDN [I] - PHI [I]) / PHIDN [I]);	0000250
QUIT: WRITE (BP, TIMER, TIME (2) / 60, TIME (3) / 60);	0000251
WRITE (BP [PAGE]);	0000252
END;	0000253
GO TO AGAIN;	0000254
DONE: END.	0000255

COMPUTER PROGRAM FOR $\bar{I}_p(F)$ PARAMETERS

PHIDOTP(F) PARAMETERS.

```

BEGIN REAL DIFF, LAMBDA, FOPP, NU, DIFFNU, SQE, F0, ROP, A, L, AA, FF 0000000
, LL; 0000001
BOOLEAN B12, B23, B3; 0000002
REAL T, T1, T2, G, GPR, FB, W, BB, P, NUD, FDB, LAMBDA, FD, FB2, FB1 0000003
; 0000004
REAL AF, HA, HQ, HN, PHIR, PHIS, LI, HS, HTH; 0000005
INTEGER CT, N, I, M, M1, Q, Q1, IQ, TEMP; 0000006
ALPHA CORE, REGION; 0000007
ARRAY F, PHIDOTP, NPHIDOTP, Y, DELPH, E [0 : 50], B [0 : 3], X [0 : 0000008
50, 0 : 3], COV [0 : 3, 0 : 3]; 0000009
LABEL LOOP, SING, DONE; 0000010
LABEL TOP, GROUP, EXIT, LAST; 0000011
LABEL AGAIN, EOF; 0000012
FORMAT FMT (7 F10.4, I10, X4, A6), F1 (X24, "F", X15, "EXP. PHIDOTP", 0000013
X9, "CALC. PHIDOTP", X11, "DEL PHIDOTP" /), F2 (X13, F16.4, 3 F22.6, " 0000014
%), F3 (" LAMBDA", X6, "NUD", X7, "FDB", X5, "LAMBDA", X6 "FOPP", 0000015
X6, "NU", X8, "FB", X11, "CT", X5, "REGION" /), F4 (X32, "DETERMINATION0000016
OF PHIDOTP VS. F PARAMETERS OF CORE ", A6 / /), F6 (/ / / X49, "C O M P0000017
U T A T I O N " /), PARAM (/ / X17, "MAIN INELASTIC SWITCHING PARAMETER0000018
S OF CORE ", A6, " TEMPERATURE =", I4, " (CENTIGRADE)" / / X39, "(L = 0000019
", F7.4, " MM A = ", F7.4, "SQ.MM)", / / X50, "LAMBDA= ", 0000020
F7.4 / X50, "FDMIN = ", F7.4 / X50, "NUD = ", F7.4 / X50, "FDB = 0000021
", F7.4 /, X50, "LAMBDA = ", F7.4, /, X50, "FOPP = ", F7.4, /, X50, "0000022
= ", F7.4, /, X50, "FB = ", F7.4, /, X50, "ROP = ", F7.4, 0000023
/, X50, "F0 = ", F7.4 / /), F7 (/ / / X26, "M E A S U R E D D A T0000024
A A N D C O M P U T E D ", "R E S U L T S " /); 0000025
FORMAT TIMER ("PROCESS TIME =", F8.4, " I/O TIME =", F8.4); 0000026
FILE CRB (2, 10); 0000027
FILE LP 4 (2, 15); 0000028
ARRAY PS, SCALES, RES, DXS [0 : 3]; 0000029

```

PROCEDURES

DECOMPOSE (N,A),

SOLVE (N,LU,B,X), and

FIT (N,M,Y,X,B,SQE,E,COV,SINGULAR),

APPENDIX B

```

AGAIN: READ (CRB, /, CORE, TEMP, N, L, A, FDB, NU, FOPP, FB, AF, HA, 0000134
HQ, HN, PHIR, PHIS, LI) [EOF]; 0000135
READ (CRB, /, FOR I + 1 STEP 1 UNTIL N DO [F [I], PHIDOTP [I]]); 0000136
FOR I + 1 STEP 1 UNTIL N DO 0000137
BEGIN F [I] + 2.06 * F [I]; 0000138
PHIDOTP [I] + PHIDOTP [I] / 2; 0000139
END; 0000140
WRITE (LP, F4, CORE); 0000141
WRITE (LP, F6); 0000142
HS + HA + HQ + HN + PHIR * (HA + HQ - HN) / PHIS; 0000143
HTH + (HS - SQRT (HS * 2 - 8 * (1 + PHIR / PHIS) * HA * HQ)) / 4; 0000144
FD + HTH * LI; 0000145
FDB + FDB * (1 + AF * (TEMP - 25)); 0000146
FOPP + FOPP * (1 + AF * (TEMP - 25)); 0000147
LAMBDA + 3000.0 * A / (L * NU); 0000148
CT + 0; 0000149
WRITE (LP, F3); 0000150
WRITE (LP, FMT, LAMBDA, NUD, FDB, LAMBDA, FOPP, NU, FB, CT); 0000151
GROUP: FOR I + 1 STEP 1 WHILE F [I] ≤ FDB AND I ≤ N DO Q + I; 0000152
IF Q = 1 THEN Q + 0; 0000153
Q1 + Q + 1; 0000154
FOR I + Q1 STEP 1 WHILE F [I] ≤ FB AND I ≤ N DO M + I; 0000155

```


IF Q = N THEN M = N;	0000156
IF M1 = M + 1 THEN GO TO LAST;	0000157
M1 = M + 1;	0000158
REGION = " II ";	0000159
WRITE (LP);	0000160
LOOP: CT = CT + 1;	0000161
FOR I = Q1 STEP 1 UNTIL M DO	0000162
BEGIN IQ = I - Q;	0000163
IF F [I] - FOPP > 0 THEN	0000164
BEGIN DIFF = F [I] - FOPP;	0000165
DIFFNU = DIFF * NU;	0000166
W = 1.0;	0000167
Y [IQ] = (PHIDOTP [I] - LAMBDA * DIFFNU) * W;	0000168
X [IQ, 1] = DIFFNU * W;	0000169
X [IQ, 2] = - LAMBDA * NU * DIFF * (NU - 1.0) * W;	0000170
X [IQ, 3] = LAMBDA * LN (DIFF) * DIFFNU * W;	0000171
END ELSE X [IQ, 1] + X [IQ, 2] + X [IQ, 3] + 0.0;	0000172
END;	0000173
FIT (M = Q, 3, Y, X, B, SQE, E, COV, SING);	0000174
LAMBDA = LAMBDA + B [1];	0000175
FOPP = FOPP + B [2];	0000176
NU = NU + B [3];	0000177
FDB = 1.15 * FOPP;	0000178
WRITE (LP, FMT, LAMBDAD, NUD, FDB, LAMBDA, FOPP, NU, FB, CT, REGION);	0000179
IF CT ≥ 50 THEN GO TO EXIT;	0000180
IF ABS (B [1]) > .001 * ABS (LAMBDA) OR ABS (B [2]) > .001 * ABS (0000181
FOPP) OR ABS (B [3]) > .001 * ABS (NU) THEN GO TO LOOP ELSE GO TO	0000182
DONE;	0000183
SING: WRITE (LP, < "COV IS SINGULAR" >);	0000184
DONE: IF B3 THEN GO TO GROUP;	0000185
REGION = " III";	0000186
WRITE (LP);	0000187
B23 = FALSE;	0000188
FB2 = FB1;	0000189
FB1 = FB;	0000190
TOP: CT = CT + 1;	0000191
T = LAMBDA * (FB - FOPP) * NU;	0000192
T1 = LAMBDA * NU * (FB - FOPP) * (NU - 1.0);	0000193
T2 = LAMBDA * NU * (NU - 1.0) * (FB - FOPP) * (NU - 2.0);	0000194
G = GPR = 0.0;	0000195
FOR I = M1 STEP 1 UNTIL N DO	0000196
BEGIN W = 1.0;	0000197
G = G + (T1 * (F [I] - FB) + T - PHIDOTP [I]) * (F [I] - FB) * W;	0000198
GPR = GPR + (T2 * (F [I] - FB) * 2 - T1 * (F [I] - FB) - T +	0000199
PHIDOTP [I]) * W;	0000200
END;	0000201
IF GPR = 0 THEN	0000202
BEGIN B3 = TRUE;	0000203
GO TO GROUP;	0000204
END;	0000205
FB = FB - G / GPR;	0000206
WRITE (LP, FMT, LAMBDAD, NUD, FDB, LAMBDA, FOPP, NU, FB, CT, REGION);	0000207
IF FB ≤ FOPP THEN	0000208
BEGIN FB = (FB + G / GPR + FOPP) / 2;	0000209
GO TO GROUP;	0000210
END;	0000211
IF CT ≥ 50 THEN GO TO EXIT;	0000212
IF ABS (G / GPR) > .001 * FB THEN GO TO TOP;	0000213
IF ABS (FB - FB2) < @-5 THEN	0000214
BEGIN CT = 50;	0000215
FB = (FB + FB1) / 2;	0000216
END;	0000217
GO TO GROUP;	0000218
LAST: EXIT: REGION = " I ";	0000219
WRITE (LP);	0000220

CT * CT + 1;	0000221
AA * LN (LAMBDA) + NU * LN (FDB - FOPP);	0000222
BB * LN (FDB - FD);	0000223
T1 * 0.0;	0000224
T2 * 0.0;	0000225
FOR I * 1 STEP 1 UNTIL Q DO	0000226
BEGIN LL * LN (F [I] - FD) - BB;	0000227
P * LN (PHIDOTP [I]) - AA;	0000228
T1 * T1 + LL * P;	0000229
T2 * T2 + LL * LL;	0000230
END;	0000231
NUD * T1 / T2;	0000232
LAMBDAD * LAMBDA * (FDB - FOPP) * NU / ((FDB - FD) * NUD);	0000233
WRITE (LP, FMT, LAMBDAD, NUD, FDB, LAMBDA, FOPP, NU, FB, CT, REGION);	0000234
WRITE (LP [PAGE]);	0000235
IF M < N THEN	0000236
BEGIN F0 * (FB * (NU - 1.0) + FOPP) / NU;	0000237
ROP * LAMBDA * NU * (FB - FOPP) * (NU - 1.0);	0000238
END ELSE F0 * ROP * Q20;	0000239
WRITE (LP, PARAM, CORE, TEMP, L * Q3, A * Q6, LAMBDAD, FD, NUD, FDB,	0000240
LAMBDAD, FOPP, NU, FB, ROP, F0);	0000241
FOR I * 1 STEP 1 UNTIL Q DO NPHIDOTP [I] * LAMBDAD * (F [I] - FD) *	0000242
NUD;	0000243
FOR I * Q1 STEP 1 UNTIL M DO NPHIDOTP [I] * LAMBDA * (F [I] - FOPP) *	0000244
NU;	0000245
FOR I * M1 STEP 1 UNTIL N DO NPHIDOTP [I] * ROP * (F [I] - F0);	0000246
FOR I * 1 STEP 1 UNTIL N DO DELPH [I] * (1.0 - PHIDOTP [I] / NPHIDOTP	0000247
[I]) * 100.0;	0000248
WRITE (LP, F7);	0000249
WRITE (LP, F1);	0000250
FOR I * 1 STEP 1 UNTIL N DO WRITE (LP, F2, F [I], PHIDOTP [I],	0000251
NPHIDOTP [I], DELPH [I]);	0000252
WRITE (LP [DBL]);	0000253
M1 * 0;	0000254
LAMBDAD * NUD * 0.0;	0000255
B3 * FALSE;	0000256
WRITE (LP, TIMER, TIME (2) / 60, TIME (3) / 60);	0000257
WRITE (LP [PAGE]);	0000258
GO TO AGAIN;	0000259
EOF: END.	0000260

APPENDIX D

COMPUTER PROGRAM FOR NONLINEAR INDUCTOR PARAMETERS

NONLINEAR INDUCTOR PARAMETERS.

```

BEGIN REAL A, B, EIB, SQE;
INTEGER TEMP, N, K, CT;
ALPHA CORE;
ARRAY PSI, I, PSS, E, PSIC, LE, LC [0 : 50], COV [0 : 2, 0 : 2], DPS [
0 : 50, 0 : 2], DE [0 : 2];
ARRAY PSIN, INN, DI, DPSI [0 : 50];
LABEL MORE, LOOP, EXIT, EOF;
FORMAT F1 (X10, 3 E20.5, I10), F2 (9 E12.3, F11.2, "%"), F3 ("CORE:",
A6, "TEMP=", I5 / / X24, "PSISAT", X15, "ISAT", X16, "LO", X11,
"CT" /), F4 (X5, "RAW I", X7, "RAW PSI", X5, "DEL I", X7, "DEL PSI",
X5, "I", X11, "PSI EXP", X4, "PSI CALC", X5, "L EXP", X7, "L CALC",
X6, "L ERROR" /), TIMER (/ / "PROCESS TIME =", F9.2, " I/O TIME =",
F9.2);
FILE CR "UFO" (1, 10), LP 4 (2, 15);
ARRAY PS, SCALES, RES, DXS [0 : 4];

```

```

0000000
0000001
0000002
0000003
0000004
0000005
0000006
0000007
0000008
0000009
0000010
0000011
0000012
0000013
0000014

```

PROCEDUREs

DECOMPOSE (N, A),

SOLVE (N, LU, B, X), and

FIT (N, M, Y, X, B, SQE, E, COV, SINGULAR),

APPENDIX B

```

PSIN [0] + INN [0] + 0.0;
PSI [0] + I [0] + 0.0;
MORE: READ (CR, /, N, CORE, TEMP) [EOF];
WRITE (LP, F3, CORE, TEMP);
FOR K + 1 STEP 1 UNTIL N DO READ (CR, /, I [K], PSI [K]);
FOR K + 1 STEP 1 UNTIL N DO
BEGIN INN [K] + (I [K] - 100) * 0-3;
PSIN [K] + ((10.26 + .005 * K) * PSI [K] - 14 * K * INN [K]) * 0-8
;
DI [K] + I [K] - I [K - 1];
DPSI [K] + PSI [K] - PSI [K - 1];
END;
A + (PSIN [2] - PSIN [1]) / (INN [2] - INN [1]);
B + INN [N] / 2;
CT + 0;
LOOP: CT + CT + 1;
FOR K + 1 STEP 1 UNTIL N DO
BEGIN EIB + EXP (- INN [K] / B);
DPS [K, 1] + 1.0 - EIB;
DPS [K, 2] + - A * EIB * INN [K] / (B * 2);
PSS [K] + PSIN [K] - A * (1.0 - EIB);
END;
FIT (N, 2, PSS, DPS, DE, SQE, E, COV, EXIT);
A + A + DE [1];
B + B + DE [2];
WRITE (LP, F1, A, B, A / B, CT);
IF (ABS (DE [1]) > .001 * ABS (A) OR ABS (DE [2]) > .001 * ABS (B))
AND CT < 20 THEN GO TO LOOP;
WRITE (LP [DBL]);
WRITE (LP, F4);
FOR K + 1 STEP 1 UNTIL N DO PSIC [K] + A * (1.0 - EXP (- INN [K] / B)
);
FOR K + 1 STEP 1 UNTIL N DO WRITE (LP, F2, I [K], PSI [K], DI [K],
DPSI [K], INN [K], PSIN [K], PSIC [K], LE [K] + (PSIN [K] - PSIN [K -

```

```

0000119
0000120
0000121
0000122
0000123
0000124
0000125
0000126
0000127
0000128
0000129
0000130
0000131
0000132
0000133
0000134
0000135
0000136
0000137
0000138
0000139
0000140
0000141
0000142
0000143
0000144
0000145
0000146
0000147
0000148
0000149
0000150
0000151
0000152

```

1)) / (INN [K] - INN [K - 1]), LC [K] + (PSIC [K] - PSIC [K - 1]) / (0000153
INN [K] - INN [K - 1]), IF LE [K] ≠ 0 THEN 100 × (LC [K] - LE [K]) /	0000154
LE [K] ELSE 100.0);	0000155
EXIT: WRITE (LP, TIMER, TIME (2) / 60, TIME (3) / 60);	0000156
WRITE (LP [PAGE]);	0000157
GO TO MORE;	0000158
EOF: END.	0000159

APPENDIX E

COMPUTER PROGRAM FOR DIODE PARAMETERS

DIODE PARAMETERS.

```

BEGIN REAL EK, IO, RD, IJ, L, SQE;
INTEGER J, CT, N, TEMP;
ARRAY I, Y, E, V [0 : 20], X [0 : 20, 0 : 4], B [0 : 4], COV [0 : 4,
0 : 4];
ALPHA ID;
FILE CR "PGANDE" (2, 10), LP 4 (3, 15);
FORMAT FMT (X15, "RD", X18, "EK", X18, "IO", X10, "CT" /);
FORMAT IDENT (/ / / X34, "DIODE:", A6, X10, "TEMP =", I4, " (CENTIGRAD
E)" / / / "PARAMETERS", X4, "RD =", F8.5, " OHM", X4, "EK =", F8.6, " V
LT", X4, "IO =", F8.6, " A-9 AMP");
FORMAT F1 (3 E20.5, I10), F2 (/ / X14, "I(AMP)", X14, "EXP. V", X13, "C
ALC. V", X13, "ERROR" /), F3 (3 F20.5, F17.2, "%"), F5 ("PROCESSOR TIME
=", F6.2, " I/O TIME =", F6.2);
LABEL EOF, SING, MORE, LOOP;
ARRAY PS, SCALES, RES, DXS [0 : 4];

```

PROCEDURES
 DECOMPOSE (N, A),
 SOLVE (N, LU, B, X), and
 FIT (N, M, Y, X, B, SQE, E, COV, SINGULAR),
 APPENDIX B

```

MORE: READ (CR, /, N, RD, EK, IO, TEMP, ID) [EOF];
FOR J + 1 STEP 1 UNTIL N DO READ (CR, /, I [J], V [J]);
CT + 0;
FOR J + 1 STEP 1 UNTIL N DO I [J] + I [J] × 10-3;
WRITE (LP, FMT);
WRITE (LP, F1, RD, EK, IO × 106, CT);
FOR J + 1 STEP 1 UNTIL N DO X [J, 1] + I [J];
LOOP: CT + CT + 1;
FOR J + 1 STEP 1 UNTIL N DO
  BEGIN IJ + I [J];
    L + LN (1.0 + IJ / IO);
    Y [J] + V [J] - RD × IJ - EK × L;
    X [J, 2] + L;
    X [J, 3] + - EK × IJ / (IO × (IO + IJ));
  END;
FIT (N, 3, Y, X, B, SQE, E, COV, SING);
RD + RD + B [1];
EK + EK + B [2];
IO + IO + B [3];
IF EK < 0 THEN EK + (EK - B [2]) / 2;
IF IO ≤ 0 THEN IO + (IO - B [3]) / 2;
WRITE (LP, F1, RD, EK, IO × 109, CT);
IF (ABS (B [1]) > .001 × ABS (RD) OR ABS (B [2]) > .001 × ABS (EK) OR
ABS (B [3]) > .001 × ABS (IO)) AND CT < 20 THEN GO TO LOOP;
WRITE (LP, IDENT, ID, TEMP, RD, EK, IO × 109);
WRITE (LP, F2);
FOR J + 1 STEP 1 UNTIL N DO Y [J] + I [J] × RD + EK × LN (1 + (I [J]
/ IO));
FOR J + 1 STEP 1 UNTIL N DO IF V [J] = 0 THEN WRITE (LP, F3, I [J], V
[J], Y [J]) ELSE WRITE (LP, F3, I [J], V [J], Y [J], 100 × (V [J] - Y
[J]) / V [J]);
WRITE (LP, F5, TIME (2) / 60, TIME (3) / 60);
SING: WRITE (LP [PAGE]);
GO TO MORE;
EOF: END.

```

APPENDIX F

COMPUTER PROGRAM FOR TRANSISTOR PARAMETERS

TRANSISTOR PARAMETERS.

```

BEGIN REAL IJ, ICJ, L, RBC, THETAM, ISC, RB, SQE, VC, M, RS;      00000000
INTEGER K, J, N, CT, TEMP, D, SCT;                                00000001
ALPHA WHICH, ID;                                                  00000002
ARRAY I, IC, V, Y, E [0 : 20], X [0 : 20, 0 : 4], COV [0 : 4, 0 : 4], 00000003
B [0 : 4];                                                         00000004
LABEL MORE, EOF, SING, LOOP, CASEB;                               00000005
FILE LP 4 (3, 15), CR "RADIO" (2, 10);                            00000006
LIST L10 (RBC, THETAM, ISC * @9, CT), L11 (RBC, 0, THETAM, ISC * @9, 00000007
CT), L12 (RB, RBC, THETAM, ISC * @9, CT + SCT), L20 (RBC, THETAM, ISC
* @9), L21 (RBC, 0, THETAM, ISC * @9), L22 (RB, RBC, 0, THETAM, ISC *
@9), L30 ((ICJ + IC [J]), (IJ + I [J]), ICJ / IJ, V [J], (VC + IJ *
RBC + THETAM * LN (1.0 + (IJ + ICJ) / ISC)), (IF V [J] = 0 THEN 100.0
ELSE 100.0 * (V [J] - VC) / V [J])), L32 ((ICJ + IC [J]), (IJ + I [J]
), ICJ / IJ, V [J], (VC + IJ * RB + (IJ + ICJ) * RBC + THETAM * LN (
1.0 + (IJ + ICJ) / ISC)), (IF V [J] = 0 THEN 100.0 ELSE 100.0 * (V [J]
J - VC) / V [J]));                                               00000015
SWITCH LIST L1 + L10, L11, L12;                                    00000016
SWITCH LIST L2 + L20, L21, L22;                                    00000017
SWITCH LIST L3 + L30, L32;                                         00000018
SWITCH FORMAT F1 + (X37, "REVERSE CHARACTERISTICS OF TRANSISTOR ", A6 00000019
/ / X47, "TEMPERATURE = ", I3, " DEG. C" / /), (X37, "FORWARD CHARACTER
ISTICS OF TRANSISTOR ", A6 / / X47, "TEMPERATURE = ", I3, " DEG. C" / 00000021
/);                                                                00000022
SWITCH FORMAT F2 + (X13, "RBC", X17, "THETAMC", X13, "ISC@9", X15, 00000023
"CT" /), (X13, "RB", X18, "RE", X18, "THETAME", X13, "ISE@9", X15, 00000024
"CT" /), (X13, "RB", X18, "RE", X18, "THETAME", X13, "ISE@9", X15, 00000025
"CT" /);                                                         00000026
SWITCH FORMAT F3 + (/ / / X55, "RBC = ", F9.5, " OHM" / X51, "THETAMC = 00000027
", F8.5, " VOLT" / X55, "ISC = ", F12.5, " @-9 AMP" / / / X15, "IE" 00000028
, X18, "IB", X18, "BETAI", X12, "EXP. VBC", X11, "CALC. VBC", X14, "ERR0000029
OR" /), (/ / / X56, "RB = ", F9.5, " OHM" / X56, "RE = ", F9.5, " OHM" 00000030
/ X51, "THETAME = ", F8.5, " VOLT" / X55, "ISE = ", F12.5, " @-9 AMP" 00000031
/ / / / X15, "IC", X18, "IB", X18, "BETAN", X12, "EXP. VBE", X11, "CALC0000032
. VBE", X14, "ERROR" /), (/ / / X56, "RB = ", F9.5, " OHM" / X56, "RE = 00000033
", F9.5, " OHM" / X56, "RC = ", F9.5, " OHM" / X51, "THETAME = ", F8.5 00000034
, " VOLT" / X55, "ISE = ", F12.5, " @-9 AMP" / / / / X15, "IC", X18, "I0000035
B", X18, "BETAN", X12, "EXP. VBE", X11, "CALC. VBE", X14, "ERROR" /); 00000036
SWITCH FORMAT F4 + (3 E20.6, I17), (4 E20.6, I17), (4 E20.6, I17); 00000037
FORMAT F5 (5 F20.8, F19.2, "%");                                  00000038
ARRAY PS, SCALES, RES, DXS [0 : 4];                               00000039

```

PROCEDUREs

DECOMPOSE (N,A),

SOLVE (N,LU,B,X), and

FIT (N,M,Y,X,B,SQE,E,COV,SINGULAR),

APPENDIX B

```

M + 2.0;                                                         0000144
MORE: READ (CR, /, N, RBC, ISC, ID, TEMP, WHICH) [EOF];         0000145
IF WHICH = "R" THEN K + 0 ELSE K + 1;                             0000146
D + 3;                                                            0000147
RB + 0.0;                                                         0000148
WRITE (LP, F1 [K], ID, TEMP);                                     0000149
WRITE (LP, F2 [K]);                                               0000150
FOR J + 1 STEP 1 UNTIL N DO READ (CR, /, V [J], I [J], IC [J]); 0000151
FOR J + 1 STEP 1 UNTIL N DO I [J] + I [J] * @-3;                0000152
FOR J + 1 STEP 1 UNTIL N DO IC [J] + IC [J] * @-3;              0000153

```

CASEB: CT + 0;	0000154
THETAM + 0.86 * M * (273 + TEMP) * Q-4;	0000155
IF K ≤ 1 THEN FOR J + 1 STEP 1 UNTIL N DO X [J, 1] + I [J] ELSE FOR J	0000156
+ 1 STEP 1 UNTIL N DO X [J, 1] + I [J] + IC [J];	0000157
LOOP: CT + CT + 1;	0000158
FOR J + 1 STEP 1 UNTIL N DO	0000159
BEGIN IJ + I [J];	0000160
ICJ + IC [J];	0000161
L + LN (1.0 + (IJ + ICJ) / ISC);	0000162
X [J, 2] + - THETAM * (IJ + ICJ) / (ISC * (ISC + IJ + ICJ));	0000163
IF D > 2 THEN X [J, 3] + L;	0000164
Y [J] + V [J] - RBC * IJ - THETAM * L;	0000165
IF K > 1 THEN Y [J] + Y [J] - RBC * ICJ - RB * IJ;	0000166
END;	0000167
FIT (N, D, Y, X, B, SQE, E, COV, SING);	0000168
RBC + RBC + B [1];	0000169
ISC + ISC + B [2];	0000170
IF ISC < 0 THEN ISC + (ISC - B [2]) / 2;	0000171
THETAM + THETAM + B [3];	0000172
WRITE (LP, F4 [K], L1 [K]);	0000173
IF (ABS (B [1]) > 0.001 * ABS (RBC) OR ABS (B [2]) > 0.001 * ABS (ISC	0000174
) OR (IF D > 2 THEN ABS (B [3]) > 0.001 * ABS (THETAM) ELSE FALSE))	0000175
AND CT < 20 THEN GO TO LOOP;	0000176
IF K = 1 AND RS ≤ RBC THEN	0000177
BEGIN K + 2;	0000178
RB + RS;	0000179
SCT + CT;	0000180
GO TO CASEB;	0000181
END;	0000182
WRITE (LP, F3 [K], L2 [K]);	0000183
FOR J + 1 STEP 1 UNTIL N DO WRITE (LP, F5, L3 [K]);	0000184
IF K = 0 THEN RS + RBC;	0000185
SING: WRITE (LP [PAGE]);	0000186
GO TO MORE;	0000187
EOF: END.	0000188

APPENDIX G

COMPUTER PROGRAM FOR A CORE-DIODE-TRANSISTOR BINARY COUNTER

```

BINARY COUNTER, USING SIMPLE INTEGRATION METHOD TO COMPUTE CURRENTS 0000000
AND VOLTAGES VS. TIME AND VSMIN FOR NOMINAL AND WORST-CASE CONDITIONS. 0000001
BEGIN COMMENT * * * * * IMPORTANT * * * DO NOT CHANGE THIS DECLARATION 0000002
* * * ;
REAL LI1, LO1, PHIR1, PHIS1, HA1, HQ1, HN1, LAMBDA1, NUD1, FDB1, 0000003
FOPP1, LAMBDA1, NU1, FB1, F01, ROP1, LI2, LO2, PHIR2, PHIS2, HA2, 0000004
HQ2, HN2, LAMBDA2, NUD2, FDB2, FOPP2, LAMBDA2, NU2, FB2, F02, 0000005
ROP2, NS1, NS2, NB1, NB2, NC1, NC2, NCL, R10, R11, R12, R2, R3, R4 0000006
, L00, ICON0, L01, ICON1, L02, ICON2, ISD, THETAMD, CJO0, VCPOTD, 0000007
ND, KD, RLD, RD, ISE, THETAME, CJOE, VCPOTE, NE, KE, RLE, RE, ISC, 0000008
THETAMC, CJOE, VCPOTE, NC, KC, RLC, RC, RB; 0000009
COMMENT * * * * * DO NOT CHANGE THE DECLARATION ABOVE * * * * * 0000010
;
ARRAY ALP, DELTEMP, D1, U, D2, G [0 : 40]; 0000011
REAL IL, ILM1, ILM2, ILDT, ILDTM1, IC, ICM1, ICM2, ICDOT, 0000012
ICDOTM1, ICL, ICLM1, ICLM2, ICLDT, ICLDTM1, IS, ISM1, ISM2, ID, 0000013
IDM1, IDM2, IB, IE, F1, F1M1, F2, F2M1, PHI1, PHI1M1, PHI1M2, 0000014
PHIDOT1, PHIDOT1M1, PHIDOTPR1, PHI2, PHI2M1, PHI2M2, PHIDOT2, 0000015
PHIDOT2M1, PHIDOTPR2, PHIDOTE1, PHIDOTEPR1, PHIDOTMA1, PHIDOTMAPR1 0000016
, PHIDOTE2, PHIDOTEPR2, PHIDOTMA2, PHIDOTMAPR2, VD, VDM1, VDM2, 0000017
IDPR, VDDOT, VDDOTM1, VPN, VPNPR, ISFD, VE, VEM1, VEM2, IEPR, 0000018
VEDOT, VEDOTM1, VBE, VBEPR, ISFE, DIEDVE, VC, VCM1, VCM2, ICPR, 0000019
VCDOT, VCDOTM1, VCE, ISFC, DICDVE; 0000020
REAL HS1, HTH1, F121, F231, V11, V21, EPS1, HS2, HTH2, F122, F232, 0000021
V12, V22, EPS2, T, TAUS, DELT, TR, T1, T2, T3, T4, PHI1F1, PHI1F2, 0000022
PHI1F3, PHI1F4, PHI2F1, PHI2F2, PHI2F3, PHI2F4; 0000023
REAL CJD, CDD, CJE, CDE, CJC, CDC, BETAI, BETAN, ALPHAI, ALPHAN; 0000024
REAL FJ, FJM1, GJ, GJM1, FPRID, GPRIS, FPRIS, GPRID, D, DELID, 0000025
DELIS, S, CONFAC, CAPIS, CAPIL, TAUC, TV, TIN, VS, PHIDOT12, NV, Q 0000026
, SL, TSL, TEMP; 0000027
INTEGER NP, IP, NA, IA; 0000028
BOOLEAN TRANS, NOSW, FAILURE, BOOL; 0000029
INTEGER LINES, COUNT, CTS, CF, MODE, CNV, CNVS, K, CQ, J; 0000030
REAL ARRAY ICN, BETN, IEI, BETI [0 : 30], NCOEF, ICOEF [0 : 3, 0 : 0000031
30]; 0000032
ARRAY VAL, NONU, WCVAL [0 : 100]; 0000033
ALPHA ARRAY GROUP1, GROUP2, NAME, NAM2, WCSIGN [0 : 100]; 0000034
INTEGER ARRAY SDIFF [0 : 100]; 0000035
FILE OWT 4 (2, 15), CR "MARS" (2, 10); 0000036
LIST LIST2 (TEMP, VS, CAPIL, TR x 106); 0000037
LIST LIST3 (T x 06, IL, IC, ICL, IS, F1, PHI1 x 08, PHIDOT1, F2, 0000038
PHI2 x 08, PHIDOT2, ID, VPN, VCE, PHIDOTE1, PHIDOTE2, CTS); 0000039
LABEL SWITCHING0, SWITCHING1, SWITCHING2, SWITCHING3, SWITCHING4, 0000040
MODE0, MODE1, MODE2, MODE3, MODE4, EXIT0, EXIT1, EXIT2, EXIT3, 0000041
EXIT4, MODE5, EXIT, READMORE, EOF; 0000042
FORMAT FMT2 (X10, "TEMP(DEGREES C)=", F5.1, X8, "VS(VOLTS)=", F5.1 0000043
, X8, "CAPIL(AMP)=", F6.3, X8, "TR(MICROSECOND)=", F6.3 /); 0000044
FORMAT FMT3 (6 F6.3, 2 F8.4, F6.3, 3 F8.4, 2 F7.3, 2 F8.4, I3, I4) 0000045
; 0000046
FORMAT FMT4 (" T", X4, "IL", X4, "IC", X4, "ICL", X3, "IS", X4, "F 0000047
1", X4, "PHI1", X3, "PHIDOT1", X2, "F2", X4, "PHI2", X3, "PHIDOT2", X3 0000048
, "ID", X6, "VPN", X4, "VCE", X4, "PHIDTE1", X1, "PHIDTE2", X1, "CTS 0000049
" /), HEAD (X45, "OUTPUT: MINIMUM SUPPLY VOLTAGE" / / X45, "TEMPERATURE 0000050
=", I4, " DEGREES C" / / / X45, "C O R E P A R A M E T E R S" /), 0000051
FF1 ("DEVICES PARAMETER NOMINAL VALUE AT T=", I3, " DEG.C ", " 0000052
ONUNIFORMITY WORST-CASE DIFFERENTIAL SIGN WORST-CASE VALUE"), DATA 0000053
(/ 24 (A6, A4, X1, A6, A2, X5, E18.4, X14, F6.2, "%", X19, A1, X18 0000054
, E14.4 /)), FF2 (X42, "C I R C U I T P A R A M E T E R S" /), 0000055
FMT5 (/ X57, "MODE", I2 / /); 0000056
FORMAT FLAG1 ("SPURIOUS TRANSISTOR TURN-ON."); 0000057
FORMAT FLAG2 ("SPURIOUS TRANSISTOR TURN-OFF"); 0000058
0000059
0000060

```


FORMAT FLAG3 ("MAXIMUM COLLECTOR-EMITTER VOLTAGE EXCEEDED");	0000061
FORMAT FLAG4 ("NO TRANSISTOR TURN-ON IN MODE 3");	0000062
FORMAT TIMER ("PROCESS TIME =", F8.4, " I/O TIME =", F8.4);	0000063
BOOLEAN NEWVS;	0000064
DEFINE LP = OWT #;	0000065
STREAM PROCEDURE TRANSFER (N, A, B);	0000066
VALUE N;	0000067
BEGIN LOCAL T;	0000068
SI ← LOC N;	0000069
DI ← LOC T;	0000070
DI ← DI + 1;	0000071
DS ← 7 CHR;	0000072
SI ← A;	0000073
DI ← B;	0000074
T (DS ← 32 WDS;	0000075
DS ← 32 WDS);	0000076
DS ← N WDS	0000077
END TRANSFER;	0000078
PROCEDURE PRINTOUT;	0000079
BEGIN REAL X;	0000080
IF COUNT MOD 10 = 0 THEN	0000081
BEGIN IF LINES MOD 50 = 0 THEN	0000082
BEGIN WRITE (OWT, TIMER, TIME (2) / 60, TIME (3) / 60);	0000083
WRITE (OWT [PAGE]);	0000084
WRITE (OWT, FMT4);	0000085
END;	0000086
WRITE (OWT, FMT3, LIST3);	0000087
LINES ← LINES + 1;	0000088
CF ← 0;	0000089
END;	0000090
END PRINTOUT;	0000091
PROCEDURE PRINTHEAD;	0000092
BEGIN WRITE (OWT [PAGE]);	0000093
IF NEWVS THEN WRITE (OWT, FMT2, LIST2);	0000094
WRITE (OWT, FMT5, MODE);	0000095
WRITE (OWT, FMT4);	0000096
WRITE (OWT, FMT3, LIST3);	0000097
LINES ← 11;	0000098
END PRINTHEAD;	0000099
PROCEDURE INTERPOL (POINTS, ICC, BET, COEF);	0000100
ARRAY COEF [0, 0], ICC, BET [0];	0000101
INTEGER POINTS;	0000102
BEGIN INTEGER J, K, L;	0000103
REAL ARRAY C [0 : 3, 0 : 3];	0000104
FOR L := 1 STEP 1 UNTIL POINTS DO	0000105
BEGIN FOR J := 0, 1, 2, 3 DO C [J, 0] := BET [L + J - 1];	0000106
FOR K := 1, 2, 3 DO FOR J := K STEP 1 UNTIL 3 DO C [J, K] :	0000107
= (C [J, K - 1] - C [J - 1, K - 1]) / (ICC [J + L - 1] - ICC	0000108
[J + L - 1 - K]);	0000109
FOR J := 0, 1, 2, 3 DO COEF [J, L] := C [J, J]	0000110
END	0000111
END INTERPOL;	0000112
REAL PROCEDURE BETA (IC, P, COEF, ICC, BET, POINTS);	0000113
INTEGER P, POINTS;	0000114
ARRAY COEF [0, 0], ICC, BET [0];	0000115
REAL IC;	0000116
BEGIN INTEGER J;	0000117
REAL B;	0000118
LABEL EX, PX;	0000119
IF IC > ICC [POINTS] THEN	0000120
BEGIN B := BET [POINTS];	0000121

```

GO TO EX                                0000122
END;                                    0000123
IF IC < ICC [1] THEN                    0000124
BEGIN B = BET [1];                      0000125
GO TO EX;                               0000126
END;                                    0000127
PX: IF IC > ICC [P + 1] THEN             0000128
BEGIN P: = P + 1;                       0000129
GO TO PX                                0000130
END;                                    0000131
IF IC < ICC [P] THEN                    0000132
BEGIN P: = P - 1;                       0000133
GO TO PX                                0000134
END;                                    0000135
B: = COEF [3, P];                      0000136
FOR J: = 3, 2, 1 DO B: = B × (IC - ICC [J + P - 2]) + COEF [J - 0000137
1, P];                                  0000138
EX: BETA: = B;                          0000139
END BETA;                               0000140

REAL PROCEDURE PHIDOTE (F, FM1, EPS, PHIDOTEPR); 0000141
VALUE F, FM1, EPS;                        0000142
REAL F, FM1, PHIDOTEPR, EPS;             0000143
BEGIN PHIDOTEPR = EPS / DELT;             0000144
PHIDOTE = (F - FM1) × PHIDOTEPR;          0000145
END PHIDOTE;                             0000146

REAL PROCEDURE PHIDOT (F, PHI, LI, LO, PHIR, PHIS, HA, HQ, HTH, HN, 0000147
, LAMBDA, NUD, FDB, FOPP, LAMBDA, NU, FB, F0, ROP, F12, F23, V1, 0000148
V2, PHIDOTPRIME);                       0000149
VALUE F, PHI, LI, LO, PHIR, PHIS, HA, HQ, HTH, HN, LAMBDA, NUD, 0000150
FDB, FOPP, LAMBDA, NU, FB, F0, ROP, F12, F23, V1, V2;          0000151
REAL F, PHI, LI, LO, PHIR, PHIS, HA, HQ, HTH, HN, LAMBDA, NUD, 0000152
FDB, FOPP, LAMBDA, NU, FB, F0, ROP, F12, F23, V1, V2, PHIDOTPRIME; 0000153
BEGIN REAL PHIDOTPRIME, PHID, PHIDOTP, PHIDOTPPRIME, S;          0000154
S = SIGN (F);                          0000155
F = S × F;                              0000156
PHI = S × PHI;                          0000157
IF F ≤ F12 THEN                         0000158
BEGIN PHID = V1 × F × LN ((F - HA × LO) / (F - HA × LI)) - PHIR 0000159
;                                         0000160
PHIDPRIME = V1 × (LN ((F - HA × LO) / (F - HA × LI)) + F × ( 0000161
1 / (F - HA × LO) - 1 / (F - HA × LI))) 0000162
END;                                    0000163
IF F12 < F AND F ≤ F23 THEN              0000164
BEGIN PHID = V2 × (F / HTH - LI + F × (1 / HN - 1 / HQ) × LN (( 0000165
1 - HN / HTH) / (1 - HN × LI / F))) - PHIR; 0000166
PHIDPRIME = V2 × (1 / HTH + (1 / HN - 1 / HQ) × (LN (F × (1 0000167
- HN / HTH) / (F - HN × LI)) - HN × LI / (F - HN × LI))) 0000168
END;                                    0000169
IF F23 < F THEN                          0000170
BEGIN PHID = V2 × (LO - LI + F × (1 / HN - 1 / HQ) × LN ((F - 0000171
HN × LO) / (F - HN × LI))) - PHIR; 0000172
PHIDPRIME = V2 × (1 / HN - 1 / HQ) × (LN ((F - HN × LO) / (F 0000173
- HN × LI)) + F × HN × (LO - LI) / ((F - HN × LO) × (F - HN 0000174
× LI))) 0000175
END;                                    0000176
IF 0 < F < F12 THEN PHIDOTP = PHIDOTPPRIME + 0.0; 0000177
IF F12 < F < FDB THEN                   0000178
BEGIN PHIDOTP = LAMBDA × (F - F12) × NUD; 0000179
PHIDOTPPRIME = LAMBDA × NUD × (F - F12) × (NUD - 1.0); 0000180
END;                                    0000181
IF FDB < F < FB THEN                    0000182
BEGIN PHIDOTP = LAMBDA × (F - FOPP) × NU; 0000183
PHIDOTPPRIME = LAMBDA × NU × (F - FOPP) × (NU - 1) 0000184
END;                                    0000185

```

IF FB < F THEN	0000186
BEGIN PHIDOT + ROP * (F - F0);	0000187
PHIDOTPRIME + ROP	0000188
END;	0000189
IF PHI < PHID THEN	0000190
BEGIN PHIDOT + S * (PHIDOT * (1 - ((2 * PHI + PHIS - PHID) / (0000191
PHIS + PHID)) * 2));	0000192
PHIDOTPRIME + (1 - ((2 * PHI + PHIS - PHID) / (PHIS + PHID))	0000193
* 2) * PHIDOTPRIME + 4 * PHIDOT * (2 * PHI + PHIS - PHID)	0000194
* (PHI + PHIS) * PHIDPRIME / (PHIS + PHID) * 3;	0000195
END ELSE PHIDOT + PHIDOTPRIME + 0;	0000196
END PHIDOT;	0000197
REAL PROCEDURE I (V, VL, II, IM1, IDOTM1, NPHIDOT, R1, L0, ICON,	0000198
IDOT);	0000199
VALUE V, VL, II, IM1, IDOTM1, NPHIDOT, R1, L0, ICON;	0000200
REAL V, VL, II, IM1, IDOTM1, NPHIDOT, R1, L0, ICON, IDOT;	0000201
BEGIN REAL L;	0000202
L = L0 * EXP (- II / ICON);	0000203
IDOT + (V - NPHIDOT - R1 * II - VL) / L;	0000204
II + IM1 + DELT * (IDOT + IDOTM1) / 2;	0000205
IF II < 0 THEN IDOT + II + 0;	0000206
I + II;	0000207
END I;	0000208
REAL PROCEDURE V (I, VJ, VM1, VDOTM1, IS, THETAM, CJ0, VCPOT, N, K	0000209
, RL, CJ, CD, ISF, VDOT, IPR);	0000210
VALUE I, VJ, VM1, VDOTM1, IS, THETAM, CJ0, VCPOT, N, K, RL;	0000211
REAL I, VJ, VM1, VDOTM1, IS, THETAM, CJ0, VCPOT, N, K, RL, CJ, CD,	0000212
ISF, VDOT, IPR;	0000213
BEGIN ISF + IS * EXP (VJ / THETAM);	0000214
IF VJ > VCPOT THEN VJ + .9999 * VCPOT;	0000215
CJ + CJ0 / ((1 - VJ / VCPOT) * N);	0000216
CD + K * ISF + CJ;	0000217
VDOT + (I - ISF + IS - VJ / RL) / CD;	0000218
VJ + VM1 + 0.5 * DELT * (VDOTM1 + VDOT);	0000219
ISF + IS * EXP (VJ / THETAM);	0000220
IF VDOT ≠ 0 THEN IPR + ISF / THETAM + 1 / RL + CD * (1 - VDOTM1	0000221
/ VDOT) / DELT + VDOT * (K * ISF / THETAM + N * CJ / (VCPOT -	0000222
VJ)) ELSE IPR + ISF / THETAM + 1 / RL;	0000223
V + VJ;	0000224
END V;	0000225
PROCEDURE INCREMENT;	0000226
BEGIN LABEL GUESS, LOOP;	0000227
CTS + 0;	0000228
PHI1M2 + PHI1M1;	0000229
PHI1M1 + PHI1;	0000230
PHIDOT1M1 + PHIDOT1;	0000231
PHI2M2 + PHI2M1;	0000232
PHI2M1 + PHI2;	0000233
PHIDOT2M1 + PHIDOT2;	0000234
ILM2 + ILM1;	0000235
ILM1 + IL;	0000236
ILDOTM1 + ILDOT;	0000237
IDM2 + IDM1;	0000238
IDM1 + ID;	0000239
ISM2 + ISM1;	0000240
ISM1 + IS;	0000241
F1M1 + F1;	0000242
F2M1 + F2;	0000243
IF MODE = 2 OR MODE = 4 OR MODE = 0 THEN	0000244
BEGIN ICLM2 + ICLM1;	0000245
ICLM1 + ICL;	0000246
ICLDOTM1 + ICLDOT;	0000247
END;	0000248

```

IF TRANS THEN
BEGIN ICM2 + ICM1;
  ICM1 + IC;
  ICDOTM1 + ICDOT;
  VEM2 + VEM1;
  VEM1 + VE;
  VEDOTM1 + VEDOT;
  VCM2 + VCM1;
  VCM1 + VC;
  VCDOTM1 + VCDOT;
END;
GUESS: PHI1 + PHI1M2 + 2.0 * DELT * PHIDOT1M1;
PHI2 + PHI2M2 + 2.0 * DELT * PHIDOT2M1;
IF T > TR OR MODE = 2 OR MODE = 4 OR MODE = 0 THEN IL + ILM2 +
2 * DELT * ILDOTM1 ELSE IL + IF T ≤ TSL THEN SL * T ELSE CAPIL
* (1.0 - 1.89 * (1.0 - T / TR) * 2.61);
ID + 2.0 * IDM1 - IDM2;
IS + 2.0 * ISM1 - ISM2;
IF MODE = 2 OR MODE = 4 OR MODE = 0 THEN ICL + ICLM2 + 2.0 *
DELT * ICLDOTM1;
IF TRANS THEN
BEGIN IC + ICM2 + 2.0 * DELT * ICDOTM1;
  VE + VEM2 + 2.0 * DELT * VEDOTM1;
  VC + VCM2 + 2.0 * DELT * VCDOTM1;
END;
LOOP: FJM1 + FJ;
GJM1 + GJ;
CTS + CTS + 1;
F1 + NS1 * IS + NB1 * ID + NC1 * IC - NCL * ICL;
F2 + NS2 * IS - NB2 * ID - NC2 * IC;
PHIDOTM1 + PHIDOT (F1, PHI1, LI1, LO1, PHIR1, PHIS1, HA1, HQ1,
HTH1, HN1, LAMBDAD1, NUD1, FDB1, FOPP1, LAMBDA1, NU1, FB1, F01,
ROP1, F121, F231, V11, V21, PHIDOTMAPR1);
EPS1 + V11 * (ABS (F1) * (1.0 / (ABS (F1) + HA1 * LO1) - 1.0 / (
ABS (F1) + HA1 * LI1))) + LN ((ABS (F1) + HA1 * LO1) / (ABS (F1)
+ HA1 * LI1)));
PHIDOTE1 + PHIDOTE (F1, F1M1, EPS1, PHIDOTEPR1);
PHIDOT1 + PHIDOTM1 + PHIDOTE1;
PHIDOTPR1 + PHIDOTMAPR1 + PHIDOTEPR1;
PHIDOTM2 + PHIDOT (F2, PHI2, LI2, LO2, PHIR2, PHIS2, HA2, HQ2,
HTH2, HN2, LAMBDAD2, NUD2, FDB2, FOPP2, LAMBDA2, NU2, FB2, F02,
ROP2, F122, F232, V12, V22, PHIDOTMAPR2);
EPS2 + V12 * (ABS (F2) * (1.0 / (ABS (F2) + HA2 * LO2) - 1.0 / (
ABS (F2) + HA2 * LI2))) + LN ((ABS (F2) + HA2 * LO2) / (ABS (F2)
+ HA2 * LI2)));
PHIDOTE2 + PHIDOTE (F2, F2M1, EPS2, PHIDOTEPR2);
PHIDOT2 + PHIDOTM2 + PHIDOTE2;
PHIDOTPR2 + PHIDOTMAPR2 + PHIDOTEPR2;
IF T > TR OR MODE = 2 OR MODE = 4 OR MODE = 0 THEN IL + I (0,
IS * R3 + 0.6, IL, ILM1, ILDOTM1, NS1 * PHIDOT1 + NS2 * PHIDOT2
, R11 + RD, LO1, ICON1, ILDOT);
IF MODE = 2 OR MODE = 4 OR MODE = 0 THEN IF T ≤ 4.6E-6 THEN ICL
+ I (VS, 1.0, ICL, ICLM1, ICLDOTM1, - NCL * PHIDOT1, R10, L00,
ICON0, ICLDOT) ELSE ICL + I (0, 3.0, ICL, ICLM1, ICLDOTM1, -
NCL * PHIDOT1, R10, L00, ICON0, ICLDOT);
IF TRANS THEN IC + I (VS, VCE, IC, ICM1, ICDOTM1, NC1 * PHIDOT1
- NC2 * PHIDOT2, R12, LO2, ICON2, ICDOT);
PHI1 + PHI1M1 + 0.5 * DELT * (PHIDOT1M1 + PHIDOT1);
PHI2 + PHI2M1 + 0.5 * DELT * (PHIDOT2M1 + PHIDOT2);
IF MODE ≠ 3 OR NOT TRANS THEN
BEGIN IF ID ≥ 0 THEN
  BEGIN VPN + ID * RD + THETAMD * LN (1 + ID / ISD);
    VPNPR + RD + THETAMD / (ISD + ID);
  END ELSE
  BEGIN ID + 0;
    VPN + NB2 * PHIDOT2 - NB1 * PHIDOT1;
  END

```

```

0000249
0000250
0000251
0000252
0000253
0000254
0000255
0000256
0000257
0000258
0000259
0000260
0000261
0000262
0000263
0000264
0000265
0000266
0000267
0000268
0000269
0000270
0000271
0000272
0000273
0000274
0000275
0000276
0000277
0000278
0000279
0000280
0000281
0000282
0000283
0000284
0000285
0000286
0000287
0000288
0000289
0000290
0000291
0000292
0000293
0000294
0000295
0000296
0000297
0000298
0000299
0000300
0000301
0000302
0000303
0000304
0000305
0000306
0000307
0000308
0000309
0000310
0000311
0000312
0000313
0000314

```

VPNPR + 0;	0000315
END;	0000316
END ELSE	0000317
BEGIN IB + - ID;	0000318
IE + IB + IC;	0000319
VE + V (IE + ALPHAI × (ISFC - ISC), VE, VEM1, VEDOTM1, ISE,	0000320
THETAME, CJOE, VCPOTE, NE, KE, RLE, CJE, CDE, ISFE, VEDOT,	0000321
IEPR);	0000322
VC + V (- IC + ALPHAN × (ISFE - ISE), VC, VCM1, VCDOTM1, ISC	0000323
, THETAMC, CJOE, VCPOTC, NC, KC, RLC, CJC, CDC, ISFC, VCDOT,	0000324
ICPR);	0000325
VBE + IB × RB + VE + IE × RE;	0000326
VCE + IE × RE + VE - VC + IC × RC;	0000327
IF VE = VEM1 THEN	0000328
BEGIN WRITE (LP, < "VE = VEM1" >);	0000329
DIEDVE + IEPR - ALPHAI × ISFC / THETAMC;	0000330
DICDVE + ALPHAN × ISFE / THETAME - ICPR;	0000331
END ELSE	0000332
BEGIN DIEDVE + IEPR - ALPHAI × ISFC × (VC - VCM1) / ((VE -	0000333
VEM1) × THETAMC);	0000334
DICDVE + ALPHAN × ISFE / THETAME - ICPR × (VC - VCM1) / (0000335
VE - VEM1);	0000336
END;	0000337
IF DIEDVE ≠ DICDVE THEN VBEPR + RB + (1 + RE × DIEDVE) / (0000338
DIEDVE - DICDVE) ELSE VBEPR + RB;	0000339
VPN + - VBE;	0000340
VPNPR + VBEPR;	0000341
END;	0000342
FJ + NB2 × PHIDOT2 - NB1 × PHIDOT1 - VPN - ID × R4;	0000343
GJ + NS2 × PHIDOT2 + NS1 × PHIDOT1 + IS × R3 - R2 × (IL - IS);	0000344
FPRID + - (NB2 × 2 × PHIDOTPR2 + NB1 × 2 × PHIDOTPR1 + R4 +	0000345
VPNPR);	0000346
GPRIS + NS2 × 2 × PHIDOTPR2 + NS1 × 2 × PHIDOTPR1 + R2 + R3;	0000347
IF FJ = 0 THEN FPRIS + 0 ELSE FPRIS + NS2 × NB2 × PHIDOTPR2 -	0000348
NS1 × NB1 × PHIDOTPR1;	0000349
GPRID + - FPRIS;	0000350
D + FPRID × GPRIS - FPRIS × GPRID;	0000351
IF D ≠ 0 THEN	0000352
BEGIN DELID + (- FJ × GPRIS + GJ × FPRIS) / D;	0000353
DELIS + (FJ × GPRID - GJ × FPRID) / D;	0000354
END ELSE DELID + DELIS + 0;	0000355
ID + ID + DELID;	0000356
IS + IS + DELIS;	0000357
IF SIGN (FJ) ≠ SIGN (FJM1) THEN ID + ID - 0.5 × DELID;	0000358
IF SIGN (GJ) ≠ SIGN (GJM1) THEN IS + IS - 0.5 × DELIS;	0000359
IF (ABS (DELID) > 0.0001 × ABS (ID) OR ABS (DELIS) > 0.0001 ×	0000360
ABS (IS)) AND CTS < 20 THEN GO TO LOOP;	0000361
IF CTS = 20 THEN CF + CF + 1;	0000362
IF ABS (PHIDOT2) < NV > ABS (PHIDOT1) AND 1 > TAUS / 2 THEN	0000363
BEGIN CNV + 1;	0000364
NOSW + TRUE;	0000365
END ELSE	0000366
BEGIN CNV + 0;	0000367
NOSW + FALSE;	0000368
END;	0000369
END INCREMENT;	0000370
DEFINE IROP1 = 15 #, ILI2 = 16 #, IROP2 = 31 #, INS1 = 32 #, INCL	0000371
= 38 #, IR10 = 39 #, IR4 = 44 #, IL00 = 45 #, IISAT2 = 50 #, IISD	0000372
= 51 #, IRD = 58 #, IISE = 59 #, IRB = 75 #;	0000373
BEGIN REAL X;	0000374
FOR J + 0 STEP 1 UNTIL 82 DO GROUP1 [J] + GROUP2 [J] + NAM2 [J]	0000375
+ " ";	0000376
GROUP1 [0] + "CORE1 ";	0000377
GROUP1 [ILI2] + "CORE2 ";	0000378
GROUP1 [INS1] + "WINDIN";	0000379

```

GROUP2 [INS1] + " GS "; 0000380
GROUP1 [IR10] + "RESIST"; 0000381
GROUP2 [IR10] + " ORS "; 0000382
GROUP1 [IL00] + "INDUCT"; 0000383
GROUP2 [IL00] + " ORS "; 0000384
GROUP1 [IISD] + "DIODE "; 0000385
GROUP1 [IISE] + "TRANSI"; 0000386
GROUP2 [IISE] + " STOR"; 0000387
FILL NAME [*] WITH "LI1 ", "LO1 ", "PHIR1 ", "PHIS1 ", "HA1 0000388
", "HQ1 ", "HN1 ", "LAMBDA", "NUD1 ", "FDB1 ", "FOPP1 ", 0000389
"LAMBDA", "NU1 ", "FB1 ", "F01 ", "ROP1 ", "LI2 ", "LO2 0000390
", "PHIR2 ", "PHIS2 ", "HA2 ", "HQ2 ", "HN2 ", "LAMBDA", "NUD2 0000391
", "FDB2 ", "FOPP2 ", "LAMBDA", "NU2 ", "FB2 ", "F02 ", 0000392
"ROP2 ", "NS1 ", "NS2 ", "NB1 ", "NB2 ", "NC1 ", "NC2 0000393
", "NCL ", "R10 ", "R11 ", "R12 ", "R2 ", "R3 ", "R4 0000394
", "L00 ", "ICON0 ", "LO1 ", "ICON1 ", "LO2 ", "ICON2 ", 0000395
"ISD ", "THETAM", "CJOD ", "VCPOTD", "ND ", "KD ", "RLD 0000396
", "RD ", "ISE ", "THETAM", "CJOE ", "VCPOTE", "NE ", "KE 0000397
", "RLE ", "RE ", "ISC ", "THETAM", "CJOC ", "VCPOTC", 0000398
"NC ", "KC ", "RLC ", "RC ", "RB "; 0000399
NAM2 [7] + "D1"; 0000400
NAM2 [11] + "1 "; 0000401
NAM2 [23] + "D2"; 0000402
NAM2 [27] + "2 "; 0000403
NAM2 [52] + "D "; 0000404
NAM2 [60] + "E "; 0000405
NAM2 [68] + "C "; 0000406
END X; 0000407
COMMENT: INITIALIZE CORE PARAMETERS.; 0000408
READMORE: READ (CR, /, TEMP) [EOF]; 0000409
BEGIN REAL PSEUDO; 0000410
LABEL DUMPLABEL; 0000411
DUMP LP (LI1, LO1, PHIR1, PHIS1, HA1, HQ1, HN1, LAMBDA1, NUD1, 0000412
FDB1, FOPP1, LAMBDA1, NU1, FB1, F01, ROP1, LI2, LO2, PHIR2, 0000413
PHIS2, HA2, HQ2, HN2, LAMBDA2, NUD2, FDB2, FOPP2, LAMBDA2, NU2 0000414
, FB2, F02, ROP2, NS1, NS2, NB1, NB2, NC1, NC2, NCL, R10, R11, 0000415
R12, R2, R3, R4, L00, ICON0, LO1, ICON1, LO2, ICON2, ISD, 0000416
THETAMD, CJOD, VCPOTD, ND, KD, RLD, RD, ISE, THETAME, CJOE, 0000417
VCPOTE, NE, KE, RLE, RE, ISC, THETAMC, CJOC, VCPOTC, NC, KC, 0000418
RLC, RC, RB, BETN, ICN, BETI, IEI) DUMPLABEL: 1; 0000419
FOR J + 0 STEP 1 UNTIL 75 DO READ (CR, /, VAL [J], NONU [J], 0000420
SDIFF [J]); 0000421
FOR J + 0 STEP 1 UNTIL 75 DO IF SDIFF [J] = 1 THEN WCSIGN [J] + "0000422
" ELSE IF SDIFF [J] = 0 THEN WCSIGN [J] + "0" ELSE WCSIGN [J] + "-"; 0000423
FOR J + 0 STEP 1 UNTIL 75 DO NONU [J] + 5 * NONU [J]; 0000424
FOR J + 0 STEP 1 UNTIL 75 DO WCVAL [J] + VAL [J] * (1 + SDIFF [ 0000425
J] * NONU [J] / 100); 0000426
WRITE (LP, HEAD, TEMP); 0000427
WRITE (LP, FF1, TEMP); 0000428
WRITE (LP, DATA, FOR J + 0 STEP 1 UNTIL IROP1 DO [GROUP1 [J], 0000429
GROUP2 [J], NAME [J], NAM2 [J], VAL [J], NONU [J], WCSIGN [J], 0000430
WCVAL [J]]); 0000431
WRITE (LP, DATA, FOR J + ILI2 STEP 1 UNTIL IROP2 DO [GROUP1 [J] 0000432
, GROUP2 [J], NAME [J], NAM2 [J], VAL [J], NONU [J], WCSIGN [J] 0000433
, WCVAL [J]]); 0000434
WRITE (LP, DATA, FOR J + INS1 STEP 1 UNTIL INCL DO [GROUP1 [J], 0000435
GROUP2 [J], NAME [J], NAM2 [J], VAL [J], NONU [J], WCSIGN [J], 0000436
WCVAL [J]]); 0000437
WRITE (LP [PAGE]); 0000438
WRITE (LP, FF2); 0000439
WRITE (LP, FF1, TEMP); 0000440
WRITE (LP, DATA, FOR J + IR10 STEP 1 UNTIL IR4 DO [GROUP1 [J], 0000441
GROUP2 [J], NAME [J], NAM2 [J], VAL [J], NONU [J], WCSIGN [J], 0000442
WCVAL [J]]); 0000443
WRITE (LP, DATA, FOR J + IL00 STEP 1 UNTIL IISAT2 DO [GROUP1 [J] 0000444
, GROUP2 [J], NAME [J], NAM2 [J], VAL [J], NONU [J], WCSIGN [J] 0000445

```

```

], WCVAL [J]);
WRITE (LP [PAGE]);
WRITE (LP, FF2);
WRITE (LP, FF1, TEMP);
WRITE (LP, DATA, FOR J + IISD STEP 1 UNTIL IRD DO [GROUP1 [J],
GROUP2 [J], NAME [J], NAM2 [J], VAL [J], NONU [J], WCSIGN [J],
WCVAL [J]);
WRITE (LP, DATA, FOR J + IISE STEP 1 UNTIL IRB DO [GROUP1 [J],
GROUP2 [J], NAME [J], NAM2 [J], VAL [J], NONU [J], WCSIGN [J],
WCVAL [J]);
WRITE (LP [PAGE]);
TRANSFER (76, WCVAL, LI1);
WRITE (LP [PAGE]);
READ (CR, /, NP, FOR J + 0 STEP 1 UNTIL NP + 1 DO [ICN [J],
BETN [J]);
READ (CR, /, IP, FOR J + 0 STEP 1 UNTIL IP + 1 DO [IEI [J],
BETI [J]);
FOR J + 0 STEP 1 UNTIL NP + 1 DO ICN [J] + ICN [J] * Q-3;
FOR J + 0 STEP 1 UNTIL IP + 1 DO IEI [J] + IEI [J] * Q-3;
DUMPLABEL: HS1 + HA1 + HQ1 + HN1 + PHIR1 * (HA1 + HQ1 - HN1) /
PHIS1;
HS2 + HA2 + HQ2 + HN2 + PHIR2 * (HA2 + HQ2 - HN2) / PHIS2;
HTH1 + (HS1 - SQRT (HS1 * 2 - 8 * HA1 * HQ1 * (1 + PHIR1 /
PHIS1))) / 4;
HTH2 + (HS2 - SQRT (HS2 * 2 - 8 * HA2 * HQ2 * (1 + PHIR2 /
PHIS2))) / 4;
F121 + HTH1 * LI1;
F122 + HTH2 * LI2;
F231 + HTH1 * LO1;
F232 + HTH2 * LO2;
V11 + (PHIS1 - PHIR1) / ((LO1 - LI1) * HA1);
V12 + (PHIS2 - PHIR2) / ((LO2 - LI2) * HA2);
V21 + (PHIS1 + PHIR1) * HQ1 / ((LO1 - LI1) * HN1);
V22 + (PHIS2 + PHIR2) * HQ2 / ((LO2 - LI2) * HN2);
RLE + RLE * RLD / (RLE + RLD);
END PSEUDO;
FOR VS + 23.2 STEP 0.1 UNTIL 23.5 DO
BEGIN COMMENT -10 DEGREES;
  BOOL + TRUE;
  CONFAC + 2.50;
  TRANS + FAILURE + FALSE;
  TR + (0.11 + 0.0023077 * (VS - 28.0)) * Q-6;
  CAPIL + 0.152 - 0.004 * (28.0 - VS);
  TSL + 0.545454 * TR;
  SL + 1.39 * CAPIL / TR;
  CAPIS + VS / R11 * R2 / (R2 + 0.6 * ROP1 * (NS1 * 2 + NS2 * 2))
  ;
  PHIDOT12 + ABS (NB2 * 0.6 * ROP1 * ((NS1 * NB2 + NS2 * NB1) *
  CAPIS - (NB1 + NB2) * FOPP1) - NB1 * 0.7) / (NB1 * 2 + NB2 * 2)
  ;
  NV + 0.001 * PHIDOT12;
  NEWVS + TRUE;
  MODES: IF MODE ≠ 0 AND NOT NEWVS THEN PRINTOUT;
  PHI1 + PHI1 - F1 * V11 * LN ((HA1 * LO1 + ABS (F1)) / (HA1 *
  LI1 + ABS (F1)));
  IF ABS (PHI1) > PHIR1 THEN PHI1 + PHIR1 * SIGN (PHI1);
  PHI2 + PHI2 - F2 * V12 * LN ((HA2 * LO2 + ABS (F2)) / (HA2 *
  LI2 + ABS (F2)));
  IF ABS (PHI2) > PHIR2 THEN PHI2 + PHIR2 * SIGN (PHI2);
  VCE + VS;
  VC + - VS;
  IL + ILM1 + ILM2 + ILDOT + ILDOTM1 + IC + ICM1 + ICM2 + ICDOT +
  ICDOTM1 + 0.0;
  ICL + ICLM1 + ICLM2 + ICLDOT + ICLDOTM1 + IS + ISM1 + ISM2 + ID
  + IDM1 + IDM2 + 0.0;
  IB + IE + F1 + F1M1 + F2 + F2M1 + 0.0;

```

PHIDOT1 + PHIDOT1M1 + PHIDOTPR1 + 0.0;	0000512
PHIDOT2 + PHIDOT2M1 + PHIDOTPR2 + 0.0;	0000513
PHIDOTE1 + PHIDOTEPR1 + PHIDOTMA1 + PHIDOTMAPR1 + 0.0;	0000514
PHIDOTE2 + PHIDOTEPR2 + PHIDOTMA2 + PHIDOTMAPR2 + 0.0;	0000515
VD + VDM1 + VDM2 + IDPR + VDDOT + VDDOTM1 + VPN + VPNPR + ISFD	0000516
+ 0.0;	0000517
VE + VEM1 + VEM2 + IEPR + VEDOT + VEDOTM1 + VBE + VBEPR + ISFE	0000518
+ DIEDVE + 0.0;	0000519
VCM1 + VCM2 + ICPR + VCDOT + VCDOTM1 + ISFC + DICDVE + 0.0;	0000520
FJ + FJM1 + GJ + GJM1 + FPRID + GPRIS + FPRIS + GPRID + D +	0000521
DELID + DELIS + DELT + 0.0;	0000522
T + 1020;	0000523
WRITE (OWT [DBL], FMT3, LIST3);	0000524
WRITE (OWT, TIMER, TIME (2) / 60, TIME (3) / 60);	0000525
CTS + CF + COUNT + CNVS + CNV + 0;	0000526
TRANS + FALSE;	0000527
T + 0.0;	0000528
IF NEWVS THEN GO TO MODE0;	0000529
IF BOOL THEN	0000530
BEGIN BOOL + FALSE;	0000531
IF MODE = 0 THEN GO TO MODE0 ELSE IF MODE = 2 THEN GO TO	0000532
MODE2 ELSE IF MODE = 4 THEN GO TO MODE4;	0000533
END;	0000534
BOOL + TRUE;	0000535
IF MODE = 0 THEN GO TO MODE1;	0000536
IF MODE = 1 THEN GO TO MODE2;	0000537
IF MODE = 2 THEN GO TO MODE3;	0000538
IF MODE = 3 THEN GO TO MODE4;	0000539
IF MODE = 4 THEN	0000540
BEGIN PHI1F4 + PHI1;	0000541
PHI2F4 + PHI2;	0000542
GO TO EOF;	0000543
END;	0000544
MODE0: MODE + 0;	0000545
IF BOOL THEN	0000546
BEGIN PHI1 + PHIR1;	0000547
PHI2 + - PHIR2;	0000548
END;	0000549
PHI1M2 + PHI1M1 + PHI1;	0000550
PHI2M2 + PHI2M1 + PHI2;	0000551
TAUS + 2 * PHIR1 * NB1 / 0.7;	0000552
DELT + TAUS / 150;	0000553
PRINthead;	0000554
NEWVS + FALSE;	0000555
SWITCHING0: T + T + DELT;	0000556
COUNT + COUNT + 1;	0000557
INCREMENT;	0000558
CNVS + CNVS + CNV;	0000559
PRINTOUT;	0000560
IF NOT NOSW AND (CNVS ≤ 30 OR PHI1 < - 0.1 * PHIR1) THEN GO TO	0000561
SWITCHING0;	0000562
GO TO MODE5;	0000563
MODE1: MODE + 1;	0000564
TAUS + 2 * PHIR1 / PHIDOT12;	0000565
PRINthead;	0000566
SWITCHING1: IF T < TR THEN DELT + TAUS / 300 ELSE IF MAX (ABS (0000567
PHIDOTMA1), ABS (PHIDOTMA2)) > 20 * NV THEN DELT + TAUS / 60	0000568
ELSE DELT + TAUS / 30;	0000569
DELT + DELT / CONFAC;	0000570
T + T + DELT;	0000571
COUNT + COUNT + 1;	0000572
INCREMENT;	0000573
IF VCE > 60 THEN WRITE (LP, FLAG3);	0000574
CNVS + CNVS + CNV;	0000575
PRINTOUT;	0000576
IF VCE < 1.0 THEN WRITE (OWT, FLAG1);	0000577

IF NOSW AND (CNVS > 30 OR PHI1 > - 0.9 * PHIR1) THEN	0000578
BEGIN T1 + T;	0000579
GO TO MODES;	0000580
END ELSE GO TO SWITCHING1;	0000581
MODE2: MODE + 2;	0000582
PHI1M2 + PHI1M1 + PHI1F1 + PHI1;	0000583
PHI2M2 + PHI2M1 + PHI2F1 + PHI2;	0000584
TAUS + 2.0 * PHIR1 * NB1 / 0.7;	0000585
DELT + TAUS / 150;	0000586
PRINthead;	0000587
SWITCHING2: T + T + DELT;	0000588
COUNT + COUNT + 1;	0000589
INCREMENT;	0000590
CNVS + CNVS + CNV;	0000591
PRINTOUT;	0000592
IF NOSW AND (CNVS > 30 OR PHI1 < - 0.1 * PHIR1) THEN	0000593
BEGIN T2 + T;	0000594
GO TO MODES;	0000595
END ELSE GO TO SWITCHING2;	0000596
MODE3: MODE + 3;	0000597
PHI1M2 + PHI1M1 + PHI1F2 + PHI1;	0000598
PHI2M2 + PHI2M1 + PHI2F2 + PHI2;	0000599
TAUS + 2 * PHIR1 / PHIDOT12;	0000600
NA + 1;	0000601
IA + 1;	0000602
INTERPOL (NP, ICN, BETN, NCOEF);	0000603
INTERPOL (IP, IEI, BETI, ICOEF);	0000604
PRINthead;	0000605
SWITCHING3: IF T < 2 * TR OR (PHI1 > PHIR1 AND PHI2 > 0.8 * PHIR2) OR (PHI1 > PHIR2 AND PHI2 < - PHIR2) THEN DELT + TAUS /	0000606
300 ELSE DELT + TAUS / 100;	0000607
DELT + DELT / CONFAC;	0000608
T + T + DELT;	0000609
COUNT + COUNT + 1;	0000610
IF VPN < - 0.1 AND NOT TRANS THEN	0000611
BEGIN TRANS + TRUE;	0000612
TV + T;	0000613
WRITE (LP, < "TV=", F10.6 >, TV * Q6);	0000614
END;	0000615
IF TRANS THEN	0000616
BEGIN BETAN + BETA (IC, NA, NCOEF, ICN, BETN, NP);	0000617
BETAI + BETA (IE, IA, ICOEF, IEI, BETI, IP);	0000618
ALPHA1 + BETAI / (1 + BETAI);	0000619
ALPHAN + BETAN / (1 + BETAN);	0000620
END;	0000621
INCREMENT;	0000622
CNVS + CNVS + CNV;	0000623
IF PHI2 > 0 < PHI1 AND VCE > 5 * VS THEN	0000624
BEGIN FAILURE + TRUE;	0000625
WRITE (OWT, FLAG2);	0000626
GO TO EXIT;	0000627
END;	0000628
PRINTOUT;	0000629
IF (NOSW AND (CNVS > 30 OR PHI1 > 0 AND PHI2 < 0)) OR (PHI1 > PHIR1 AND PHI2 < - 1.20 * PHIR2) OR (PHI1 ≥ PHIR1 AND PHI2 < - PHIR2 AND VCE > VS) OR (IC ≤ 0.001 AND PHI1 > 0 > PHI2) THEN	0000630
BEGIN T3 + T;	0000631
IF NOT TRANS THEN	0000632
BEGIN WRITE (LP, FLAG4);	0000633
GO TO EXIT;	0000634
END ELSE GO TO MODES;	0000635
END ELSE GO TO SWITCHING3;	0000636
MODE4: MODE + 4;	0000637
PHI1M2 + PHI1M1 + PHI1F3 + PHI1;	0000638
PHI2M2 + PHI2M1 + PHI2F3 + PHI2;	0000639
TAUS + 2 * PHIR1 * NB1 / 0.7;	0000640
	0000641
	0000642
	0000643

DELT + TAUS / 150;	0000644
PRINTHEAD;	0000645
SWITCHING4: T + T + DELT;	0000646
COUNT + COUNT + 1;	0000647
INCREMENT;	0000648
CNVS + CNVS + CNV;	0000649
PRINTOUT;	0000650
IF NOSW AND (CNVS > 30 OR PHI1 < - 0.1 × PHIR1) THEN	0000651
BEGIN T4 + T;	0000652
GO TO MODES;	0000653
END ELSE GO TO SWITCHING4;	0000654
EXIT;	0000655
END;	0000656
EOF: WRITE (LP, < 2 F20.2 >, TIME (2) / 60, TIME (3) / 60);	0000657
END.	0000658

REFERENCES

1. D. Nitzan, "Flux Switching in Multipath Cores," Report 1, for Jet Propulsion Laboratory, Contract 950095 under NASw-6, SRI Project 3696, Stanford Research Institute, Menlo Park, California (November 1961).
2. D. Nitzan and V. W. Hesterman, "Flux Switching in Multipath Cores," Report 2, for Jet Propulsion Laboratory, Contract 950095 under NASw-6, SRI project 3696, Stanford Research Institute, Menlo Park, California (November 1962).
3. D. Nitzan and V. W. Hesterman, "Flux Switching in Multipath Cores," Report 3, for Jet Propulsion Laboratory, Contract 950095 under NASw-6 SRI Project 3696, Stanford Research Institute, Menlo Park, California (June 1964).
4. D. Nitzan and V. W. Hesterman, "Flux Switching in Multipath Cores," Report 4, for Jet Propulsion Laboratory, Contract 950943 under NAS7-100, SRI Project 5094, Stanford Research Institute, Menlo Park, California (July 1965).
5. L. Néel, "Principles of a New General Theory of Coercive Force," *Ann. Univ. Grenoble*, Vol. 22, pp. 299-343 (1946). (English translation, ATS - 57H12F.)
6. J. E. Knowles, "A Further Explanation of the Shape of the Hysteresis Loop of 'Square Loop' Ferrites," *Proc. Phys. Soc. (GB)*, Vol. 77, pp. 225-229 (February 1961).
7. C. Kittel and J. K. Galt, "Ferromagnetic Domain Theory," *Solid State Physics*, Vol. III, pp. 437-565 (Academic Press, New York, N.Y. 1956).
8. D. Nitzan and V. W. Hesterman, "Elastic Flux-Switching Properties of a Thin Ferrite Core," *J. Appl. Phys.*, Vol. 37 (to be published March 1967).
9. F. C. Hewitt and W. M. Overn, "History Effect of Time-Limited Excitation," *J. Appl. Phys.*, Vol. 34, pp. 1117-1118 (April 1963).
10. N. Menyuk and J. B. Goodenough, "Magnetic Materials for Digital Computer Components, I--A Theory of Flux Reversal in Polycrystalline Ferromagnetics," *J. Appl. Phys.*, Vol. 26, pp. 8-18 (January 1955).
11. M. K. Haynes, "Model for Nonlinear Flux Reversals of Square-Loop Polycrystalline Magnetic Cores," *J. Appl. Phys.*, Vol. 29, pp. 472-474 (March 1958).
12. C. H. Lindsey, "The Square-Loop Ferrite Core as a Circuit-Element," *Proc. IEE (London)*, Vol. 106C, pp. 117-124 (September 1959).
13. W. Hilberg, "A Contribution to the Theory of Magnetic Reversal in Ferrites, II -- Wall-Shifting Model Taking into Account Non-Homogeneities and Anisotropies," *Frequenz*, Vol. 18, pp. 186-202 (June 1964). (English translation, FSTC 381 - T6470.)
14. G. T. Rado, R. W. Wright, and W. H. Emerson, "Ferromagnetism at Very High Frequencies, III -- Two Mechanisms of Dispersion in a Ferrite," *Phys. Rev.*, Vol. 80.2, pp. 273-280 (October 1950).
15. J. Smit and H. P. J. Wijn, *Ferrites*, Ch.14 (John Wiley & Sons, Inc., New York, N.Y., 1959).
16. G. T. Rado, V. J. Folen, and W. H. Emerson, "Effect of Magnetocrystalline Anisotropy on the Magnetic Spectra of Mg-Fe Ferrites," *Proc. IEE (London)*, Vol. 104, pp. 198-205 (October 1956).
17. S. E. Harrison, C. J. Kriessman, and S. R. Pollack, "Magnetic Spectra of Manganese Ferrites," *Phys. Rev.*, Vol. 110.4, pp. 844-849 (May 1958).
18. D. Nitzan, "Computation of Flux Switching in Magnetic Circuits," *IEEE Trans. on Magnetics*, Vol. MAG-1, pp. 222-234 (September 1965).
19. V. W. Hesterman, "Flux-Switching Properties of a Partially Set Core," Tech. Report 5, Contract Nonr 2712(00), SRI Project 2697, Stanford Research Institute, Menlo Park, California (November 1963).

20. V. W. Hesterman, "Switching Properties of a Partially Set Square-Loop Ferrite Core," *IEEE Trans. on Magnetics*, Vol. MAG-1, pp. 309-314 (December 1960).
21. V. T. Shahan and O. A. Gutwin, "Threshold Properties of Partially Switched Ferrite Cores," *J. Appl. Phys.* Vol. 33, Supplement, pp. 1049-1050 (March 1962).
22. P. E. Gray, D. DeWitt, A. R. Boothroyd, and J. F. Gibbons, *Physical Electronics and Circuit Models of Transistors* (John Wiley & Sons, Inc., New York, N.Y., 1964).
23. C. L. Searle, A. R. Boothroyd, E. J. Angelo, Jr., P. E. Gray, and D. O. Pederson, *Elementary Circuit Properties of Transistors* (John Wiley & Sons, Inc., New York, N.Y., 1964).
24. W. Hochwald and C. T. Kleiner, "Digital Simulation of Nonlinear Electromagnetic Circuits," *IEEE Trans. on Magnetics*, Vol. MAG-2, pp. 532-539 (September 1966).
25. J. B. Scarborough, *Numerical Mathematical Analysis*, Ch. 9 (John Hopkins Press, Baltimore, Md., 1950).

INDEX

- Active-region of transistor, experiment, 121
- Air flux, 18, 33
- Analysis of binary counter, 140, 143-161
 - worst case, 175, 179-182
- Anisotropy constant, 40

- Beta vs. I_c of a transistor:
 - inverse, 127, 130
 - normal, 127, 129
- Binary counter, core-diode-transistor:
 - circuit, 68-69
 - computer analysis, 140, 143-211
 - circuit equations, 140, 143-144
 - computation methods, 144-150
 - computer program, 150-161, 201-211
 - modes of operation, 68, 70-71
 - plots of $\phi_1(F_1)$ and $\phi_2(F_2)$, 175-178
 - $T = -10^\circ\text{C}; V_s = 15 \text{ V}$, 176
 - $T = 25^\circ\text{C}; V_s = 28 \text{ V}$, 177
 - $T = 85^\circ\text{C}; V_s = 50 \text{ V}$, 178
 - propagation of COUNT states, 71-73
 - table of core and circuit parameters, 141-142
 - $V_{s,\text{max}}$ factors, 78-80
 - flow chart, 80
 - $V_{s,\text{min}}$ factors, 74-77
 - flow chart, 76
 - waveforms of flux and drive currents, 68, 70
 - waveforms of time variables, exp. vs. comp., 161-175
 - discussion, 174-175
 - $T = -10^\circ\text{C}; V_s = 15 \text{ V}$, 162-165
 - $T = 25^\circ\text{C}; V_s = 28 \text{ V}$, 160-169
 - $T = 85^\circ\text{C}; V_s = 50 \text{ V}$, 170-173
 - worst-case $V_{s,\text{min}}$, 175, 179-182
 - computation method, 152, 179
 - conclusions, 182
 - for $d_{\text{max}} = 0$, 179
 - initial ϕ_1 and ϕ_2 at each mode, 180, 182
 - sign S determination, 180
 - $V_{s,\text{min}}$ vs. d_{max} , 179-181

- Capacitance, diode model, 86-87, 120
- Capacitances, transistor model:
 - diffusion, 88-89, 133-139
 - junction, 88-89, 130-134
- Circuit, binary counter, 68-69
- Circuit parameters, binary counter, table of, 141-142

- CLEAR MMF:
 - binary counter, 68-73
 - flux-switching experiment, 15-17
- Coaxial transmission line—See Transmission line
- Collector-base equations in transistor model, 89
- Complex permeability, 19, 41-43
- Computation of:
 - binary-counter analysis, 140, 143-161
 - binary-counter, worst case, 175, 179-182
 - core parameters, dynamic, 102, 105
 - core parameters, static, 97, 100
 - diode parameters, 116
 - $F(t)$ for voltage drive, 47-49
 - inductor parameters, 109
 - transistor parameters, diffusion
 - capacitances, 134, 136-139
 - transistor parameters, junction
 - capacitances, 131, 133
 - transistor parameters, static, 126-127
- Computer program:
 - binary counter, 150-161, 201-211
 - diode parameters, 116, 197
 - inductor parameters, 109, 195
 - static $\phi(F)$ parameters, 97, 100, 187-190
 - transistor parameters, 127, 199-200
 - voltage drive, 48-49, 183-185
 - $\dot{\phi}_p(F)$ parameters, 105, 191-193
- Constant:
 - anisotropy, 40
 - viscous, 40
- Core parameters:
 - E-6, 36
 - Lockheed 100SC1, 141
- Core holder, 53
- Core model, 81-83
 - elastic flux switching, 81-82
 - inelastic flux switching, 82
 - parameters, 83
 - static $\phi(F)$, 82-83
- Core-model parameters, 91-107
 - dimensions, 91
 - dynamic, $\dot{\phi}_p(F)$, 100-107
 - computation, 102, 105
 - discussion, 105
 - measurement, 100, 102
 - results, exp. vs. comp., 102-105
 - temperature effect on, 105-107
 - static $\phi(F)$, 91-100
 - computation, 97, 100
 - discussion, 100
 - measurement, 91-97
 - results, exp vs. comp., 97-99
 - temperature effect on, 100-101
- Core parameters, table of, 141
- COUNT, propagation of in a binary counter, 71-73
- Counter, binary—See binary counter, core-diode-transistor

Cut-off region of transistor, experiment, 123

Damped precession of magnetization, 9-10

Damping coefficient ζ :

- definition, 12
- rotational, 37
- wall motion, 37

Damping, viscous—See Viscous damping

Decaying inelastic flux-switching component, 21-24

- disappearance in high F , 44-45
- effect in partial-set switching, 63

Delay line in mercury-relay pulser, 30-32

Delta noise, 23-24

Demagnetized state, 51

Dimensions of core, 91, 141

Diode model, 85-87

- dynamic characteristics, 86-87
- parameters, 87
- static characteristics, 85-86

Diode-model parameters, 109, 114-120

- dynamic, 120
- static, forward, 109, 114-116
 - computation, 116
 - measurement, 109
 - results, exp. vs. comp., 114-116
 - temperature effect on, 116-117
- static, reverse, 116, 118-119
 - measurement, 116
 - temperature effect on, 116, 119

Disappearance of $\dot{\phi}$ component:

- $\dot{\phi}_i$ in high F , 44-45
- $\dot{\phi}_{ew}$ in high transverse field, 18

Dispersion of magnetic spectrum, 19

Displacement, wall—See Domain-wall displacement

Distribution of H_{th} , 6-7

Domain-wall displacement:

- effect on partial-set switching, 57, 63
- elastic, 4
 - equation of motion, 7-8
- inelastic, 4
- irreversible, 5
- reversible, 5

Domain-wall motion:

- disappearance in high transverse field, 18-19
- elastic, 4, 19-20
 - equation, 7-8
- irreversible, 5
- mass, 7
- reversible, 5
- stiffness, 7
- types, 4-5
- viscous damping, 7

Domain-wall position, effect on:

- energy, 2
- energy gradient, 3

Duration:

- between pulses, 51, 52
- of pulses, 51

Dynamic properties of:

- core, 100-107
- diode, 120
- transistor, 127-139

Ebers-Moll model, 90

Elastic flux-switching model:

- components, evidence for, 18-19
- experimental verification, 33-36
- rotational component, 20
- total, 20-21
- wall-motion component, 19-20

Elastic switching parameters, 33-34

Elastic wall displacement:

- condition, 4
- definition, 4
- equation of motion, 7-8

Emitter-base equations in transistor model 87-88

Energy gradient vs. wall position, 3

Energy vs. wall position, 2, 63

Equation of motion of elastic wall displacement, 7-8

Experiment:

- diode static parameters, 109, 116
- flux switching, 15-18, 26, 29-33
- flux switching from partially set states, 51, 53
- inductor parameters, 108
- static $\phi(F)$ parameters, 91-97
- transistor parameters:
 - dynamic, 130-131, 133, 135
 - static, 121-123

$\dot{\phi}_p(F)$ parameters, 100, 102

Experimental verification for flux-switching models:

- $T_r = 65$ ns, 26-27
- $T_r = 13$ ns, 26, 28
- $T_r = 0.4$ ns, 33-40
 - elastic $\dot{\phi}$ only, 33-36.
 - elastic and inelastic $\dot{\phi}$, 34-40

Fall time of PARTIAL-SET pulse, 51

Ferrite:

- copper-manganese, 57
- dispersion of magnetization, 11, 44
- grains, 63
- magnesium-manganese-zinc, 40

Failure of binary counter operation, 74-81

$V_{s,max}$, 78-80

$V_{s,min}$, 74-77

Flow chart for spurious transistor turn-off:

$V_{s,max}$, 80

$V_{s,min}$, 76

Flux, air—See Air flux

- Flux-switching experiment:
 - from partially-set states, 51, 53
 - general, 15-18
 - with short T_r , 26, 29-33
- Flux-switching experimental results—See
Experimental verification for flux-switching models
- Flux switching from partially switched state, 51-66
- Flux-switching model, 81-83
 - elastic, 81, 82
 - inelastic, 82
 - parameters, 83
 - static $\phi(F)$, 82-83
- Flux-switching model components:
 - elastic, 18-21
 - rotational, 20
 - total, 20-21
 - wall-motion, 19-20
 - inelastic, 21-28
 - decaying $\dot{\phi}_i$, 21-24
 - main $\dot{\phi}_{ma}$, 24-28
- Flux-switching parameters:
 - core E-6, 36
 - core 100SC1, 141
- Forward characteristics of:
 - diode, 109, 114-116
 - transistor, 121-127
- Gilbert equation:
 - coefficients, 12-14
 - in rectangular coordinates, 8
 - in spherical coordinates, 9
 - solution for M along applied H, 10-11
- Grains, ferrite, 63
- History effect on flux switching, 51
- Holder, core, 53
- INCREMENT PROCEDURE, 152, 154, 159-161
- Inductor model, 83-85
 - parameters, 8
- Inductor-model parameters, 108-114
 - computation, 109
 - measurement, 108
 - results, exp. vs. comp., 108-113
 - temperature effect on, 109, 114
- Inelastic flux-switching model:
 - decaying $\dot{\phi}$ component, 21-24
 - experimental verification, 26-28, 34-40
 - main $\dot{\phi}_{ma}$ component, 24-28
- Inelastic wall displacement, 4
- Inertial terms in $\dot{\phi}_e$ model:
 - rotation of magnetization, 11, 20
 - wall motion, 7, 19
- Inverse-region of transistor, experiment, 122-123
- Irreversible wall displacement, 5
- Landau-Lifshitz equation:
 - coefficients, 12-14
 - in rectangular coordinates, 8
 - in spherical coordinates, 9
 - solution for M along applied H, 10-11
- Listing of computer programs:
 - binary counter, core-diode-transistor, 201-211
 - diode parameters, 197
 - inductor parameters, 195
 - static $\phi(F)$ parameters, 187-190
 - transistor parameters, 199-200
 - voltage drive, 183-185
 - $\dot{\phi}_p(F)$ parameters, 191-193
- Magnetic spectrum, 41-43
- Magnetization:
 - damped precession, 9-10
 - remanent, 5
 - rotation, 8-15
- Main inelastic flux-switching component, 24-28
- Maximum supply voltage of binary counter, 78-80
- Measurement of parameters:
 - core model:
 - dynamic, $\dot{\phi}_p(F)$, 100, 102
 - static $\phi(F)$, 91-97
 - diode model, static, 121-123
 - inductor model, 108
 - transistor model:
 - diffusion capacitances, 133, 135
 - junction capacitances, 130-131
 - static, 121-123
- Mercury-relay pulser, 29-33, 53
- Minimum supply voltage of binary counter, 74-77
- MMF vs. $\dot{\phi}$ and ϕ , iterative computation of, 45-46
- Model of:
 - core, 81-83
 - elastic flux switching, 81-82
 - inelastic flux switching, 82
 - parameters, 83
 - static $\phi(F)$ curve, 82-83
 - diode, 85-87
 - dynamic characteristic, 86-87
 - parameters, 87
 - static characteristic, 85-86
 - inductor, nonlinear, 83-85
 - parameters, 83
 - transistor, 87-90
 - parameters, 90
 - static and dynamic, 87-89
 - static (Ebers-Moll), 90
- Models for flux-switching components:
 - elastic:
 - experimental verification, 33-36
 - rotational, 20
 - total, 20-21
 - wall motion, 19-20

Models for flux-switching components: *continued*
 inelastic: .
 decaying ϕ_i , 21-24
 experimental verification, 26-28, 34-37
 main $\dot{\phi}_{ma}$, 24-28, 52, 58, 60, 65

Modes of operation, binary counter, 68, 70-71

Modification of parabolic model, 58, 60

Mounting, core, 53

Newton-Raphson method, 140-150

Noise, delta—*See* Delta noise

Nonuniformity of parameters, 150-151, 179-182

Operation, binary counter 68-73

Oscillograms of waveforms—*See* Waveforms of

Oscilloscope:
 overshoot, 53
 response time, 32, 34, 53

Outline of computer programs:
 binary counter, INCREMENT PROCEDURE, 159-161
 binary counter, main, 152-158
 voltage drive, 48-49

Parabolic model for $\dot{\phi}(\phi)$, 24-25, 58, 60, 63, 65, 82

Parameter determination for:
 core model, 91-107
 dimensions, 91
 dynamic $\dot{\phi}_p(F)$, 100-107
 static $\phi(F)$, 91-100
 diode model, 109, 114-120
 dynamic, 120
 static, forward, 109, 114-116
 static, reverse, 116, 118-119
 inductor model, 108-114
 transistor model, 120-139
 dynamic, 127-139
 static, 121-127

Parameter determination method, 90

Parameters of binary-counter device model,
 table of, 141-142

Parameters of Core E-6, 33-34, 36

Parameters of model of:
 Core, 83
 diode, 87
 inductor, 83
 transistor, 90

Parameter nonuniformity, 150-151, 179-182

PARTIAL-SET pulse, 51-65

Partial setting effects, 51-52, 54, 57, 65

Partially set flux switching, 51-66

Peak $\dot{\phi}$ vs. F :
 determination, 100-107
 model, 86-87

Peak of $\dot{\phi}(t)$, 52, 60, 63

Peaking time of $\dot{\phi}(t)$, 51, 52, 65

Permeability:
 complex, 19, 41-43
 resonance, 42-43

Precession of magnetization, damped, 9-10

Predictor-corrector method, 145

Program, binary counter:
 features, 150-152
 initial conditions, 151
 listing, 201-211
 modes, 151-152
 outline, 152-161

Program, voltage drive:
 listing, 183-185
 outline, 48-49

Propagation of COUNT states in a binary
 counter, 71-73

Pulse, current, 26-36, 51-52, 54

Pulser, mercury-relay, 29-33, 53

Rectangular voltage drive, 47, 49-50
 $F(t)$ waveform, computed, 50

Re-entrant $M(H)$ loop, 5-6

Relaxation effects, 51, 54, 57, 65

Relaxation of magnetization, 51-52

Remanent magnetization, 5

Resonance:
 frequency, 42-43
 μ value, 43

Response time of oscilloscope, 32, 34, 53

Reverse characteristics of:
 diode, 116, 118-119
 transistor, 119, 127

Reversible wall displacement, 5

Rise time, effect on C_i , 23

Rise time effect on $\dot{\phi}_e$ differential equation, 19-21

Rise-time in flux-switching experiment:
 $T_r = 65$ ns, 26-27
 $T_r = 13$ ns, 26, 28
 $T_r = 0.4$ ns, 18, 26, 29-33

Rise time of oscilloscope, 32, 34, 53

Rotation of magnetization, component along
 applied field vs. t :

 Landau-Lifshitz or Gilbert eq., 10-11
 relationship among coefficients, 12-14
 second-order diff. eq., 11-12

Rotation of magnetization, equation of motion, 8-15
 Gilbert equation, 8
 in spherical coordinates, 8-9
 Landau-Lifshitz equation, 8

Rotation of magnetization, model for, 20

- Second-order differential equation for elastic $\dot{\phi}$:
 - domain-wall motion, 7, 19
 - rotation of magnetization, 11, 20
- Sense winding, 29-30, 53
- Short-rise time experiment, 26, 29-33
- Shuttle switching, 17
- Sinusoidal voltage drive, 47-50
 - $F(t)$ waveform, computed, 50
- Slope of:
 - energy hill, 3-5, 63
 - $\dot{\phi}_p(F)$, 51, 54, 58
- Spectrum, magnetic—See Magnetic spectrum
- Spurious transistor turn-off in binary counter, 74-81
 - $V_{s,max}$, 78-80
 - $V_{s,min}$, 74-77
- Squareness ratio ϕ_r/ϕ_s , 44
- States of COUNT in a binary counter, 71-73
- Static $M(H)$, 5-7
- Static $\phi(F)$:
 - computation, 97, 100
 - discussion, 100
 - measurement, 91-97
 - results, exp. vs. comp., 97-99
 - temperature effect on, 100-101
- Susceptibility:
 - rotational, 14-15
 - wall-motion, 8
- Switching—See Flux switching
- Switching parameters—See Flux-switching parameters
- Table of core and circuit parameters of binary counter, 141-142
- Table of COUNT propagation in binary counter, 72
- Temperature effect on:
 - core static parameters $\phi(F)$, 100-101
 - core $\dot{\phi}_p(F)$ parameters, 105-107
 - diode parameters, 116-117, 119
 - inductor parameters, 109, 114
 - transistor capacitance parameters, 133-134, 139
 - transistor static parameters, 127-130
- TEST pulse, 29-32, 51-63
- Thermodynamics:
 - first law, 2
 - of magnetization, 2-3
- Thin core, 36, 52
- Threshold of:
 - H , 4-6
 - static $\phi(F)$, 57, 63, 82-83
 - $\dot{\phi}_i$, 21-23
 - $\dot{\phi}_p(F)$, 25, 51, 54, 57-58, 82
- Time duration T_b , 51
- Transistor model, 87-90
 - parameters, 90
 - static and dynamic, 87-89
 - static (Ebers-Moll), 90
- Transistor-model parameters, 120-139
 - diffusion capacitances, 133-139
 - computation, 134, 136-139
 - measurement, 133, 135
 - oscillograms of $i_c(t)$, 137-138
 - results, exp. vs. comp., 139
 - temperature effects on, 139
 - junction capacitances, 130-134
 - computation, 131, 133
 - measurement, 130-131
 - results, exp. vs. comp., 131-133
 - temperature effect on, 133-134
 - static parameters, 121-127
 - computation, 126-127
 - measurement, 121-123
 - results, exp. vs. comp., 123-127
 - $R_{\phi_e}; R_{\phi_c}$, 119, 127
 - temperature effect on, 127-130
 - β_s vs. I_s , 127, 130
 - β_n^t vs. I_c^c , 127, 129
- Transistor turn-off, spurious, in binary counter, 74-81
 - $V_{s,max}$, 78-80
 - $V_{s,min}$, 74-77
- Transmission line, 29-33, 53
- Transverse field effect on $\dot{\phi}_{ew}$, 18-19
- Turns of binary-counter winding, 141
- Variation in core and circuit parameters, effect on $V_{s,min}$, 175, 179-182
- Viscous damping:
 - constant, 8, 40
 - rotation of magnetization, 8
 - wall motion, 7
- Voltage drive, 45-51
 - computer program, 48-49
 - $F(t)$ waveforms for rectangular and sinusoidal $\dot{\phi}(t)$, 50
 - iterative computation of $F(\dot{\phi}, \phi)$, 45-46
 - rectangular $\dot{\phi}(t)$, 47, 49-50
 - sinusoidal $\dot{\phi}(t)$, 47-50
- Voltage reference, 53
- $V_{s,max}$ in a binary counter, 78-80
- $V_{s,min}$ in a binary counter:
 - computed, worst case, 175, 179-182
 - factors, 74-77
- Wall of domain—See Domain wall
- Waveforms of:
 - current and flux linkage of nonlinear inductor, 109
 - drive currents and flux in binary counter, 70
 - $i_c(t)$ in response to Δi_b , 138
 - $F(t)$ for rectangular and sinusoidal $\dot{\phi}(t)$, 50

INDEX

Waveforms of: *continued*

- $F(t)$ and $\dot{\phi}(t)$ in flux-switching experiment, 16
 - $F(t)$ and $\dot{\phi}_e(t)$ in saturation, $T_r = 0.4$ ns, 35-36
 - time variables of a binary counter:
 - $T = -10^\circ\text{C}$; $V_s = 15$ V, 162-165
 - $T = 25^\circ\text{C}$; $V_s = 28$ V, 166-169
 - $T = 85^\circ\text{C}$; $V_s = 50$ V, 170-173
 - $\dot{\phi}(t)$ in the beginning of switching:
 - $T_r = 65$ ns, 27
 - $T_r = 13$ ns, 28
 - $T_r = 0.4$ ns, 38-40
 - $\dot{\phi}(t)$ for two F values and two T_{ps} values, 64
 - $\dot{\phi}(t)$ for two T_{ps} values, 62
 - $\dot{\phi}(t)$ for $\phi_{ps} \approx \phi_r$, 65
 - $\dot{\phi}(t)$ with F as a parameter, 62
 - $\dot{\phi}_e(t)$ components, 17
 - $\dot{\phi}_e(t)$ without and with magnet transverse field, 18
- Windings:
- binary counter, 69, 141
 - core, 53
- Worst-case analysis of binary counter, 175, 179-182
- computation method, 152, 179
 - conclusions, 182
 - $d_{\max} = 0$, 179
 - initial ϕ_1 and ϕ_2 in each mode for
 - $V_s = V_{s,\min}$, 180, 182
 - sign S determination, 180
 - $V_{s,\min}$ vs. d_{\max} , 179-181

**STANFORD
RESEARCH
INSTITUTE**

**Menlo Park
California**

Regional Offices and Laboratories

Southern California Laboratories
820 Mission Street
South Pasadena, California 91031

Washington Office
1000 Connecticut Avenue, N.W.
Washington, D.C. 20036

New York Office
270 Park Avenue
New York, New York 10017

Detroit Office
1025 East Maple Road
Birmingham, Michigan 48011

Chicago Office
103 S. Stone Avenue
La Grange, Illinois 60525

Huntsville, Alabama
4810 Bradford Drive, N.W.
Huntsville, Alabama 35805

European Office
Pelikanstrasse 37
Zurich 1, Switzerland

Japan Office
Nomura Securities Building
1-1 Nihonbashidori, Chuo-ku
Tokyo, Japan

Retained Representatives

Toronto, Ontario, Canada
Cyril A. Ing
86 Overlea Boulevard
Toronto 17, Ontario, Canada

Milan, Italy
Lorenzo Franceschini
Via Macedonio Melloni, 49
Milan, Italy